بسم الله الرحمن الرحيم

Vertical Transport through an InAs/GaSb Heterojunction at High Pressures and Magnetic Fields

Umar Manzoor Khan-Cheema

A thesis submitted for the degree of
Doctor of Philosophy

Worcester College
Oxford
Hilary Term 1996

RADCLIFFE SCIENCE LIBRARY OXFORD
DEPOSITED
26 JUN 1997
THESIS

بسم الله الرحمن الرحيم

Vertical Transport through an InAs/GaSb Heterojunction at High Pressures and Magnetic Fields

Umar Manzoor Khan-Cheema

A thesis submitted for the degree of Doctor of Philosophy
Worcester College, Oxford
Hilary Term, 1996

ABSTRACT

The conduction band of InAs lies lower in energy than the GaSb valence band. In order to preserve continuity of the Fermi level across the interface, charge transfer takes place resulting in a confined quasi two dimensional electron gas (2DEG) in the InAs and a confined quasi two dimensional hole gas (2DHG) in the GaSb.

This is the first detailed study into vertical transport in an n-InAs/p-GaSb single heterojunction (SHET). Application of a forward bias (InAs negative with respect to GaSb) increases the 2DEG and 2DHG concentrations and, therefore, their confinement energies. Eventually a critical bias is reached where the electron confinement energy moves above the hole confinement energy (the theoretical voltage induced semimetal/semiconductor transition V_c). Any subsequent increase in voltage is expected to result in a current decrease, and a region of negative differential resistance (NDR) should occur.

The SHET can be grown with two distinct interface types, 'InSb-like' and 'GaAs-like'. This study shows for the first time that the SHET vertical transport characteristic is very dependent upon this interface monolayer. For example, the temperature dependence of the I/V trace in a SHET with a 'GaAs-like' interface is found to be weak, with similar current peak to valley ratios (PVR) at 300 and 77K. The 'InSb-like' SHET, however has a PVR that is very close to 1 at 300K, rising above 2 at 77K.

Hydrostatic pressure is used to alter reversibly the InAs conduction/GaSb valence band overlap Δ. Vertical transport measurements taken at pressure confirm that Δ reduces at the same rate for both interface types and that it is larger for the 'InSb-like' interface. Experimental I/V traces at various pressures are compared with the corresponding results from self-consistent band profile calculations. The subsequent discoveries are that NDR occurs after V_c for both interfaces, and that each interface supports a different conduction mechanism - with the 'GaAs-like' interface exhibiting NDR when the band overlap is calculated to be ~ -100 meV.

Magnetic fields have been applied both perpendicular and parallel to the SHET interface. The perpendicular field results provide additional evidence that the conduction process must be different at both interfaces and that NDR occurs after V_c. Parallel field I/V traces reveal an entirely different response for the two interface types.

بسم الله الرحمن الرحيم

For my parents who have nurtured and supported me through all aspects of life, my loving wife whose warmth and encouragement have aidied me to complete this study and my baby daughter Hafsah whose smiles light up my life every day

ACKNOWLEDGEMENTS

I would like to thank the many people who have helped me during the course of this DPhil. Dr Philip Klipstein, my supervisor, takes the majority of my gratitude. His all-round physics knowledge, research experience and non-stop enthusiasm have been an important factor throughout my research.

I would also like to thank Jason, my partner in crime, with whom I had many adventures and whose constant support and help have been invaluable; Sergey, for his troubleshooting abilities in both physics and computing; Bill who, despite supporting Crystal Palace, always managed to have a smile on his face; Thane, whose regular supply of cakes from Maison Blanc brightened up many a tea break; Georg whose enthusiasm and willingness to be patient with me whilst explaining theoretical concepts has been astounding; Andy who managed to turn his laboratory into a sci-fi lover's paradise; Peter, who's now making bombs or something; Ivan and Alex whose regular visits from Russia always bemused me; Hyunsik and Wahid for being gentle with me whilst attempting to understand my explanations and Dr Nigel Mason whose aspiration, it would seem, is to become a stand-up comedian.

I would also like to thank the army of laboratory technicians, managers and administrative staff who ensure the smooth running of the Clarendon every day.

Away from the hustle and bustle of the Clarendon, I owe a permanent debt of thanks to my parents who are always there when I need them and who financed my studies, my wife who has been very supportive throughout my write-up and my baby daughter for many an hour of stress during the night and stress relief during the day !

LIST OF ABBREVIATIONS

2D	2 Dimensional
2DEG	2 Dimensional Electron Gas
2DHG	2 Dimensional Hole Gas
3D	3 Dimensional
DMM	Digital Multimeter
HRTEM	High Resolution Transmission Electron Microscopy
IFM	Interface mode
I/V	Current/Voltage
LHE	Liquid Helium
LN	Liquid Nitrogen
MBE	Molecular Beam Epitaxy
MOVPE	Metal Organic Vapour Phase Epitaxy
NCA	Nickel-Chromium-Aluminium
NDR	Negative Differential Resistance
OI	Oxford Instruments
RHEED	Reflection High Energy Electron Diffraction
RITS	Resonant Interband Tunnel Structure
S&HC	Sample and Hold Circuit
SET	Stark Effect Transistor
SHET	(InAs/GaSb) Single HETerojunction
SiN	(non stoichiometric) Silicon Nitride
SL	SuperLattice
SRAM	Static Random Access Memory
TEM	Transmission Electron Microscopy
U/V	Ultra Violet

CONTENTS

1 INTRODUCTION AND BACKGROUND 1

1.1 Introduction 2
1.2 III-V Semiconductors 3
1.3 The Esaki Tunnel Diode 5
1.4 Semiconductor Heterostructures 7
1.5 The InAs/GaSb Single Heterojunction 9
1.5.1 Unusual Properties of the Antimonide System 11
1.5.2 Resonant Conduction 12
1.6 Potential Application of Antimonides 15
1.6.1 Static Random Access Memory 15
1.6.2 Stark Effect Transistor 16
1.6.3 Mid Infra-red Laser 16
1.7 Outline of Thesis 17
1.8 References 19

2 SAMPLE GROWTH, CHARACTERISATION AND PROCESSING 22

2.1 Introduction 23
2.2 MOVPE Growth 23
2.2.1 Molecular Beam Epitaxy 25
2.3 Interface Characterisation 26
2.3.1 Raman Measurements 26
2.3.2 Transmission Electron Microscopy 29
2.4 Sample Processing and Contacting 31
2.5 References 35

3 EXPERIMENTAL TECHNIQUES 36

3.1 Introduction 37
3.2 Vertical Transport Measurements 37
3.2.1 I/V measurements 37
3.2.2 Hysteresis in the I/V 39
3.2.3 Pulsed Measurements 41
3.3 Hydrostatic Pressure 42
3.3.1 The 'Cambridge' Cell 42
3.3.2 The 'Russian' Cell 45
3.4 Low Temperatures 47
3.5 High Magnetic Fields 49
3.5.1 DC Field 49
3.5.2 Pulsed Field 50
3.6 References 51

4 BAND PROFILE CALCULATIONS 53

4.1 Introduction 54
4.2 Initial Potential Approximation 56
4.3 The Schrödinger Equation 58
4.4 The Poisson Equation 60
4.5 Background Doping 61
4.5.1 GaSb 61
4.5.2 InAs 62
4.5.3 Interface States 63
4.5.4 Effect on the Band Profile 64
4.6 InAs Band Non-Parabolicity 65
4.7 The Fermi Level 66
4.8 Applying a Bias 67
4.9 Pressure Dependence 68
4.10 References 69

5 SAMPLE DEVELOPMENT AND TEMPERATURE DEPENDENCE 71

5.1 Introduction 72
5.1.1 Naming Convention and Accuracy of Readings 73
5.2 Sample Development 74
5.2.1 The Early Samples 74
5.2.2 The Latest Samples 76
5.2.2.1 Switching Sequence C 77
5.2.2.2 Switching Sequence B 80
5.2.2.3 Switching Sequence A 81
5.2.3 Summary 83
5.3 Temperature Dependence 84
5.3.1 Effect of Temperature on the InAs/GaSb SHET 84
5.3.2 Experimental Results from 1.4 to 300K 87
5.3.2.1 The 'InSb-like' Interface 88
5.3.2.2 The 'GaAs-like' Interface 90
5.3.3 Discussion of Low Temperature Results 92
5.4 The Background Current 93
5.5 References 97

6 I/V MEASUREMENTS AT HYDROSTATIC PRESSURE 99

6.1 Introduction 100
6.2 Effect of Hydrostatic Pressure on SHETs 102
6.3 Reverse Bias Characteristics at Hydrostatic Pressure 104
6.3.1 Experimental Results 106
6.3.2 Comparison with Literature 108
6.4 Dependence of NDR on Hydrostatic Pressure 111
6.4.1 Results for the 'InSb - like' Interface 112
6.4.2 Results for the 'GaAs - like' Interface 119
6.4.3 The Background Current's Variation with Pressure 124
6.5 The NDR Mechanism Revisited 126
6.5.1 'InSb-like' Interface 126

6.5.2 'GaAs-like' Interface 131
6.6 Summary 133
6.7 References 133

7 MAGNETIC FIELD MEASUREMENTS 136

7.1 Introduction 137
7.1.1 Electrons in a Magnetic Field 138
7.2 Field Perpendicular to the Interface 140
7.2.1 'InSb - like' Interface 143
7.2.2 'GaAs - like' Interface 148
7.3 Field Parallel to the Interface 152
7.3.1 'InSb - like' Interface 153
7.3.2 'GaAs - like' Interface 155
7.4 Summary 156
7.5 References 157

8 CONCLUDING REMARKS 159

8.1 Summary 159
8.2 Future Development 162

APPENDIX A 165

APPENDIX B 166

1 Introduction and Background

1.1 Introduction 2
1.2 III-V Semiconductors 3
1.3 The Esaki Tunnel Diode 5
1.4 Semiconductor Heterostructures 7
1.5 The InAs/GaSb Single Heterojunction 9
1.5.1 Unusual Properties of the Antimonide System 11
1.5.2 Resonant Conduction 12
1.6 Potential Application of Antimonides 15
1.6.1 Static Random Access Memory 15
1.6.2 Stark Effect Transistor 16
1.6.3 Mid Infra-red Laser 16
1.7 Outline of Thesis 17
1.8 References 19

1.1 Introduction

In an ever changing world of improving technology we often take for granted what people just a few decades ago would never have dreamt of. The modern scramble for virtual reality, global communication systems, remote satellite sensing and intelligent household appliances all rely on the same fundamental building block - the humble silicon p-n junction.

The quest for faster and more efficient systems is pushing these technologies to their limits and the need to investigate alternatives has never been greater. Other bulk semiconductors proved not to be able to better the inherent advantages of silicon, such as the relative ease with which it could be gated.

With the advent of heterostructure growth, however, possibilities opened up for the production of devices with improved performance. Already, low power, low noise electrical components and low power lasers whose properties are 'tuned' at growth time are commercially available. Also, enhanced optical-electrical communication looks more of a reality as a result of studies into the vertical cavity laser [1].

The nearly lattice matched antimonide system is one of the newer and more promising heterostructure systems. It has already produced the highest frequency room temperature solid-state oscillator [2] and a static random access memory (SRAM) that is much smaller than the equivalent silicon based component [3].

This thesis contains the first detailed investigation into the vertical transport properties of a subset of the antimonide system, namely the InAs/GaSb single heterojunction (SHET). The SHET is interesting not only because of its unique physics, but also because of its potential use in industrial applications such as mobile proximity sensing equipment.

By varying the external conditions experienced by the SHET such as temperature, pressure and magnetic field, it has been possible to characterise the conduction mechanism in this structure for the first time. Not only does this thesis contain a plethora of previously unreported phenomena, but it also acts as a stepping stone on

the path to further technological advancement.

The aim of this first chapter is to provide a background for the research presented here. Accordingly, section 1.2 introduces some general solid-state physics concepts which aid in the understanding of semiconductor phenomena. Armed with the necessary knowledge, section 1.3 delves into the history of semiconductor research and discovers the Esaki tunnel diode. This diode is particularly relevant to the subject matter of this thesis as it was the first semiconductor component to exhibit negative differential resistance (NDR), and its transport mechanism is related to that of the SHET.

Semiconductor heterostructures are a relatively new innovation and an account of their history and usefulness is given in section 1.4. An introduction to the InAs/GaSb system is provided in section 1.5 with particular reference to its unique properties. Additionally, this section acts as a foundation for any future discussion regarding SHET resonant conduction.

The antimonide heterostructure family contains a rich variety of possible structures which form the basis for a large array of optical and electrical devices. An introduction to this topic would not be complete without a description of some experimentally realised antimonide based components, and section 1.6 presents the results of such studies. The chapter finishes with a thesis outline, mapping out the new observations made during this research and their possible implications.

1.2 III-V Semiconductors

This study begins by describing some general properties of III-V semiconductor compounds and the way in which these properties are represented in semiconductor physics.

Elements from group III and group V of the periodic table form III-V compounds by sp^3 hybridisation of their outer electrons, resulting in a lattice in which each element is tetrahedrally co-ordinated. This provides the crystal with a zincblende structure which consists of a face centred cubic lattice with a two atom basis (figure 1.1).

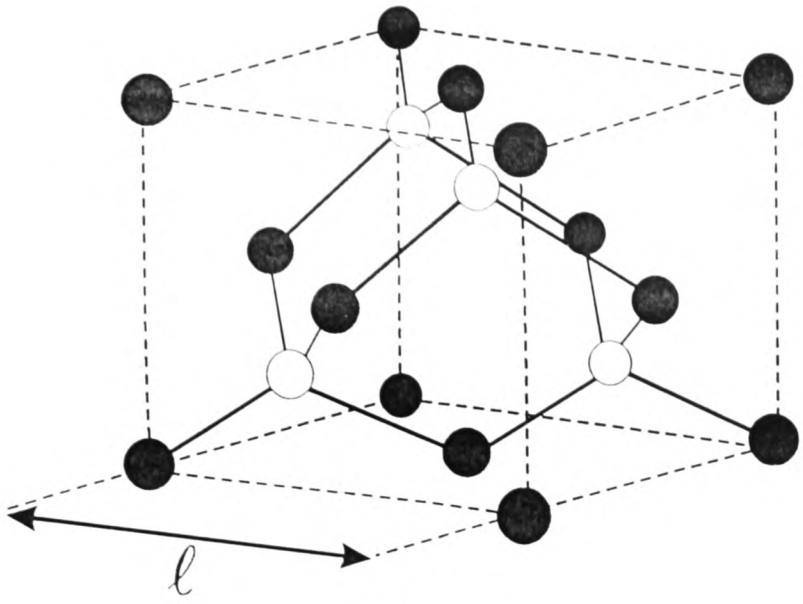


Figure 1.1. Conventional unit cell for the zincblende structure. It consists of a face centred cubic lattice with a basis of two elements, where each is offset in real space by (¼ℓ, ¼ℓ, ¼ℓ) from the other where ℓ is the lattice constant as depicted.

The wavefunction overlap of neighbouring electrons in the crystal cause degenerate atomic energy levels to broaden into a band, the lower and upper edges of which have bonding-type and antibonding-type wavefunctions respectively. The symmetry properties of the lattice mean these bands can be represented in reciprocal ($\boldsymbol{k}$) space by considering only the first Brillouin zone which for the zincblende structure forms a truncated octahedron (figure 1.2). In III-V structures the valence band, formed by bonding-type states, and the conduction band, formed by antibonding-type states, are separated by a $\boldsymbol{k}$-dependent energy gap. This gap can be small, as in the case of InSb, or can contain doping levels within roughly k_BT (where k_B is the Boltzmann constant) of either band edge as in GaAs - either of which makes III-V compounds behave as semiconductors. The effect of spin-orbit coupling on the valence band is to split its six-fold degeneracy at $\boldsymbol{k} = 0$, resulting in a four-fold degeneracy at the band edge and a two-fold degeneracy lying lower in energy (the spin split-off band). For $\boldsymbol{k} \neq 0$, the four-fold degeneracy splits, forming the light and heavy holes.

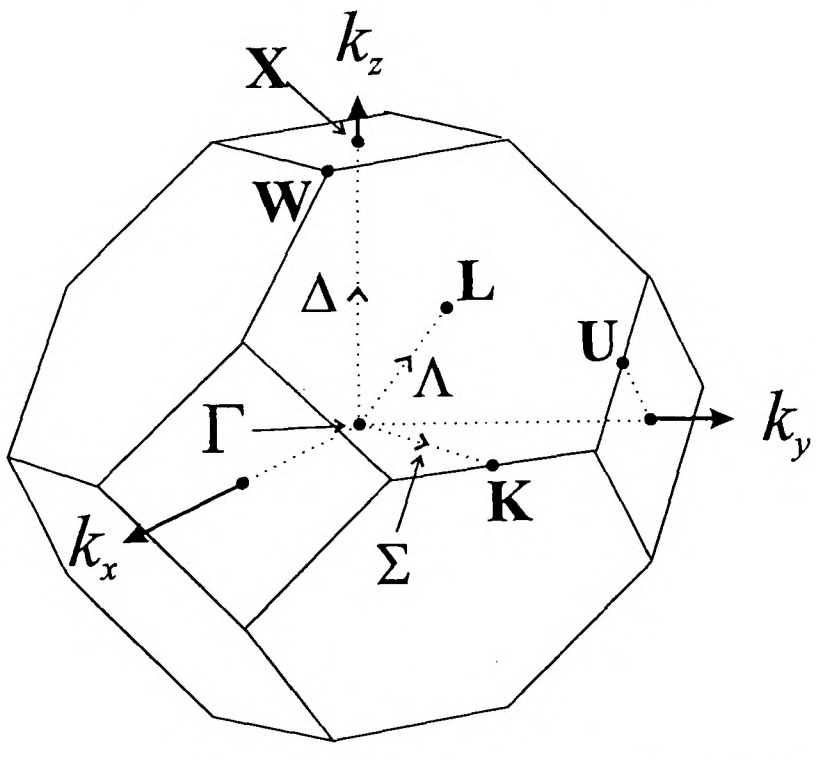


Figure 1.2. First Brillouin zone of the zincblende crystal lattice

In this thesis, only points in $\boldsymbol{k}$-space very close to the Brillouin zone centre (Γ point) are important as the III-Vs studied are direct gap semiconductors - where the conduction band

minimum and valence band maximum are coincident at the Γ point.

1.3 The Esaki Tunnel Diode

Having been acquainted with the tools and terminology of a semiconductor physicist, a well known and researched electronics component is introduced, namely the Esaki tunnel diode. This is not only because it was the first semiconductor device to exhibit NDR, but also because the transport behaviour is related to that of the structure under investigation in this thesis - the InAs/GaSb SHET.

1948 saw the beginning of a technological revolution - Bardeen and Brattain fabricated the first p-n junction using germanium [4]. They named it the transistor and predicted its usefulness as an amplifier, oscillator and a general replacement for the vacuum tube. Semiconductor research continued to advance at a startling rate during the 1950s, aided by improvements in silicon and germanium crystal quality and better manufacturing techniques.

It was amidst this fervent activity that, in 1958, Esaki proposed and demonstrated his tunnel diode [5]. This was simply a heavily doped p-n junction made from germanium with donor and acceptor concentrations in the region of 10^{19} cm^{-3}. The high level of doping meant the Fermi level lay well into the conduction band on the n-type side and well into the valence band on the p-type side, and it also allowed a very narrow junction width approaching 200Å.

The current/voltage (I/V) characteristic of a tunnel diode is illustrated schematically in figure 1.3, together with schematic representations of the band structure at various positions on the curve. With a small forward bias (n-side negative with respect to the p-side) a band of energies exists in which filled electron states on the n-side correspond to hole states on the p-side. The electrons can thus tunnel from the n-side to the p-side. The peak current is reached (point 2 on the curve) when the maximum number of electron and hole states are available for tunnelling. Any further increase in bias reduces the number of crossing electron and hole states, leading to a reduction in current as in point 3 on the curve. Applying a sufficient additional forward bias pushes the bottom of the conduction band opposite the top of the valence band (point 4)

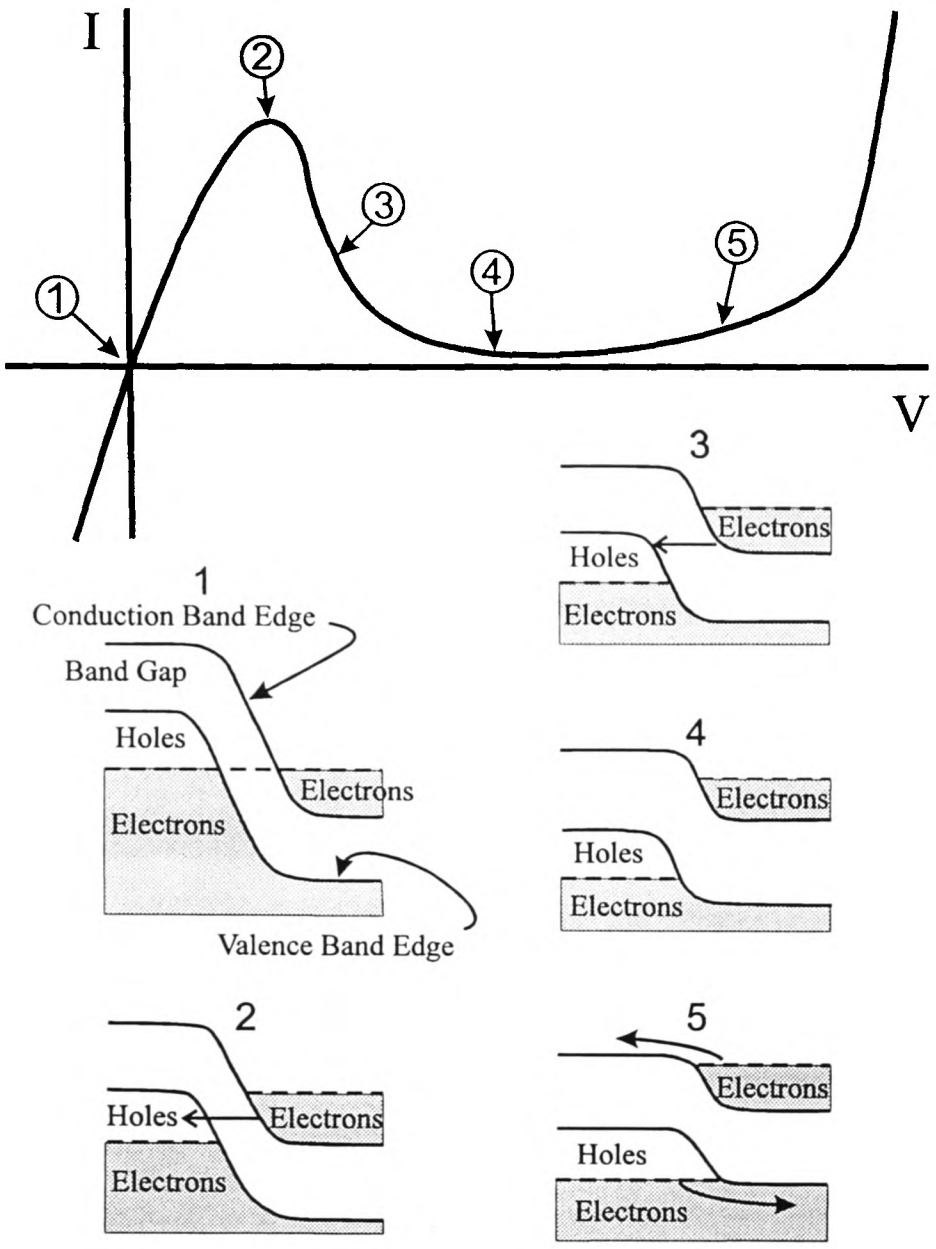


Figure 1.3. Schematic I/V characteristic of an Esaki Tunnel diode exhibiting NDR with schematic 0 K representations of the band structure at various positions on the curve.

where there are no available electron and hole states at the same energy and so any tunnel current is blocked by the band gap. Increasing the bias still further (point 5) allows the thermal current to take over where the potential barrier for the electrons (and holes) is no longer insurmountable.

Such was the status of semiconductor research at the time that, *in the same year it was first reported*, the tunnel diode was investigated thoroughly, to the extent that most journals in 1958 had articles ranging from basic uses of the device [6] to possible combination devices utilising existing technologies [7].

Other devices exhibiting NDR have since appeared on the scene such as the Gunn diode [8] which makes use of the transfer of electrons from a low effective mass conduction band valley to a high effective mass valley at a threshold electric field after which the electron velocity decreases as the field is increased, and the IMPATT diode which employs impact ionization and transit time properties of semiconductor devices to produce NDR at microwave frequencies [9].

One of the main advantages of semiconductors that exhibit NDR is their inherent instability. A random fluctuation of carrier density at any point in the sample produces a momentary space charge that grows exponentially with time. This makes them ideal

as microwave amplifiers, oscillators and signal generators, and makes sure there is always a search on for even higher frequency sources.

1.4 Semiconductor Heterostructures

Research for these higher frequencies seems to be concentrated in the area of semiconductor heterostructures. This constitutes only one of the many new low dimensional semiconductor devices which are now possible entirely because of the existence of the improvement in growth techniques. This section introduces the evolution and properties of heterostructures and discusses some of their potential uses.

The improvement in controllable growth techniques such as Metal Organic Vapour Phase Epitaxy (MOVPE - section 2.2) and the more recent Molecular Beam Epitaxy (MBE - section 2.2.1), opened up whole new areas of research in the fields of materials, physics and device engineering during the 1970s. For the first time it was possible to 'grow' very pure and well ordered semiconductors with the unprecedented precision of one atomic layer. Thus the semiconductor heterostructure, where different materials are 'grown' on top of each other forming an artificial structure, was finally a reality providing an accessible arena for the investigation and observation of quantum mechanical phenomena such as the 'particle in a one dimensional box' [10]. The resulting plethora of 'grown to order' semiconductor structures has provided a variety of new optical and electrical devices whose properties are mainly determined by the quantum confinement of electrons and/or holes [11]. There also exists a potential for the contraction of device proportions still further into the one and zero dimensional quantum realms [12].

This artificial breed of hybrid semiconductor can be invaluable to the experimental physicist for a number of reasons :

- studies can be made on quasi two dimensional electron gasses under varying external conditions such as magnetic field or pressure [13,14];

- direct use can be made of the microscopic phenomenon of quantum tunnelling which can yield results visible on a macroscopic scale [15];

- electron and hole confinement manifests itself readily in optical absorption measurements [16];

- the device response can be tailored for a specific need using the wide array of growth parameters available.

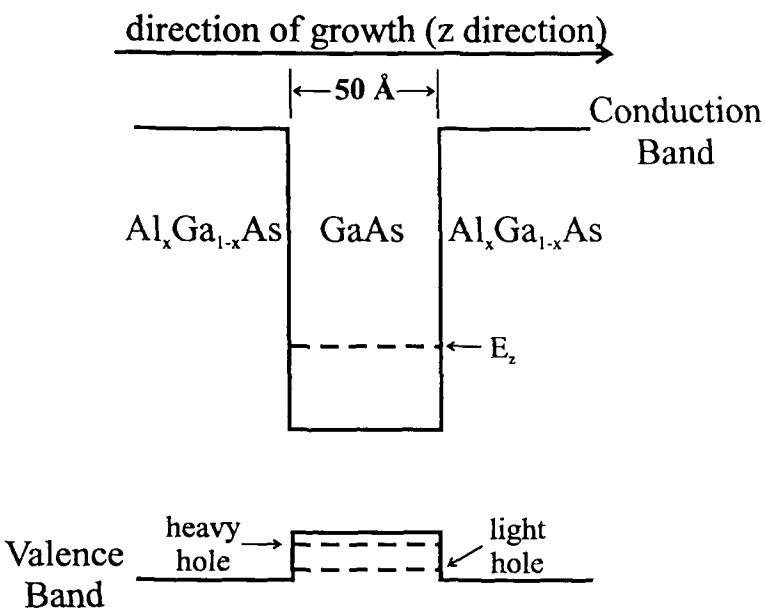


Figure 1.4. Schematic representation of the band structure of a GaAs/$Al_xGa_{1-x}As$ quantum well neglecting any band bending, showing confinement of electrons and holes in GaAs in the direction of growth with an indication of a typical well width.

The distinctive properties of a semiconductor heterostructure usually result from a mismatch in band structure in the direction of growth [17] which alters the electric potential that the electron and/or hole experiences, thus confining the charge carriers in that one particular dimension. A schematic representation of the band structure of a quantum well grown using GaAs and $Al_xGa_{1-x}As$ is shown in figure 1.4, illustrating this process. The band gap of $Al_xGa_{1-x}As$ is much larger than that of GaAs and its conduction band edge lies higher in energy, so the conduction band electrons become confined in the GaAs with a resulting energy quantization in the z (growth) direction (shown by E_z). The heavy and light holes are also confined in the GaAs valence band following a similar argument. In the x and y directions, however, the motion is free electron-like leading to a dispersion relation of the form :

$$E = E_z + \frac{\hbar^2}{2m_{\parallel}^*}\left(k_x^2 + k_y^2\right) \qquad \textbf{(1.1)}$$

where E_z is the energy of the charge carriers in the z direction and $m_{\parallel}^*$ is their effective mass in the plane perpendicular to the interface. Hence the confined electron subband can be described as being a two dimensional energy continuum with its zero of energy at E_z.

Aside from purely academic interest, these structures presented (and still do) the possibility of improving existing semiconductor device speeds and efficiencies as well as providing brand new ones. Even though it is such a young field compared to the established silicon and germanium technologies, mass produced commercial quantized semiconductor structures already exist such as quantum well lasers for compact disc players and low noise transistors in direct-broadcast satellite receivers.

Uses from more efficient lasers [18] through faster switches [19] to higher frequency microwave oscillators [20,21] have been realised and, because the device properties can be optimised at growth time, the ideal structure for the particular requirement can be engineered. Hence, a detailed understanding of the underlying band structure is crucial to any device production - the phrase now used for this process is 'band gap engineering' [22].

1.5 The InAs/GaSb Single Heterojunction

Nearly all of the original heterostructure research was concentrated on the lattice matched GaAs/$Al_xGa_{1-x}As$ system and consequently, since Tsu and Esaki proposed tunnelling in a finite superlattice [23] and Dingle et al. first demonstrated optical absorption from a single quantum well [16], substantial improvements have been made with the optimisation of growth techniques, purer substrates, Ohmic contacts and the understanding of the underlying physics involved in electrical and optical processes.

Other heterostructure material systems such as GaN/InN and ZnSe/ZnS are only at the start of their experimental lifetimes yet already show much promise. The nearly lattice matched 'antimonide' system, of which InAs and GaSb are a subset (InAs and GaSb have a lattice mismatch of ~ 0.6%), was first suggested as a candidate for a novel polytype heterostructure by Sai-Halasz et al. in 1977 [24] and falls into the category of being relatively unexplored.

The relative energies of the conduction and valence band minima for InAs and GaSb at 0K are shown on the left hand side of figure 1.5. Herein lies the main reason for the interesting and novel physics in the InAs/GaSb single heterojunction (SHET) - the GaSb valence band lies above the InAs conduction band by an energy, Δ (the band

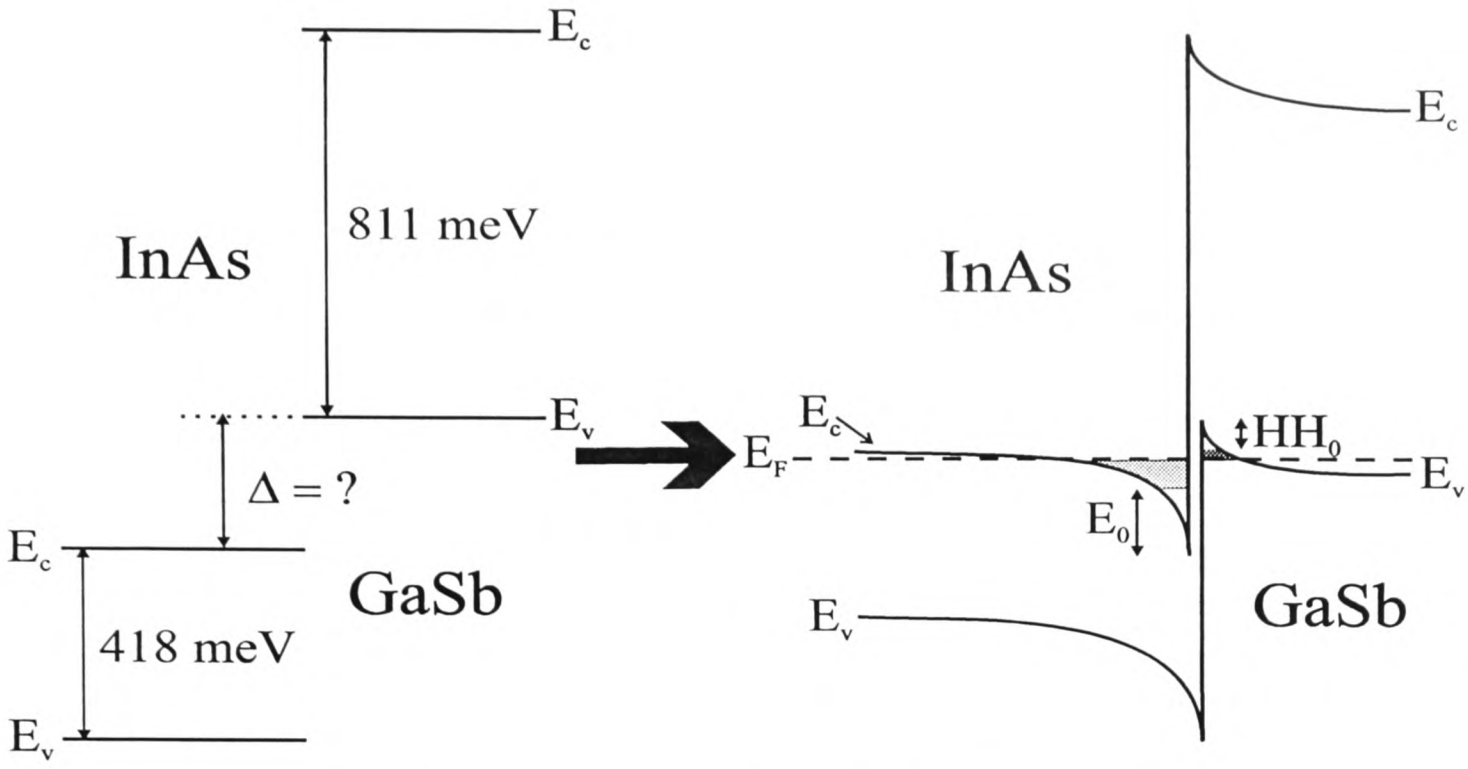


Figure 1.5. The left hand side of the diagram shows the relative energies of the conduction and valence band extrema at 0K with the value of the band overlap, Δ, as yet unknown (approximately 100-200 meV). To the right of the arrow is a schematic SHET band profile at 0K, where a charge transfer process results in the back to back confinement of quasi 2-dimensional electron and hole gasses at the interface.

overlap).

When the two semiconductor materials are brought together to form a heterojunction as in the case of epitaxial growth, the structure has to compensate internally in order to preserve the continuity of the Fermi level across the interface (in order for it to be a conductor). A charge transfer process results with electrons from the GaSb valence band flowing into the InAs conduction band, leaving behind holes. This transfer of charge changes the electric field in the vicinity of the interface which, obeying Poisson's equation, causes the conduction and valence bands to bend. The consequence of this bending is a band profile in the z (growth) direction which confines the charge. The transferred quasi two dimensional electron gas (2DEG) and quasi two dimensional hole gas (2DHG) now coexist in a 'back to back' manner at equilibrium (to the right of the arrow in figure 1.5) with a confined z motion (and, therefore, a quantized E_z) and a free electron like dispersion in the plane perpendicular to the interface.

A heterojunction in which the valence band edge of one material lies above the conduction band edge of the other is described as being extreme type-II in nature, and the only lattice matched or nearly lattice matched system to exhibit this behaviour is

the InAs/GaSb one. Consequently, some unique and unusual physical properties result which are described section 1.5.1. This thesis explores the vertical transport properties of SHET structures, so an understanding of the response of the band profile to an applied bias and any subsequent conduction mechanism is essential. Section 1.5.2 introduces a number of possible conduction mechanisms, all of which are compared in later chapters to the observed I/V traces.

1.5.1 Unusual Properties of the Antimonide System

The unique physics exhibited in the nearly lattice matched antimonide system is due almost entirely to the way the bands line-up at the interface. Indeed, it is the only artificially grown heterostructure in which the conduction band of one material lies lower in energy than the valence band of another (figure 1.5). The resulting charge transfer process yields very high 2D mobile charge concentrations without the need of potentially performance degrading doping. Hence the physicist is presented with a very high quality intrinsic system with quasi two-dimensional confined electron and hole gasses in close proximity.

Vertical transport in these structures exploits the interaction of InAs conduction band states with those of the GaSb valence band. It is not entirely surprising to discover that the high mobile 2D charge concentrations in these interband conduction devices result in extremely high peak current densities (see next section and [25]). As a result of the relatively low charge carrier effective masses, these devices are potentially very useful as high frequency oscillators.

Another interesting and potentially useful feature of InAs/GaSb heterostructures arises from the lack of any common element between the two bulk compounds. This enables structures to be grown that are identical apart from the monolayer at the interface. For the ideal heterojunction which is uniform and abrupt, there are two possible growth sequences resulting in either an 'InSb-like or 'GaAs-like' monolayer interface (figures 1.6 and 1.7). The effect this change may have on the electronic structure has been the subject of a number of theoretical studies (which are discussed in section 6.3.2). The predictions vary, but seem to seem to centre round different values for the InAs conduction GaSb valence band overlap, Δ. A general consensus that Δ is larger for

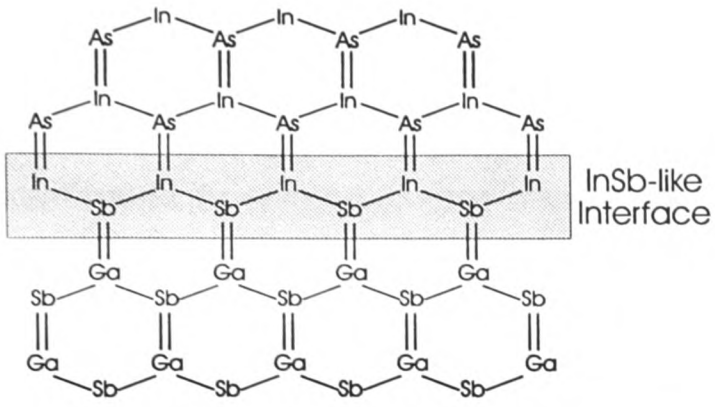


Figure 1.6. [110] projection of SHET with an 'InSb-like' interface. Single lines are bonds in the plane of the paper and the double lines are bonds projected up from or down through it.

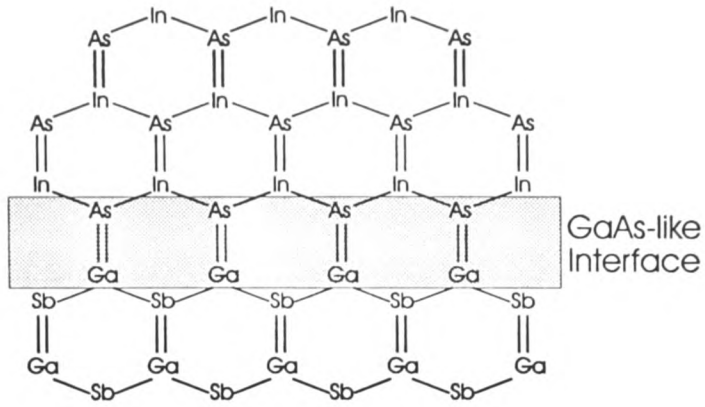


Figure 1.7. [110] projection of SHET with a 'GaAs-like' interface. Single lines are bonds in the plane of the paper and the double lines are bonds projected up from or down through it.

the 'InSb-like' interface has emerged, but the magnitude of this energy difference remains a point of contention. The excellent quality samples grown at the Clarendon laboratory together with the wide variety of optical and electrical characterisation experiments available have facilitated a resolution of this argument, the results of which are presented in section 6.6.

It is also worth mentioning that the inclusion of the nearly lattice matched barrier material for this system, AlSb, in the epitaxial growth sequence allows a large range of possible band alignments which can be used to fabricate a wide array of structures for transport and optical use [25]. These will be described further in section 1.6.

1.5.2 Resonant Conduction

There are very few publications investigating vertical transport in SHET structures. The first reported observation of NDR was from a sample grown by MBE on a GaAs substrate by Collins et al. [26] which did not consider any possible difference in device characteristic arising from changes in interface composition, nor did it discuss the resonant conduction mechanism in any detail. The only other reports to my knowledge have been those based on results obtained in the pursuit of this thesis [27,28,29,30].

A long process of InAs/GaSb growth optimisation at the Clarendon Laboratory (see section 2.2) has enabled a high degree of control of InAs/GaSb heterointerface composition. This has resulted in samples with almost intrinsic character (where the 2DEG concentration equals that of the 2DHG) and SHETs exhibiting uniform and reproducible vertical transport characteristics (see section 5.2). The origin of NDR in

these structures in the absence of a classical barrier is understood in terms of changes in the electronic structure at the interface and the consequent electric field induced semimetal to semiconductor transition. The remainder of this section describes these changes in detail and introduces likely vertical transport mechanisms, the accuracy of which can be compared with actual device performance in later chapters.

The effect of forward bias (InAs negative with respect to GaSb) on a SHET is to increase the charge in the InAs conduction band. If, as is possible, no conduction path exists the structure would behave as a capacitor, dropping a voltage across it but allowing no DC current through. The observed I/V behaviour, however, indicates the SHET has a finite resistance which means charge is able to flow across the interface and a conduction path must exist.

Figure 1.8 (top left) shows the zero bias SHET band profile at 0K in the vicinity of the Fermi energy. Forward bias increases the InAs conduction electron concentration near the interface and therefore the band bending, thus raising the electron confinement energy, E_0. A similar mechanism exists for the holes in the GaSb valence band where an increase in the hole concentration near the interface increases the band bending there too, raising the hole confinement energy, HH_0, resulting in a band profile similar to that shown in the top right of figure 1.8. The application of a bias, therefore, simply raises the energy of the 2DEG and lowers that of the 2DHG, indicated in figure 1.8 by

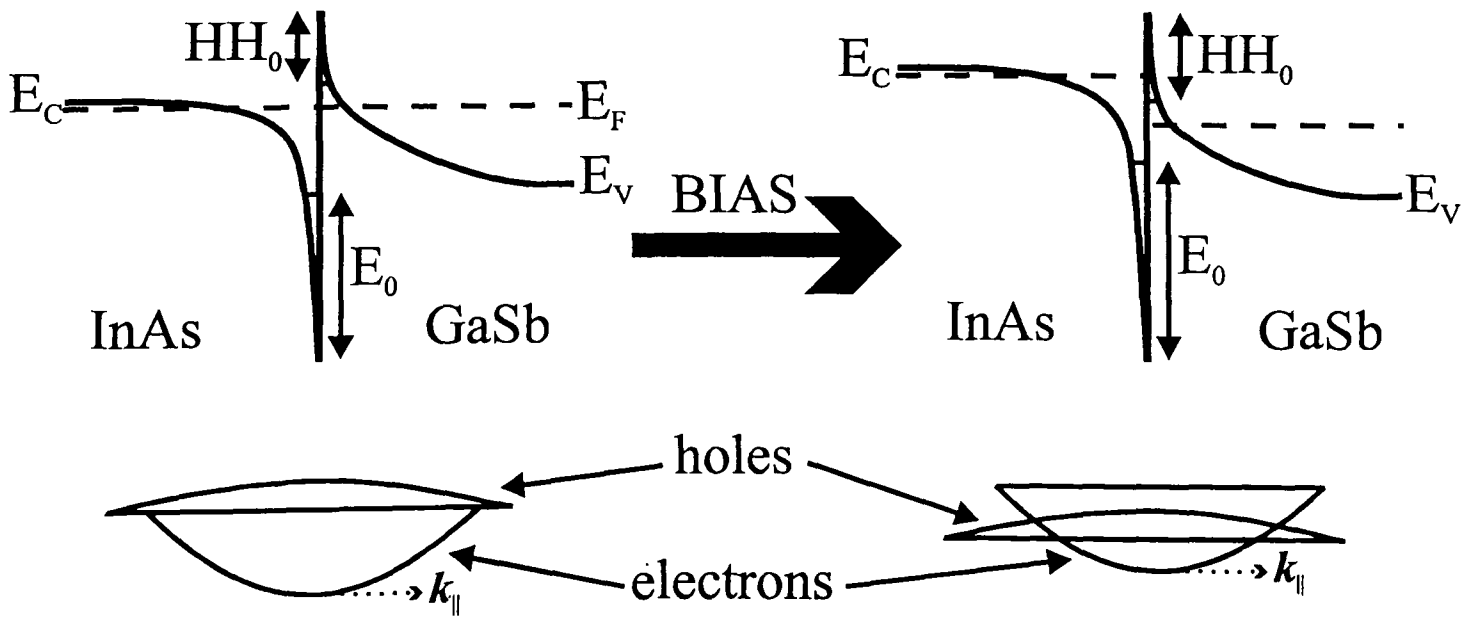


Figure 1.8. Top left shows the zero bias, zero temperature SHET band edge profile in the vicinity of the Fermi energy. Application of forward bias (InAs negative with respect to GaSb) increases the electron (hole) concentration which increases the band bending, resulting in an increase in E_0 (HH_0) which is shown in the top right. Also shown are the relative positions of the in-plane dispersions for electrons and heavy holes (light and split-off hole dispersions are not shown for clarity) for both cases.

the movement of the in-plane energy dispersions. Eventually at some critical voltage, V_c, E_0 has the same energy as HH_0 and with any further increase the parabolic dispersions no longer contain states that overlap in $\boldsymbol{k}$-space.

At low biases the electron and heavy hole sub-band dispersions contain states with equal energy and $\boldsymbol{k}_{||}$. If this overlap occurs at finite values of $\boldsymbol{k}_{||}$ the bands mix, creating a region of anticrossing, resulting in an electron-hole coupling which is stronger for large $\boldsymbol{k}_{||}$. This coupling provides a current path, conserving both energy and momentum. At low biases the sub-band anticrossing occurs at large $\boldsymbol{k}_{||}$ and a small increase in voltage results in an increase in current, due to the increased 2D charge. As E_0 moves towards HH_0, the anticrossing shifts towards smaller $\boldsymbol{k}_{||}$ and the coupling becomes less efficient, a factor which starts to dominate over the increasing 2D concentrations, resulting in a current peak followed by a region of NDR. The I/V trace that might be expected from this conduction mechanism is illustrated schematically in figure 1.9.

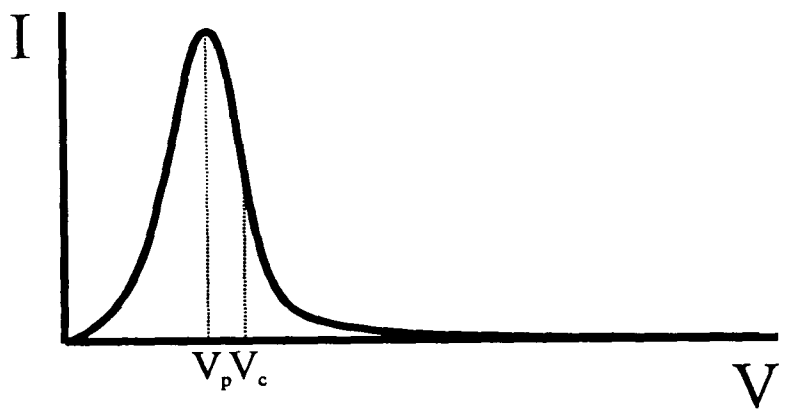


Figure 1.9. Resonant conduction component of the SHET I/V trace indicating a possible position for V_c, the point at which the sub-bands uncross.

A conduction process that may occur simultaneously with direct electron-hole coupling is one in which electrons scatter into heavy (or light) hole states via phonon emission. This can occur at any value of $\boldsymbol{k}_{||}$ and is capable of providing a significant current beyond V_c. Calculations based on a 2-band model in the limit of no mixing have been carried out and are described in chapter 4. They can be used to give a relatively accurate estimate of the movement of the 2DEG and 2DHG sub-bands with bias and provide a valuable aid in determining which predicted current mechanism is dominant by comparison with the experimentally observed data.

Reverse bias in a SHET exhibits altogether different I/V curves. Bulk GaSb valence band states and bulk InAs conduction band states overlap and a current flows, rather like reverse bias in an Esaki tunnel diode but without the barrier. Detailed discussion of this is reserved until section 6.3.

1.6 Potential Application of Antimonides

The fact that three compounds make up the nearly lattice matched antimonide heterostructure system provides the band gap engineer with tremendous flexibility in design. The extremely low electron effective mass of InAs allows the possibility of very fast switching times, and Ohmic contacting is very easy as well. Indeed, an InAs/AlSb/InAs/AlSb/InAs quantum well currently holds the record as the highest frequency room temperature solid state oscillator [31]. Superlattices can be grown which have the potential to fill the gap in currently available technology for mid infra-red detectors. Additionally, low power oscillators which may someday provide mobile proximity sensing detectors for everyday use in equipment such as cars are under development.

There are many equally significant antimonide devices under development, three of which have been chosen as a representative cross section of those available and are presented in sections 1.6.1-1.6.3. They are the static random access memory, the Stark effect transistor and the mid infra-red laser.

1.6.1 Static Random Access Memory

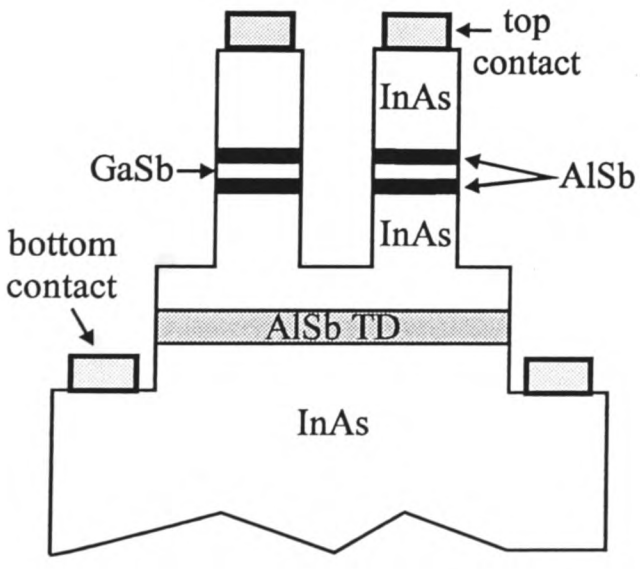


Figure 1.10. Cross section of an SRAM cell. After Shen et al. [3].

One of the more recent developments is that of Shen et al. [3] who have succeeded in fabricating an SRAM from antimonide based resonant tunnelling diodes. They used a back to back arrangement of InAs/AlSb/GaSb/AlSb/InAs resonant interband tunnel structures (RITS) as shown in figure 1.10, each of which had a room temperature current peak to valley ratio of up to 30. As the two RITS are connected in series, when appropriately biased the middle node is bistable. Thus, by connecting a tunnel diode to the middle node, information can be written to and read from the memory cell. This research is still in its infancy, but already the RITS based SRAM is

capable of saving a factor of four in cell area design and is a viable alternative in components such as programmable logic arrays where speed is the premium requirement.

1.6.2 Stark Effect Transistor

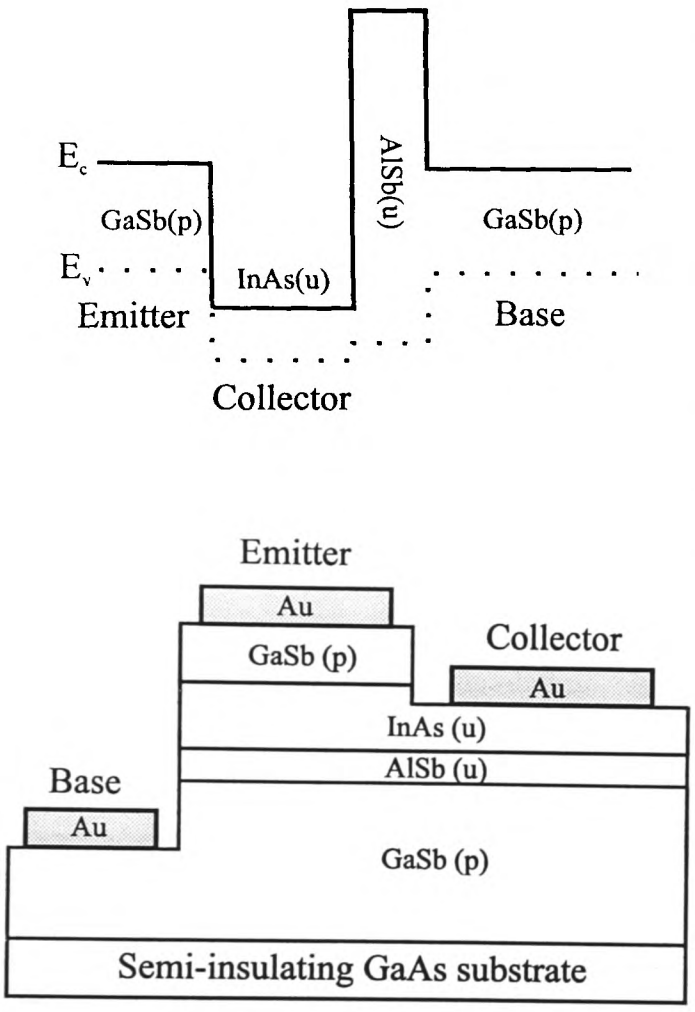


Figure 1.11. Band profile and cross section of a Stark Effect Transistor. After Collins et al. [19].

Collins et al. [19] reported current gains as high as 50 at room temperature in a Stark effect transistor (SET). This device, illustrated in figure 1.11, was the first to make use of Stark shifts of energy levels in a quantum well to exhibit transistor action at room temperature. The emitter and collector, when viewed in isolation, form a quasi-SHET. Any current flowing from the base to the collector however, has to tunnel through an AlSb barrier. This makes the base-collector I/V trace sufficiently different from that of the quasi-SHET to enable the device to act as a transistor. Here the AlSb barrier allows a voltage to be applied between the base and collector that can electrostatically control the current through the quasi-SHET. This component is potentially useful in the fabrication of high speed and high frequency electronic circuits.

1.6.3 Mid Infra-red Laser

Antimonide based mid infra-red semiconducting lasers could provide the next generation of atmospheric monitoring devices. Since many atmospheric pollutants absorb in the 2-5 μm range, strong absorption of a laser signal can give information about the amount of pollutant present.

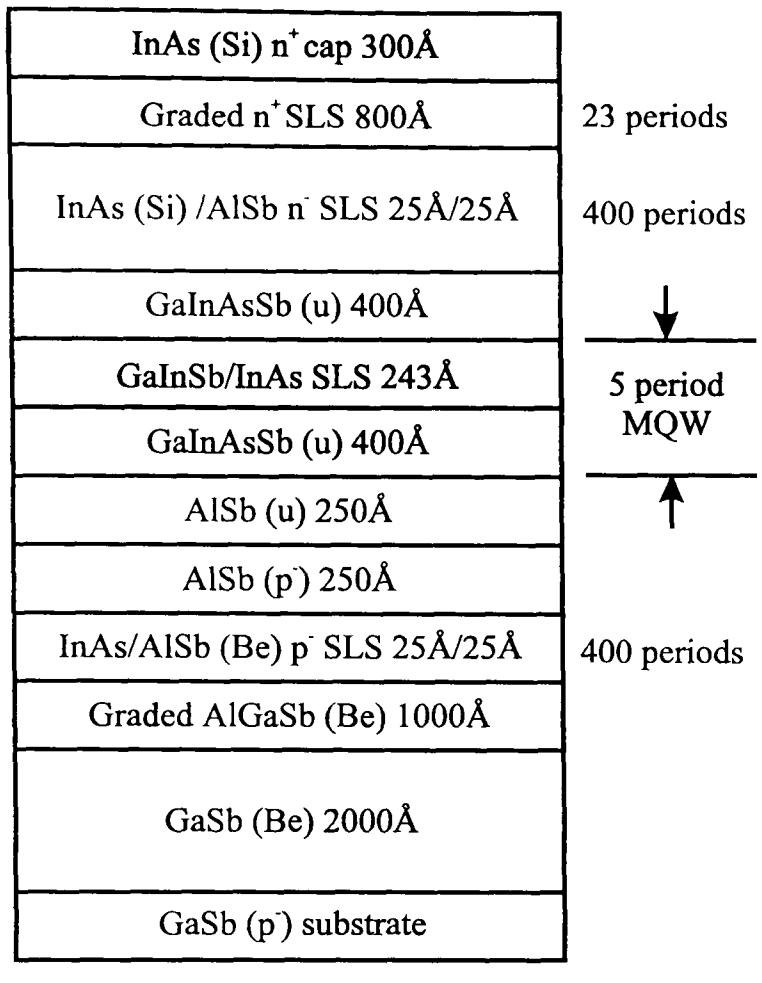


Figure 1.12. Schematic layer structure for GaInSb/ InAs superlattice based diode laser. After Hasenberg et al. [32].

A typical laser structure is shown in figure 1.12. This has a novel multiple quantum well active region consisting of $Ga_{0.75}In_{0.25}As_{0.22}Sb_{0.78}$ barriers, and wells made from $Ga_{0.75}In_{0.25}Sb$/InAs superlattices. Alloys are used to introduce strain into the quantum well system, thus splitting the heavy and light holes and reducing the hole effective mass. This reduces Auger recombination and free carrier absorption. By altering the periodicity of the superlattice quantum well, it is possible to vary the laser emission wavelength. Already, pulsed operation of lasers emitting at between 3.28 μm (at 170K) and 3.90 μm (at 84K) have been achieved [32]. Continuing improvements in growth and the optimisation of active area band structure mean these structures could soon be commercially viable.

The remainder of this thesis builds upon the introduction provided in the chapter thus far in order to explore vertical transport in an InAs/GaSb SHET. An outline of the remaining chapters follows.

1.7 Outline of Thesis

This section provides a brief outline of the contents of subsequent chapters.

High quality samples are a prerequisite for semiconductor research. Since 1993 an intensive process of growth optimisation at the Clarendon Laboratory involving a number of collaborators has resulted in InAs/GaSb heterostructures of extremely high quality. Chapter 2 documents the improvements made in the control of interface composition as observed by Raman and transmission electron microscopy (TEM)

measurements. Once grown the samples require advanced micron scale processing before they are ready for vertical transport measurements. Chapter 2 concludes by describing this procedure which is carried out in Sheffield, typically taking three to four months.

Data for this thesis has been obtained by recording the change in a sample's vertical transport behaviour as external conditions are varied. Chapter 3 describes the experimental techniques used for I/V measurement under ambient conditions and as temperature, pressure and/or magnetic field are altered.

Chapter 4 describes in detail the two band model employed to calculate the band edge profile of the single interface structure under investigation. This involves a self-consistent solution for the Schrödinger and Poisson equations, and is an essential aid to understanding the device's behaviour with bias.

Chapter 5 begins by documenting the change in the SHET I/V characteristic due to the improved growth methods mentioned in chapter 2 and shows the samples to be very sensitive to any variation in interface composition. It then investigates the temperature dependence of vertical transport and discovers a definite, repeatable, difference in this response for near identical samples whose only difference is the one monolayer 'InSb-like' or 'GaAs-like' interface. A short investigation at the end of this section concludes that the excess (background) current seen in these samples is not a thermally activated one.

The application of hydrostatic pressure increases the energy gaps of both bulk InAs and GaSb at a known rate. This increase will influence the SHET band edge profile, providing a method of investigating the change in I/V characteristic with the relative band line-up at the interface. Chapter 6 uses this information to confirm an interface dependent difference in the electronic band structure of SHET samples. It then proceeds to investigate the conduction mechanism giving rise to NDR and discovers that the two different monolayer interfaces support different vertical transport processes. The chapter then addresses the pressure dependence of the background current, and concludes with a more comprehensive consideration of possible SHET conduction mechanisms.

The application of a magnetic field to an electron gas produces a known change in its dispersion. I/V traces of SHETs have been monitored in continuous fields up to 15T and pulsed fields up to 40T. These are applied both perpendicular and parallel to the interface and the results are reported in chapter 7 where this phenomenon is used in order to gain further information about the observed sample NDR. Confirmation of the interface dependence of vertical transport and of the revised transport mechanism of chapter 6 are obtained.

Chapter 8 provides a summary of the new discoveries contained in this thesis, a round-up of work that still has to be investigated in order to clarify certain points and a view to the future for possible further research.

1.8 References

[1] Y H Lee, J L Jewell, A Scherer, S L McCall, J P Harbison & L T Florez. Electronics Letters 25, p1377 (1989).

[2] E R Brown, J R Söderström, C D Parker, L J Mahoney, K M Molvar & T C McGill. Applied Physics Letters 58, p2291 (1991).

[3] J Shen, G Kramer, S Tehrani, H Goronkin & R Tsui. IEEE Electron Device Letters 16, p178 (1995).

[4] J Bardeen & W H Brattain. Physical Review 74, p230 (1948).

[5] L Esaki. Physical Review 109, p603 (1958).

[6] R A Pucel. Solid State Electronics 1, p22 (1958).

[7] I A Lesk & H A Jensen. Solid State Electronics 1, p183 (1958).

[8] J B Gunn. Solid State Communications 1, p88 (1963).

[9] S M Sze. Semiconductor Devices - Physics and Technology, p229, Wiley, New York, (1985).

[10] R Tsu & L Esaki. Applied Physics Letters 19, p246 (1971).

[11] J Singh. Physics of Semiconductors and their Heterostructures, McGraw-Hill, Singapore (1993).

Continued ...

References Continued ...

[12] C Weisbuch & B Vinter. Quantum Semiconductor Structures - Fundamentals and Applications, Academic Press Inc., San Diego, p189 (1991).

[13] See for example the Proceedings of the 6th International Conference on High Pressure Semiconductor Physics. Vancouver, Canada, 22-24 August 1994.

[14] See for example the Proceedings of the 11th International Conference on the Application of High Magnetic Fields in Semiconductor Physics. Boston, Mass., USA, 8-12 August 1994.

[15] L L Chang, L Esaki & R Tsu. Applied Physics Letters 24, p593 (1974).

[16] R Dingle, W Wiegmann & C Henry. Physical Review Letters 33, p827 (1974).

[17] The convention used in this thesis is to describe the direction of growth as the z direction

[18] R D Burnham, W Streifer & T L Paoli. Journal of Crystal Growth 68, p370 (1984).

[19] D A Collins, D H Chow & T C McGill. Applied Physics Letters 58, p1673 (1991).

[20] T C L G Sollner, W D Goodhue, P E Tannenwald, C D Parker & D D Peck. Applied Physics Letters 43, p588 (1983)

[21] E R Brown, J R Söderström, C D Parker, L J Mahoney, K M Molvar & T C McGill. Applied Physics Letters 58, p2291 (1991).

[22] F Capasso. Semiconductors and Semimetals, 24, p319, Academic Press, New York (1987).

[23] R Tsu & L Esaki. Applied Physics Letters 22, p562 (1973).

[24] Sai-Halasz, Applied Physics Letters 30, p651 (1977). M Sweeny & Jingming Xu. Applied Physics Letters 54, p546 (1989).

[25] D A Collins, D H Chow, E T Yu, D Z-Y Ting, J R Söderström, Y Rajakarunanayake & T C McGill. Paper in Resonant Tunnelling in Semiconductors - Physics and Applications, edited by L L Chang et al., p515, Plenum Press, New York (1991).

[26] D A Collins, E T Yu, Y Rajakarunanayake, J R Söderström, D Z-Y Ting, D H Chow & T C McGill. Applied Physics Letters 57, p683 (1990).

[27] U M Khan-Cheema, P C Klipstein, J M Smith, D G Austing, N J Mason, P J Walker & G Hill. Solid State Electronics 37, p977 (1994).

Continued ...

References Continued ...

[28] U M Khan-Cheema, P C Klipstein, N J Mason, P J Walker & G Hill. Journal of Physics and Chemistry of Solids 56, p463 (1995).

[29] P C Klipstein (invited), S G Lyapin, I Trojan, N J Mason, U M Khan-Cheema, D M Symons, M S Daly, M Lakrimi, R J Nicholas, I J Murgatroyd, T Y Seong, G R Booker, G Hill & P J Walker. Proceedings of the International Conference of Semiconductor Heteroepitaxy, Montpellier, 4-7 July 1995, (edited by B Gil and R L Aulombard). World Scientific, Singapore, p515 (1995).

[30] P C Klipstein (invited). Joint XV International Association for High Pressure Research (AIRAPT) and XXXIII European High Pressure Research Group (EHPRG) International Conference, Warsaw, Poland, September 11-15, 1995.

[31] E R Brown, J R Söderström, C D Parker, L J Mahoney, K M Molvar & T C McGill. Applied Physics Letters 58, p2291 (1991).

[32] T C Hasenberg, D H Chow, A R Cost, R H Miles & L West. Electronics Letters 31, p275 (1995).

2 Sample Growth, Characterisation and Processing

2.1 Introduction 23

2.2 MOVPE Growth 23

2.2.1 Molecular Beam Epitaxy 25

2.3 Interface Characterisation 26

2.3.1 Raman Measurements 26

2.3.2 Transmission Electron Microscopy 29

2.4 Sample Processing and Contacting 31

2.5 References 35

2.1 Introduction

The ability to carry out experiments on III-V semiconductor heterostructures which give reliable information about the underlying physics depends very much on the degree of control over sample growth. Small fluctuations in structure or uniformity can alter the observed electrical or optical properties drastically. Hence, it is very important to ascertain how near the experimental structures are to being ideal.

SHET vertical transport structures exhibiting NDR were grown at the Clarendon Laboratory for the first time using atmospheric pressure Metal Organic Vapour Phase Epitaxy (MOVPE) by Mason and Walker in 1992 [1]. Since then a program of growth optimisation has been carried out, exploiting the large array of in-house experimental techniques available to determine sample quality [2,3].

Section 2.2 summarises the MOVPE growth of InAs/GaSb heterostructures, including a discussion of the growth optimisation parameters. Section 2.3 then goes on to describe the available evidence for improvement in sample quality over this period using Raman and Transmission Electron Microscopy (TEM) analysis.

In order to make vertical transport measurements, sample preparation and contacting has to be carried out. This non-trivial procedure, described in section 2.4, was the rate limiting step in being able to gather information for this thesis on many occasions. The processing is carried out elsewhere, and a typical wait between a sample's growth and its availability for testing is 4 months.

2.2 MOVPE Growth

It is possible to fabricate III-V semiconductor heterostructures only because of the availability of controlled epitaxial growth techniques. The samples used in this thesis were grown in the Clarendon Laboratory using atmospheric pressure MOVPE, a description of which follows.

A palladium diffuser is used to remove any trace of impurity from a flow of pure

hydrogen gas. The resulting gas then passes along a series of pipes, is ejected into a manifold and on into a silica growth cell through a small outlet whose size ensures gas turbulence, promoting mixing [4]. Laminar flow follows where the gas proceeds uniformly over a growth substrate, along the remainder of the silica cell and out through a vent. Metal-organic compounds (precursors) can be introduced into this flow by allowing a pre-set proportion of the hydrogen gas to bubble through a container of the required compound before reaching the manifold. Group III and group V precursors are introduced in this way, injected into the manifold, mixed in the turbulent flow region and pass under laminar flow over the heated substrate where they react, depositing the III-V compound evenly over the substrate surface.

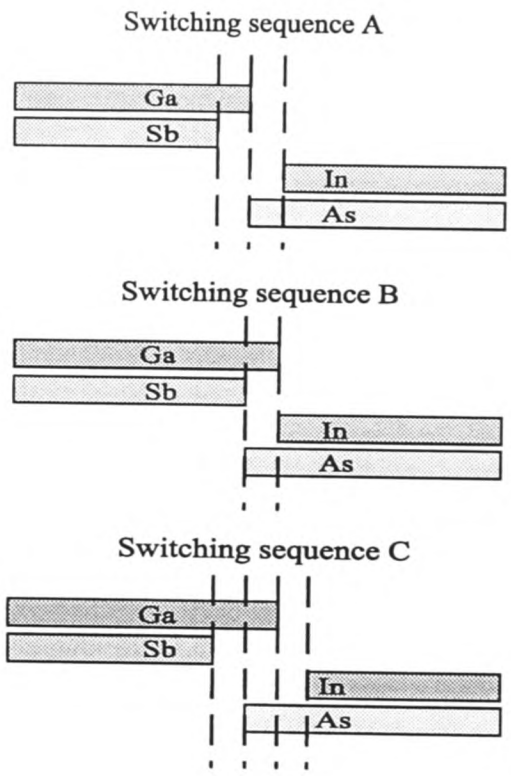


Figure 2.1. The three MOVPE switching sequences used to bias the interface towards 'GaAs-like'. The vertical dashed lines represent events separated by ½ second.

Precursors used for the SHET structures presented in this thesis were :

- Trimethylantimony for Sb;
- Trimethylgallium for Ga;
- Trimethylindum for In;
- Tertiarybutylarsene for As

which were all required to be of the highest purity.

For binary growth, two precursors containing the required group III and group V elements respectively are allowed into the silica cell to form the III-V compound on the heated substrate. Heterostructures require a similar initial procedure but, at the interface, the precursors are switched off for a short time (typically ½ s) and the new precursors, containing the new group III and group V elements, are switched on.

As mentioned in section 1.5.1, because InAs and GaSb share no common anion or cation their heterostructures can be grown with two different types of interface - 'InSb-like' and 'GaAs-like'. In practice this is achieved by staggering the precursor switching in a pre-determined manner. There are three switching sequences which have been investigated at the Clarendon laboratory, illustrated for a 'GaAs-like'

interface and labelled A, B and C in figure 2.1. In sequence A the interface is grown by allowing only one of its constituent elements in at a time. For the 'GaAs-like' interface illustrated, the Ga precursor continues for ½ s after the Sb has been switched off before being turned off itself. Only then is the As precursor switched on, biasing the interface towards 'GaAs-like', followed by the In precursor ½ s later.

Using sequence B, the Ga and As precursors are in the reactor at the same time and there is always a binary growing. Sequence C is a combination of A and B.

The effects of the different sequences on interface quality have been studied extensively by Raman and TEM and form the basis of section 2.3. Perhaps surprisingly, the different switching sequences can also influence the vertical transport characteristics of resonant conduction SHET structures, and this is discussed in section 5.2.

Other factors such as substrate temperature and III-V precursor ratio can alter the optical and electrical properties of the resulting samples [2,3] and a long term study has enabled Mason and Walker to optimise the growth conditions, producing heterostructures that are very close to the desired theoretical structures.

Mason and Walker recently introduced an in-situ method of monitoring the progress of sample growth. A deuterium lamp and UV detector are placed at opposite sides of the silica cell upstream of the substrate. As the precursors pass through the beam they absorb the UV light. A 'well switched interface' results in a stepped change in absorption from the detector, whereas a ramp or spiked output is indicative of a non-ideally switched interface. This is a quick and reliable method of checking interface switching control.

2.2.1 Molecular Beam Epitaxy

Molecular Beam Epitaxy (MBE) is described briefly here as it was the first epitaxial growth technique that successfully produced a superlattice (SL) [5] and is still the most widely used and well understood growth technique.

Growth is carried out in a liquid nitrogen shrouded ultra high vacuum environment for

minimum sample contamination. A vacuum interlock is provided for the transfer of substrates. The source elements are evaporated from separate effusion ovens onto a slowly revolving heated substrate. In-situ growth analysis by reflection high energy electron diffraction (RHEED) and mass spectroscopy is possible because of the high vacuum environment, providing a method of accurately controlling growth thickness.

For reasons not completely understood, MBE grown InAs/GaSb SLs are highly extrinsic in nature, with electron to hole ratios of 4:1 [6]. This may have something to do with the one minute switching time at the interface while the chamber is emptied of all the previous III-V molecules and the substrate temperature is altered. MOVPE, with switching times of ½ s, produces near intrinsic samples with electron to hole ratios approaching 1.

2.3 Interface Characterisation

Ideally, the heterointerface should be abrupt and one monolayer wide. In practice, however, non-ideal growth can result in interface steps or to interfaces of variable thickness. This in turn can lead to dislocations and poor electrical and optical sample properties. A determination of the interface layer thickness and uniformity for the three switching sequences A, B and C (see section 2.2) carried out by Lyapin using Raman techniques is summarised in section 2.3.1.

Transmission Electron Microscopy (TEM) and High Resolution Transmission Electron Microscopy (HRTEM) by Murgatroyd have also been carried out, the results of which are presented in section 2.3.2.

The following findings show switching sequence A produces the best quality monolayer interfaces, but the differences between samples grown using methods A, B and C are far greater for the 'GaAs-like' than the 'InSb-like' interface.

2.3.1 Raman Measurements

III-V semiconductors all have their own characteristic phonon modes which will alter if anything is introduced that disturbs the lattice, i.e. dislocations, impurities, strain,

etc. Monitoring these modes is, therefore, a very useful (and quick) way of determining the lattice ordering of bulk materials.

In the case of a SL, the bulk phonon dispersions of the constituent III-Vs are folded due to the reduction of the first Brillouin zone dimension. In samples with abrupt (1 monolayer) interfaces and uniform periodicity it should be possible to observe these folded phonons as periodic peaks in the Raman spectra, diminishing in amplitude. Additionally, in InAs/GaSb there exist localised elastic interface modes (IFM) whose energies are dependent upon the nature of this interface and its environment.

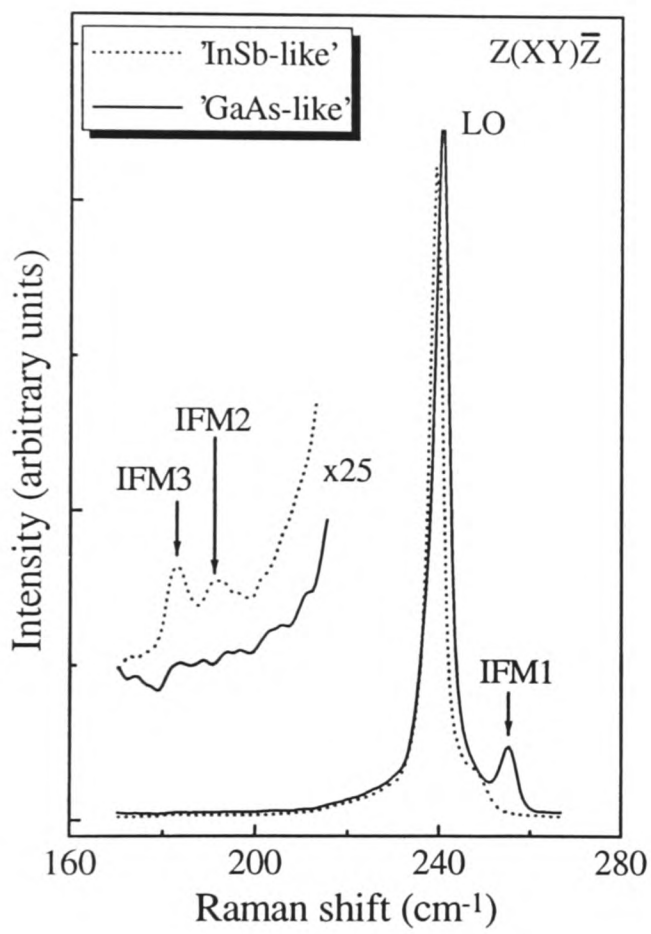


Figure 2.2. Raman spectra of two SL structures measured at 8K. The solid line is from a sample grown with 'GaAs-like' interfaces and the dotted line from one with 'InSb-like' interfaces. The interface modes (IFMs) for both interfaces are indicated, together with a disorder activated IFM and the strain induced shift in the GaSb LO phonon.

One way to assess the interface quality of SHET structures is to perform Raman measurements on them to check for the existence of the relevant IFMs. Multiple interface structures produce an amplified Raman signal, so InAs/GaSb SL samples grown in the same MOVPE reactor as the SHET structures studied in this thesis were chosen for testing. In this way, an accurate characterisation of the interface quality produced by a particular growth condition was possible. Lyapin performed these experiments, and the remainder of this section contains a short summary of his findings [7].

A 'GaAs-like' interface supports a fairly strong localised IFM phonon with an energy of 31.5 meV (254 cm^{-1}), indicated in figure 2.2 by IFM1. A good quality SL grown with its interface biased towards an 'InSb-like' configuration should not exhibit a peak at this point. The 'InSb-like' interface supports a weak phonon, indicated by IFM3 in figure 2.2, which should not appear in the spectrum of an ideal structure grown with 'GaAs-like' interfaces. The samples from which the spectra in

figure 2.2 were taken were grown using switching sequence B. They show that the 'GaAs-like' IFM can still be observed as a weak shoulder even in the 'InSb-like' SL (dotted line). This could be caused by interface steps which would lead to interface bonds of both 'InSb-like' and 'GaAs-like' character. The strength of this effect is weakest for sequence A.

In SLs with 'GaAs-like' interfaces grown using methods B and C, the GaSb LO phonon is up-shifted by 3 cm^{-1} from the bulk value, whereas in method A this difference is much smaller. The LO shift can be attributed to regions of more than one monolayer of GaAs which has a smaller bulk lattice constant (5.6533 Å) than InAs (6.0583 Å) and GaSb (6.0959 Å) and compresses the GaSb layers by ~ 1%. For the 'InSb-like' interface (with a bulk lattice constant of 6.4794 Å) the GaSb LO down-shift is less than 1 cm^{-1} for all three growth methods, but is largest for sequence C.

Figure 2.3 shows results from three SLs, each of which were grown biased towards a 'GaAs-like' interface using the different switching sequences, A, B and C. The dotted

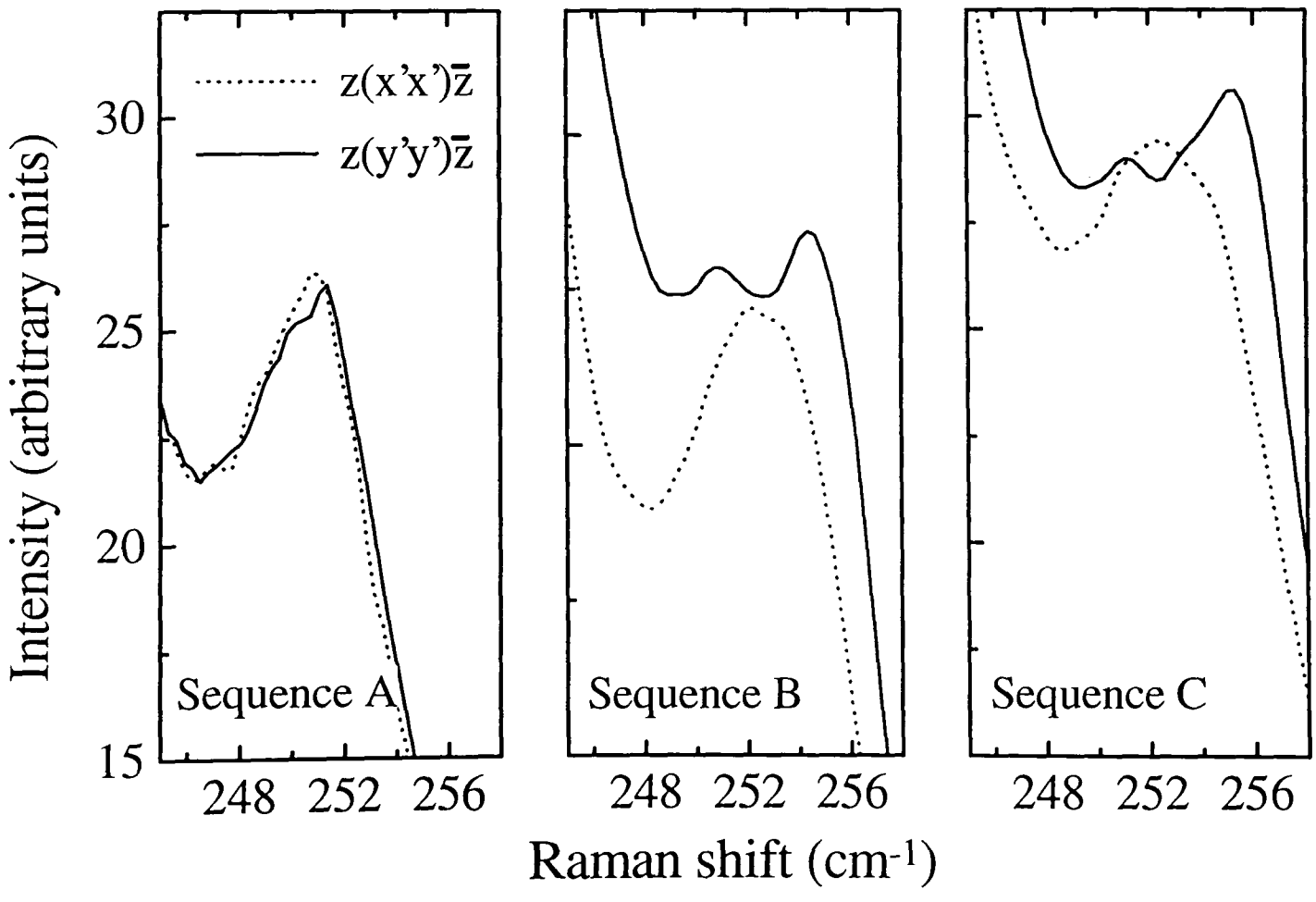


Figure 2.3. Comparison of Raman spectra from three SLs, each nominally identical except for the switching sequence used during growth. All samples have a 'GaAs-like' interface, and the portion of Raman spectrum shown is that of the GaAs interface mode (IFM1). The solid and dotted lines indicate data collected using different incident light polarisation. Spectra were taken at 300K.

and solid lines indicate the results achieved by changing the polarisation of the incident and scattered light. Using the IFM polarisation selection rules [7] it is possible to characterise each interface (InAs on GaSb or GaSb on InAs) separately. Sequence A shows IFM1 to be sharp and very similar for both light polarisations, indicating the environments of both interfaces are alike. For sequences B and C, however, GaSb on InAs exhibit a good quality interface environment, whereas InAs on GaSb shows evidence of steps or interdiffusion. This has implications for SHET structures grown with a 'GaAs-like' interface as they are all grown with InAs on GaSb (solid line) because of the lack of high quality InAs substrates.

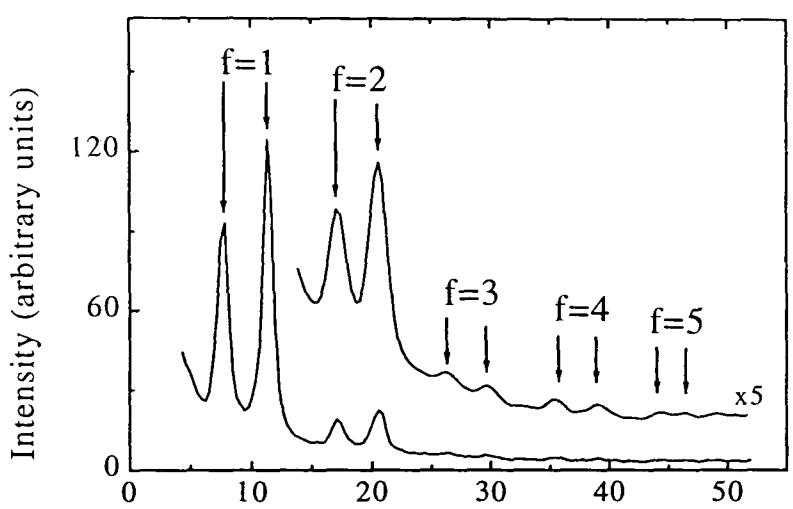


Figure 2.4. FLAPs for a SL structure showing five doublets. This is indicative of excellent periodicity and planar interfaces.

Finally, figure 2.4 shows the folded longitudinal acoustic phonons (FLAPs) exhibited by a MOVPE grown SL. The number of doublets visible is usually taken to be a measure of the periodicity and planar nature of the interfaces. No more than two doublets have previously been reported for InAs/GaSb SL structures so five, as in this case, is evidence of excellent interface control and sample growth.

2.3.2 Transmission Electron Microscopy

In addition to Raman characterisation, TEM was carried out on SL samples by Murgatroyd. Resolutions of up to 1.5 Å were obtained, enabling close inspection of interface stepping, dislocations and the quality of layering [8].

Figure 2.5 shows a TEM image of a SL grown in the same batch as 1771 and 1772. It clearly shows a very ordered SL structure, indicating good control over growth. An HRTEM image of a SL sample can actually show ordering of the rows (parallel to the (100) viewing direction) of the heavy constituent III-V atoms and allows a view of interface structure as well as possible stepping.

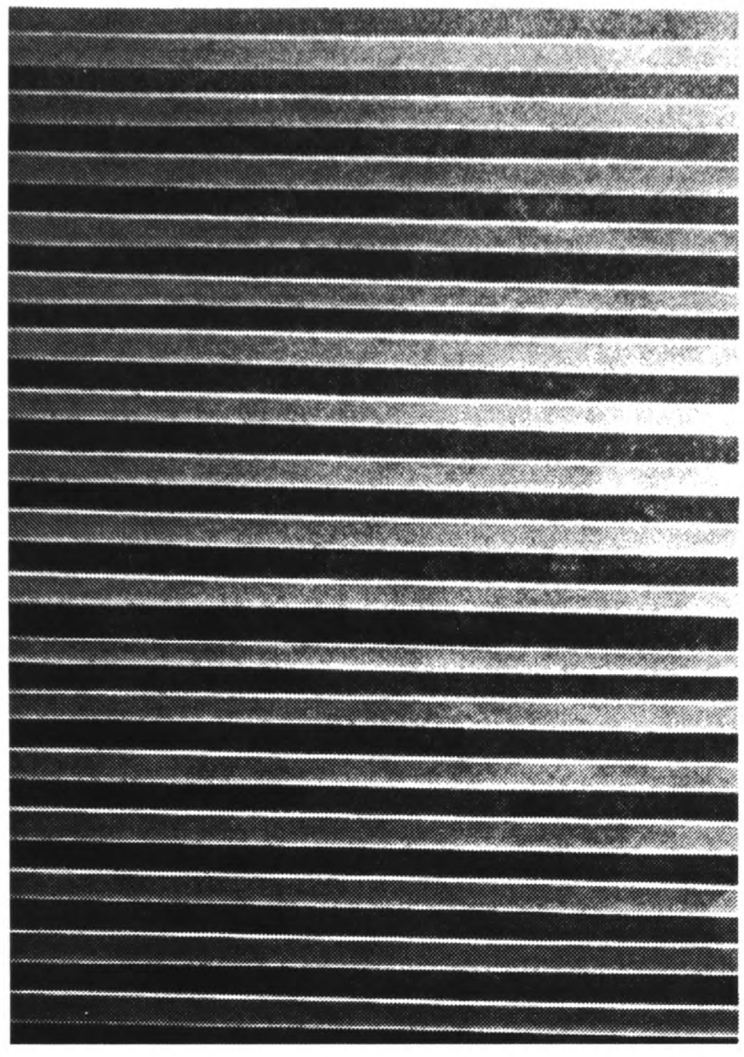


Figure 2.5. TEM picture of SL structure 1698 grown using MOVPE. Courtesy of Murgatroyd.

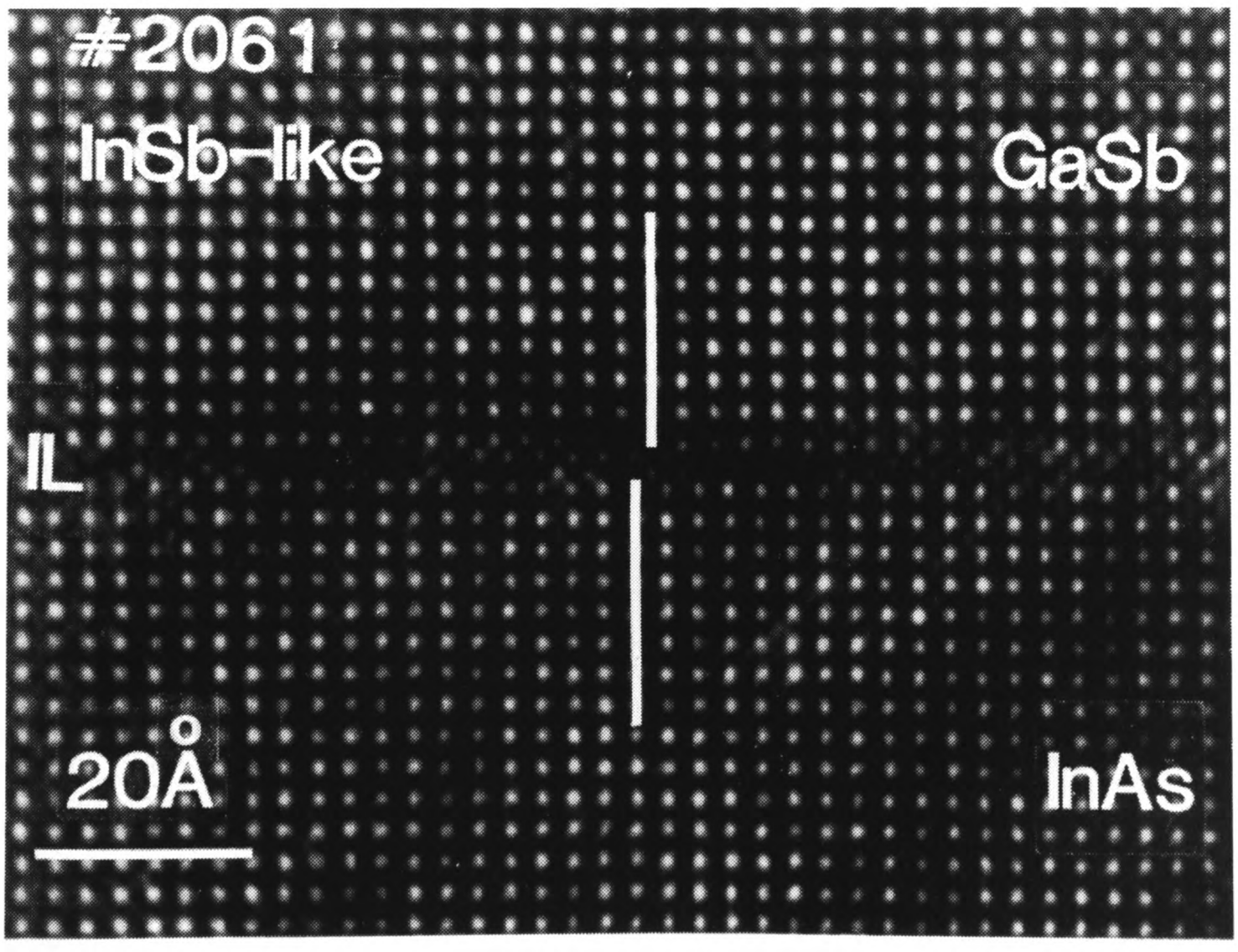


Figure 2.6. HRTEM image of an 'InSb-like interface taken from 2061. This (100) projection actually shows ordering of the rows of heavy constituent III-V atoms and a one monolayer interface.

Over the range sampled, figure 2.6 shows a clean, monolayer wide 'InSb-like' interface. Similar quality results have been observed for a 'GaAs-like' interface.

Note that TEM and other ex-situ techniques have also been used to analyse the quality of growth of bulk materials and SLs using different precursors [9].

2.4 Sample Processing and Contacting

To make electrical measurements for vertical transport, contacts must be made to the samples. As mentioned in section 1.5.1, one of the important properties of InAs/GaSb interband resonant conduction structures is a very high current density. In order to keep the measured currents in the range of milliamps to reduce joule heating effects, it is therefore necessary to restrict the diameter of the devices to the order of microns. This requires intricate processing, and is performed by Hill and co-workers at the University of Sheffield. The structure of InAs/GaSb SHETs used in this thesis is illustrated in figure 2.7. A 6000 Å nominally undoped GaSb buffer layer is grown on top of a p^+ GaSb substrate followed by a 50 Å layer of undoped InAs. The structure is capped by a 3000 Å layer of n-type InAs to aid in contacting. An outline of the procedures involved in making contacts for an InAs/GaSb SHET follows.

First the sample is cleaved into an area of around 1 cm^2 and cleaned. Next, 5 nm of gold is evaporated onto the p^+ GaSb substrate. The purpose of this initial gold layer is simply to provide the next element for evaporation, zinc, a surface it can adhere to. 20 nm of zinc is then evaporated on top of the gold. The back contact is completed with an evaporation of 200 nm of gold followed by an anneal at 360°C. At this temperature, the evaporated layers partially diffuse into the sample, forming an ohmic contact with the p^+ GaSb substrate. Figure 2.7 shows a schematic side view of a SHET

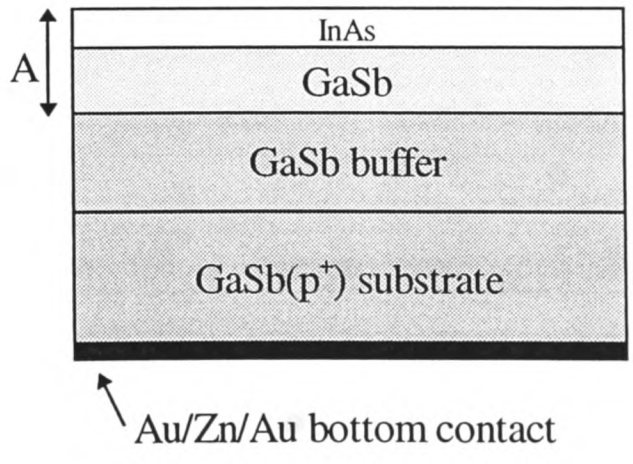


Figure 2.7. Side view of sample indicating the active region, A. The first stage of processing involves the evaporation of the Au/Zn/Au bottom contact onto the substrate followed by an anneal.

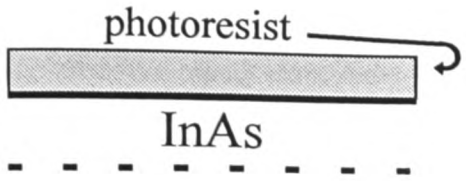


Figure 2.8. An even layer of photoresist is spun onto the InAs.

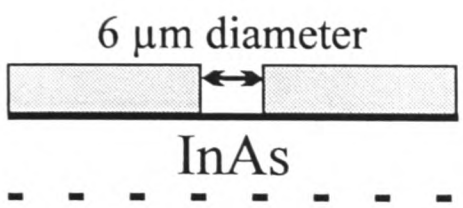


Figure 2.9. A 'hole' is removed from the photoresist by exposure to high intensity U/V light through an appropriate mask, followed by immersion in developer.

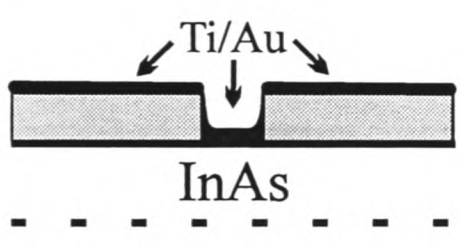


Figure 2.10. Ti/Au is evaporated onto the InAs.

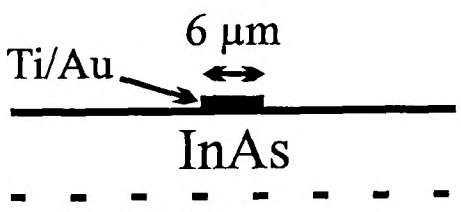


Figure 2.11. Lift - off leaves a 6µm contact behind.

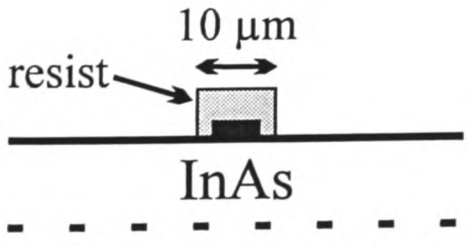


Figure 2.12. Gold cylinder covered with photoresist before the cylindrical device (mesa) is defined.

structure, indicating the active region A.

A layer of photoresist is spun onto the InAs (figure 2.8). A photographic mask of 6µm diameter blacked circles with their centres spaced 300 µm apart is placed over the sample, and a high intensity ultraviolet (U/V) lamp is used to expose the resist. Developing leaves 6 µm diameter 'holes' behind (figure 2.9).

The next procedure is to evaporate titanium/gold for the top contact. A layer of titanium, 20 nm thick, is evaporated first. This helps the adhesion of the 200 nm of gold, which is evaporated next, to the InAs (figure 2.10). The remaining photoresist is dissolved in acetone in a lift-off process, leaving 6 µm titanium/gold contacts on the surface of the InAs (figure 2.11).

The sample is again covered in a layer of photoresist, masked, exposed and developed. The remaining resist forms 10 µm 'cylinders' above the gold (figure 2.12) which protect the contact from degradation during the next processing step. The sample is now ready to etch. It is placed in a solution of hydrobromic acid, acetic acid and potassium dichromate and left for a known time until the etchant has gone through the InAs and penetrated the GaSb layer by the required depth (usually 200 nm). Removing the remaining photoresist results in the structure shown in figure 2.13. This etched structure (mesa) has a diameter of approximately 9 µm because the etchant etches in all directions.

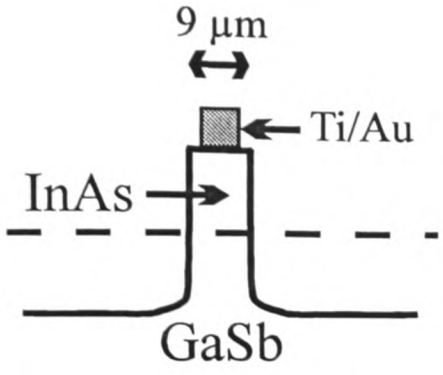


Figure 2.13. The etched sample mesa with photoresist removed.

Consequently, an etch down 500 nm also etches into the side of the mesa by the same amount. The removal of 500 nm all around the 10 µm structure, therefore, results in a mesa of diameter 9 µm. The 6 µm contact pad is too small for a direct connection to be made, as probe bonding techniques require a surface of diameter at least 80 µm. Further processing is therefore necessary.

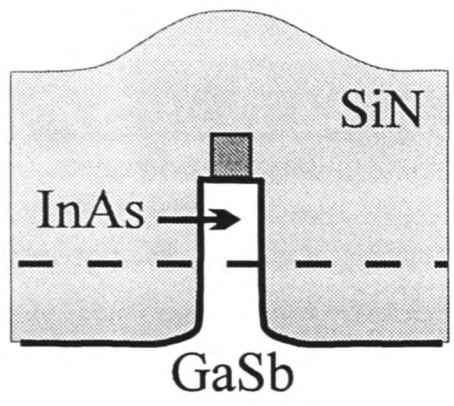


Figure 2.14. 600 nm of SiN is deposited, providing electrical insulation and a secure base upon which to evaporate the gold bond pad.

The sample is then placed in a nitrider and 600 nm of non-stoichiometric silicon nitride (SiN_x - commonly referred to as SiN) is deposited onto the surface (figure 2.14). This provides any necessary electrical insulation.

Following this, a layer of photoresist is spun onto the top of the SiN, and a mask similar to that used for figure 2.9 is placed on top. Exposure to U/V and developing follows. This leaves behind a layer of photoresist on top of the SiN which has 6µm diameter holes directly above the mesa (figure 2.15).

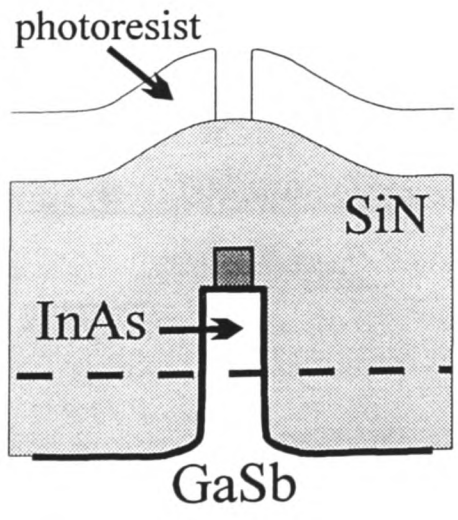


Figure 2.15. Showing 6µm holes in photoresist directly above the gold capped mesa.

A Freon[14] - oxygen plasma etch, where a radio frequency discharge produces •O and •F free radicals to react with the SiN making SiF_4 and SiO_2, is used to etch down through the holes in the resist to the relatively inert gold cap. The resist is then removed leaving a channel through the SiN to the gold contact on top of the mesa (figure 2.16).

A final layer of photoresist is spun onto the structure and a mask of 100 µm blacked circles is placed on top with their centres directly above the centres of the mesas. Exposure and developing leaves 100 µm

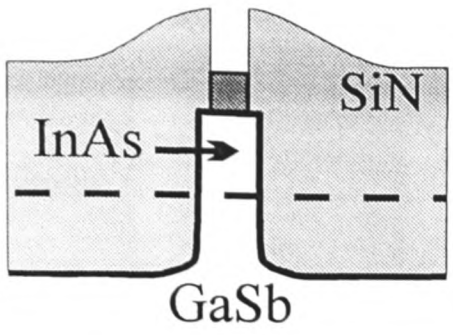


Figure 2.16. 6μm channel in the SiN exposing the gold contact for further processing.

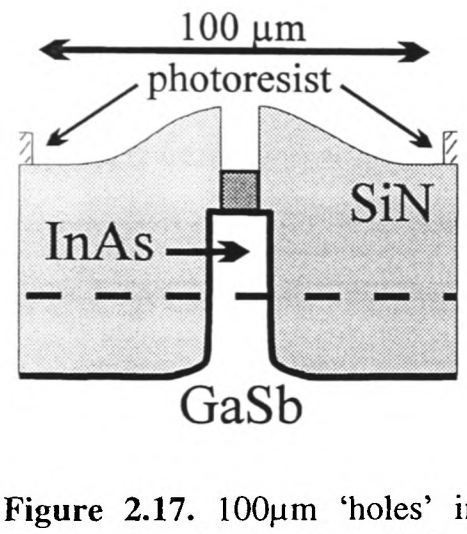


Figure 2.17. 100μm 'holes' in the resist ready for further evaporation of Ti/Au to form the 100μm bond pad.

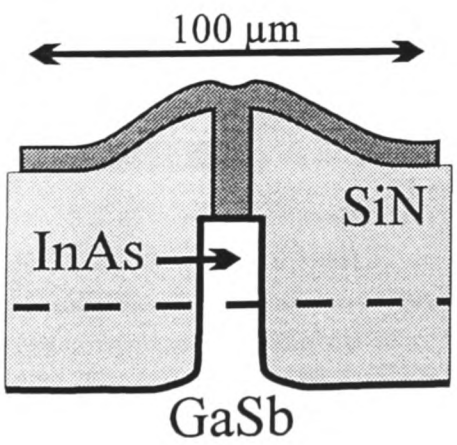


Figure 2.18. Completed mesa with bond pad ready to cleave and mount in H4 package.

holes in the resist (figure 2.17). A further evaporation of titanium/gold followed by a lift-off process to remove any photoresist and excess gold leaves each mesa with a 100 μm bond pad above it (figure 2.18). The structure is now ready for contacting.

When processed, the samples are cleaved into 'chips', leaving four to six mesas on each. These 'chips' are then mounted in H4 semiconductor packages (figure 2.19). These are manufactured by LEW Techniques Ltd for microwave applications and consist of a conducting, gold coated, top rim which is separated from the bottom gold coated disk by insulating bakelite. Inside is a copper pedestal on which the sample substrate is fixed with gold epoxy. A gold wire is bonded from the top of one 100 μm bond pad to the package rim.

It is worth mentioning that SHET structures were also grown on [001] oriented GaAs substrates which were pre-coated with a GaSb buffer layer. During processing, rather than evaporate gold onto the substrate, an attempt was made to contact to the first GaSb epilayer from the mesa side (*top contact the base*). This, if successful, would have provided a method of contacting SHET structures whose electrical properties were not hindered by those of the GaSb or GaAs substrate. Additionally, it would have been possible to grow SHET structures on [111] oriented GaAs substrates and observe any change in vertical transport. Unfortunately, it was not possible with the available technology to etch down through the structure in a controlled enough manner for the

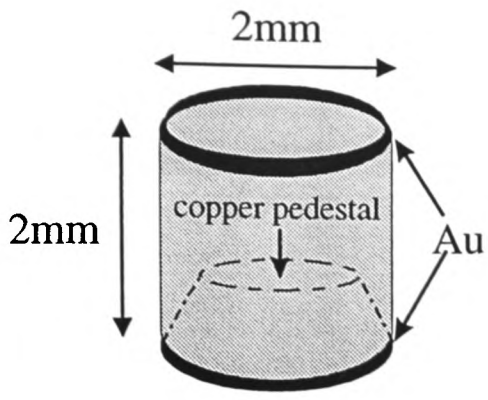


Figure 2.19. H4 package in which samples are mounted ready for experiments.

contacts to be applied to the GaSb epilayer, but improvements are being made in this area.

2.5 References

[1] G D Austing. DPhil Thesis, Oxford (1992).

[2] G R Booker, P C Klipstein, M Lakrimi, S Lyapin, N J Mason, R J Nicholas, T-Y Seong, D M Symons, T A Vaughan & P J Walker. Journal of Crystal Growth 145, p778 (1994).

[3] G R Booker, P C Klipstein, M Lakrimi, S Lyapin, N J Mason, I J Murgatroyd, R J Nicholas, T-Y Seong, D M Symons & P J Walker. Journal of Crystal Growth 146, p495 (1995).

[4] N J Mason & P J Walker. Journal of Crystal Growth 107, p181 (1991).

[5] S G Lyapin, P C Klipstein, N J Mason & P J Walker. Physical Review Letters 74, p3285 (1995).

[6] See for example S Holmes, W T Yuen, T Malik, J S Chung, A G Norman, R A Stradling, J J Harris, D K Maude & J C Portal. Journal of Physics and Chemistry of Solids 56, p445 (1995).

[7] S G Lyapin, P C Klipstein, N J Mason & P J Walker. Superlattices and Microstructures 15, p499 (1994).

[8] B R Pamplin (Ed.). Crystal Growth 2nd edition, Pergamon, 1980.

[9] R M Graham, A C Jones, N J Mason, S Rushworth, A Salesse, T-Y Seong, G Booker, L Smith & P J Walker. Semiconductor Science and Technology 8, p1797 (1993).

3 Experimental Techniques

3.1 Introduction 37

3.2 Vertical Transport Measurements 37

3.2.1 I/V measurements 37

3.2.2 Hysteresis in the I/V 39

3.2.3 Pulsed Measurements 41

3.3 Hydrostatic Pressure 42

3.3.1 The 'Cambridge' Cell 42

3.3.2 The 'Russian' Cell 45

3.4 Low Temperatures 47

3.5 High Magnetic Fields 49

3.5.1 DC Field 49

3.5.2 Pulsed Field 50

3.6 References 51

3.1 Introduction

Changing external parameters like temperature or magnetic field from those under ambient conditions is a well established solid state technique for probing the properties of semiconductors. This thesis contains results from two-terminal vertical transport I/V measurements of InAs/GaSb single heterojunction (SHET) structures taken at pressures ranging from 1 bar to 22 kbar, temperatures from 2K to 300K, continuous magnetic fields up to 15T and pulsed fields up to 40T. Sections 3.2 - 3.5 describe the experimental set-up used in each case.

3.2 Vertical Transport Measurements

The way in which I/V and d*I*/d*V* traces were acquired is detailed in section 3.2.1 and in section 3.2.2 the main problem with 2 terminal measurements is discussed, namely the effect parasitic resistances have on sample data. Finally, section 3.2.3 introduces a novel way to obtain accurate I/V information from large area samples, where unwanted series resistances are always prominent.

3.2.1 I/V measurements

After the processing steps described in section 2.4 the sample may be handled easily, protected by its H4 package. A length of gold wire of diameter 0.05 mm and approximately 5 mm long is indium soldered onto the rim of the H4 package to provide the top electrical contact. A similar length of gold wire is indium soldered onto the base to provide the second contact.

To take room temperature I/V measurements at 1 bar and without a magnetic field, the gold wires connected to the H4 package have to be indium soldered onto the ends of two copper wires, the other ends of which are fed into the inputs of a home made I/V measuring unit designed by Smith [1] (figure 3.1).

This unit supplies a steady voltage, V_{in}, either internally generated or externally provided, ranging from 0 to 15V to a voltage amplifier, AMP 1, which drives terminal

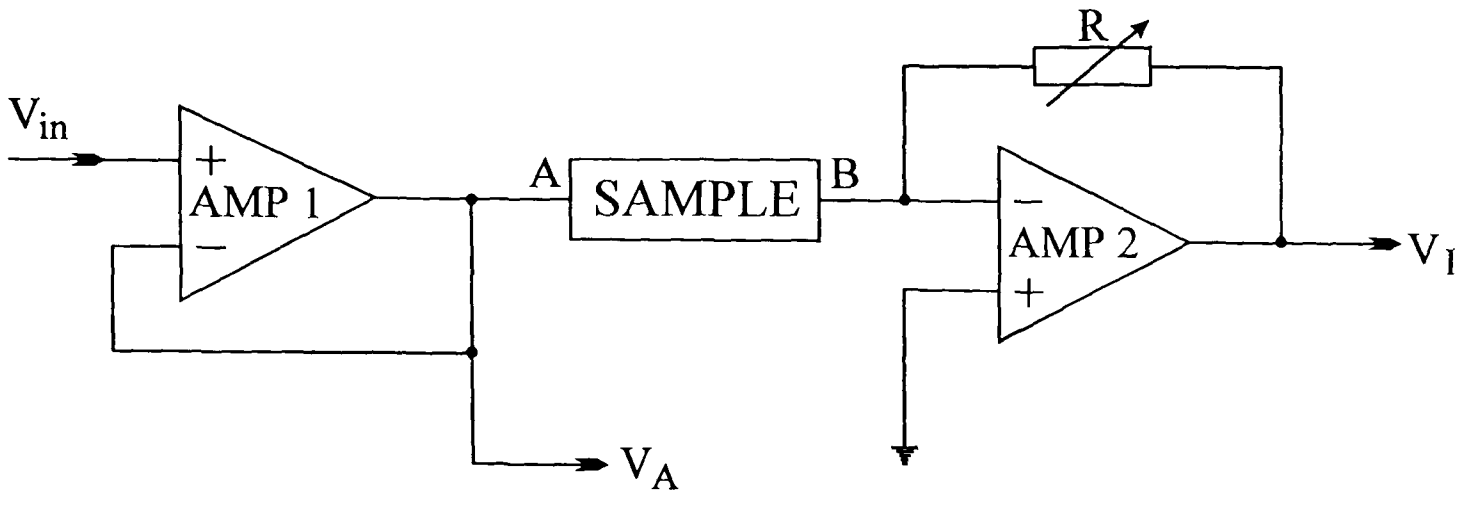


Figure 3.1. Basic circuit for I/V measuring unit.

A of the sample. Negative feedback keeps AMP 2 'ideal' so V_B is equal to the voltage at its positive input, making V_B a 'virtual earth' - very close to 0V. This means the voltage across the sample is accurately given by V_A. The current fed back through R to the amplifier input will exactly cancel the current flowing in the sample, so the sample current is given by :

$$I_S = -\frac{V_I}{R} \qquad \textbf{(3.1)}$$

where V_I is the output from AMP 2 in figure 3.1.

This arrangement means that both current and voltage signals are available as voltages relative to ground, and the current monitoring system does not affect the voltage experienced by the sample.

The resistor, R, can be switched to give output sensitivities ranging from 10 μA/V up to 10 mA/V, allowing the output to be kept between 0 and 10V for optimal use with digital voltmeters. The voltage output V_A is read by a Keithley model 195 digital multimeter (DMM) to an accuracy of 0.1 mV, and the current V_I by a Keithley model 196 DMM to 5 decimal places.

In practice, data acquisition is controlled by a computer program called "NDR for Windows" which I developed and wrote. It controls all initialisation procedures, the voltage ramp via a PCL-711S digital to analogue (DAC) converter made by Advantech Co. Ltd, the data acquisition via a Keithley KPC-488.2 IEEE-488 interface card and plots the I/V trace on the screen as it proceeds.

If weak features of the I/V characteristic need to be identified clearly, a Stanford Research Systems SR510 Lock-In Amplifier is used to measure dI/dV as a function of V (the conductance characteristic). The applied DC voltage has a small AC signal added to it and the resulting current-proportional voltage (see V_I in figure 3.1) can be represented by a DC component C, and a modulated component $B\sin\omega t$. The voltage V_I is fed into the lock-in where it is multiplied by a reference sine wave signal $A\sin\omega t$ from the same source as the applied modulation, yielding :

$$-\frac{1}{R}\left(\frac{AB}{Z_1}\sin^2\omega t+\frac{CA}{Z_0}\sin\omega t\right), \qquad \textbf{(3.2)}$$

where $Z_0(V_{in})$ is the DC resistance of the sample and Z_1 is dV/dI measured at V_{in} which is the small signal differential resistance at an applied voltage V_{in}. Equation 3.2 can be rewritten as :

$$-\frac{AB}{2RZ_1}(1+\cos 2\omega t)-\frac{CA}{RZ_0}\sin\omega t\,. \qquad \textbf{(3.3)}$$

Providing equation 3.3 is integrated over a sufficiently long time, a value proportional to $1/Z_1$ $(= \mathrm{d}I/\mathrm{d}V|_{V_{in}})$ results.

Numerical differentiation of dI/dV using Microcal Origin, a plotting program with its own built in routine, yields the second derivative of the current with respect to the voltage, $\mathrm{d}^2I/\mathrm{d}V^2$. It is therefore possible to pinpoint accurately very weak I/V features that might otherwise remain unresolved.

For measurements at 1 bar and 77K, the sample is simply lowered into a bucket of liquid nitrogen, and data is acquired as above.

3.2.2 Hysteresis in the I/V

Occasionally it was observed that measurements made while the voltage increased from a low to high value yielded a different I/V curve to that obtained while the voltage decreased towards zero (figure 3.2). Under these conditions it is necessary to consider the sample load line.

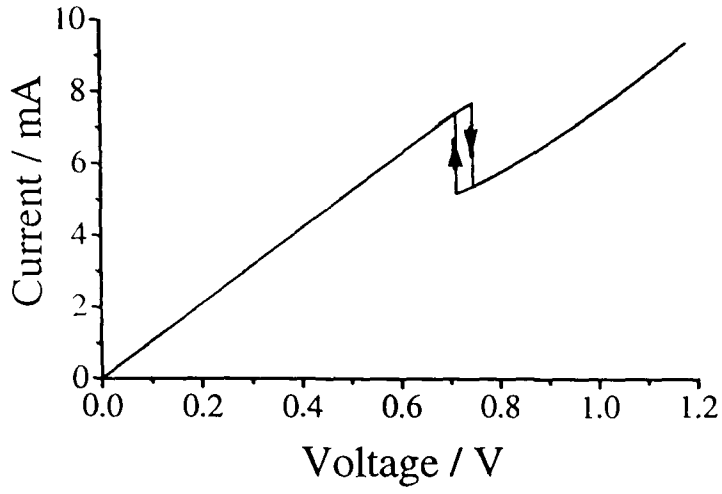


Figure 3.2. I/V curve of SHET in forward bias showing hysteresis. The arrows indicate the direction of the voltage.

The effective circuit can be treated as an ideal device in series with a resistance which represents the parasitic lead and contact resistances (figure 3.3). If V_D is the voltage across the ideal device, and V_t the actual voltage across the device together with its parasitic resistance R_u, then for a current I_t the equation of the load line is :

$$V_D = V_t - I_t R_u . \qquad \textbf{(3.4)}$$

The situation for a sample with a significant parasitic series resistance is plotted schematically in figure 3.4. The observed voltage, V_t, is given by the intercept of the load line with the voltage axis.

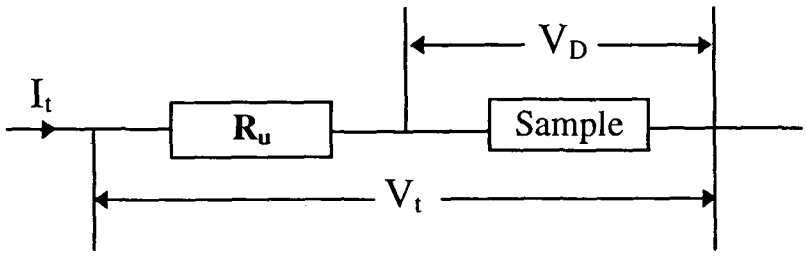


Figure 3.3. Simple representation of a sample with a parasitic series resistance, R_u.

The observed peak current, unaffected by the parasitic resistance, is the true current through the ideal device and is given by the intercept of the load line with the ideal characteristic.

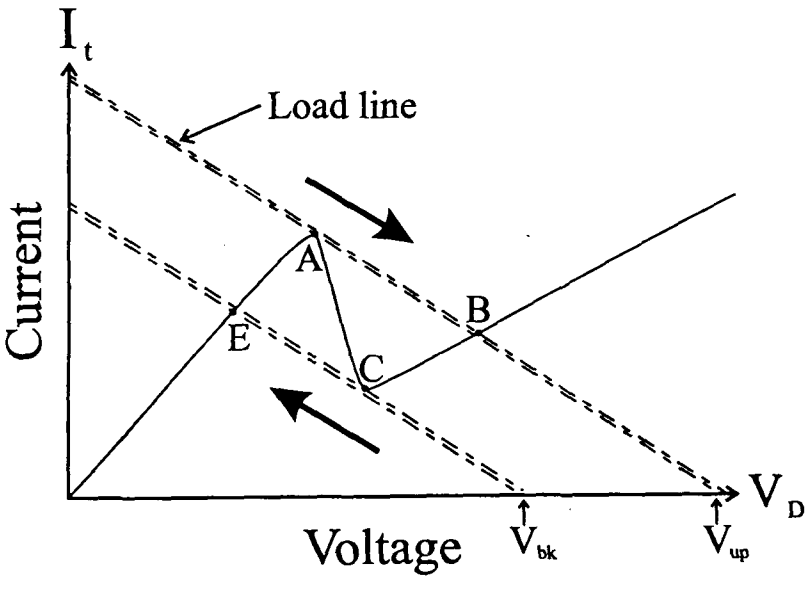


Figure 3.4. Typical SHET characteristic (solid) and for load lines (dashed) at biases in the vicinity of the resonance on scanning up and down.

On increasing V_t the current will increase to the peak current of the ideal device, given by point A in figure 3.4, when $V_t = V_{up}$ and $V_D = V(\mathrm{A})$. Any further increase in V_t means the current has to switch to that at point B, but the correct valley current is given by point C so that measured at point B is not correct.

The correct valley current may only be observed by decreasing the voltage through the resonance from above, when a switch from point C to point E in figure 3.4 will occur at an applied voltage, $V_t = V_{bk}$. In this case the valley current is correct, but the peak is not. The resulting I/V curve (figure 3.2) when scanned up and down will therefore give accurate information about the currents (but not the voltages) at which the device exhibits NDR.

3.2.3 Pulsed Measurements

For the observation of currents greater than 40 mA, a pulser was designed and built by Smith [1]. In order to minimise Joule heating effects, a 10 μs voltage pulse of up to 20V is supplied to the sample when triggered. The voltage and current, measured in the same way as section 3.2.1, are sampled and held in a two stage circuit, holding the output with negligible drift over minutes.

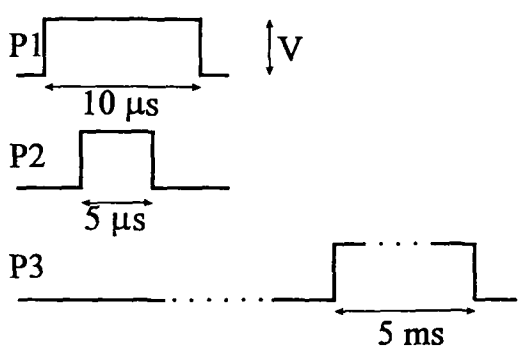


Figure 3.5. The second pulse, P2, triggers the first sample and hold circuit. It lasts for 5 μs and starts 3 μs after the current pulse, P1. P3 triggers the second sample and hold circuit, sampling the output to the first over a relatively large time. This gives an output that drifts negligibly over minutes.

A 10 μs pulse, P1, defines the duration of the current pulse (figure 3.5). A second pulse, P2, of duration 5 μs and delayed 3 μs from the start of P1 is generated to enable the first sample and hold circuit (S&HC). This is timed to be on only during a stable part of the current pulse - after starting transients have decayed, and before switch off transients start.

The second S&HC has a sample period, P3, of 5 ms. This starts shortly after the end of the current pulse and samples the output of the first S&HC, holding the output steady over minutes.

For samples with large diameters (roughly 100 μm), peak currents in the range of Amps can be expected (section 1.5.1). The pulser is potentially very useful in these situations as samples with 10 μm diameters require advanced micron fabrication techniques (section 2.4) whereas it is possible, in theory, to prepare 100 μm mesas in-house. This would provide a quick way of screening the grown samples before

sending the best ones to be processed into smaller devices. One drawback, however, is the inability of a positive going pulse, as in P1, to exhibit the full sample characteristic in the case of hysteresis. Such large area samples typically have resistances of 0.5 Ω, and with parasitic resistances (leads and contacts) several times this value, hysteresis is inevitable (see section 3.2.2).

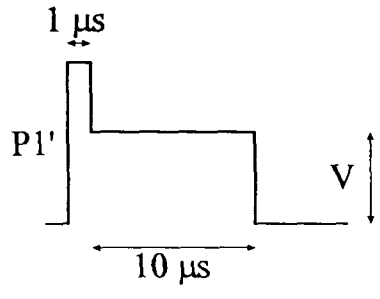


Figure 3.6. P1′ is modified to allow for the measurement of hysteresis by pulsed methods. The sample 'sees' a voltage decreasing to a value, V.

Following the arguments in section 3.2.2, the voltage in these cases has to be decreased from a value above the resonance in order to enable measurement of the correct valley. The pulser has been designed, therefore, to supply a voltage pulse, P1′, of a pre-set value (above the resonant voltage) for a duration of 1 μs before decreasing to the required voltage to be measured (figure 3.6). In this way the sample is able to experience a voltage *V* which has decreased from a value above the resonance. P2 and P3 are unaltered (see figure 3.5) and are timed from when P1′ switches to a value, *V*.

3.3 Hydrostatic Pressure

The application of hydrostatic pressure to an InAs/GaSb heterojunction reversibly alters its band structure [2]. This can have profound effects on the vertical transport characteristics, yielding useful information about the underlying physics.

Two pressure cells have been used to obtain results for this thesis. The first, designed at the Cavendish Laboratory, Cambridge by Friend and Simmonds, is capable of pressures up to 16 kbar at 77K (section 3.3.1). The second was designed by Eremets at the Vereshchagin Institute for High Pressure Physics, Moscow. This can reach pressures in excess of 27 kbar at 77K (section 3.3.2). A summary of both cells and their operation follows.

3.3.1 The 'Cambridge' Cell

The principle of operation of both the 'Cambridge' and the 'Russian' cells are simple.

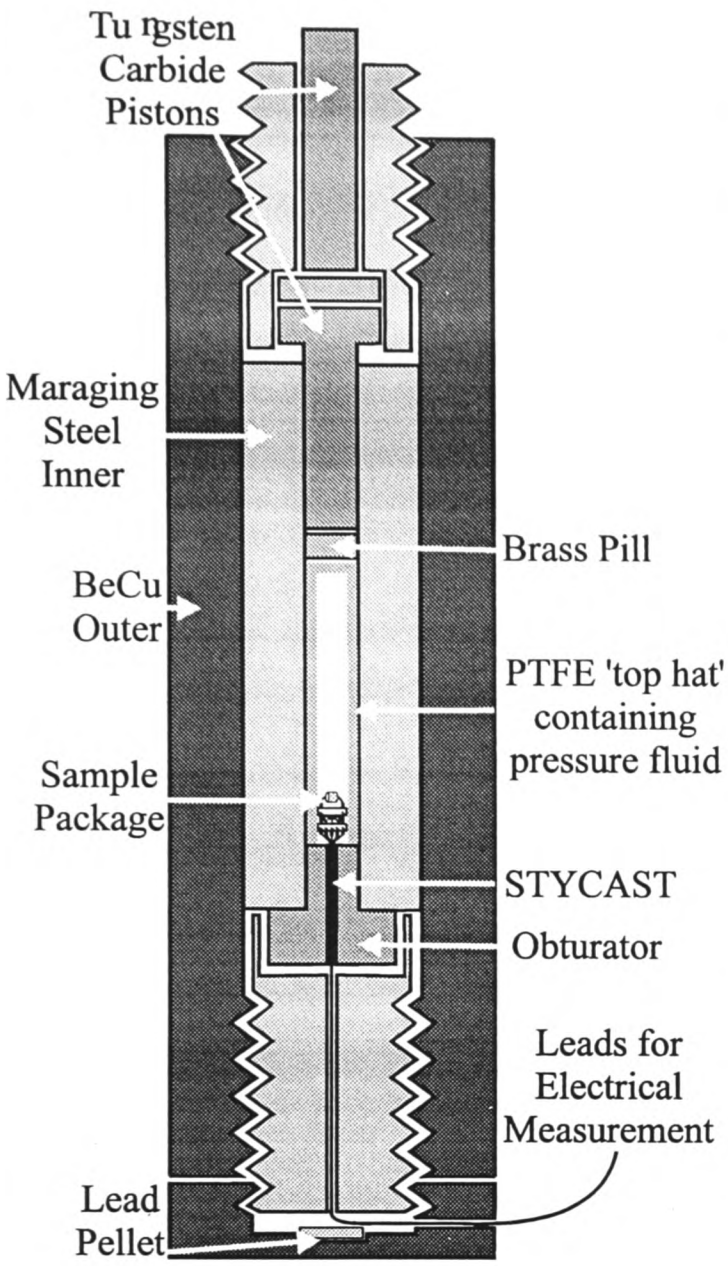


Figure 3.7. Cross section of the 'Cambridge' cell.

They involve the compression of a liquid which is confined in a PTFE (teflon) capsule. The H4 package (section 2.4) also sits in this fluid, and the sample experiences elevated hydrostatic pressures.

The 'Cambridge' cell has a high volume two component cylindrical pressure vessel. Shown in figure 3.7, the beryllium-copper cell body measures 120 mm long and has an outside diameter of 34 mm. A 60 mm long maraging steel cylinder with a 9.5 mm diameter precisely honed bore is wedged inside this outer body. This two stage system, where the body and pressure core are separate, is safer and allows a higher operating pressure than a single component pressure vessel because the pressure core is actually under compression at 1 bar.

In order to make electrical measurements while the samples are under pressure, electrical leads have to be introduced into the sample space, and a seal around these wires has to be formed which is able to withstand the operating conditions. Ten leads of 40-gauge copper wire are fed through a hole in the middle of the electrical feedthrough (obturator). STYCAST 2850FT epoxy resin is cured with catalyst 9 and the mixture is evacuated after mixing and before use to remove any dissolved air. This resin is then pulled through the hole in the obturator under vacuum, coating the leads and taking care not to allow any air sacs to form. The resulting STYCAST once left to harden overnight is an excellent electrical insulator, has unusually high thermal conductivity and a low thermal expansion. Such properties are ideally suited for the role of providing electrical insulation between the leads, allowing any cooling of the cell to be as uniform as possible and keeping the obturator hole plugged over the

required temperature and pressure ranges.

The ten wires left exposed at the top of the obturator are soldered onto a sample stage (figure 3.8). Four of these leads are used for four terminal measurements on a coil of manganin wire [3] which acts as a manometer. The resistance of this wire at *constant temperature* has a known pressure dependence :

$$P = \alpha\left(\frac{R_P - R_0}{R_0}\right) + \beta\left(\frac{R_P - R_0}{R_0}\right)^2 \qquad \textbf{(3.5)}$$

where R_0 is the resistance of the wire at 1 bar, R_P at a pressure P, and α and β are constants that depend upon the temperature at which the measurements are made (see table 3.2) [4]. A current of 1 mA is supplied to the manganin wire using a current source designed and built in the Electronics Department of the Physics sub-faculty. This current is measured by a Keithley model 197A DMM and the four terminal measurement is completed using a Keithley model 2000 DMM to measure the voltage across the manometer. The resistances are calculated from these values and a pressure is determined using equation 3.5.

Temperature	α	β
300K	395.3	200
77K	391	200
4K	375	200

Table 3.1. Table of coefficients used in the calculation of pressure from the resistance of a manganin wire.

Two H4 packages can be comfortably soldered to the top of the sample stage. This requires four further obturator leads to provide two sets of two-terminal sample measurements. The remaining two leads are only used in case of a breakage or short circuit of any of the other leads in use.

A brass washer is placed around the obturator (figure 3.8) to aid in the sealing of the teflon capsule. This will start to flow above 6 kbar and seal in the pressure medium. BDA petroleum spirit is used for the medium because of its excellent hydrostatic properties [3].

A teflon capsule (figure 3.8), filled with petroleum spirit, fits snugly over the top of the obturator. They are then pushed into the maraging steel bore together and a holding bolt is screwed in, firmly securing the obturator into position. At the other end of the cell a brass pill is placed on top of the teflon capsule followed by a tungsten carbide piston. The pill is to prevent the teflon, once compressed, jamming the piston inside the bore by 'leaking' up its side. Another securing bolt which has its threads coated with molybdenum disulphide lubricant as a precaution against seizure is then screwed onto the top of the cell.

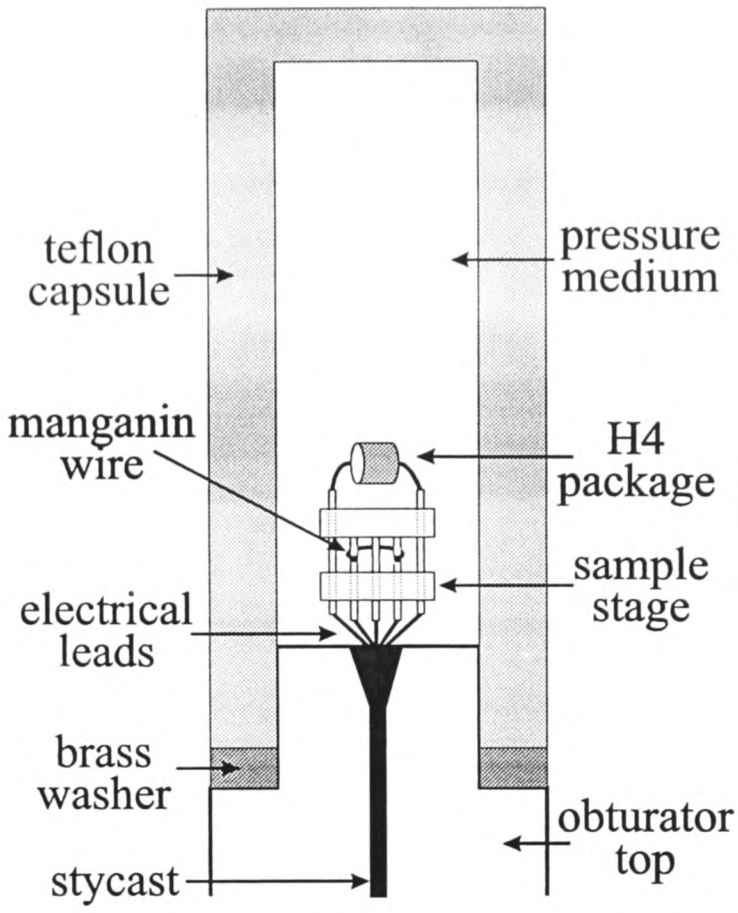


Figure 3.8. Close up view of teflon capsule, sealing brass washer and sample stage used for 'Cambridge' cell.

Force is applied using an LCP 20 hydraulic pump press manufactured by Unipress which pushes a tungsten carbide rod down onto the piston, compressing the teflon capsule and the medium in which the sample resides. At room temperature, pressures as high as 20 kbar can be achieved using a force of 20 tonnes. On cooling to 77K and below, this reduces to 16 kbar because of the thermal contraction of the pressure medium.

3.3.2 The 'Russian' Cell

This is also a two component pressure vessel. It is, however, much smaller than the 'Cambridge' cell, with the outer beryllium-copper body measuring just 27 mm in diameter and 47 mm in length. The inner is made from a strong, non-magnetic Nickel-Chromium-Aluminium alloy (NCA), 20 mm in length and with a 4 mm bore which was first developed for Russian military usage (figure 3.9).

Although the principle of operation is the same as the 'Cambridge' cell, the difference

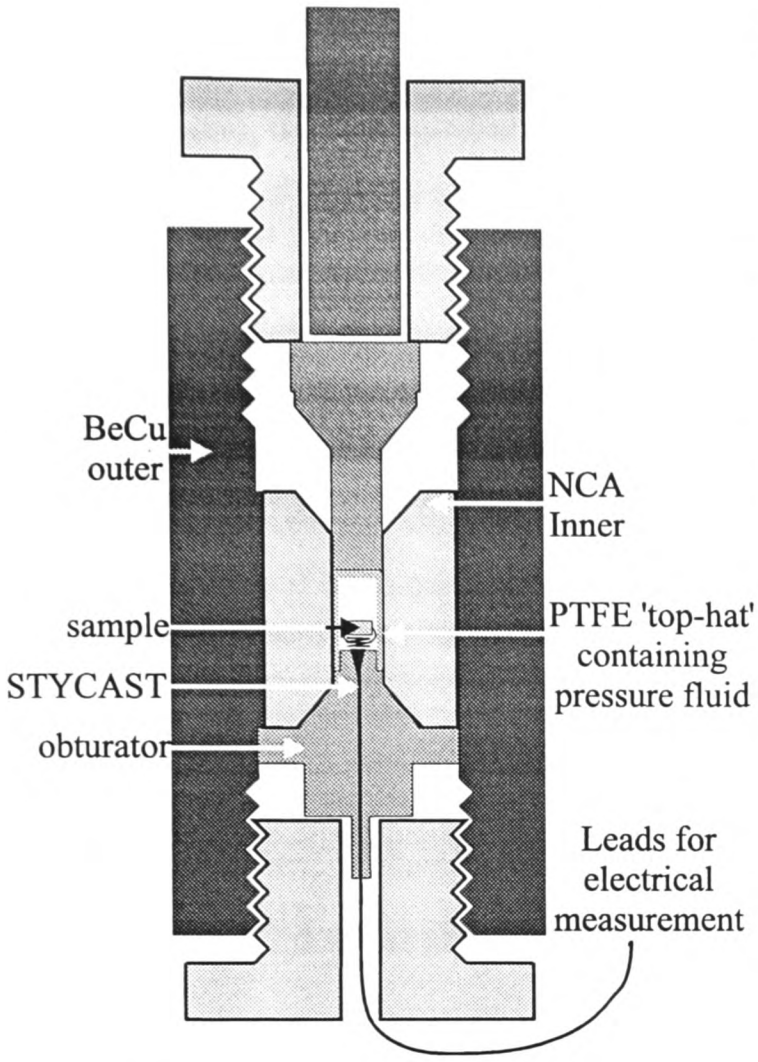


Figure 3.9. Cross section of the 'Russian' cell.

in size requires smaller components and some alternative techniques. Twelve 46-gauge insulated copper wires provide the electrical connections. The STYCAST is prepared in the same way as in section 3.3.1, but instead of being drawn through the NCA obturator under vacuum, a 1 cm section of the leads is coated in the resin and simply pulled through very slowly. The very small obturator hole (diameter 450±50 μm) means that the force exerted on the STYCAST here is much smaller than for the 'Cambridge' cell at the same pressure.

The manganin wire and each of its ends are attached to two leads. The manometer is wound into a coil which is as flat as possible to the obturator top, providing maximum space for the one H4 package that can be housed by the cell, which is connected directly to two more obturator leads with gold wire. The 9 mm long teflon capsule is then filled with petroleum spirit and pushed over the obturator top, forming a seal with the brass washer. The obturator and capsule fit into the NCA bore and are secured by the bottom fixing bolt. A brass washer fits over the top of the teflon capsule, followed by a tungsten carbide top piston and a securing top bolt.

The force required to reach a given pressure by the 'Russian' cell is much smaller than that for the much larger bore 'Cambridge' cell. The highest pressure, in the region of 28 kbar at room temperature, is reached with a force no greater than 3 Tonnes. This pressure reduces to 27 kbar at 77K.

A summary of the advantages and disadvantages of both cells are shown in table 3.2.

'Cambridge' cell	'Russian' cell
Takes two samples at once	Only has space for 1 sample
Easier to seal	More problematic to seal pressure fluid
Larger diameter bore requires much more force for a given pressure	Requires little force for high pressures
Large liquid volume contains a lot of stored energy at high pressures	Smaller volume houses less energy and is therefore safer to use
Can only attain 16 kbar at 77K	Can reach 27 kbar at 77K
Maraging steel bore cannot be used for measurements in a magnetic field	NCA alloy is non-magnetic

Table 3.2. A comparison of the advantages and disadvantages of both pressure cells.

3.4 Low Temperatures

For the collection of data at low temperatures (< 77K), either with pressure or without, an Oxford Instruments (OI) model CF 1200 continuous flow cryostat was employed. The combination of this and an OI model ITC502 temperature controller allowed control of the sample temperature over the required range.

Figure 3.10 is a schematic diagram of the low temperature experimental set-up. One end of a vacuum insulated transfer tube (OI's GFS 300) is dipped into a dewar of liquid helium (LHE). The other end attaches to the cryostat and is sealed. A capillary now runs from the helium dewar to the bottom of the cryostat. A wider tube, effectively from the top of the cryostat to an OI model VC 30 gas flow controller, leads to a needle valve. This needle valve is used to control the strength of the pressure differential created by a Compton pump, the output of which is vented into the Clarendon's helium return system.

The LHE is drawn from the dewar and through the cryostat by the Compton pump at a rate determined by the position of the needle valve. A heater wire and one end of a gold(iron)-chrome thermocouple, T1, are located at the bottom of the cryostat on a copper block fairly near the helium capillary tube entrance. The temperature controller senses both changes in temperature and the rate of change by measuring fluctuations in the induced e.m.f. across the thermocouple, the other end of which is

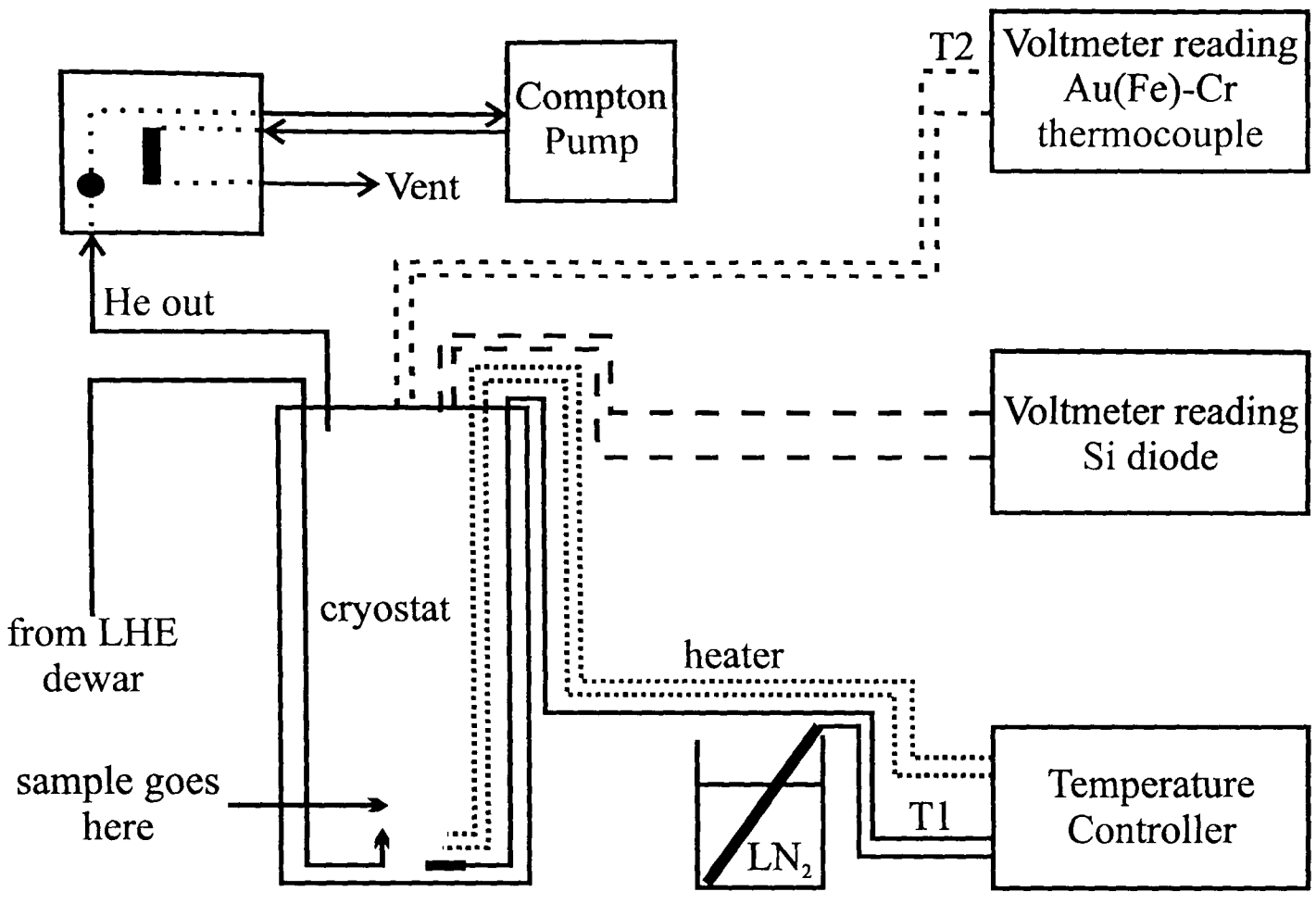


Figure 3.10. Schematic diagram of low temperature experimental set-up.

immersed in liquid nitrogen (LN). It then supplies the heater with a suitable voltage in order to converge to the desired temperature as quickly as possible.

Both pressure cells can be attached to the end of a long thin walled stainless steel rod with electrical wires running up its length. This is called an insert and fits snugly (with either pressure cell) into the cryostat. The whole system is sealed with tight clamps over rubber 'O-rings', preventing helium leakage. The insert has a silicon diode, calibrated against temperature, located just above the pressure cell holder. This is supplied with a 10 μA current by a current source made in the Electronics Department. The voltage across it is measured using a Keithley model 195 DMM, yielding the temperature at the silicon diode.

The working cryostat has a vertical temperature gradient, where the bottom is much colder than the top. This implies that the diode is actually hotter than the sample. A small correction is made by monitoring a second gold(iron)-chrome thermocouple, T2, which has one end attached to electrically insulated copper wires, thermally anchored to the same copper block as that in which the diode is located and the other end of which is strapped to the pressure cell. A Keithley model 197 DMM is used to read the thermocouple voltage, and hence the temperature difference between D1 and

the pressure cell. The combination of T2 and D1 provides sample temperature measurement accurate to ± 1K when the system is at equilibrium.

Two terminal I/V measurements can now be made as in section 3.2.1 over a wide range of temperatures.

3.5 High Magnetic Fields

The effect a magnetic field has on a free electron gas is well established [5]. Any change in the distribution of the 2DEG or 2DHG in an InAs/GaSb SHET will alter its vertical transport characteristics in a manner which may provide valuable information about the underlying physics of the device.

The samples were placed in steady magnetic fields up to 15 T and the equipment used for this is described in section 3.5.1. Pulsed fields up to 40 T were also used and section 3.5.2 describes this experimental set-up.

3.5.1 DC Field

An OI superconducting magnet was used for the steady field measurements. An OI PC120 power supply is used to provide the LHE cooled superconducting coils with currents up to 120A at up to 10V (in reality, 120 A is never reached as this would quench the magnet). The system gives steady fields up to 15T at 4.2K and 17.4T at 2K.

The copper-titanium and copper-niobium superconducting magnet coils are contained in a LHE bath. A continuous flow cryostat designed by Cosier and made by Rawlings is used for accurate control of the sample temperature. This sits in the middle of the coils. A capillary runs from the helium bath via a needle valve to the base of the inside of the cryostat, enabling LHE to be drawn from the bath itself. The other difference between this set-up and that of figure 3.10 is the temperature sensor used by the temperature controller (Thor Instruments model 3010 II) to control the heater voltage. In the place of a thermocouple, rhodium-iron and carbon-glass resistors are used. The former is very stable over long time periods (> 1 year) but has a strongly field

dependent resistance ($\Delta T/T = 30\%$ at 40K and B = 14 T) and the latter is less stable but with only a very small field dependence ($\Delta T/T = 1.3\%$ at 45K and B = 14 T).

The insert is designed so the 'Russian' cell can fit into the cryostat such that the sample is at field centre which is homogeneous over a spherical volume of approximately 1 cm^3. Again, rhodium-iron and carbon-glass resistors, just above the cell holder, are used to monitor the sample temperature.

Once the magnet has been trained and the necessary sample temperature reached, the field is swept up to the required value and an I/V curve taken as in section 3.2.1.

Using "NDR for Windows", it is possible to take measurements of dI/dV against magnetic field. The computer reads the output of the SR510 Lock-in amplifier via an IEEE interface, and the magnetic field direct from the power supply via an RS232 interface. This data is potentially very useful in monitoring of the movement of Landau levels with field.

3.5.2 Pulsed Field

The Clarendon houses a 50T pulsed field magnet with a total pulse length of 20 ms [6]. Four 8 mF banks of ten capacitors connected in parallel can be charged up to 2 kV to provide the huge discharge needed for the solenoid, inducing a large field, *B*. The coil [7] consists of two sections - the inner, made from copper-niobium, and the outer, from an Al_2O_3 dispersion hardened copper. The inner, high stress, region needs a high strength material which typically will have a high resistivity. In order to minimise coil heating and extend the solenoid working life, a low overall resistance is desirable and the outer material is therefore chosen to have a higher conductivity and a moderate strength.

The magnet is immersed in a LN dewar and a stainless steel vacuum insulated insert is placed in the inner cavity. This can then be filled with LHE or LN for sample cooling as required. The H4 package is soldered onto the end of an insert (made from bakelite and stainless steel to limit heating from eddy currents) making sure the connecting leads used for I/V measurement form a twisted pair. dB/dt is measured from a pick up coil situated on the sample insert and read by Analogic's 4 channel 16 bit Data

Precision 6100 transient recorder every 5 μs. "WinPulse", a computer program written by Summers, is used to read this information via a high speed optical link, integrating it to give an accurate reading of B vs. t.

A voltage saw-tooth is applied to the sample over a period of 1 ms when the 20 ms field pulse is changing least, the forward bias peak of which is set to coincide with the maximum field. This optimises the forward bias measurements for peak field. The current and voltage are measured using the same circuitry as described in 3.2.1 and are read by two inputs of the transient recorder every 5 μs, then loaded straight into "WinPulse".

Note that a new pressure cell has been made by Eremets to fit inside the pulsed coils. This is a one stage clamp cell made entirely of NCA with an outer diameter of 15 mm and a bore of 3.8 mm. It has been tested up to 16 kbar at room temperature, falling to 12 kbar at 4K. Special attention had to be paid to restricting eddy currents due to the presence of such a large volume of metal at field centre. An insert for the magnet is currently being made to house the cell for future experiments in pulsed fields at high pressures.

3.6 References

[1] Dr David Smith is the head of the Electronics section of the Physics sub-faculty, Nuclear Physics Building, Oxford.

[2] The change in band structure is only completely reversible if the elastic limit of the material is not breached. See "Physical Properties of Crystals" by J F Nye. Oxford University Press, Oxford (1985).

[3] H Fujiwara, H Kadomatsu & K Tohma. Review of Scientific Instruments. 51, p1347 (1980).

[4] M Eremets, Vereshchagin Institute for High Pressure Physics, Moscow. Private Communication.

[5] C Kittel. Quantum Theory of Solids 2nd edition, Wiley, New York, p217 (1987).

[6] W J Siertsema & H Jones. IEEE Transactions on Magnetics 30, p1809 (1994).

Continued ...

References Continued ...

[7] H Jones, R G Jenkins, M Van Cleemput, R J Nicholas, W J Siertsema & M Van der Burgt. Physica B 201, p546 (1994).

4 Band Profile Calculations

4.1 Introduction 54
4.2 Initial Potential Approximation 56
4.3 The Schrödinger Equation 58
4.4 The Poisson Equation 60
4.5 Background Doping 61
4.5.1 GaSb 61
4.5.2 InAs 62
4.5.3 Interface States 63
4.5.4 Effect on the Band Profile 64
4.6 InAs Band Non-Parabolicity 65
4.7 The Fermi Level 66
4.8 Applying a Bias 67
4.9 Pressure Dependence 68
4.10 References 69

4.1 Introduction

Band profile calculations play a central role in the understanding of vertical transport, and an important part of this thesis concerns itself with exactly these calculations for an InAs/GaSb SHET. Self-consistent band edge profile calculations have been performed for an GaSb/InAs/GaSb double heterojunction by Beerens et al. [1] who used a simple variational approach to obtain a one-sub-band analytical solution following the method of Bastard [2]. More recently Symons et al. used a similar formalism with improved accuracy to calculate band edge profiles for InAs/GaSb superlattices and double heterojunctions [3]. They solved exactly for the InAs quantum well but used the Fang Howard variational method [4] to approximate a one band solution for GaSb. Although this is a valid assumption for those structures where any error in GaSb confinement energies is small compared to those in InAs, the behaviour of a SHET when biased is very dependent upon the number of sub-bands present, the proportion of each one occupied and their exact energy. Hence the model employed for calculations throughout this thesis solves for both the InAs and GaSb system exactly (at the Γ point) in a self-consistent way. The calculations are performed in the limit of no mixing and the effects of forward bias and pressure on the system are also included.

Figure 4.1 shows the band edge profile of a SHET whose shape is solely determined by the initial band overlap Δ, and the charge transfer process at the interface in which electrons from the GaSb valence band transfer to the InAs conduction band causing the bands to bend. The resulting InAs conduction (GaSb valence) band profile provides a confining potential for the electrons (holes) in the growth (z) direction allowing them to behave as free electrons (holes) in the plane. This leaves a 2DEG in InAs adjacent to a 2DHG in GaSb. It is the back-to-back confinement of these gases that causes this system to exhibit its unusual properties.

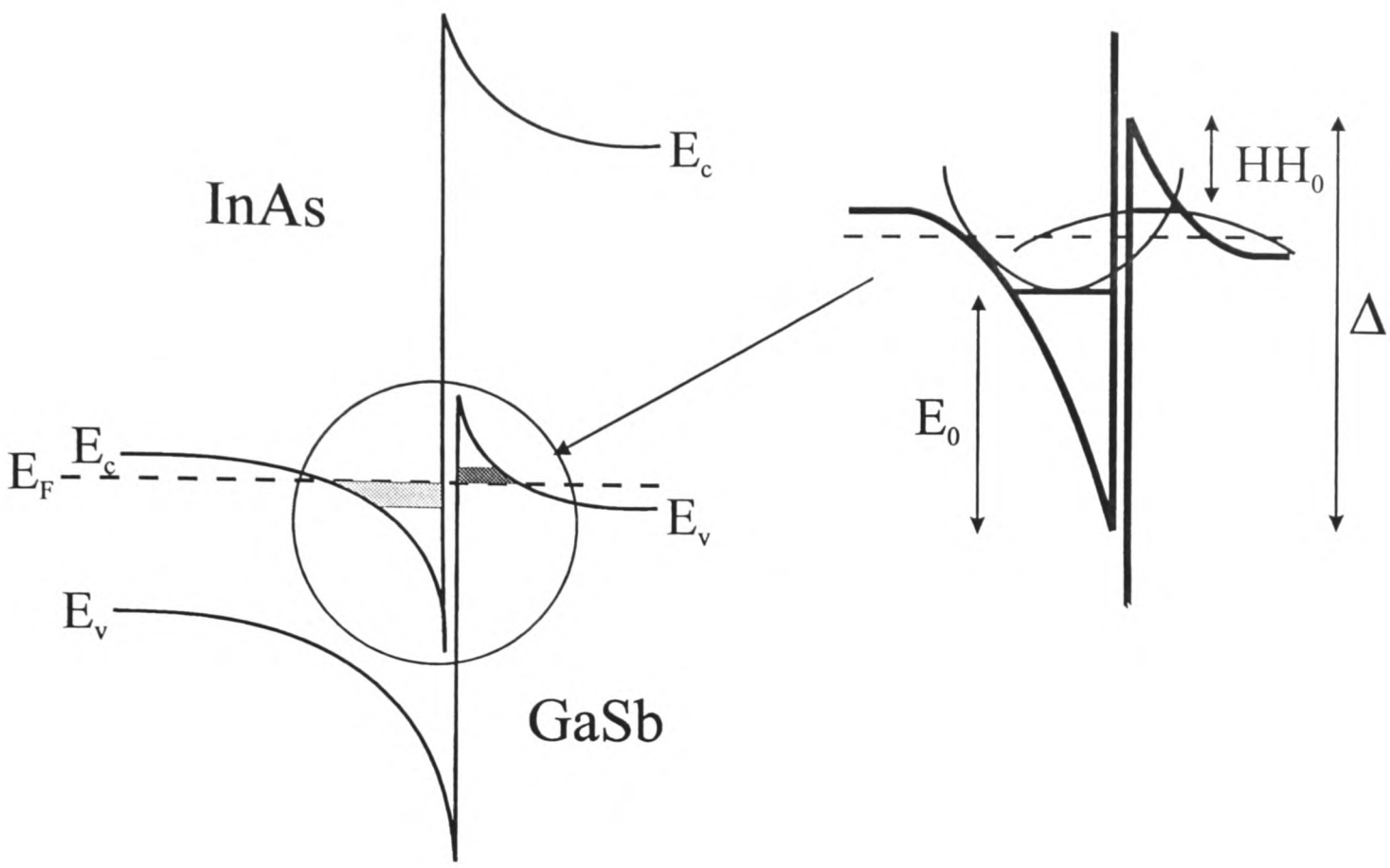


Figure 4.1. Band edge profile of an InAs/GaSb SHET near the interface showing E_c^{InAs} lying below E_v^{GaSb}. The 2DEG, with confinement energy E_0, the 2DHG with confinement energy HH_0, and the band overlap Δ are shown together with a schematic representation of the in-plane dispersions.

Providing the InAs conduction (GaSb valence) band profile is known, the confining potential in the z direction when inserted into the one dimensional Schrödinger equation (equation 4.6) yields certain eigenvalues with their associated eigenvectors for the electrons (holes). In order to calculate the potential energy in the z direction, however, it is necessary to solve the Poisson equation (section 4.4). This in turn requires knowledge of the charge distribution, which is in itself proportional to the square of the wavefunction. Hence the calculation needed is a self-consistent one and the remainder of this section presents each part of the procedure and any assumptions made. A detailed flow diagram illustrating the calculation's structure can be found at appendix A.

The basic procedure is to make an initial approximation for the confining potential energy V (section 4.1) using the Fang-Howard variational method [4], then work out confinement energies and wavefunctions using a transfer matrix formalism (section 4.3) and finally use these wavefunctions to find a new V (section 4.4) by the application of Poisson's equation. The process can then be repeated using this new, better, approximation for V and eventually the calculation converges providing a self-consistent solution. Modifications to this first approach are necessary to include the

effects of background doping and InAs band non-parabolicity. These are discussed in section 4.5.

All data collected in this thesis concerns current/voltage (I/V) measurements. Hence, it is necessary for the model to provide information regarding any change in the band profile and electron (hole) distributions that result from the application of a bias. This is included in section 4.8, using the assumption that all the applied voltage is dropped over the interface region. The application of hydrostatic pressure further alters the band profile at all biases and certain variables must be changed for the calculation to accommodate for this. This is described in section 4.9.

It is assumed throughout these calculations that electrons and heavy-holes are the dominant carriers in these vertical transport structures. Light holes have an effective mass in the direction of growth of $0.05m_0$, whereas the heavy holes have one of $0.3m_0$ [5] and it is therefore the latter that provide the band bending contribution. The light hole confinement energy is usually calculated to lie above the GaSb Fermi level, which means it is unpopulated and cannot contribute significantly to the vertical transport process.

Matlab by The Math Works Inc. was the computer package chosen for the development of a mathematical model because of its wide range of in-built routines, ease of use and portability between operating systems (PCs running Windows and Sun Sparc stations running UNIX). A single band profile calculation took an average of 8 hours using this method and it was therefore decided to transfer the Matlab code to C. Once completed, the C program running on a Pentium processor took between 10 and 20 minutes per calculation, yielding a 50 fold efficiency increase.

4.2 Initial Potential Approximation

In order to solve the Schrödinger equation (equation 4.6), it is necessary to know the potential energy V. At the beginning of the calculation, however, this is an unknown and any solution of the Poisson equation (equation 4.10) requires knowledge of the one-dimensional wavefunction $\chi(z)$ so an approximate value is needed for the first iteration. This is provided by the Fang-Howard variational method [4] which gives a

potential energy :

$$V(z)=\begin{cases} \dfrac{e^2 n}{\varepsilon_r^{InAs}\varepsilon_0}\left(\dfrac{3}{b}-\left\{-2z+\dfrac{3}{b}+\dfrac{bz^2}{2}\right\}e^{bz}\right) & z\le 0 \\ \Delta-\dfrac{e^2 p}{\varepsilon_r^{GaSb}\varepsilon_0}\left(\dfrac{3}{b}-\left\{2z+\dfrac{3}{b}+\dfrac{bz^2}{2}\right\}e^{-bz}\right) & z>0 \end{cases} \qquad \textbf{(4.1)}$$

Here n (p) is the two dimensional (2D) electron (hole) concentration, ε_r^x is the relative permittivity of substance x, Δ is the band overlap and z is the direction of growth with the interface situated at $z = 0$. b is the variational parameter in a trial wavefunction of the form :

$$\chi(z)=\begin{cases} -z\left(\dfrac{b^3}{2}\right)^{\frac{1}{2}}\exp\left(\dfrac{bz}{2}\right) & z\le 0 \\ -z\left(\dfrac{b^3}{2}\right)^{\frac{1}{2}}\exp\left(-\dfrac{bz}{2}\right) & z\ge 0 \end{cases}, \qquad \textbf{(4.2)}$$

which turns out to be :

$$b=\begin{cases} \left(\dfrac{33m_z^{e*}e^2 n}{8\varepsilon_r^{InAs}\varepsilon_0\hbar^2}\right)^{\frac{1}{3}} & z\le 0 \\ \left(\dfrac{33m_z^{h*}e^2 p}{8\varepsilon_r^{GaSb}\varepsilon_0\hbar^2}\right)^{\frac{1}{3}} & z>0 \end{cases} \qquad \textbf{(4.3)}$$

where m_z^{e*} (m_z^{h*}) is the effective mass of the electrons (heavy holes) for motion perpendicular to the plane of the interface.

Thus, the Fang Howard variational method uses a simple wavefunction with a variational parameter b which enables the problem to be solved analytically for one occupied sub-band on either side of the interface. The approach enables a fair initial approximation to be made but has a large error, so more detailed numerical methods are required for a precise answer.

4.3 The Schrödinger Equation

The familiar single particle time independent Schrödinger equation for three dimensions is :

$$\left[-\frac{\hbar^2}{2m^*}\nabla^2 + V(x,y,z)\right]\Psi = E\Psi \tag{4.4}$$

where m^* is the isotropic effective mass, E is the total energy and V is the potential energy. For the SHET, $V = V(z)$ as the confinement is in the z direction only. This allows a separation of variables, yielding eigenvalues and eigenvectors of the form :

$$\Psi(x,y,z) = \chi_i(z)\mathrm{e}^{i(k_x x + k_y y)}$$
$$E = E_{z,i} + \frac{\hbar^2}{2m^*}\left(k_x^2 + k_y^2\right) \tag{4.5}$$

where $E_{z,i}$ is the confinement energy of the i^{th} sub-band and $\chi_i(z)$ is its corresponding z dependent wavefunction which are solutions to the one dimensional Schrödinger equation :

$$\left[-\frac{\hbar^2}{2m_z^*}\frac{\mathrm{d}^2}{\mathrm{d}z^2} + V(z)\right]\chi_i(z) = E_{z,i}\chi_i(z)\,. \tag{4.6}$$

Here m_z^* is the particle's effective mass in the direction of growth. Inspection of equation 4.5 shows an effective 2D gas results with its zero of dispersion at $E_{z,i}$.

With knowledge of the potential energy, V, Schrödinger's equation (equation 4.6) can be solved numerically using the transfer matrix formalism. This technique splits z up into smaller parts and treats V as a constant in each part, an approach that works well providing the points are sufficiently closely spaced.

The basic formula is :

$$\begin{bmatrix} \chi_R \\ \frac{1}{m_z^*}\frac{\mathrm{d}\chi_R}{\mathrm{d}z} \end{bmatrix} = \tilde{\mathrm{T}}\begin{bmatrix} \chi_L \\ \frac{1}{m_z^*}\frac{\mathrm{d}\chi_L}{\mathrm{d}z} \end{bmatrix} \tag{4.7}$$

where the transfer matrix, $\tilde{T}$, is :

$$\tilde{T} = \begin{bmatrix} \cos k\delta z & \frac{m_z^*}{k}\sin k\delta z \\ -\frac{k}{m_z^*}\sin k\delta z & \cos k\delta z \end{bmatrix} \quad \text{where} \begin{cases} k = \sqrt{\frac{2m_z^*(E-V)}{\hbar^2}} \\ \delta z \text{ is spatial separation} \\ \text{between points on } V(z) \end{cases} \tag{4.8}$$

and χ_L and χ_R are the values of the wavefunction at the left and right hand sides of a slab with thickness δz. χ and $\frac{1}{m_z^*}\frac{d\chi}{dz}$ are continuous across the interface between adjacent slabs.

If the calculation is started at $V(0)$ with $\chi_L = \chi(0)$ and $d\chi_L/dz = d\chi(0)/dz$, these can be multiplied by the V dependent transfer matrix at the next point right to yield χ_R and $d\chi_R/dz$. Writing $\chi^1{}_L = \chi_R$ and $d\chi^1{}_L/dz = d\chi_R/dz$, the process can be repeated with the next transfer matrix, continuing until one of two criteria is reached :

- $\chi_R = 0$ and $d\chi_R/dz = 0$ or,
- $\chi_R = Ae^{-kz}$ and $d\chi_R/dz = -kAe^{-kz}$ where the wavefunction and its gradient both fulfil the necessary conditions for decay into a potential barrier.

The resulting $\chi_i(z)$ and confinement energy, $E_{z,i}$, can then be used to find a new $V(z)$ using equation 4.12. The spatial extension of V chosen was sufficient to let χ decay to zero (~ 3000 Å).

The initial conditions are chosen as :

$$\chi(0) = 0 \qquad \left.\frac{d\chi}{dz}\right|_{z=0} = -1. \tag{4.9}$$

The first condition of equation 4.9 corresponds to zero barrier penetration of χ. This is a fair assumption because of the barrier height between symmetry-matched band edges. The second condition is an arbitrary assignment as the real value of the initial gradient of the wavefunction is determined by normalisation.

4.4 The Poisson Equation

The charge distribution of the electron (hole) gas is proportional to the modulus of the wavefunction squared $|\chi_e|^2$ ($|\chi_h|^2$). Poisson's equation for this problem given by :

$$\frac{\mathrm{d}^2\phi(z)}{\mathrm{d}\,z^2} = \begin{cases} \dfrac{en}{\varepsilon_r\varepsilon_0}|\chi_e|^2 & z \le 0 \\ -\dfrac{ep}{\varepsilon_r\varepsilon_0}|\chi_h|^2 & z \ge 0 \end{cases}, \tag{4.10}$$

with :

$$V(z) = \begin{cases} -e\phi(z) & z \le 0 \\ \\ \Delta - e\phi(z) & z \ge 0 \end{cases} \tag{4.11}$$

can be used to find the potential profile generated by this normalized χ_e (χ_h).

Equation 4.10 can be integrated by parts to give [6] :

$$V(z) = \begin{cases} -\dfrac{e^2}{\varepsilon_r^{InAs}\varepsilon_0}\sum_i n_i\left[z + \int_0^z (z-z')\left|\chi_{e,i}(z')\right|^2 \mathrm{d}z'\right] & z \le 0 \\ \Delta - \dfrac{e^2}{\varepsilon_r^{GaSb}\varepsilon_0}\sum_i p_i\left[z - \int_0^z (z-z')\left|\chi_{h,i}(z')\right|^2 \mathrm{d}z'\right] & z \ge 0 \end{cases} \tag{4.12}$$

which is generalised to account for more than one occupied energy level, each with concentration n_i (p_i for holes) and wavefunction $\chi_{e,i}$ ($\chi_{h,i}$ for holes). The boundary conditions used are :

$$\left.\frac{\mathrm{d}\phi}{\mathrm{d}z}\right|_{z=0} = \begin{cases} \dfrac{en}{\varepsilon_r\varepsilon_0} \\ \\ \dfrac{ep}{\varepsilon_r\varepsilon_0} \end{cases} \quad \text{and} \quad \phi(0) = \begin{cases} 0 & z \le 0 \\ \\ \Delta & z \ge 0 \end{cases} \tag{4.13}$$

where $n = p$, ensuring the continuity of the electric field at the interface.

If the calculations mentioned so far are performed on their own, the Fermi energy is found to lie above the InAs conduction band and below the GaSb valence band

whereas it is known to be pinned to the acceptor level in bulk GaSb [7] (which corresponds to $V(\infty)$). In order to correct these discrepancies, therefore, the ionized background charge must be taken into account.

4.5 Background Doping

Nominally undoped GaSb and InAs grown in-house by MOVPE (section 2.2) have a background doping of magnitude ~ 10^{16} cm^{-3} which is capable of altering band profiles away from the interface. In bulk GaSb the Fermi level is known to be pinned to the acceptor level, the implications of which are discussed in section 4.5.1. For InAs, such studies have not been carried out, and section 4.5.2 details the assumptions made in the absence of such information.

4.5.1 GaSb

Nominally undoped GaSb grown in-house by MOVPE is p-type with p^{bulk} ~ 10^{16} cm^{-3}. Far enough away from the SHET interface, GaSb acts like the bulk material pinning the Fermi level 34 meV above the valence band edge [7] (figure 4.2).

Although residually p-type, the material is compensated by a smaller concentration of donors. It is the ionization of these donors that can contribute to the band bending. Consider figure 4.2 where, far away from the interface, the Fermi level is pinned to the acceptor level. The donors have ionized, losing their electrons to the acceptors leaving each positively charged donor balanced by a negatively charged acceptor. As the valence band edge (and therefore the acceptor level) bends upwards, the ionized acceptor, now above the Fermi level, is unable to retain its extra electron. The acceptors are neutral and the donors ionized - contributing a 2D charge density ${N_D}^{GaSb} z_A$ to the band bending where ${N_D}^{GaSb}$ is the compensated donor concentration and z_A is the (acceptor) depletion length.

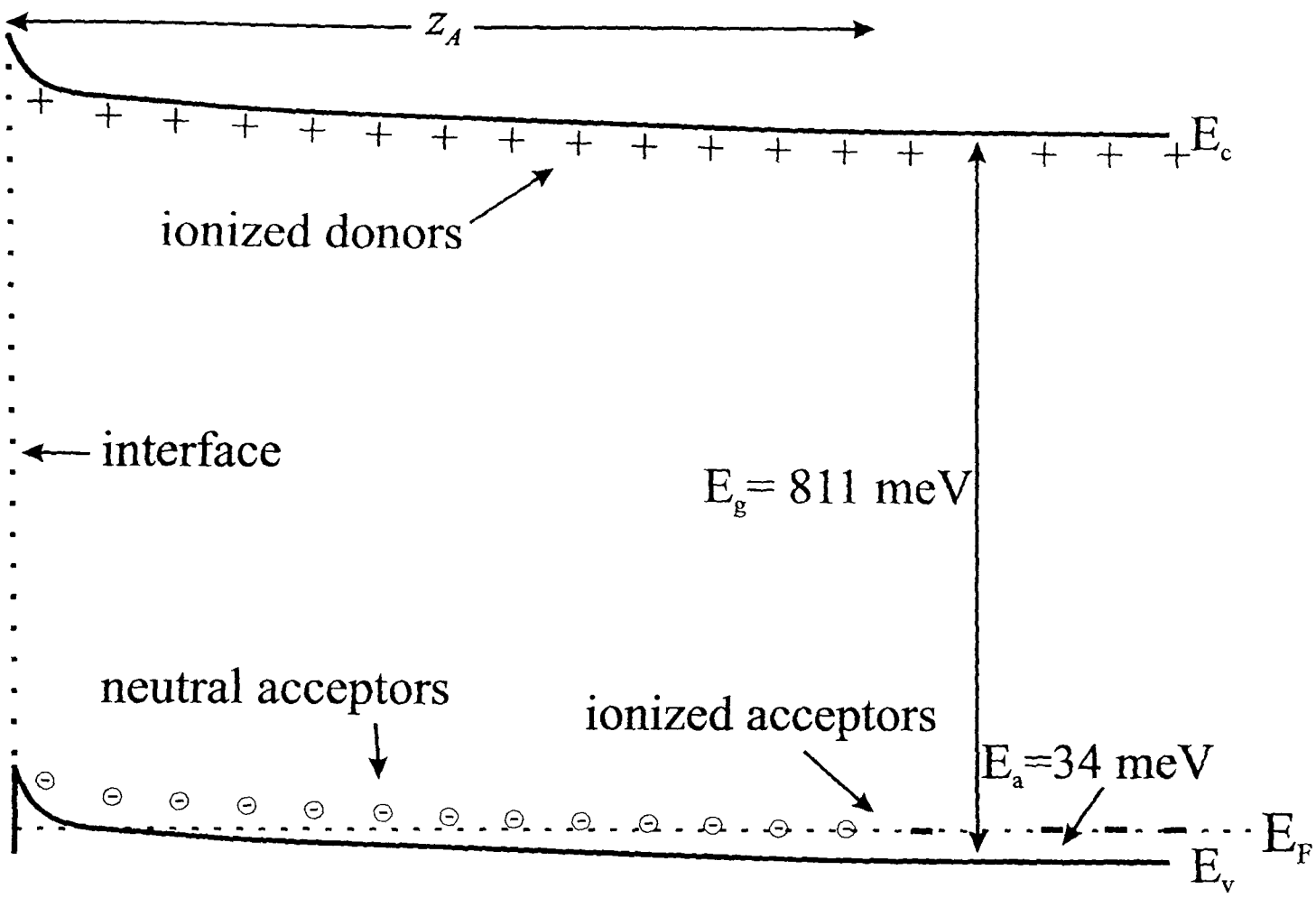


Figure 4.2. 1 bar, 0K band profile for GaSb side of SHET. The Fermi level away from the interface is pinned by the acceptor level. The concentration of donors, N_D^{GaSb}, multiplied by the distance of band-bending, z_A, yields a 2D charge density that contributes to the band bending. The sharp initial bending is due to the 2D mobile charge (heavy holes).

4.5.2 InAs

The hydrogenic ionization energy (IE) is 13.6 eV. For semiconductors, an electron in the presence of a donor impurity can be represented as a particle of charge e and mass m^* moving in free space in the presence of a positive charge e/ε_r. This is a modified hydrogen problem with the IE multiplied by m^*/ε_r^2 [8], yielding an IE for InAs donors of 2 meV.

Compensation is also a feature of this material which means acceptors are present. Following a similar argument to that used in section 4.5.1, all the acceptors and donors must be ionized far away from the interface if the Fermi level is assumed to be pinned to the donor level. In the depletion region, acceptors remain ionized but donors become neutral, contributing a net negative 2D charge density, $N_A^{InAs} z_D$, to the band bending where N_A^{InAs} is the compensated acceptor concentration and z_D is the (donor) depletion length.

The assumption that E_F^e is pinned to the hydrogenic donor level has been investigated for various pressures by varying this pinning. The 1 bar results for $N_A^{InAs} = N_D^{GaSb} = 10^{15}\text{cm}^{-3}$ displayed in table 4.1 exhibit the largest absolute confinement energy discrepancies and even this does not exceed 1.5 meV. Hence, the calculations are all performed assuming the electron Fermi Energy is pinned at the InAs hydrogenic donor level.

E_F^e pinning assumption :	Zero background. No pinning	Pinned to donor level	Pinned 20 meV below flat band.
E_0 (meV)	75.73	75.97	76.14
E_1 (meV)	102.22	103.3	103.85
Δ-HH_0 (meV)	123.33	123.35	123.19
n (cm^{-2})	4.7×10^{11}	4.56×10^{11}	4.47×10^{11}
p (cm^{-2})	4.43×10^{11}	4.47×10^{11}	4.46×10^{11}

Table 4.1. Table illustrating the effect on selected output parameters of changing the pinning criterion for E_F^e in InAs at 1 bar. The largest discrepancies appear between values of E_1 and are no greater than 1.5 meV for the two extreme cases.

4.5.3 Interface States

Impurities at a heterointerface can provide additional localised states in the interface region band gap which can behave as trapping and recombination states. In the case of InAs/GaSb grown by MOVPE these states are known to be donor-like as pre-optimisation SL samples had a significant *n/p* ratio approaching 1.5. The latest samples however have much improved ratios of 1.02 which is far closer to intrinsic values. In this case additional background charge provided by these interface donors is relatively small and therefore neglected in the calculation.

Note that samples grown by MBE typically have *n/p* ratios in the region of 4 for reasons that are not fully understood, and for these samples the charge contribution from interface states would have to be included in the calculation

4.5.4 Effect on the Band Profile

Background doping is incorporated into the calculation as an additional term in the Poisson equation :

$$\frac{d^2\phi}{dz^2} = \begin{cases} \dfrac{en}{\varepsilon_r\varepsilon_0}|\chi_e|^2 + \dfrac{eN_A^{InAS}}{\varepsilon_r\varepsilon_0} & z \le 0 \\ -\dfrac{ep}{\varepsilon_r\varepsilon_0}|\chi_h|^2 - \dfrac{eN_D^{GaSb}}{\varepsilon_r\varepsilon_0} & z \ge 0 \end{cases} . \qquad \textbf{(4.14)}$$

MOVPE-grown InAs is known to be n-type with $n^{bulk} \sim 4\times10^{16}$ cm^{-3}, and GaSb to be p-type with $p^{bulk} \sim 10^{16}$ cm^{-3}. Their compensated minority charge, however, is not known. For the purposes of the calculation, $N_A{}^{InAs}$ and $N_D{}^{GaSb}$ were chosen to be 10^{15} cm^{-3} which is roughly one tenth of the majority dopant concentration. A study was carried out to discover what effect a change in these values would have on the zero bias confinement energies and 2D concentrations by varying the input parameters $N_A{}^{InAs}$ and $N_D{}^{GaSb}$ between 10^{15} and 4×10^{15} cm^{-3} at various pressures (see section 4.9 for details of how pressure is included into the calculation). Selected results are shown in table 4.2 and table 4.3 for 1 bar and 10 kbar respectively.

N_A (cm^{-3}) N_D (cm^{-3})	10^{15} 10^{15}	4×10^{15} 10^{15}	10^{15} 4×10^{15}	4×10^{15} 4×10^{15}
E_0 (meV)	75.97	76.45	76.04	76.73
Δ-HH_0 (meV)	123.35	123.05	123.2	122.96
n (cm^{-2})	4.56×10^{11}	4.33×10^{11}	4.55×10^{11}	4.37×10^{11}
p (cm^{-2})	4.47×10^{11}	4.49×10^{11}	4.15×10^{11}	4.24×10^{11}

Table 4.2. Table illustrating the effect on selected output parameters of changing N_A and N_D at 1 bar.

The changes in confinement energy involved are small so, coupled with findings from section 4.5.2, the evidence suggests values can be quoted with a maximum error of ±2 meV.

N_A (cm^{-3})	10^{15}	4×10^{15}	10^{15}	4×10^{15}
N_D (cm^{-3})	10^{15}	10^{15}	4×10^{15}	4×10^{15}
E_0 (meV)	32.11	32.62	32.27	32.77
Δ-HH_0 (meV)	45.25	45.03	44.84	44.62
n (cm^{-2})	1.35×10^{11}	1.36×10^{11}	1.16×10^{11}	1.17×10^{11}
p (cm^{-2})	1.22×10^{11}	1.26×10^{11}	0.95×10^{11}	0.98×10^{11}

Table 4.3. Table illustrating the effect on selected output parameters of changing N_A and N_D at 10 kbar.

4.6 InAs Band Non-Parabolicity

Bulk InAs has a very small band gap of only 418 meV at 4K [9]. For these small band gap semiconductors the effect of the valence band states on the conduction band states (and vice-versa) cannot be ignored. This changes the approximately parabolic energy dispersion near the Γ point, introducing non-parabolicity where the effective mass alters significantly with energy. A conduction band dispersion results of the form [10] :

$$E_c(\boldsymbol{k}) = \frac{\hbar^2 \boldsymbol{k}^2}{2m^*} + \frac{K_2}{E_g}\left(\frac{\hbar^2 \boldsymbol{k}^2}{2m^*}\right)^2 = \frac{\hbar^2 \boldsymbol{k}^2}{2m^*(\boldsymbol{k})} \tag{4.15}$$

where E_g is the band gap energy, K_2 is a material dependent non-parabolicity constant (equal to -0.86 for InAs [1]), m^* is the parabolic mass and $m^*(\boldsymbol{k})$ is a $\boldsymbol{k}$ dependent effective mass which is a convenient way to describe the non-parabolicity. Clearly this approximation is only good for small corrections to the parabolic case and if we limit this correction to 5 %, rearranging equation 4.15 for any one direction yields the one dimensional dispersion relation :

$$E(k_x) = \frac{\hbar^2 k_x^{\,2}}{2m_x^*}\left[1 + \frac{K_2 \hbar^2 k_x^{\,2}}{2E_g m_x^*}\right] \tag{4.16}$$

where the subscript, x, indicates any one arbitrary direction. The 5% correction

imposes the limit $K_2\hbar^2 k_x^{\,2} / 2m_0^* E_g \leq 0.05$ thus limiting the range over which equation 4.15 is a good approximation to $k_x \leq 0.0014$ bohr^{-1}. In the plane of the interface, typical electron Fermi wavevectors are $k_x \sim 0.01$ bohr^{-1} over which range the non-parabolic approximation is not valid. Hence, non-parabolic effects are not included in the calculation of in-plane dispersion relations, introducing a slight error into these plots. For the same reason, the density of states in the parabolic case is used in the calculation of the Fermi energy (section 4.7).

By rearranging equation 4.15 and expanding terms in $\boldsymbol{k}^2$ binomially, a non-parabolic effective mass :

$$m_z^*(k_z) \approx m^*\left(1 - \frac{K_2}{E_g}\frac{\hbar^2}{2m^*}k_z^2\right) \qquad \textbf{(4.17)}$$

emerges which is used for calculations in the growth direction. The limit of equation 4.17's validity is again taken to be $(\Delta m^*/m^*) \leq 5$ % which is the case for all of the bias and pressure ranges under investigation. Indeed, the maximum mass deviation is found to be ~ 1.1 %.

In summary, the simple non-parabolic approximation to the energy dispersion is used in the calculation of a $\boldsymbol{k}$ dependent effective mass for use in the band edge profile calculation. However, it is found not to be a good approximation for the in-plane dispersion relations. Parabolic dispersions are therefore utilised for this purpose, introducing a small error into these plots.

4.7 The Fermi Level

The density of states for a 2D electron gas is constant, and without the inclusion of the effects of band non-parabolicity a Fermi energy of :

$$E_F = \frac{\pi\hbar^2 n}{m_{||}^*} \qquad \textbf{(4.18)}$$

results. Here $m_{||}^*$ is the effective mass for motion in the plane of the interface and n is

the 2D electron concentration which is replaced by p for the holes.

If more than one sub-band is present, the density of states in the ideal case is $Am_{\|}^{*}/\pi\hbar^{2}$ for energies between E_0 and E_1 (where A is the area). At E_1 it exhibits a step-like change and remains constant at $A/\pi\hbar^{2}\left[m_{E_0,\|}^{*}+m_{E_1,\|}^{*}\right]$ for energies up to E_2 and so on, altering the Fermi energy from equation 4.18 to :

$$E_F = \frac{\pi\hbar^{2}n + \sum_{i=0} m_{E_i,\|}^{*}\left(E_i - E_0\right)}{\sum_{i=0} m_{E_i,\|}^{*}}, \qquad \textbf{(4.19)}$$

where $m_{E_i,\|}^{*}$ is the effective in-plane mass of sub-band E_i and E_0 is taken as the zero of energy. Replacing E by HH and n by p yields the hole Fermi energy.

4.8 Applying a Bias

The predicted effect of forward bias (InAs negative with respect to GaSb) on the band profile of a SHET has been described in section 1.5.2, where increased charge at the interface causes the bands to bend more, thus raising the electron and hole confinement energies. This movement of sub-band energies can be simulated by increasing the InAs and GaSb 2DEG and 2DHG concentrations until the quasi Fermi energies are the required voltage apart, which is achieved in practice by altering the convergence criteria.

At zero bias the calculation is given a convergence criterion of $E_F^{e} + E_0 + HH_0 + E_F^{h} - \Delta = 0$ (see figure 4.3a) which yields a Fermi level that is continuous across the interface. To determine the band profile and associated confinement energies for any particular applied bias, V, the convergence criterion is changed to $E_F^{e} + E_0 + HH_0 + E_F^{h} - \Delta - V = 0$ which gives results when the quasi hole Fermi energy E_F^{h} lies V millivolts below the electron quasi Fermi energy E_F^{e} (figure 4.3b). A picture of sub-band alignments versus applied bias can be obtained using this method (e.g. figure 6.11 on page 117).

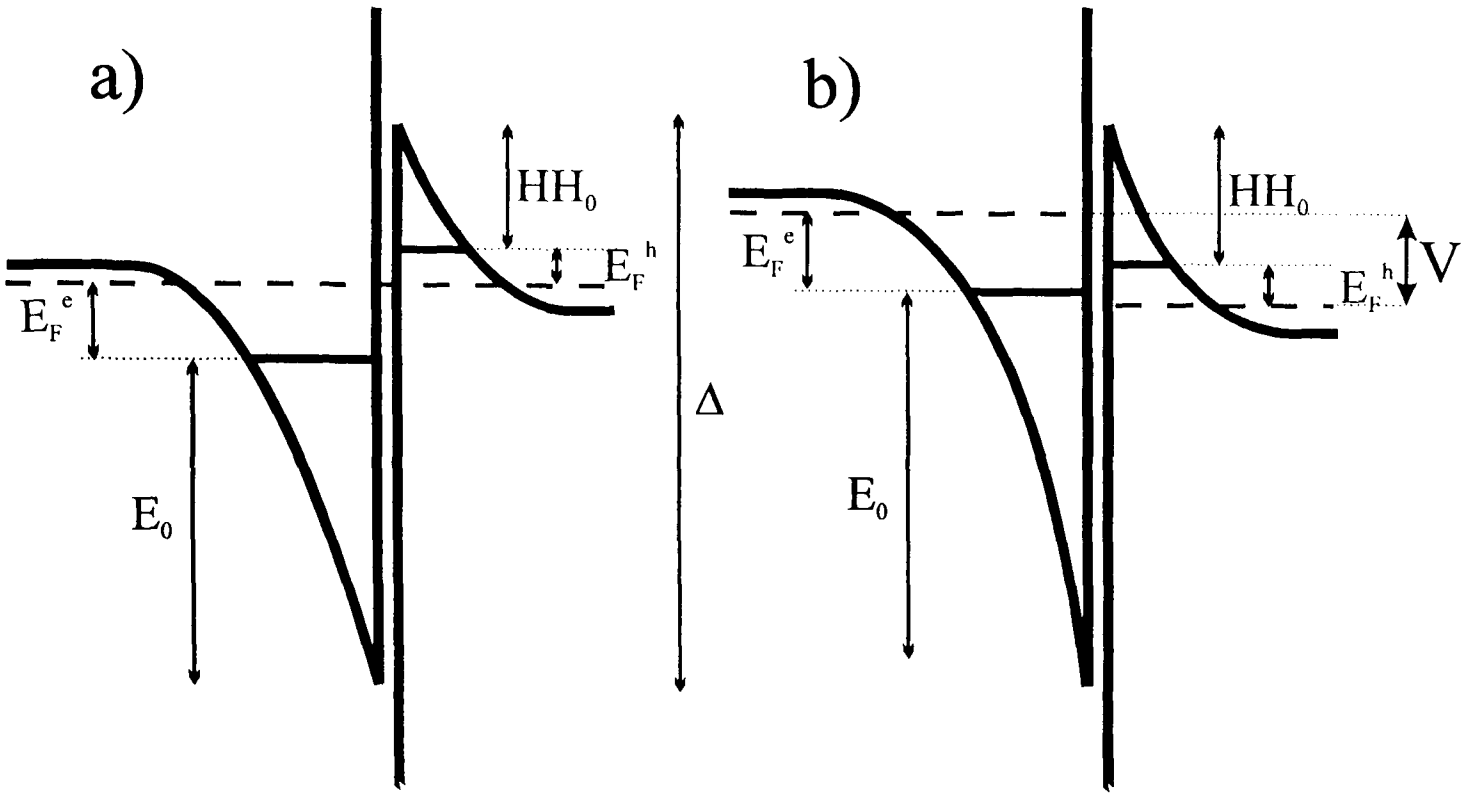


Figure 4.3. a) shows a simplified schematic band edge profile in the vicinity of the Fermi level for the zero bias situation with E_0 and HH_0 confinement energies indicated. The Fermi level is continuous across the interface if the convergence criterion $E_F^e + E_0 + HH_0 + E_F^h = \Delta$ is met. b) is the situation with an applied forward bias, V, assuming all of it is dropped across the interface. The calculation now converges when $E_F^e + E_0 + HH_0 + E_F^h = \Delta + V$ where E_F^e and E_F^h are now quasi Fermi energies.

The implicit assumption is that all of the applied bias is dropped across the interface. Any voltage dropped across a series resistance can be accounted for later on as an additional factor *IR* in the experimental trace where *I* is the current through the sample and *R* is the resistance.

A calculation of the current density needs a more sophisticated model, one which incorporates sub-band mixing effects as described in section 6.5.1. Useful information can, however, be obtained regarding the predicted behaviour of the sub-bands with bias and analysis of any change in this behaviour with the application of hydrostatic pressure.

4.9 Pressure Dependence

Bulk InAs and GaSb have Γ point band gaps that increase with pressure at the rate of 10 and 14 meV/kbar respectively, the implications of which for the SHET band profile are discussed in detail in chapter 6. It is sufficient to summarise here by stating that increasing hydrostatic pressure decreases the band overlap, Δ, at a rate of - 9.5 meV/kbar.

Other input parameters also have to be altered slightly. The InAs conduction band edge effective mass increases with pressure so that [11] :

$$m_P^* = \left(m_0^* + 6.67 \times 10^{-4} P\right) \tag{4.20}$$

where P is the pressure in kbar. The non-parabolic mass contains the term E_g (equation 4.17) which is also pressure dependent and must be replaced by the expression :

$$E_g = E_g^{1bar} + \frac{\delta E_g}{\delta P} P \tag{4.21}$$

where $\delta E_g/\delta P$ = -9.5 meV/kbar for InAs as stated earlier. Results from these calculations can be seen in chapter 6 and a flow diagram indicating its structure is displayed at appendix A.

4.10 References

[1] J Beerens, G Grégoris, J C Portal, E E Mendez, L L Chang & L Esaki. Physical Review B, p4742 (1987).

[2] G Bastard, E E Mendez, L L Chang & L Esaki. Journal of Vacuum Science and Technology 21, p531 (1982).

[3] D M Symons, M Lakrimi, R J Warburton, R J Nicholas, N J Mason, P J Walker, M I Eremets & G Hill. Physical Review B 49, p16614 (1994).

[4] T Ando, A B Fowler & F Stern. Review of Modern Physics 54, p437 (1982).

[5] Landölt & Bornstein. Semiconductors, Physics of Group IV Elements and III-V Compounds, Springer-Verlag, Berlin, p262 (1982).

[6] Y Takada & Y Uemura. Journal of the Physical Society of Japan 43, p139 (1977).

[7] E T R Chidley, S K Haywood, A B Henriques, N J Mason, R J Nicholas and P J Walker. Semiconductor Science and Technology 6, p95 (1991).

[8] N W Ashcroft & N D Mermin. Solid State Physics International Edition, Saunders College, p579 (1976).

Continued ...

References Continued ...

[9] Landölt & Bornstein. Semiconductors, Physics of Group IV Elements and III-V Compounds, Springer-Verlag, Berlin, p297 (1982).

[10] E D Palik, G S Picus, S Teitler & R F Wallis. Physical Review 122, p475 (1961).

[11] M L Shubnikov, D V Masovets & R V Parfenev. Soviet Physics Semiconductors 9, p989 (1976).

5 Sample Development and Temperature Dependence

5.1 Introduction 72
5.1.1 Naming Convention and Accuracy of Readings 73
5.2 Sample Development 74
5.2.1 The Early Samples 74
5.2.2 The Latest Samples 76
5.2.2.1 Switching Sequence C 77
5.2.2.2 Switching Sequence B 80
5.2.2.3 Switching Sequence A 81
5.2.3 Summary 83
5.3 Temperature Dependence 84
5.3.1 Effect of Temperature on the InAs/GaSb SHET 84
5.3.2 Experimental Results from 1.4 to 300K 87
5.3.2.1 The 'InSb-like' Interface 88
5.3.2.2 The 'GaAs-like' Interface 90
5.3.3 Discussion of Low Temperature Results 92
5.4 The Background Current 93
5.5 References 97

5.1 Introduction

Good quality samples are a prerequisite for any detailed study into the properties of a semiconductor. This chapter therefore begins by summarising the results that were obtained in an investigation which I carried out into the effect of different switching sequences on the SHET vertical transport I/V characteristic. Since the resonant conduction process is dependent upon the band profile at the interface, this I/V characteristic should be very sensitive to the interface quality and its environment. These are properties that have been shown to be dependent on switching sequence by the Raman measurements reported in section 2.3.1, enabling a comparison to be made between the quality of growth in multiple and single interface structures.

A problem with the earliest samples exhibiting negative differential resistance (NDR) was the difference in I/V curves between any two mesas from the same wafer. This indicated either uneven growth or bad contacts and made a reliable study of the resonant conduction mechanism difficult. The latest samples included in this thesis were grown with the three different switching sequences described in section 2.2, and for each sequence two samples were grown - one with an 'InSb-like' interface and one with a 'GaAs-like' interface. Improvements in the growth procedure aided by Raman and Transmission Electron Microscopy (TEM) measurements (section 2.3) are found to be reflected in the SHET vertical transport characteristics, resulting in samples with mesa-independent I/V behaviour.

Once suitable samples have been identified, an investigation into the I/V temperature dependence can begin. Knowledge of the temperature dependence of a solid state device is essential for both the semiconductor physicist and the electronic engineer. If for example the sample under investigation performs a task efficiently at 77K but becomes an expensive diode at room temperatures, then its applicability is limited. One of the main problem areas for artificially grown heterostructures so far has been exactly this temperature induced device degradation. An insight into the response of a heterostructure I/V to temperature can also help isolate the causes of performance-impeding non resonant current components. No detailed investigation into the temperature dependence of vertical transport in a SHET has yet been published, so

this chapter contains the first such study.

Section 5.2 charts the improvement in InAs/GaSb single heterojunction (SHET) vertical transport characteristics since the first samples exhibiting NDR were grown at the Clarendon. This provides a background to some of the initial difficulties and also includes a justification of the choice of samples for presentation in this thesis.

Studying the evolution of resonant conduction with temperature may provide a valuable aid in the optimisation of device properties so, as this has never been investigated, section 5.3 presents data from curves between 300 and 1K. It shows a valley current that is very insensitive to temperature and, for the first time, that samples with an 'InSb-like' interface have a stronger temperature dependence than those grown with 'GaAs-like' interfaces.

Section 5.4 discusses the origin of the background current in these samples and finds it not to be thermally activated. Various other possibilities are explored such as tunnelling and phonon scattering.

5.1.1 Naming Convention and Accuracy of Readings

The notation used to identify each device is [*wafer number*]#[*mesa number*], hence the seventh mesa tested from the 1500th wafer grown is named 1500#7.

For voltage readings the digital multimeter (DMM) read to an accuracy of ±0.05 mV but the repeatability of the sample characteristic was found to be ±0.5 mV, so voltages are quoted to the nearest mV. Similarly, for current readings the DMM used was capable of more decimal places than those quoted, but repeatability of the sample I/V trace occurred with an error of ±0.5 μA on an output setting of 1 mA/V (see section 3.2.1). The current is therefore quoted to the nearest μA on readings taken with this sensitivity and is scaled accordingly for other settings.

5.2 Sample Development

SHET resonant conduction structures exhibiting NDR have been grown by MOVPE at the Clarendon since March 1992. As has been shown in section 2.3, a significant improvement in interface control has been achieved since then. The vertical transport mechanism of SHET structures is predicted to be very dependent on the electronic band edge profile at the interface (section 1.5.2) and therefore very sensitive to small fluctuations in interface composition. SHET samples grown for vertical transport both before and after the program of MOVPE growth optimisation have been tested and this section will concentrate on differences in their 1 bar I/V behaviour at 300 and 77K together with the reproducibility of measurements taken from different areas of the same wafer.

5.2.1 The Early Samples

Samples numbered from 1189 through to 1192, the salient properties of which are shown in table 5.1, were grown pre-optimisation using switching sequence C (section 2.2) and were the first to be investigated. 1189 and 1192 had their interfaces biased towards 'InSb-like' and were nominally the same structures, but grown on different GaSb substrates. The primary reason for this was that GaSb substrate growth technology was in its infancy and epitaxial growth on undoped substrates yielded epilayers with shinier surfaces than those grown on doped ones, which may have been indicative of more even growth.

Sample number	GaSb Substrate batch and type	Interface type
1189	Batch 1180. Undoped	'InSb-like'
1190	Batch 1154. p^+ : Zn doped	'unbiased'
1191	Batch 1154. p^+ : Zn doped	'GaAs-like'
1192	Batch 1154. p^+ : Zn doped	'InSb-like'

Table 5.1. Table of properties for the earliest SHET samples. Substrates were grown by MCP Wafer Technology Ltd.

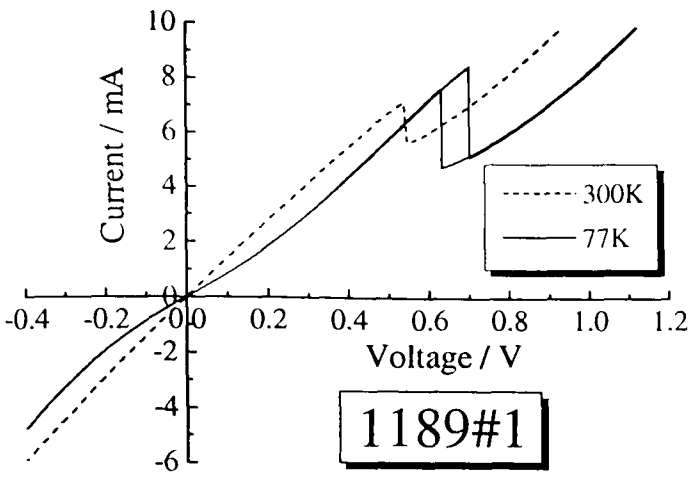


Figure 5.1. Representative I/V plot for sample 1189, grown on an undoped GaSb substrate, at 300 and 77K.

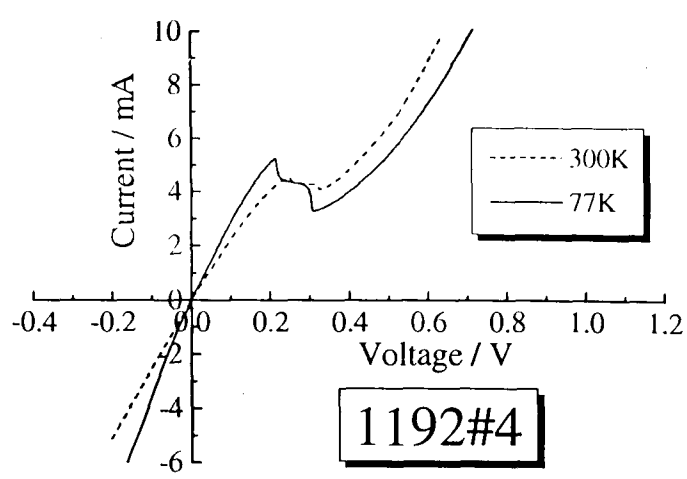


Figure 5.2. Representative I/V plot for sample 1192, grown on a p^+ GaSb substrate, at 300 and 77K

Typical I/V plots for 1189 and 1192 are shown in 5.1 and 5.2. A notable difference between these nominally identical samples is the voltage position of the start of the NDR region, known as the peak voltage, V_p. The higher value for V_p and the existence of I/V hysteresis in 1189 indicates a large parasitic resistance in series with the active region of the device (section 3.2.2). This can be explained by the properties of the undoped GaSb substrate - it is more resistive and harder to attach Ohmic contacts to than its doped counterpart. Additionally, the undoped substrate exhibits carrier freeze-out at low temperatures, behaving as an electrical insulator by 4K. The p^+ GaSb substrate shows no signs of this however, allowing a measurable NDR characteristic which survives below 77K. The unfavourable performance of the undoped substrate meant that the same batch of p^+ GaSb substrates used for 1192 was employed for all subsequent SHET growth runs.

A discussion about the effects of interface composition upon resonant conduction characteristics will be carried out throughout the remainder of this thesis and is not, therefore, elaborated upon here.

Figures 5.3 and 5.4 show I/V curves for two different mesas of 1191. These plots illustrate one of the main problems with the early samples, namely non uniformity in growth. As can be seen, the temperature behaviour of the two is rather different. At 300K 1191#3 shows a larger NDR than 1191#2. The difference in 77K voltage characteristic indicates a large parasitic resistance in series with 1191#3 which is due to either the contact or to the sample itself freezing out at low temperatures - even though the sample, substrate and contacting procedure are the same for both.

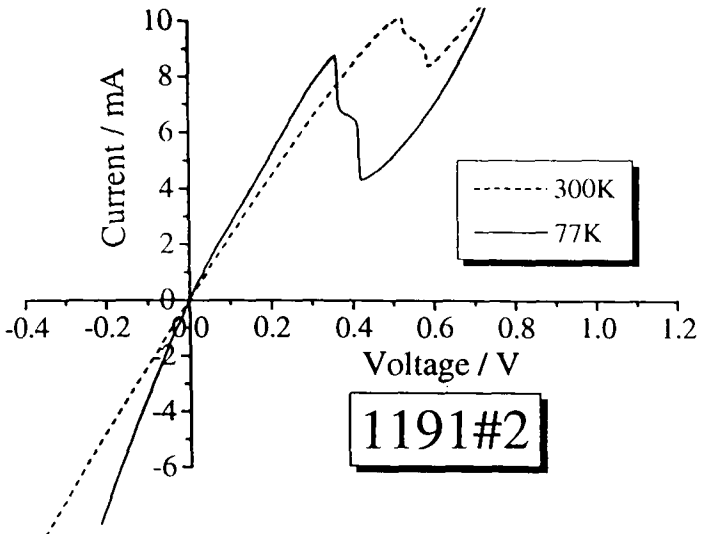


Figure 5.3. I/V plot for 1191#2 at 300 and 77K illustrating the non-uniformity of the grown wafer

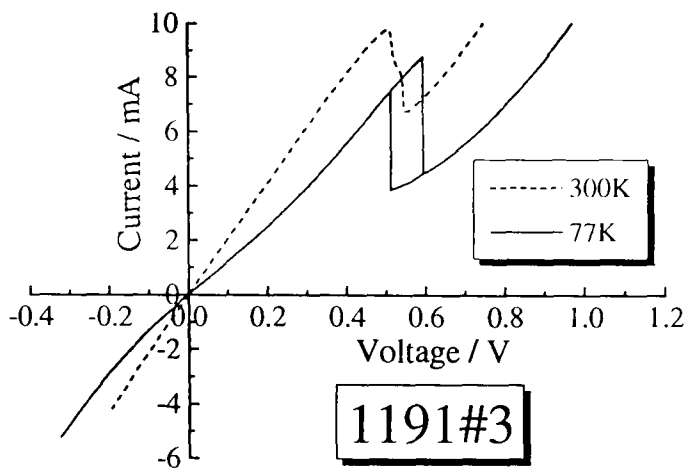


Figure 5.4. I/V plot for 1191#3 at 300 and 77K illustrating the non-uniformity of the grown wafer.

Sample 1190 was grown in the same way as 1191 and 1192 except for the interface precursor switching sequence. Here, both the Ga and Sb precursors were turned off at the same time, followed by a pause of 1 s, and then by the simultaneous switching on of the In and As precursors. This procedure was designed to create an 'unbiased' interface. An I/V trace for 1190#5 can be seen in figure 5.5. When compared with 1191 and 1192 the 77K current peak to valley ratio (PVR) appears very large - in fact the PVR of 2.6 that this sample exhibits is by far the highest published 77K value recorded for any InAs/GaSb SHET structure [1].

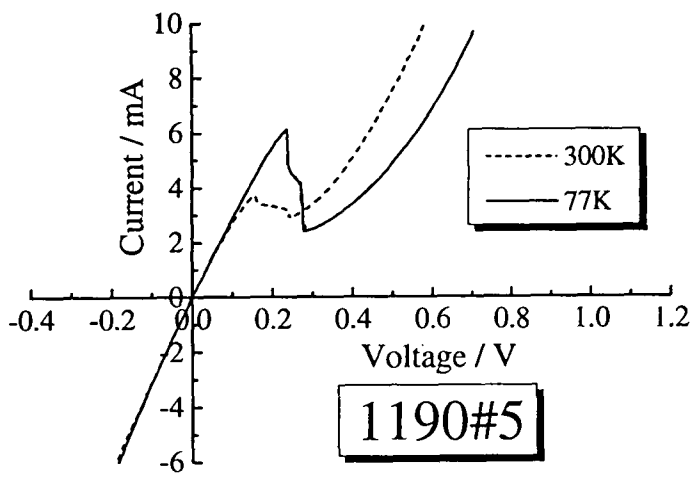


Figure 5.5. I/V plot of 1190#5 at 77 and 300K

5.2.2 The Latest Samples

The improvements in SL growth resulting from different MOVPE switching sequences have been documented in section 2.3. This sub-section highlights the changes in SHET vertical transport characteristics over the same period by examining the I/V traces of six samples whose salient properties are shown in table 5.2. These are

the most recent samples and form the basis for the majority of the analysis in this thesis.

Sample Number	Interface Type	Switching sequence
1765	'InSb-like'	C
1766	'GaAs-like'	C
1767	'GaAs-like'	B
1768	'InSb-like'	B
1771	'InSb-like'	A
1772	'GaAs-like'	A

Table 5.2. The six most recent SHET samples that were grown to study the effect of switching sequence on the vertical transport characteristics.

5.2.2.1 Switching Sequence C

The 'InSb-like' Interface.

Figures 5.6 and 5.7 show the I/V characteristics at 300 and 77K for two different mesas of sample 1765, grown with an 'InSb-like' interface using switching sequence C. Table 5.3 gives their peak voltages and currents. The similarity between the I/V behaviour of these two mesas at 300K indicates more uniform sample growth across the wafer than the earliest samples. The two traces at 77K exhibit similarities, but the hysteresis and differing peak voltages may still suggest a parasitic resistance in series

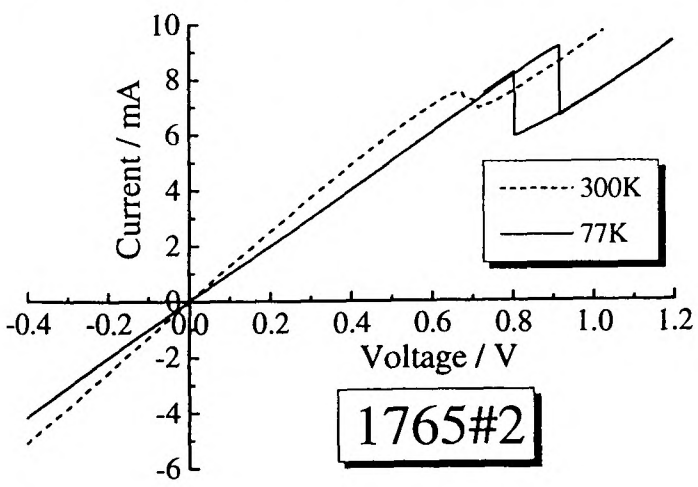


Figure 5.6. I/V plot for sample 1765#2 at 300 and 77K. Grown with an 'InSb-like' interface using switching sequence C.

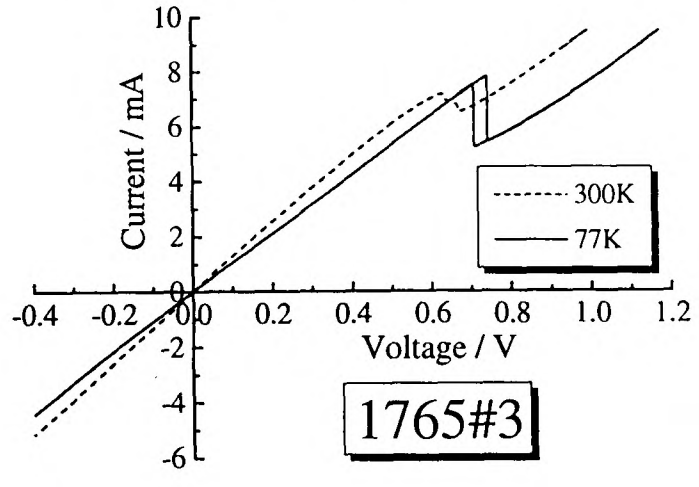


Figure 5.7. I/V plot for sample 1765#3 at 300 and 77K. Grown with an 'InSb-like' interface using switching sequence C.

	1765#2		1765#3	
	300K	77K	300K	77K
V_p	672 mV	916 mV	630 mV	744 mV
I_p	7.502 mA	9.165 mA	7.142 mA	7.790 mA
I at -0.2 V	-2.563 mA	-2.021 mA	-2.587 mA	-2.145 mA

Table 5.3. Peak voltage, peak current and current read at -0.2 V for mesas 2 and 3 of sample 1765 ('InSb-like' interface) at 300 and 77K.

with the interface (active region).

The substrate used for these runs was MCP growth run number 1154 which had previously been found to be of uniform quality and of sufficient p^+ nature to rule out its participation in any low temperature freeze-out. A reliable method to compare parasitic resistances and active device areas is to cross reference the peak current in the forward bias direction with the current at a fixed reverse bias since the two readings are dependent upon different transport mechanisms. A fuller explanation of the SHET band edge profile under reverse bias is given in section 6.3.

As explained in section 3.2.2, a large resistance in series with the active region (interface) of a mesa alters its observed I/V characteristic. Although the measured voltages change due to the load line, the actual and measured current peak values should remain the same since the current passes through all components in a series circuit.

The peak currents at 300K indicate that 1765#2 has a larger active interface region than 1765#3 which could be due to a slight difference in the area of the etched mesas or part of the interface of 1765#3 being damaged and unable to support a current.

From the position of the voltage peaks at 300K 1765#2 has a larger series parasitic resistance which is confirmed by the current readings at -0.2 V. When the mesas are cooled to 77K, the changes in V_p and I_p suggest the parasitic resistance in 1765#2 has a more pronounced temperature dependent behaviour than 1765#3. R_p (= V_p/I_p) values and those of R at -0.2 V at this temperature show 1765#2 to be more resistive by about 5.8 Ω and 4.5 Ω respectively than 1765#3. The difference in 77K peak currents could

not arise solely from differing etched mesa sizes since the I_p values at 300K do not show such large discrepancies. Rather, it is probably due to non-uniformity in the interface, where poorer quality regions no longer provide a current path at 77K. In summary, the growth quality is variable across this wafer.

The 'GaAs-like' Interface.

Figures 5.8 and 5.9 show the I/V traces of two mesas of sample 1766, grown with a 'GaAs-like' interface using switching sequence C, at 300 and 77K. Table 5.4 reveals the striking similarity in peak current values for both temperatures and a striking dissimilarity in the peak voltages and reverse bias currents.

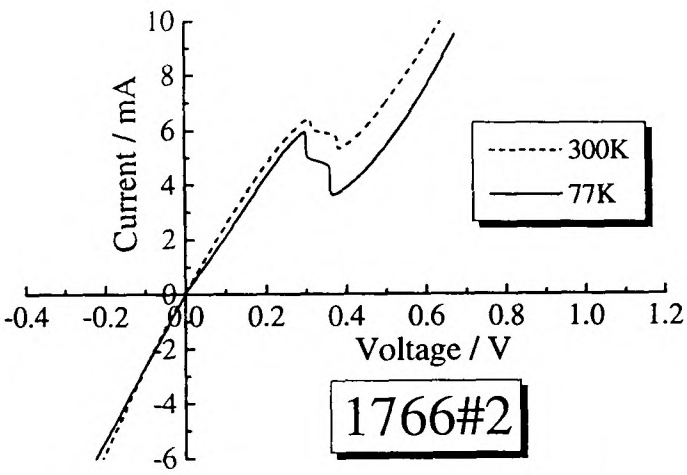


Figure 5.8. I/V plot for sample 1766#2 at 300 and 77K. Grown with an 'GaAs-like' interface using switching sequence C.

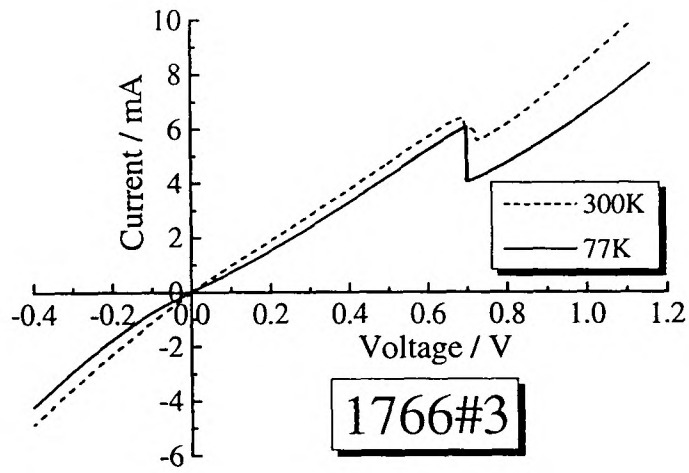


Figure 5.9. I/V plot for sample 1766#3 at 300 and 77K. Grown with an 'GaAs-like' interface using switching sequence C.

	1766#2		1766#3	
	300K	77K	300K	77K
V_p	310 mV	298 mV	691 mV	701 mV
I_p	6.405 mA	5.938 mA	6.400 mA	6.080 mA
I at -0.2 V	-5.781 mA	-5.345 mA	-2.287 mA	-1.735 mA

Table 5.4. Peak voltage, peak current and current read at -0.2 V for mesas 2 and 3 of sample 1766 ('GaAs-like' interface) at 300 and 77K

1766#2 has a resistance at -0.2 V that increases by 2.82 Ω when cooled from 300 to 77K. According to R_p values, however, the resistance increases by only 1.79 Ω which means the resistance due to the interface has decreased over the same temperature range.

1766#3 obviously has a large parasitic resistance in series with its active region. This increases by about 20% when the temperature is lowered to 77K according to the reverse bias currents. It only increases by approximately 10% in the forward bias direction, however, which is consistent with a decrease in the resistance due to the interface.

The peak currents are very similar, indicating homogenous interface growth and etched mesas of the same size. The large series resistance for 1766#3 is probably due to bad contacts.

5.2.2.2 Switching Sequence B

The 'InSb-like' Interface.

Figure 5.10 shows a typical I/V curve for a mesa grown with an 'InSb-like' interface using switching sequence B. The most striking difference between this plot and figure 5.6 is the lack of any region of NDR. There is a strong non-linear feature at 77K which indicates some sort of resonant conduction process, but this is engulfed by a parallel current path. This parallel current path is possibly due to a preponderance of interface states or interface dislocations. Further information regarding 1768 can be found in reference [2].

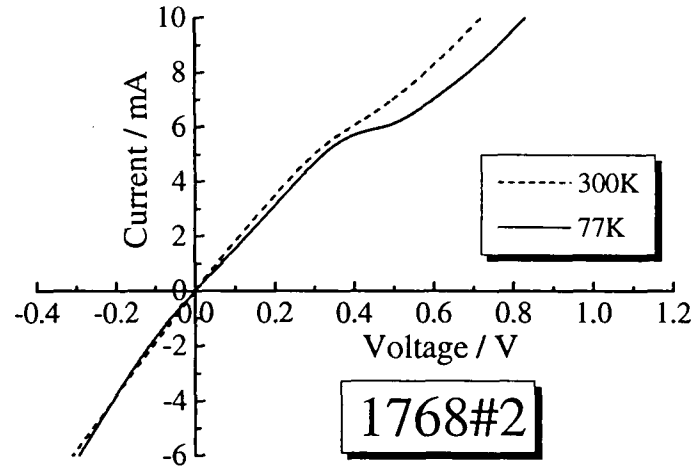


Figure 5.10. I/V plot for 1768#2 at 300 and 77K. Grown with an 'InSb-like' interface using switching sequence B, the NDR is absent even at 77K, although there is an obvious 'feature' at 350 mV.

The 'GaAs-like' Interface.

For the 'GaAs-like' interface, only one out of the three mesas available for testing yielded an I/V trace. Mesas 1 and 3 exhibited very noisy traces with resistances above

20 MΩ which was due to either extremely bad contacts or to a very disordered sample.

For mesa 2 the peak voltages and currents and the current at a fixed reverse bias at 300 and 77K are listed in table 5.5. The reverse bias currents seem to indicate a decrease in any resistance present at 77K, whereas R_p is larger for the 77K measurement. The behaviour of this mesa is very similar to that of 1766#2 which has a 'GaAs-like' interface and is grown with switching sequence C.

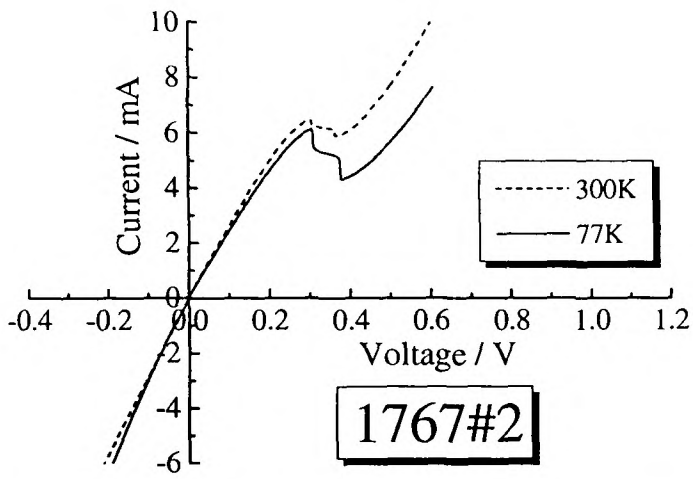


Figure 5.11. I/V plot for 1767#2 at 300 and 77K. Grown with an 'GaAs-like' interface using switching sequence B.

	1767#2	
	300K	77K
V_p	302 mV	306 mV
I_p	6.433 mA	6.122 mA
I at -0.2 V	-5.651 mA	-6.303 mA

Table 5.5. Peak voltage and current at 298 and 77K for 1767#2 grown with a 'GaAs-like' interface using switching sequence B.

5.2.2.3 Switching Sequence A

The 'InSb-like' Interface.

The I/V behaviour for all 10 tested mesas of 1771 were almost identical, as figures

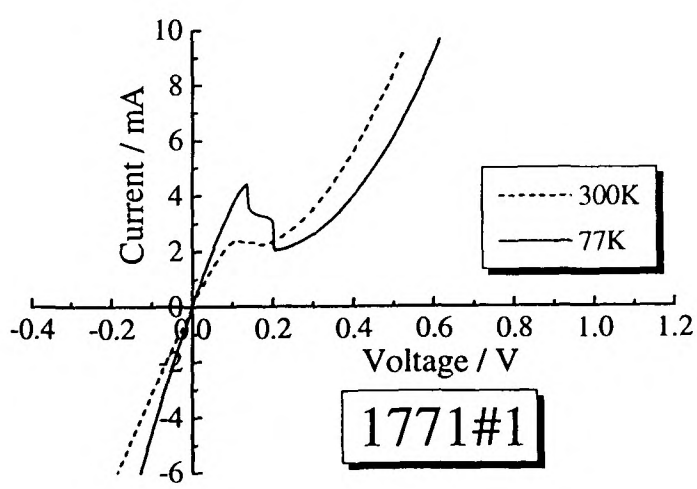


Figure 5.12. 'InSb-like' interface grown with switching sequence A at 77 and 300K.

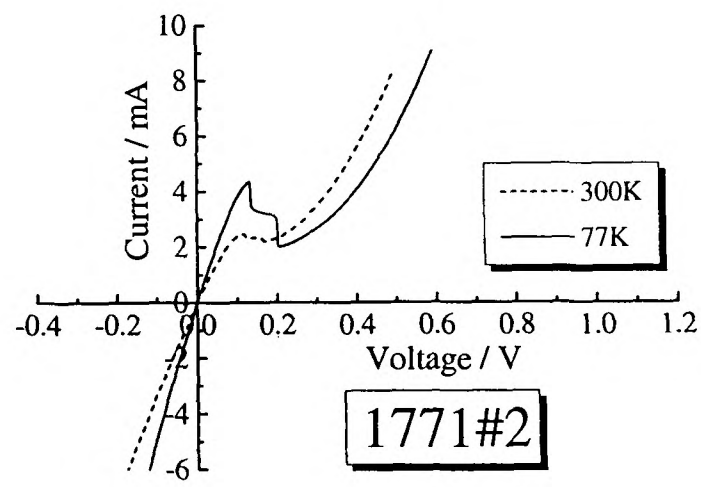


Figure 5.13. 'InSb-like' interface grown with switching sequence A at 77 and 300K.

	1771#1		1771#2	
	300K	77K	300K	77K
V_p	115 mV	136 mV	117 mV	131 mV
I_p	2.413 mA	4.409 mA	2.457 mA	4.334 mA
I at -0.2 V	-6.539 mA	-9.874 mA	-6.902 mA	-10.563 mA

Table 5.6. Peak voltage, peak current and current read at -0.2 V for mesas 1 and 2 of sample 1771 ('InSb-like' interface) at 300 and 77K.

5.12 and 5.13 and table 5.6 show.

R_p differs between mesas by only 0.1% at 300K, increasing to 2% at 77K. The peak voltages are not only very low which in itself indicates very little or no parasitic resistance, but also remarkably uniform across the whole wafer. Currents at -0.2 V actually show a decrease of roughly 10 Ω as the temperature is reduced from 300 to 77K and R_p reduces by approximately 17 Ω over the same temperature range, implying extremely low parasitic resistances.

These results are in excellent agreement with those presented in section 2.3, namely that switching sequence A produces the best quality interfaces which are the most uniform across the whole wafer.

The 'GaAs-like' Interface.

From values of I_p in table 5.7, a difference between the active device areas of 1772#1

	1772#1		1772#2	
	300K	77K	300K	77K
V_p	396 mV	357 mV	416 mV	363 mV
I_p	8.361 mA	8.206 mA	9.024 mA	8.770 mA
I at -0.2 V	-5.184 mA	-5.681 mA	-5.294 mA	-6.079 mA

Table 5.7. Peak voltage, peak current and current read at -0.2 V for mesas 1 and 2 of sample 1772 ('GaAs-like' interface) at 300 and 77K.

and 1772#2 is discernible. 1772#1 has a smaller etched diameter or a damaged interface region that does not support resonant conduction. The spread in V_p values is small and 1772#1 has a larger R_p by 2.5% at 300K, rising to 5% at 77K. Reverse bias current measurements support the argument that 1772#1 has a smaller etched mesa size because the ratio of resistances for each mesa at either temperature is almost identical to the ratios for R_p.

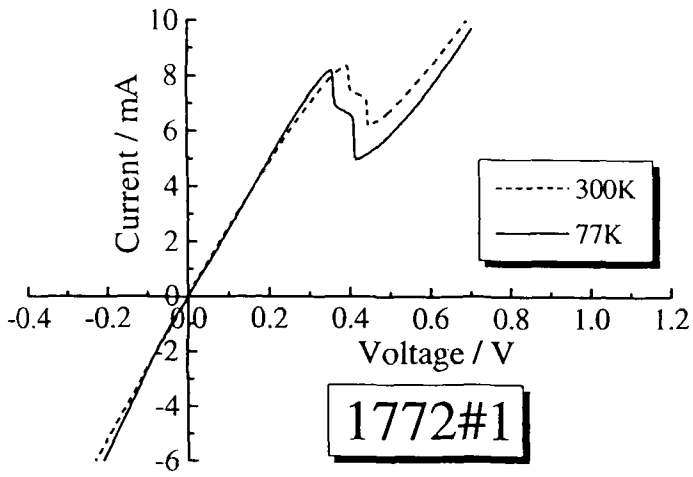


Figure 5.14. 'GaAs-like' interface grown with switching sequence A at 77 and 300K.

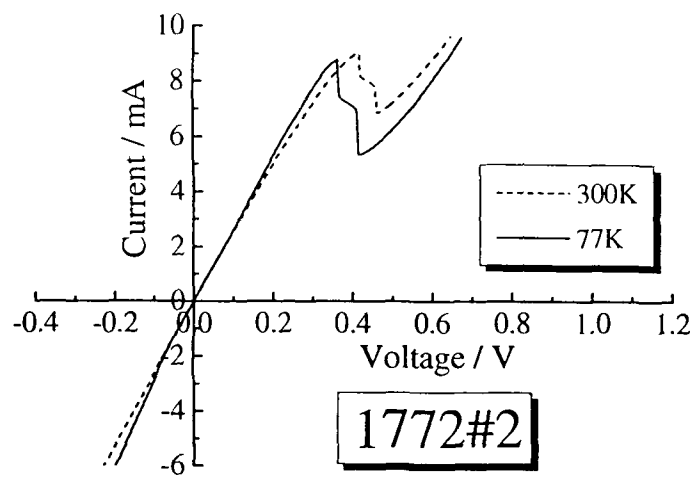


Figure 5.15. 'GaAs-like' interface grown with switching sequence A at 77 and 300K.

Thus, the 'GaAs-like' interface grown using switching sequence A provides samples with reproducible characteristics. Although the wafer uniformity does not seem to be as precise as for structures with an 'InSb-like' interface, these mesas can be used to characterise vertical transport properties of SHETs grown with this switching sequence.

5.2.3 Summary

Section 5.2 has demonstrated an agreement in interface quality characterisation between vertical transport in SHET structures and Raman and TEM performed on SLs. Switching sequence A is found to provide samples with either interface that have a nearly uniform I/V characteristic across the whole wafer, implying even interface growth.

The temperature dependence of NDR from both interfaces as illustrated by figures 5.12 and 5.14 reveal an unexpected interface dependent difference, with the 'GaAs-like' interface exhibiting a significant current peak to valley ratio (PVR) even at room temperature. 'GaAs-like' interfaces grown using switching sequences B and C have a

temperature dependence somewhere between that of both interface types grown using sequence A. This is consistent with the Raman evidence, where samples grown biased towards a 'GaAs-like' interface using growth sequence B or C produce interfaces with both 'InSb-like' and 'GaAs-like' characteristics.

The samples grown with switching sequence A, 1771 and 1772, will be used throughout the remainder of this thesis to demonstrate the interface dependent properties of vertical transport in SHETs.

5.3 Temperature Dependence

Figures 5.12 and 5.14 show the I/V characteristic for both interface types to be temperature dependent. Practical devices require a large current peak to valley ratio (PVR) so for room temperature operation, a SHET with a 'GaAs-like' interface would be chosen over one with an 'InSb-like' interface. At 77K, however, an 'InSb-like' SHET has a greater PVR and would therefore be preferable over one with a 'GaAs-like' interface. Hence, a study towards the understanding of this differing temperature dependence may provide additional information for future 'band gap engineering'.

It is very difficult to anticipate any changes the I/V characteristic may exhibit with temperature, as there are a number of competing processes that influence the band edge profile and/or the electron/hole distributions. Section 5.3.1 introduces these processes, and the experimental results presented in section 5.3.2 are used to clarify which temperature effect, if any, influences the forward bias I/V characteristic between 300 and 1.4K. Any dependence upon interface type is also investigated.

5.3.1 Effect of Temperature on the InAs/GaSb SHET

Electrons (and holes) obey Fermi-Dirac statistics where the probability of occupation of an allowed state with energy E at a temperature T is :

$$f(E) = \frac{1}{\exp\left((E - E_F)/k_B T\right) + 1}, \qquad \textbf{(5.1)}$$

where k_B is the Boltzmann constant and E_F the Fermi energy.

The calculated SHET band edge profile in the vicinity of the Fermi energy at 1 bar and 0K is shown in figure 5.16, a detailed explanation of which is reserved for section 6.4.

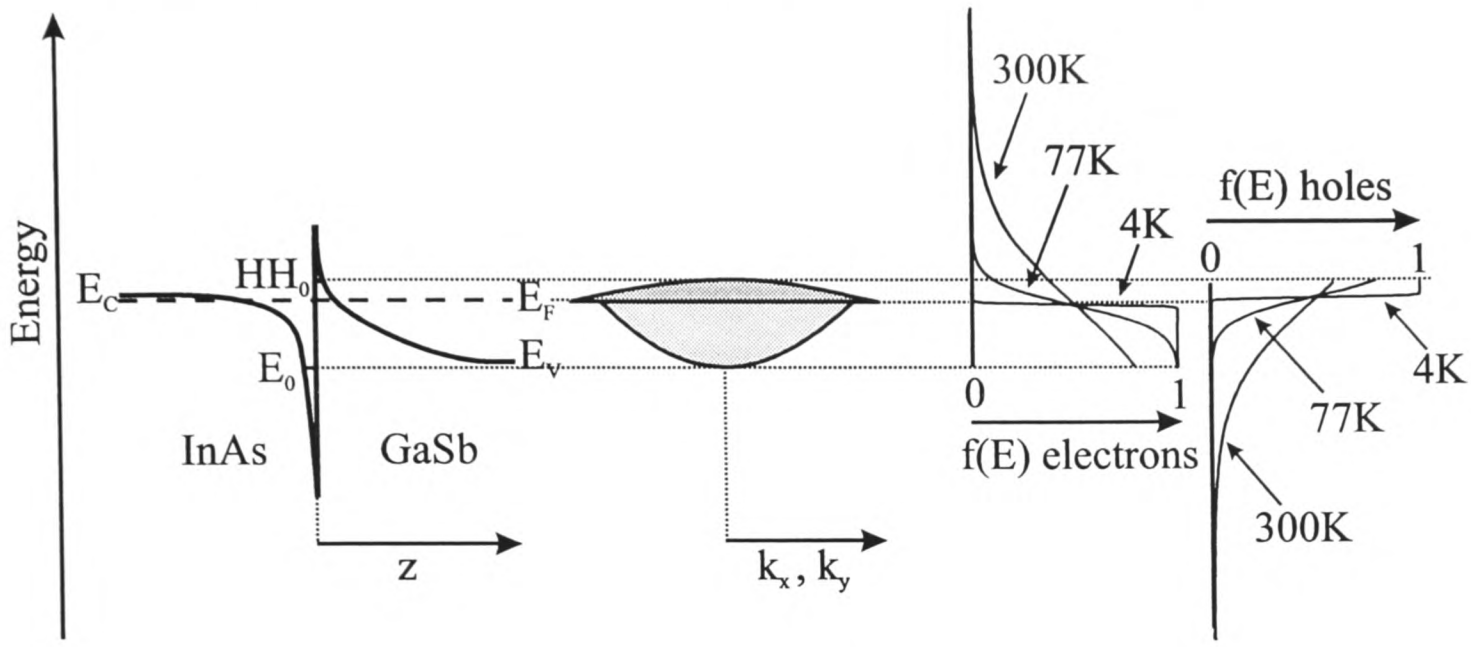


Figure 5.16. 1 bar SHET band edge profile and corresponding electron and hole dispersion relations and Fermi functions for E_0 and HH_0 only. Results are from self-consistent calculations for a SHET with an 'InSb-like' interface and are to scale. At 300K, the electron and hole distributions are noticeably smeared out. Light hole and split-off states are unoccupied and are not shown for clarity. Typical values for E_F^e of 35 meV and E_F^h of 9 meV have been used.

InAs and GaSb bulk band gaps increase as the temperature is lowered which can have two possible effects on the 0K band profile. The first involves the band overlap Δ directly. Symons [3] found it increased by roughly 30 meV as the temperature was raised from 4.2 to 300K for SL samples grown in the same reactor as the SHETs studied here by fitting magnetotransport data to a 2 band model (electrons and heavy holes only with no mixing). The second possible effect involves an increasing thermal population of electrons (holes) in the InAs conduction (GaSb valence) band through the ionisation of impurities. Both of these effects tend to raise the zero bias 2DEG and 2DHG concentration with increasing temperature, thus contributing to the band bending.

Increasing the temperature from 0 to 300K will also increase the population of higher electron and hole sub-bands with respect to E_0 and HH_0 respectively, altering the zero bias band edge profile with temperature.

The isotropic in-plane dispersions of E_0 and HH_0 are shown in figure 5.16, illustrating a mismatch in the zero bias, zero temperature Fermi electron and hole wavevectors. The effect of this mismatch on I/V properties at low temperatures is potentially

dramatic. It is due, in part, to the difference in occupation of the two electron and heavy hole sub-bands. To ensure the electric field at the interface is continuous, the total 2D charge on both sides of the interface must be equal. The 2DEG concentration is now split between E_0 and E_1, lowering the Fermi energy because of the increased density of states above E_1. The 2DHG concentration is similarly split, but to a lesser extent as HH_1 is only just occupied. Another factor affecting the mismatch is the differing contribution to the electric field given by the ionised background charge on either side of the interface, the result of which is a SHET where $n \neq p$, although this effect is quite small.

Using a simple transport picture we find that, for parallel momentum $\boldsymbol{k}_{\|}$ to be conserved in the resonant conduction process, occupied electron and hole states with the same energy and $\boldsymbol{k}_{\|}$ must exist. This is clearly not the case at zero bias if the electron and hole Fermi wavevectors are unequal. Applying a bias moves the zero of the electron dispersion up in energy with respect to that of the hole dispersion. In this simple model, no current should be able to flow until the bias is increased to the point where occupied electron and hole states overlap. The consequence of this should be a low temperature I/V which has an initial region of high resistance followed by the usual trace as soon as eV (where V is the bias) is large enough to compensate for the mismatch in $\boldsymbol{k}_{\|}$. In practice the in-plane dispersion relations are very different to this simple picture due to sub-band mixing effects (section 6.5) so the accuracy of the calculations in this respect is limited.

At 77K, k_BT is 6.6 meV, which reduces to 0.36 meV by 4K. A typical Fermi energy for the electrons is 35 meV and for the holes is 9 meV, for which calculated Fermi distributions are illustrated in figure 5.16. At 300K the 2DEG and 2DHG are extremely 'smeared out', which may be consistent with a significant device temperature dependence.

At 77K, the 2DEG and 2DHG distributions have much shorter Fermi tails. One might expect, therefore, the peak current to be higher than at 300K since more charge is present in the states that are close to overlapping and so are expected to contribute to the current. At a temperature between 77 and 4K, processes conserving parallel momentum become blocked for small biases because the thermal energy of the 2DEG

and 2DHG is limited. Hence, a smaller initial current is expected.

Mendez et al. [4] have used a GaSb/AlSb/InAs/AlSb/GaSb double barrier resonant tunnelling structure to demonstrate momentum conservation in that system. They provided an additional $\boldsymbol{k}_{\parallel}$ using a magnetic field parallel to the interface, effectively moving the electron and hole dispersions with respect to one another, and observed the change in the zero bias conductance.

There is an additional possible effect on the SHET I/V characteristic of lowering the temperature that is independent of interface properties. As undoped GaSb is by definition an insulator at 0K, the buffer layer could freeze-out, displaying a very high resistance at low temperature, as observed by Austing [5]. The test for freeze-out is if the peak voltage starts moving up faster than the valley voltage as the temperature is lowered (i.e. V_p - V_v is smaller) , as this is indicative of an increasing resistance in series with the active region.

The next section investigates the experimentally observed temperature response of I/V traces from 1771 and 1772.

5.3.2 Experimental Results from 1.4 to 300K

For the solid-state physicist, the variation of temperature provides a valuable tool with which to investigate the behaviour of a semiconductor. This helps in gaining a better understanding of the underlying physics, and provides information that is useful in the optimisation of practical room temperature devices. Additionally, in the case of the SHET it provides a probe into the thermally activated component of the unusually high background current. Experiments were carried out to determine the temperature dependence of the vertical transport I/V characteristics of SHETs at 1 bar and without a magnetic field. This section presents results for samples with both interface types and briefly discusses the findings. Certain aspects of the I/V data obtained at the lowest temperatures appear not to be consistent with results solely from the calculations described in chapter 4. However, if band mixing effects are included agreement is much closer. Any in-depth analysis is therefore reserved until after a detailed introduction of the conduction mechanism in section 6.5.

5.3.2.1 The 'InSb-like' Interface

The temperature dependence of the I/V characteristic of 1771 at 1 bar is shown in figure 5.17. By 50K a slight 's-shape' has developed in the vicinity of the origin which indicates the onset of behaviour induced by the charge carriers not having enough thermal energy to overcome the Fermi wavevector mismatch. By 1.4K this behaviour is very obvious. At 1.4K both forward and reverse bias directions exhibit the same I/V trace up to 10 mV where the currents are 27.5 μA and -27.4 μA respectively. However, with any further increase the forward bias direction is more resistive than its reverse bias counterpart, and by 30 mV the current readings are 240.0 μA and -386.9 μA respectively. A full discussion regarding the reverse bias conduction mechanism is reserved for section 6.3, but the significance of the above findings are that they are consistent with a gradual change from 2D to bulk-like transport in the reverse bias regime.

Note that the parameters used to calculate the band edge profile for an 'InSb-like' interface are different to those used for the 'GaAs-like' interface. A full explanation of

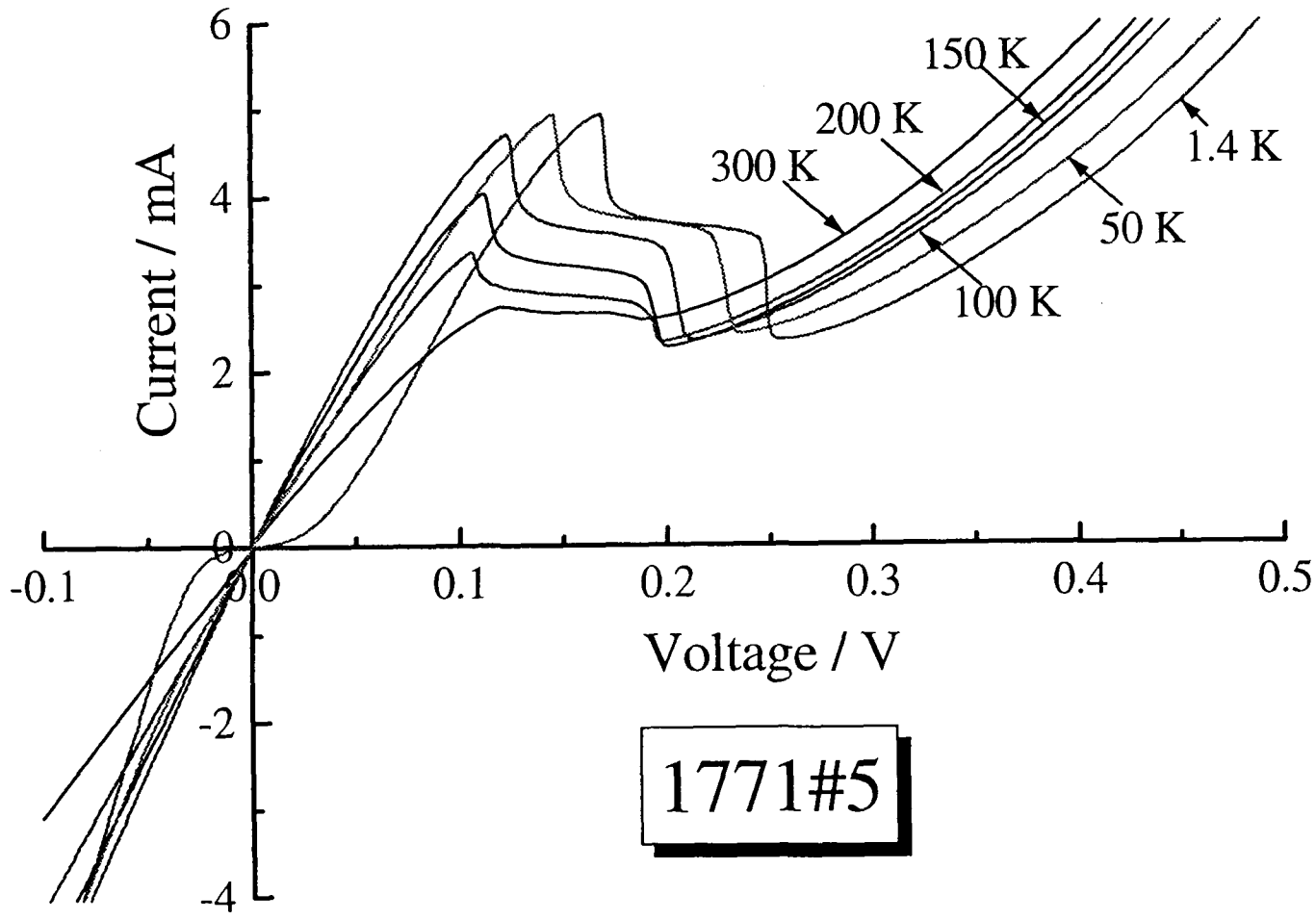


Figure 5.17. Temperature dependence of a SHET with an 'InSb-like' interface. Results were taken every 25K, but for clarity they are only shown for every 50K. Results displayed are for sample 1771#5.

why they are different and from where these differences arise is given in section 6.3.1.

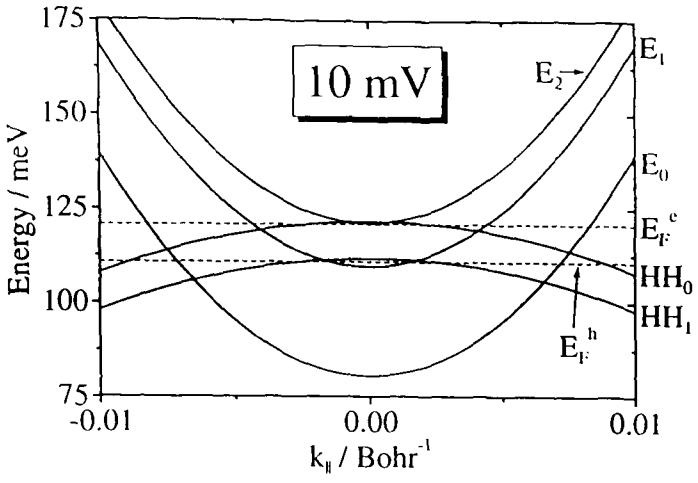


Figure 5.18. Calculated in-plane dispersion curves for 1771 at 10 mV. Light hole states are not shown as they are unoccupied

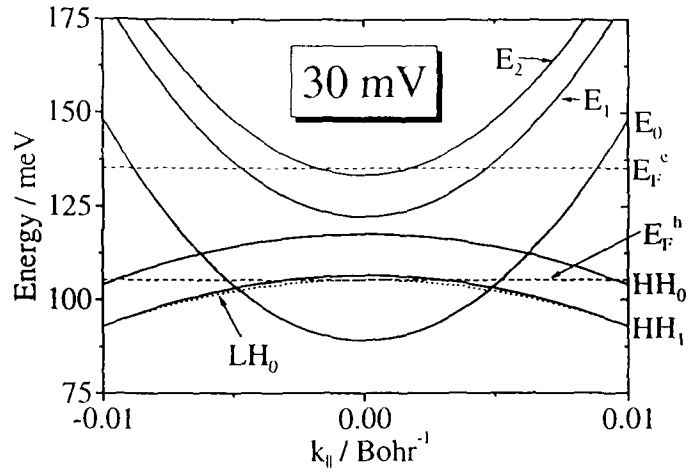


Figure 5.19. Calculated in-plane dispersion curves for 1771 at 30 mV.

Calculated forward bias in-plane dispersion relations for the 2DEG and 2DHG in an 'InSb-like' sample in the limit of no mixing (and without the inclusion of in-plane band non-parabolicity for InAs as discussed in section 4.6) are shown in figures 5.18 and 5.19 at 10 mV and 30 mV respectively. According to these plots, there is already a resonant conduction path at 10 mV as electron and hole states exist which have the same energy and $k_{||}$ (given by the intersection of two parabola between the quasi Fermi levels). By 30 mV, only E_0 appears to be able to couple to heavy hole states. Thus, the calculation appears to have underestimated the bias needed to overcome $k_{||}$ which from figure 5.17 is approximately 20 mV. The inclusion of in-plane non-parabolic effects for InAs would effectively flatten the electron dispersions somewhat and actually reduce the predicted bias needed to overcome $k_{||}$. Thus, in order for momentum conservation to be responsible for the 's-shape' at the origin, band mixing effects must change the in-plane dispersions noticeably as discussed further in section 6.5. The calculated in-plane dispersions can therefore only be used to provide an idea of the actual picture and are considered here solely because of the absence of more detailed calculations.

Figure 5.20 is a plot of the movement of peak and valley currents with temperature. Below 200K I_v does not change significantly which suggests the background current is not a thermal one (discussed in more detail in section 5.4), and above 200K it only increases slightly. I_p, however, has a large initial temperature dependence, increasing from 2.741 mA at 300K to 4.923 mA by 75K, after which it remains fairly steady with

a current PVR of 2.1.

Figure 5.21 is a plot of the movement of peak and valley voltages with temperature. It shows that V_p - V_v is roughly constant at 96 mV between 200 and 4K, decreasing to 68 mV at 300K.

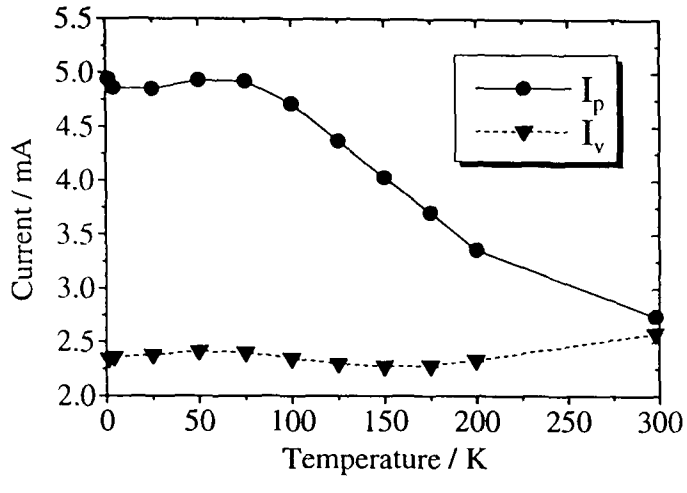


Figure 5.20. Peak and valley currents plotted against temperature for 1771#5.

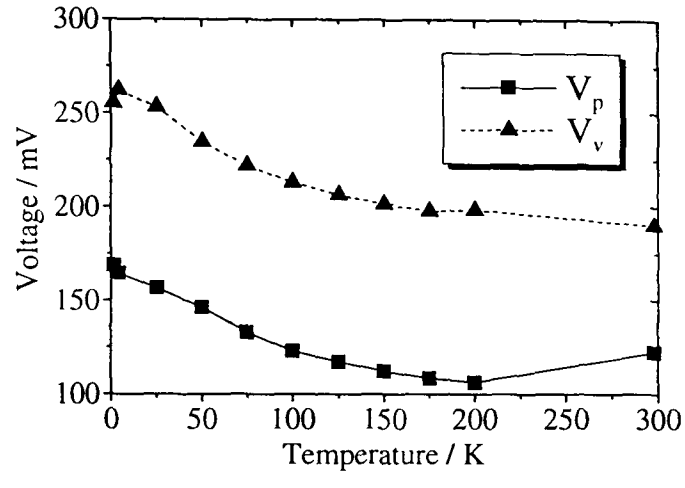


Figure 5.21. Peak and valley voltages plotted against temperature for 1771#5.

5.3.2.2 The 'GaAs-like' Interface

Figure 5.22 shows the variation in the I/V plot with temperature for 1772#6. This

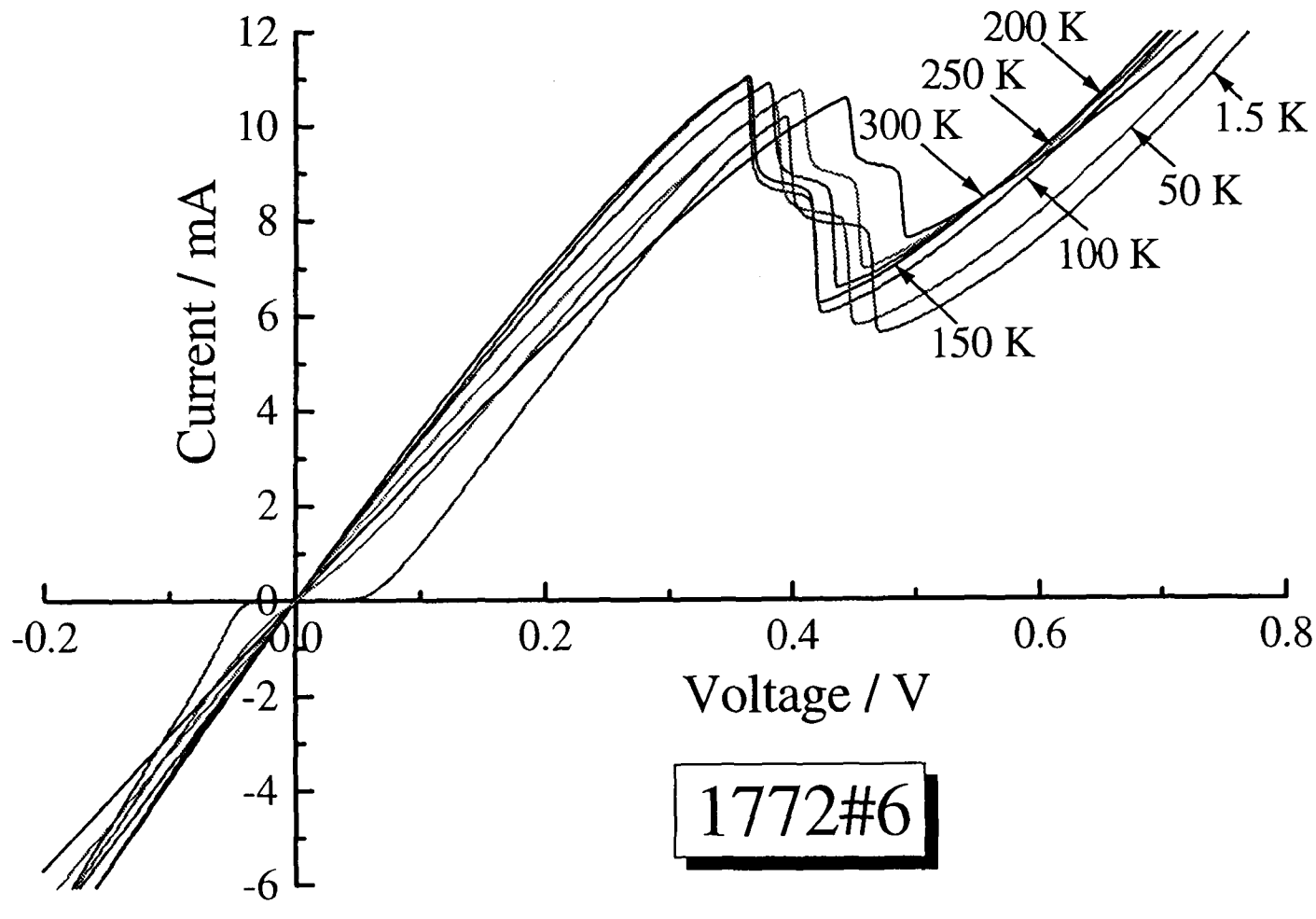


Figure 5.22. I/V plot for 1772#6 at 1 bar and various temperatures.

sample, which has a 'GaAs-like' interface, has a very different temperature response to 1771#5. At 300K it has a large PVR of 1.4 compared to 1.04 for the 'InSb-like' SHET, increasing to only 1.8 at 4K compared to 2.1. The peak voltages and currents are higher also, and the Fermi wavevector mismatch seems to be larger, as the region of high resistance spans a greater voltage.

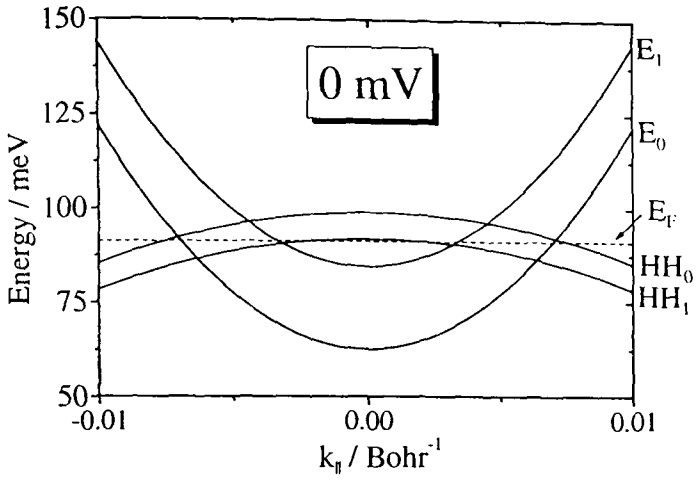


Figure 5.23. Calculated in-plane dispersion curves for sample with a 'GaAs-like' interface at zero bias. Light hole states are not shown as they are unoccupied

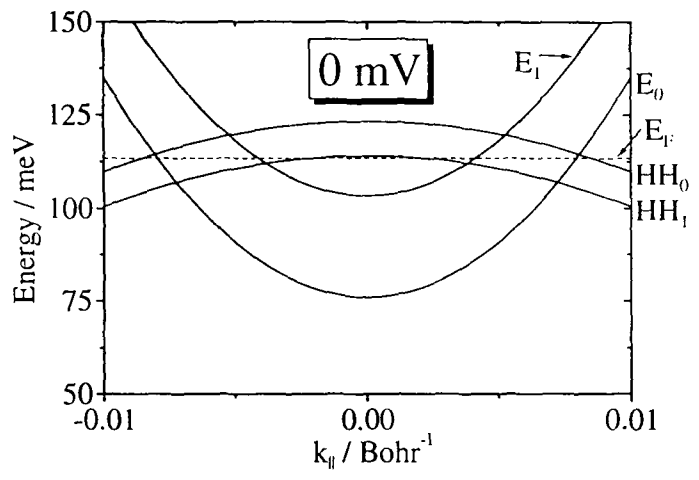


Figure 5.24. Calculated in-plane dispersion curves for sample with an 'InSb-like interface at zero bias. Light hole states are not shown as they are unoccupied

At ±10 mV, the current in reverse bias is -1.8 μA and in forward bias is 1.7 μA. These are an order of magnitude smaller than the equivalent current supported by the other interface, and the Fermi wavevector mismatch seems to have a larger effect. One explanation for this could be a difference in the mismatch of electron and hole Fermi wavevectors at zero bias. Figures 5.23 and 5.24 show the calculated zero bias dispersions for 'GaAs-like' and 'InSb-like' interfaces respectively. According to these results the Fermi wavevector mismatch is very similar for both cases. HH_1, however, is only just occupied in the 'GaAs-like' calculation. Even a small change in effective mass could depopulate this second heavy hole level. As the ratio of 2D electrons to holes is :

$$\frac{n}{p} = \frac{\left[k_F^{E_0}\right]^2 + \left[k_F^{E_1}\right]^2}{\left[k_F^{HH_0}\right]^2 + \left[k_F^{HH_1}\right]^2} \qquad (5.2)$$

where k_F^x is the zero bias value of $k_{||}$ at the Fermi level for a confined level x, any depopulation of HH_1 would lead to a larger initial mismatch between $k_F^{E_0}$ and $k_F^{HH_0}$, and hence a more pronounced region of high resistance. By 30 mV, the currents are -

20.1 μA and 10.4 μA and by 60 mV they are -890.5 μA and 136.7 μA respectively. Again, the reverse bias direction has a smaller resistance.

Figure 5.25 shows V_p - V_v to be constant below 200K at approximately 75 mV which is a similar trend to that of the 'InSb-like' interface. Otherwise, peak and valley voltages and currents for 1772 have a very different temperature response to those exhibited by 1771. This is the first evidence of an unexpected finding, namely that changing the monolayer at the SHET interface results in very different vertical transport behaviour.

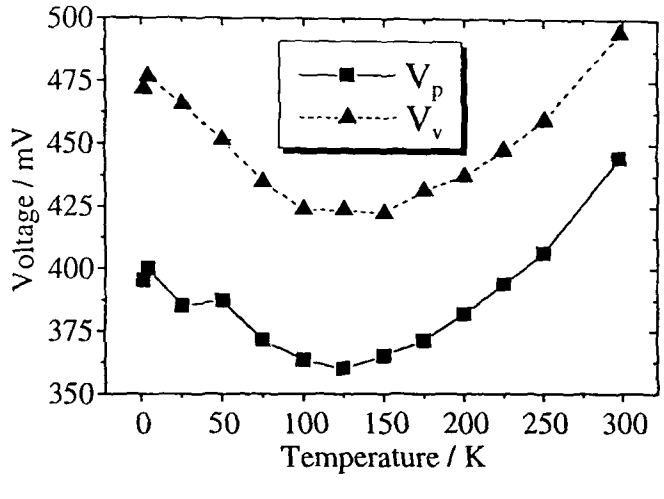


Figure 5.25. Peak and valley voltages plotted against temperature for 1772#6.

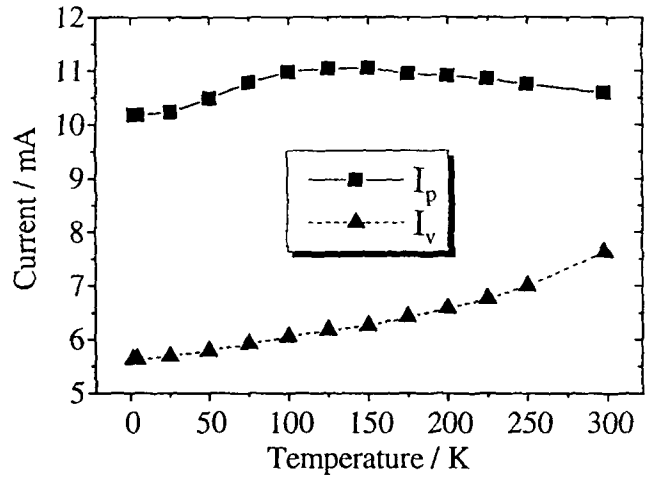


Figure 5.26. Peak and valley currents plotted against temperature for 1772#6.

5.3.3 Discussion of Low Temperature Results

There are a number of issues upon which the calculations of chapter 4 and experimental results differ. Consider the 1K plots in figures 5.17 and 5.22, since k_BT is very small and these represent a zero temperature approximation.

The calculation predicts more than one confined level as illustrated in the dispersion plots 5.23 and 5.24 for example, but not even second derivative measurements of the current with respect to voltage show any evidence of confined levels moving past each other. A number of features in $\mathrm{d}^2I/\mathrm{d}V^2$ might be expected as the sub-bands move past each other with increasing voltage.

Also, the valley current, I_v, is large compared with the ideal case and relatively insensitive to changes in temperature. Possible sources of this background current are described in section 5.4.

Clearly there is a need to address these discrepancies as well as the seemingly interface dependent differences in order to explain the sample temperature dependence. More basic information regarding band overlap values will be obtained in section 6.3 and forward bias I/V measurements at different pressures in subsequent sections will yield a further insight into the SHET conduction mechanism. Additional discussion, therefore is reserved until section 6.5.

5.4 The Background Current

The SHET background current is large considering the InAs and GaSb band gaps should block any conduction process (figure 5.27). A number of possible explanations exist that may explain this discrepancy and an attempt will be made during the course of this thesis to use the background current's temperature and pressure dependencies to eliminate some of these possibilities, thereby achieving a better understanding of the SHET conduction system as a whole.

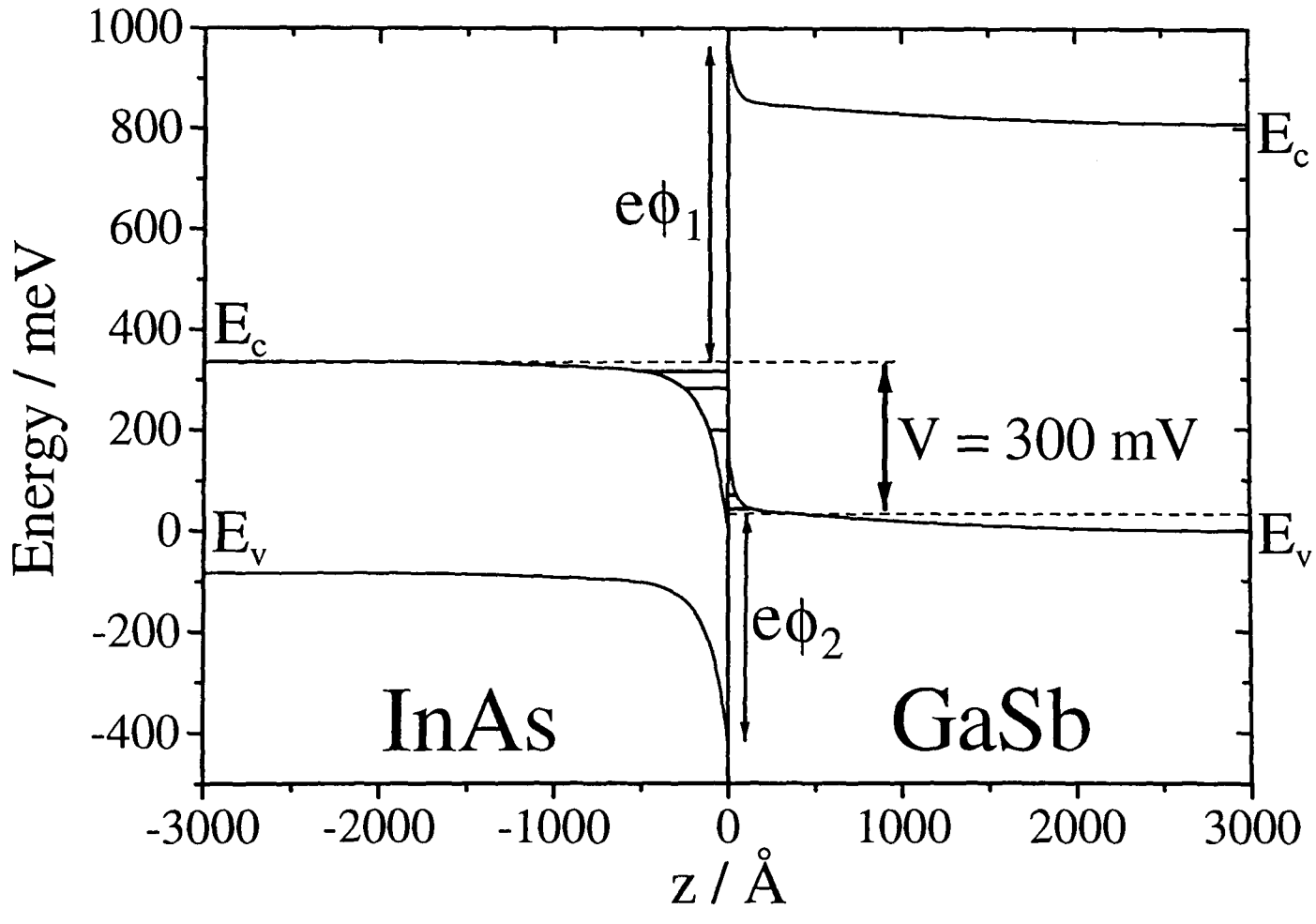


Figure 5.27. Calculated band edge profile for SHET with an 'InSb-like' interface at 0K, 1 bar and 300 mV assuming all the potential is dropped over the interface region. The confined electrons cannot tunnel into the GaSb conduction band as they are blocked by the band gap. The heavy and light holes are similarly blocked.

The first possible mechanism to be considered is a thermal one. In theory, electrons from the conduction band of InAs can be thermally excited over the GaSb band gap barrier and into the GaSb conduction band. Similarly, holes can be excited into the InAs valence band. Figure 5.27 shows the calculated band edge profile and confined electron/hole levels for a SHET with an 'InSb-like' interface at 300 mV and 0K (comment and discussion regarding calculated band profiles is reserved for chapter 6). The GaSb conduction band edge is roughly 700 meV above the electron quasi Fermi energy and the InAs valence band edge is approximately 500 meV below the hole quasi Fermi energy. Experiments show a large background current even at 1K and so the possibility of a significant thermal contribution is small.

The thermal activation energy of the electrons can be approximately given by thermionic emission theory [6]. The Richardson formalism, assuming an approximately linear shift of the quasi Fermi energy with bias and ignoring any tunnelling, yields a temperature dependent background current density of :

$$J_e = A^*_{InAs,e} T^2 \exp\left(-\frac{e\phi_1(V)}{k_B T}\right)\left[1-\frac{A^*_{GaSb,e}}{A^*_{InAs,e}}\exp\left(-\frac{\alpha_1 eV}{k_B T}\right)\right] \tag{5.3}$$

$$J_h = A^*_{GaSb,h} T^2 \exp\left(-\frac{e\phi_2(V)}{k_B T}\right)\left[1-\frac{A^*_{InAs,h}}{A^*_{GaSb,h}}\exp\left(-\frac{\alpha_2 eV}{k_B T}\right)\right]$$

for the electrons and holes respectively, where $e\phi_1$ is the difference in energy between the electron quasi Fermi energy in InAs and the GaSb conduction band edge at the interface (as in figure 5.27) and $e\phi_2$ is the corresponding quantity for holes. $A^*_{x,y}$ is the effective Richardson constant for charge carrier y in material x, V is the voltage and α is the constant by which the electron and hole quasi Fermi energies move apart with bias. All other symbols have their usual meaning. As all the effective Richardson constants are of the same magnitude, for $\alpha eV >> k_B T$ the current density can be approximated as :

$$J_{tot} = A^*_{InAs,e} T^2 \exp\left(-\frac{e\phi_1(V)}{k_B T}\right) + A^*_{GaSb,h} T^2 \exp\left(-\frac{e\phi_2(V)}{k_B T}\right). \tag{5.4}$$

Since ϕ_2 is smaller than ϕ_1 and $A^*_{InAs,e}$ is roughly one tenth of $A^*_{GaSb,h}$, the second term on the right hand side of equation 5.4 should be the dominant factor, implying that a plot of $\ln(J/T^2)$ against $1/T$ at fixed V should yield a straight line with a gradient of $-e\phi_2/k_B$. Figures 5.28 and 5.29 show these relationships for samples with 'InSb-like' and 'GaAs-like' interfaces respectively, yielding little evidence of the existence of a thermal activation process as neither plot results in a straight line and even the gradients are of the wrong sign.

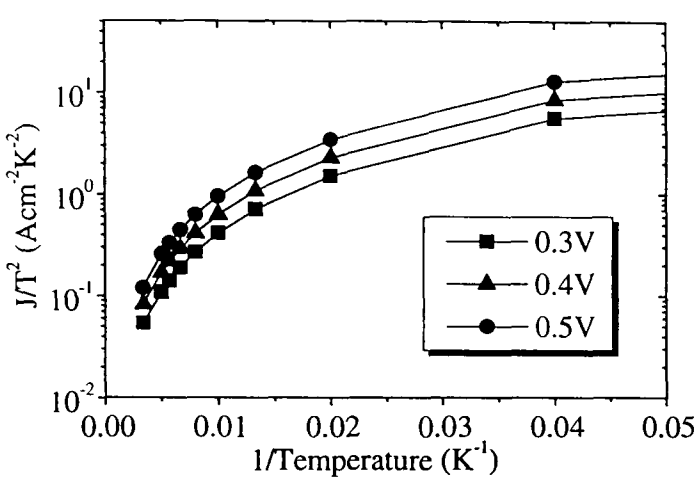


Figure 5.28. Temperature dependence of the background current density of 1771 at various forward biases. This only weakly depends on 1/T suggesting thermal excitation processes provide little contribution.

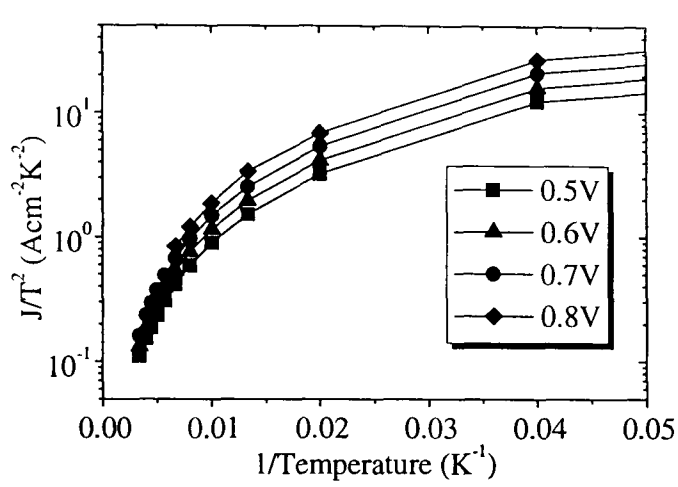


Figure 5.29. Temperature dependence of the background current density of 1772 at various forward biases. This only weakly depends on 1/T suggesting thermal excitation processes provide little contribution

These findings are not altogether surprising considering $e\phi_{1,2} >> k_BT$ over the range of temperatures considered, and only small changes in the valley current are observed as the temperature is lowered.

In systems exhibiting a larger variation in valley current with temperature, the above analysis has proven useful. Shen [7], for example, has used similar arguments to determine that the unexpectedly large background current in the InAs/AlSb/GaSb/AlSb/InAs system is partly due to this thermal contribution.

Tunnelling of electrons from the InAs to GaSb conduction band or holes from GaSb to InAs valence band is also a possible mechanism for the large background current. Figure 5.27 is the calculated zero temperature band edge profile of a sample with an 'InSb-like' interface at 300 mV, showing quite categorically that there is no way for this tunnelling to happen as a one-step process.

Thermal excitation followed by tunnelling could be a promising candidate if the valley current were not so temperature insensitive. The steep curvature of the GaSb conduction and InAs valence bands are also over a region spanning up to 500 Å which makes the one-step tunnelling probability small.

Impurity scattering proved to be the main cause of the excess current in the Esaki tunnel diode [8]. These structures were very highly doped ($> 10^{19}$ cm^{-3}), providing states within the energy gap with a high probability of hopping conductivity. The SHET, however, has a background doping of 10^{16} cm^{-3}, significantly reducing any impurity level density of states. A possible mechanism does exist though where electrons (holes) tunnel into local impurity levels located in the band gap and then lose (gain) energy through phonon emission into the GaSb valence (InAs conduction) band. Alternatively, the density of interface impurity states may be sufficient to allow phonon emission to mediate the transfer of electrons (holes) to hole (electron) states. For a one phonon process, a current at a fixed bias versus temperature plot might be expected to follow the Stokes scattering probability of $1+n^{Stokes}$ where $n^{Stokes} = \left[\exp(E_{phonon} / k_B T) - 1\right]^{-1}$ if this were the dominant contribution to the background current. As figure 5.30 shows, the agreement between current densities for 1772 at a fixed bias beyond the resonance and $1+n^{Stokes}$ is reasonable for low temperatures, after which the two trends diverge. This is perhaps not surprising since more than one inelastic scattering process would be needed to provide the charge carrier with sufficient energy to scatter.

One further possible origin of the background current is a consequence of the allowed mixing of light hole and electron sub-bands at any value of $k_{\|}$ so the electrons (light holes) have a permanent light-hole (electron) like component and therefore a penetration into GaSb (InAs). This penetration improves the probability of electrons (light holes) scattering into the GaSb valence (InAs conduction) band via phonon or multiple phonon emission.

In summary, this section has shown the background current cannot be a thermally activated one, nor can it be due to a purely tunnelling process. Various other inelastic possibilities have been discussed and seem the most likely explanation.

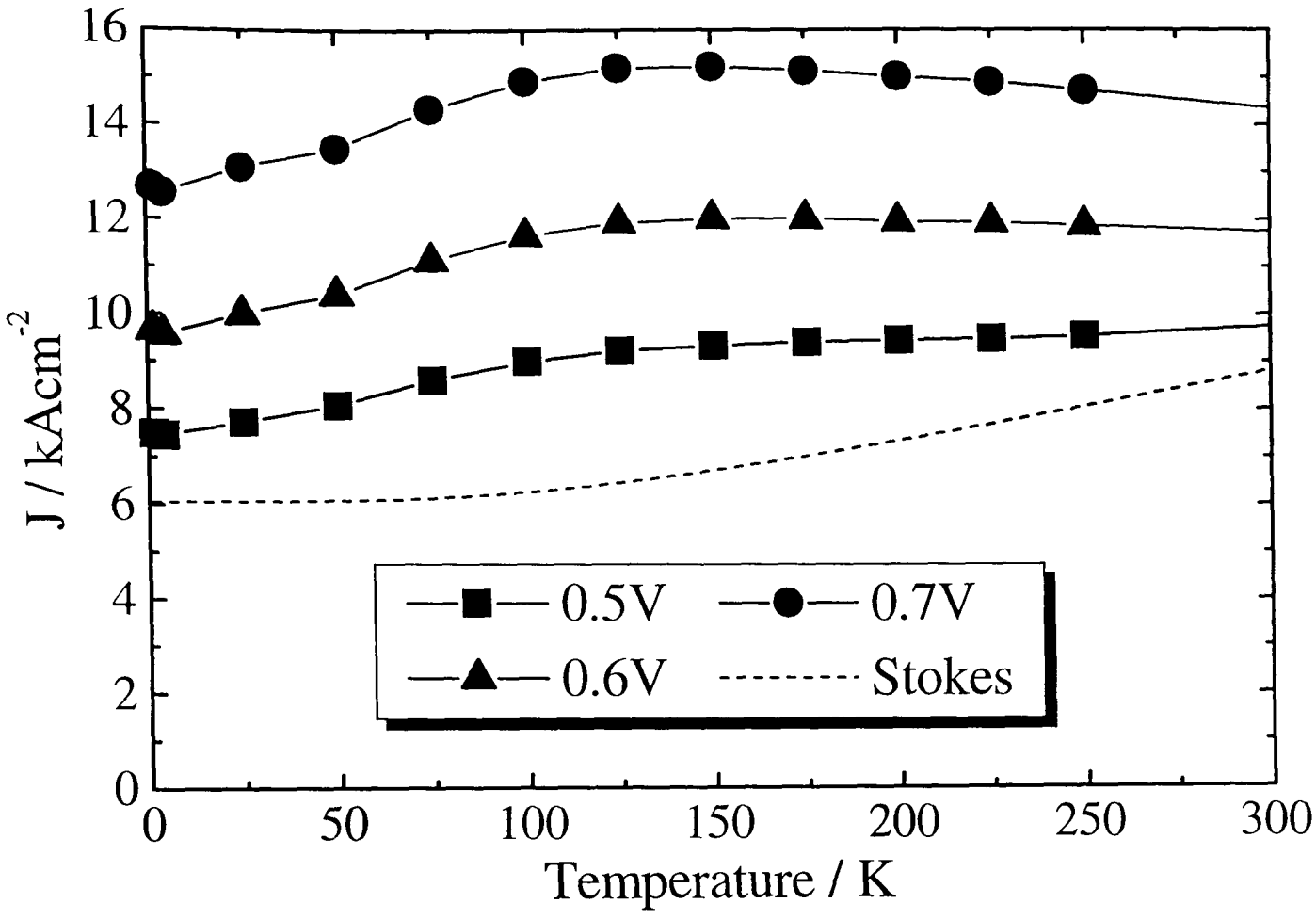


Figure 5.30. Current density versus temperature for 1772. Also shown for comparison is $1 + n^{Stokes}$ Stokes scattering probability for a one phonon process with $E_{phonon} = 30$ meV.

An additional insight into the origin of the large background current may be provided in the next chapter by study of its variation with hydrostatic pressure.

5.5 References

[1] U M Khan-Cheema, P C Klipstein, J M Smith, D G Austing, N J Mason, P J Walker & G Hill. Solid State Electronics 37, p977 (1994).

[2] U M Khan-Cheema, P C Klipstein, N J Mason, P J Walker & G Hill. Journal of Physics and Chemistry of Solids 56, p463 (1995).

[3] D M Symons. DPhil thesis, Oxford (1995).

[4] E E Mendez, J Nocera & W I Wang. Physical Review B 45, p3910 (1992).

[5] G D Austing. DPhil thesis, Oxford, (1992).

[6] S M Sze. Physics of Semiconductor Devices 2nd edition, Wiley, New York, p255 (1981).

[7] J Shen. Journal of Applied Physics 78, p6220 (1995).

Continued ...

References Continued ...

[8] T Yajima & L Esaki. Journal of the Physical Society of Japan 13, p1281 (1958).

6 I/V Measurements at Hydrostatic Pressure

6.1 Introduction 100
6.2 Effect of Hydrostatic Pressure on SHETs 102
6.3 Reverse Bias Characteristics at Hydrostatic Pressure 104
6.3.1 Experimental Results 106
6.3.2 Comparison with Literature 108
6.4 Dependence of NDR on Hydrostatic Pressure 111
6.4.1 Results for the 'InSb - like' Interface 112
6.4.2 Results for the 'GaAs - like' Interface 119
6.4.3 The Background Current's Variation with Pressure 124
6.5 The NDR Mechanism Revisited 126
6.5.1 'InSb-like' Interface 126
6.5.2 'GaAs-like' interface 131
6.6 Summary 133
6.7 References 133

6.1 Introduction

This chapter describes the first study of the variation of the InAs/GaSb SHET vertical transport characteristic with hydrostatic pressure and contains some remarkable conclusions.

The potential use of hydrostatic pressure to the solid state physicist is well documented [1]. In general, the application of hydrostatic pressure on a body causes it to experience forces that compress it evenly in all directions resulting in a stress tensor with no off-diagonal elements. These forces cause a reduction in the lattice constant and a subsequent increase in the Coulomb interaction, thus altering the band structure in a way that is reversible [2,3].

For the III-V semiconductor family, experiments characterising exactly how the bands change with pressure were performed in the 1960s. Zallen and Paul used reflectance [4] and Tsay et al. used transmission [5] to determine that the Γ point energy gap for bulk InAs increased with pressure at a rate of $dE_{g,\Gamma}/dP$ = 10±0.2 meV/kbar. Measurements by Noack et al. using photoluminescence [6] have determined a Γ point band gap increase of $dE_{g,\Gamma}/dP$ = 14±0.5 meV/kbar for bulk GaSb.

Recent magnetotransport measurements on SL samples grown in the same reactor and under the same conditions (temperature, switching sequence, etc.) as the SHETs studied in this thesis have been carried out under hydrostatic pressure by Daly et al. [7]. They suggest the change in bulk band gaps alters the band overlap Δ at a rate of -9.5±0.5 meV/kbar. Also, by fitting their results to a self consistent calculation [8] they obtain 1 bar values of Δ that differ depending upon the composition of the monolayer interface, with a Δ for the 'InSb-like' interface of 155±5 meV and one for the 'GaAs-like' interface of 125±5 meV.

The vertical transport properties of InAs/GaSb SHETs are anticipated to be very sensitive to the GaSb valence - InAs conduction band overlap. Any changes in the absolute energy values of the band edges leading to a change in their relative alignment can therefore be expected to manifest themselves in the I/V characteristic.

One way of testing the predicted mechanism for negative differential resistance (NDR) is, therefore, to apply sufficient pressure to reduce the band overlap to zero and see if the resonant conduction feature vanishes at this point.

In order to understand any change in SHET I/V characteristic with hydrostatic pressure, a further appreciation of the effect it has on the zero bias SHET band edge profile is needed. Section 6.2 provides this by first demonstrating any possible consequences in a qualitative manner, then supplying a short analysis based upon results from the calculations described in chapter 4.

Before the proposed test for the predicted NDR mechanism can be carried out, band overlap values for the SHETs under investigation have to be established. This is achieved in section 6.3 by measuring the pressure-induced change in the reverse bias SHET characteristic for samples with either type of interface. Values for $d\Delta/dP$ and the critical pressure P_c (the pressure at which $\Delta = 0$) are shown to be consistent with results from parallel transport on SLs [7], further proving the excellent quality of the SHET structures. These values are then compared with theoretical and experimental results from the literature.

Armed with a knowledge of the band overlap, section 6.4 attempts to find out if the predicted forward bias mechanism described in section 1.5.2 is really the one responsible for NDR in these structures by comparing the experimental forward bias characteristic and its variation with pressure with results from the calculations described in chapter 4. It will establish, for the first time, that the 'InSb-like' interface behaves with pressure as theory predicts whereas the 'GaAs-like' interface does not and consequently must support a different vertical transport mechanism. Section 6.4 ends by discussing the variation of the background current with pressure, following on from section 5.4.

Section 6.5 describes the mechanism for vertical transport in the 'InSb-like' interface in more detail and compares it with experimental results, then proceeds to consider possible new mechanisms giving rise to NDR in the 'GaAs-like' interface. Section 6.6 provides a brief summary of this chapter's main discoveries.

6.2 Effect of Hydrostatic Pressure on SHETs

It is necessary to document the effects of hydrostatic pressure on the zero bias SHET band profile before any study of the change in I/V trace can be understood. Hence this section contains a short introduction to the relevant phenomena.

Figure 6.1 is a schematic diagram of the expected zero bias SHET band edge profile before and after the application of hydrostatic pressure. As the bulk band gaps increase, the GaSb valence band edge, E_v^{GaSb}, moves down in energy relative to the InAs conduction band edge, E_c^{InAs}. The band overlap, $\Delta = E_v^{GaSb} - E_c^{InAs}$, will therefore decrease with increasing pressure causing the transferred electrons in the InAs conduction band to recombine with holes in the GaSb valence band, thereby reducing the overall charge in both confining potentials. This in turn alters the electric field at the interface in the direction of growth which changes the potential profiles of E_v^{GaSb} and E_c^{InAs}, thus modifying the electron and hole confinement energies.

In order to illustrate these predictions, the calculated zero bias band edge profile is

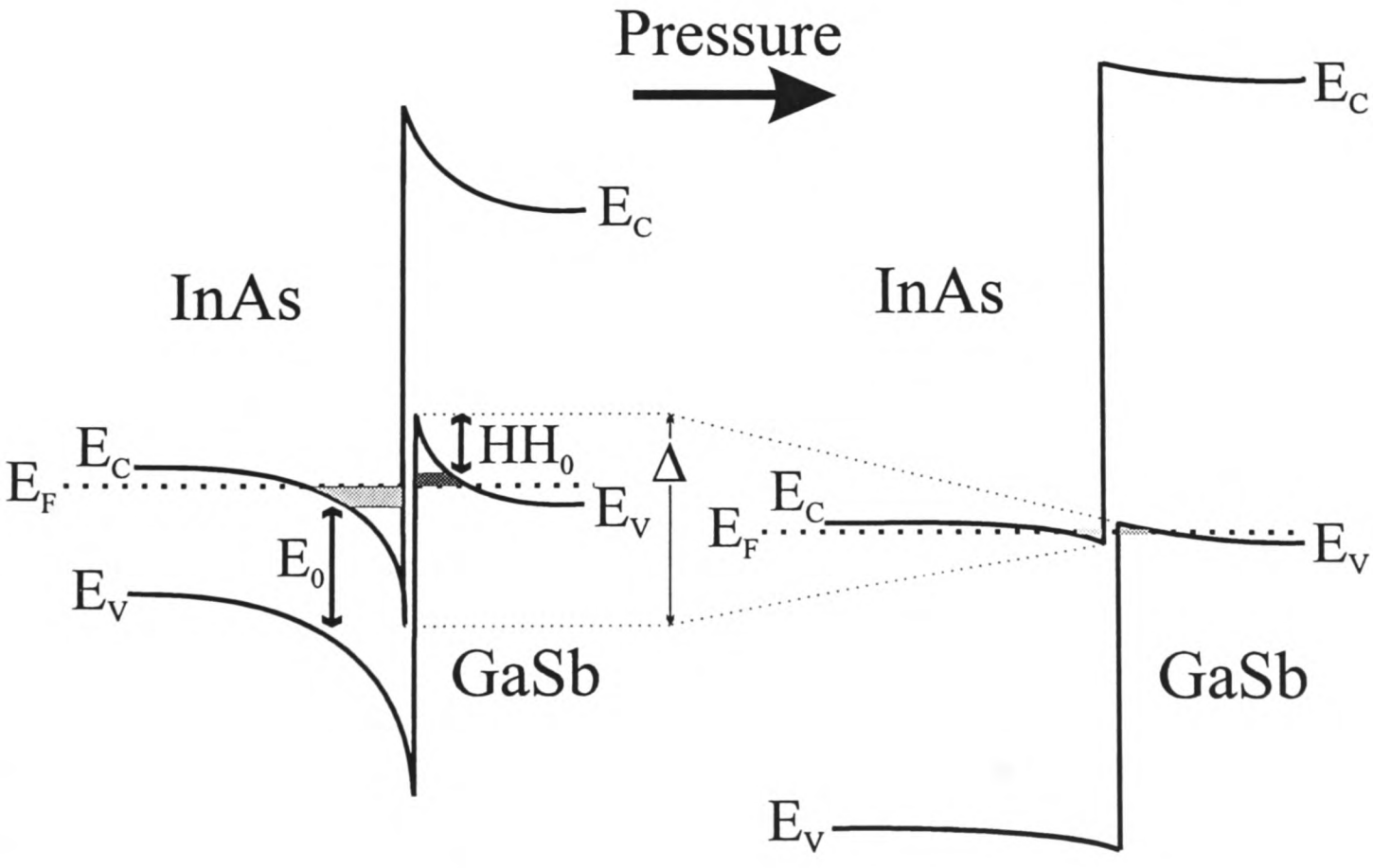


Figure 6.1. Schematic zero bias band edge profile of an InAs/GaSb SHET before and after hydrostatic pressure is applied. The Γ point energy gaps of both InAs and GaSb increase with increasing pressure causing a decrease in the band overlap, $\Delta = E_V^{GaSb} - E_C^{InAs}$, forcing charge recombination and a consequent change of interface electric field. This change in charge distribution influences the vertical transport properties.

presented for a SHET with a 1 bar band overlap of 155 meV at 0K in figure 6.2. For this structure the 2DEG and 2HDG concentrations in the InAs conduction and GaSb valence bands respectively are $n = 4.56\times10^{11}$ cm^{-2} and $p = 4.47\times10^{11}$ cm^{-2}. There are two confined electron energy levels, two heavy hole levels (the second of which is less than 1 meV above the Fermi level) but no occupied light hole levels predicted using this model.

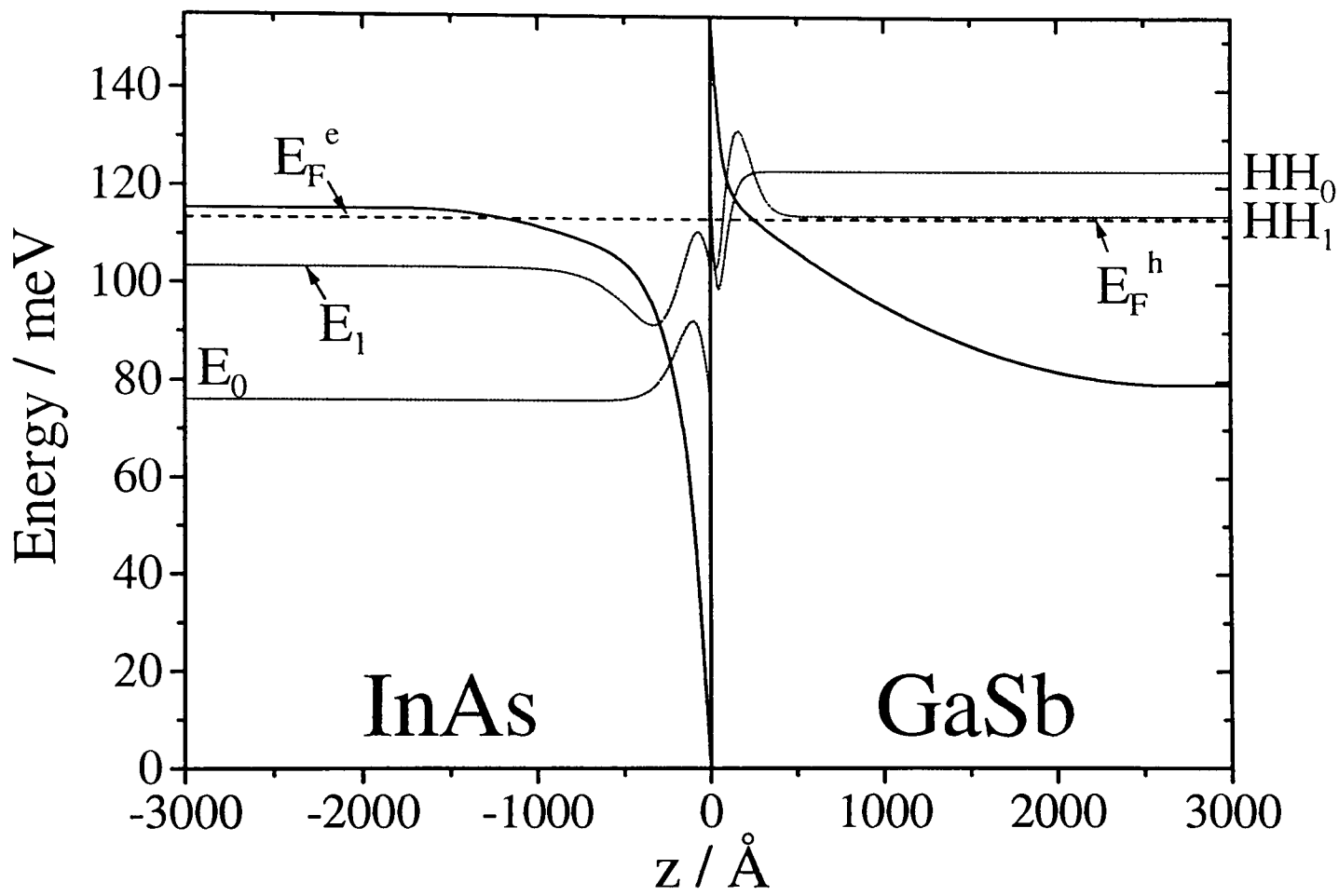


Figure 6.2. Calculated band edge profile for a SHET with a band overlap, Δ, of 155 meV at 1 bar and 0K in the vicinity of the Fermi energy.

Assuming a movement of band overlap with pressure, dΔ/dP of -9.5 meV/kbar, Δ for this structure will reduce to 107.5 meV by 5 kbar, yielding the band profile shown in figure 6.3. By then the 2D concentrations have fallen to $n = 2.93\times10^{11}$ cm^{-2} and $p = 2.81\times10^{11}$ cm^{-2} and the second heavy hole level is less than 0.1 meV above the Fermi level - an occupation which is at least an order of magnitude smaller than the accuracy of the calculations. The lowest confined hole and electron levels are closer to each other in energy at 5 kbar with HH_0 - E_0 having fallen to 29 meV from its 1 bar value of 47 meV.

These calculations quantify the qualitative description of the effects of pressure on the zero bias band edge profile of a SHET with an arbitrary band overlap Δ, given at the

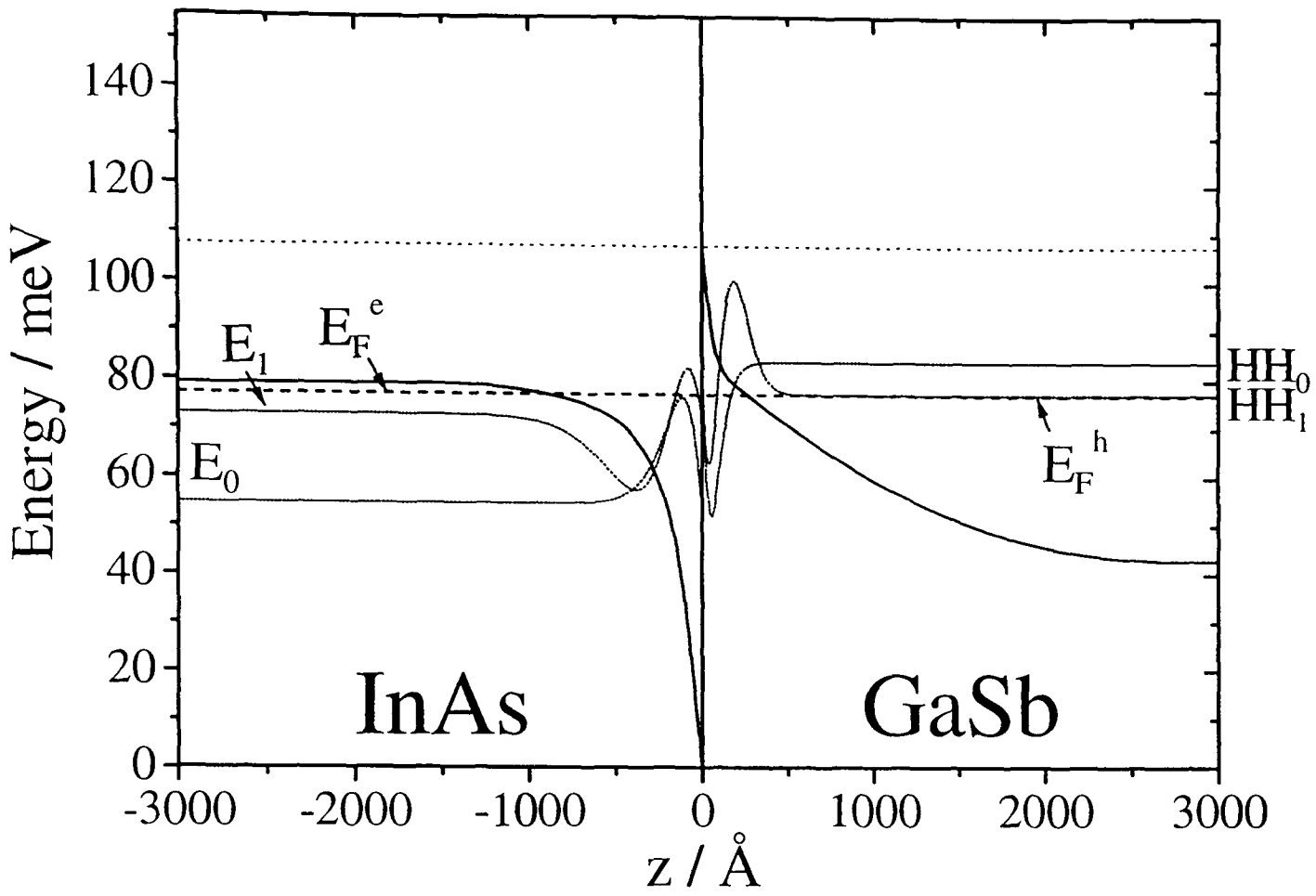


Figure 6.3. Calculated band edge profile at 5 kbar for the SHET in figure 6.2 assuming $d\Delta/dP$ = -9.5 meV/kbar. The dotted line at 107.5 meV indicates the position of the new band overlap.

start of the section. It provides a basis upon which to build an understanding of experimental results with the inclusion of bias once values for Δ have been established for the SHETs under investigation. These are found in the next section by considering the response of the reverse bias I/V characteristic to hydrostatic pressure.

6.3 Reverse Bias Characteristics at Hydrostatic Pressure

Reverse bias (InAs positive, GaSb negative) in SHET structures is expected to exhibit diode-like behaviour so little new physics is expected from the I/V data. This section provides an insight into the predicted reverse bias mechanism and shows, contrary to first impressions, that these measurements can play a vital role in the determination of the band overlap Δ.

Figure 6.4 shows the effect of reverse bias on the SHET band edge profile. The familiar zero bias picture is shown in a). A small reverse bias decreases the

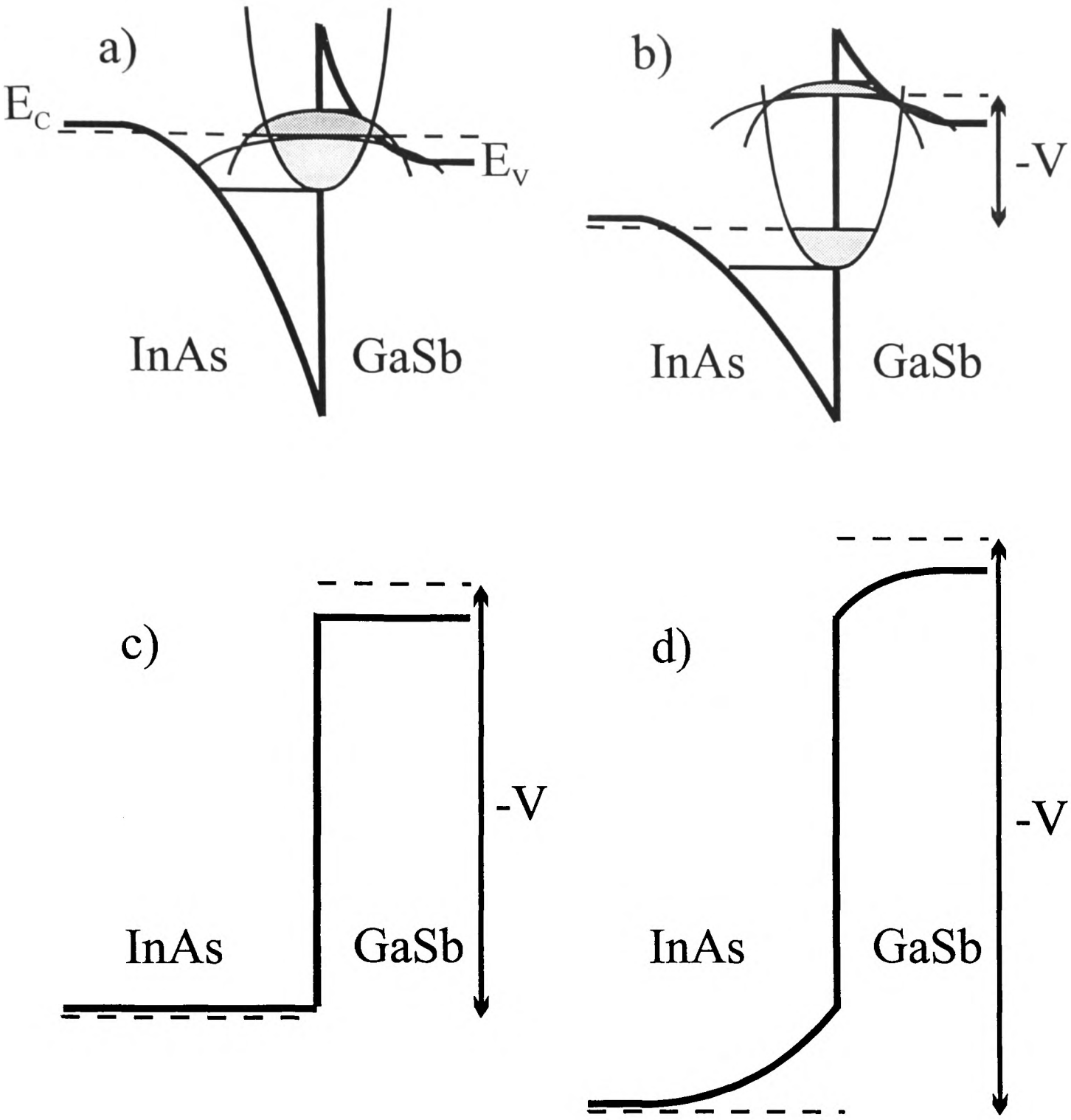


Figure 6.4. Schematic band profile for SHET under reverse bias at 0K. Only in-plane dispersions for E_0, HH_0 and LH are shown for clarity. The familiar zero bias situation is shown in a). Case b) shows the bands and 2D dispersions for a small reverse bias where empty 2D electron states overlap with full 2D hole states. Case c) is the situation when the reverse bias, $V = \Delta + E_{donor}^{InAs} + E_{acceptor}^{GaSb}$, and only 3D states remain. Figure d) shows the bands for a reverse bias larger than in case c).

concentrations of the 2D hole and electron gasses, lessening the band bending, thereby lowering the confinement energies of the lowest electron and heavy hole sub-bands, E_0 and HH_0. In this reverse bias direction, empty 2D GaSb hole states overlap with empty 2D InAs electron states. Additionally, filled bulk GaSb states overlap with empty bulk InAs conduction band states.

The persistence of a high resistance region into reverse bias for low temperatures presented in section 5.3.2 implies the reverse bias mechanism is initially 2D-like as in figure 6.4b. Additionally, the observation that departure from this behaviour occurs

sooner in the reverse bias direction is consistent with a transition from 2D to 3D conduction processes with increasing reverse bias.

A larger reverse bias, more specifically $V = \Delta + E_{donor}^{InAs} + E_{acceptor}^{GaSb}$, is needed to produce the band profile in figure 6.4c, where the conduction process only involves bulk states. Any additional bias moves the band structure into the regime shown in figure 6.4d. Consideration of the variation of this reverse bias current at a fixed voltage is capable of yielding valuable information concerning Δ as shown in the next section.

6.3.1 Experimental Results

Figure 6.5 shows the reverse bias characteristics for 1771#4 at pressures up to 19.8 kbar, illustrating a decrease in current magnitude with increasing pressure. In order to explain these trends and fully appreciate the significance of the results in terms of the 1 bar band overlap values, it is necessary to have a picture of the change in SHET band edge profile in reverse bias with pressure.

For a sufficiently large reverse bias V and while $\Delta > 0$, full bulk GaSb valence band

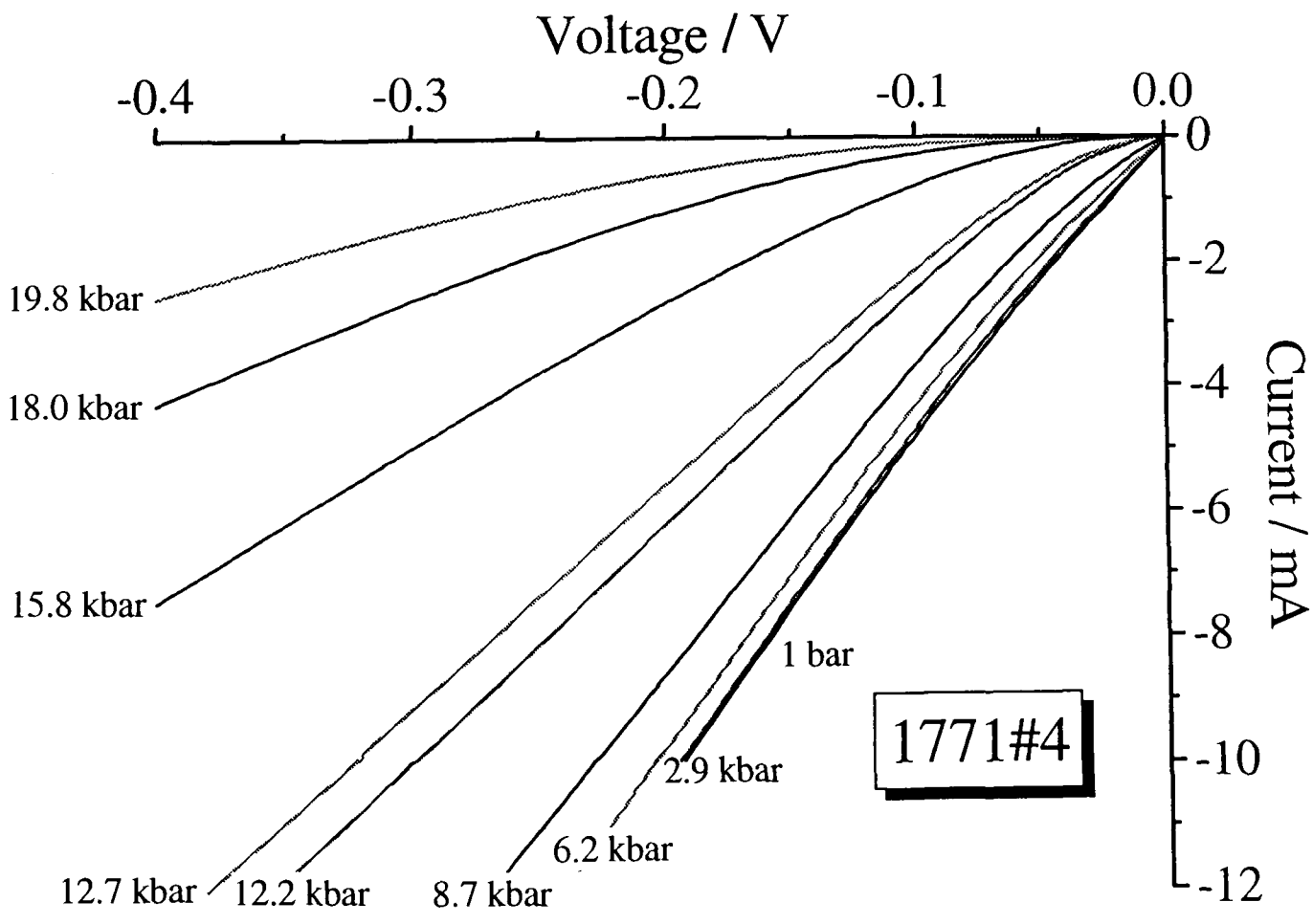


Figure 6.5. Reverse bias I/V plot for 1771#4 at 77K and various pressures.

states overlap with empty states in the InAs conduction band and are expected to be the dominant conduction path allowing a current to flow - processes represented by the solid arrows in figure 6.6a. Tunnelling processes also exist, represented by the dashed arrows, but they are not expected to contribute as much to the current. Figure 6.6b shows the situation after the bands have uncrossed (i.e. for $P > P_c$ where P_c is the pressure at which Δ=0) with the same negative voltage, V, applied as in a). The only processes that can now contribute to the current are tunnelling ones, so a smaller current is expected for this situation. Hence, the current at a fixed reverse bias should be a fairly linear function of pressure for $0 << P < P_c$ but more exponential for $P > P_c$.

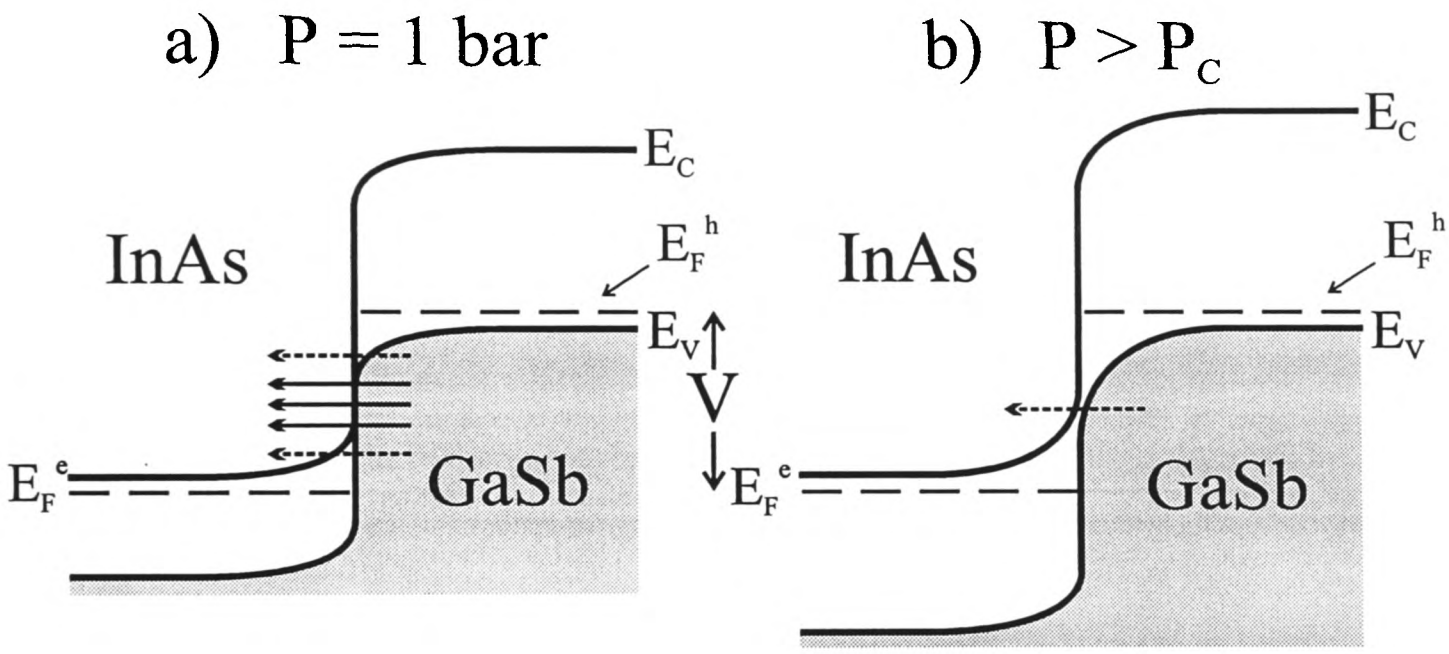


Figure 6.6. Schematic band diagram of a SHET at a fixed reverse bias, V, for a) $P = 1$ bar and b) $P > P_c$. Two types of conduction process are shown at 1 bar - those indicated by solid arrows are expected to be dominant over those indicated by dashed arrows, which involve the electrons tunnelling through a barrier. For $P > P_c$, only the tunnelling processes are available to contribute to the current.

The reduction in reverse bias current with pressure shown in figure 6.5 is typical of tested mesas with either interface. To examine the relative rates of current decrease with pressure, it is more informative to plot the current at a fixed negative bias (normalised to its 1 bar value) against pressure. Results are shown for samples with both interface types in figure 6.7 where the 'InSb-like' interface clearly shows the current reaching 50% of its 1 bar value later than the 'GaAs-like' interface. Furthermore, a point of inflexion occurs at roughly 16 kbar for 1771#4 and one at approximately 13 kbar for 1772#4 which, if taken as evidence for a value of P_c (separating linear from exponential regions) is remarkably similar to those measured by parallel transport [7]. The dotted line shows results for the 'GaAs-like' interface shifted up in pressure by 3 kbar. It is nearly coincident with results from the 'InSb-like

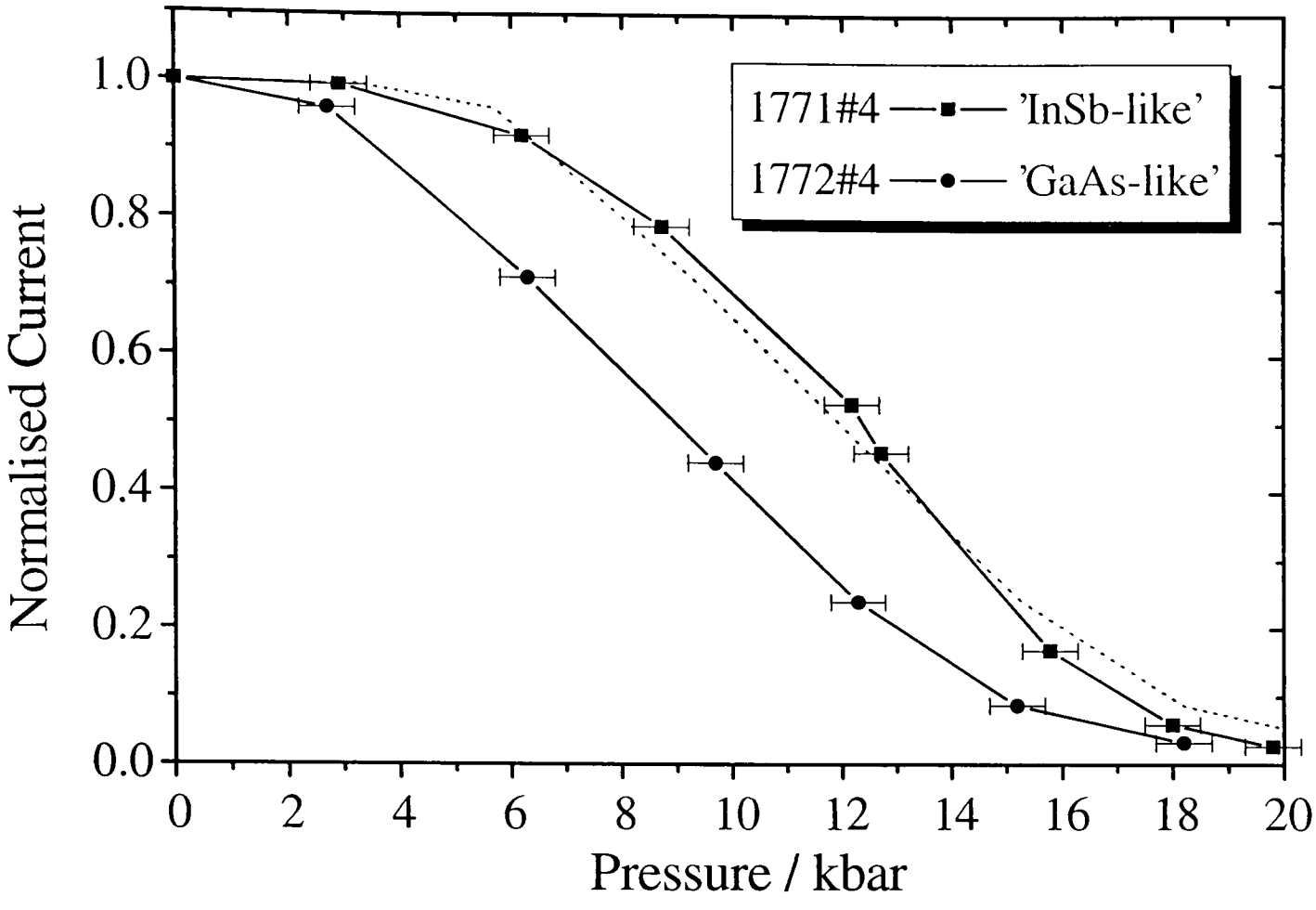


Figure 6.7. Normalised current at a fixed reverse bias versus pressure for samples with an 'InSb-like' and a 'GaAs-like' interface, measured at 77K. 1771#4 exhibits a point of inflexion at roughly 16 kbar, and 1772#4 at 13 kbar. The dotted line is simply the plot for 1772#4 moved along the x axis by 3 kbar.

interface within the errors, showing that P_c is roughly 3 kbar greater for the 'InSb-like' interface and that $d\Delta/dP$ is similar for both.

These results prove for the first time on single interface structures that :

- P_c is approximately 3 kbar larger for the 'InSb-like' interface than the 'GaAs-like' interface.
- $d\Delta/dP$ is similar for both interfaces,

both of which are consistent with results from parallel transport on multiple interface samples [7] of $\Delta = 155\pm5$ meV for the 'InSb-like' interface, 125 ± 5 meV for the GaAs interface and $d\Delta/dP = -9.5\pm0.5$ meV/kbar. Knowledge of these values enables a comparison to be made of forward bias conduction mechanisms in section 6.4.

6.3.2 Comparison with Literature

Since Sai-Halasz et al. first established that the InAs conduction band edge lies 150 ± 50 meV below the GaSb valence band edge using optical absorption techniques

on InAs/GaSb SLs in 1978 [9], the search has been on to find a precise value for Δ.

During the early and mid 1980s, before the introduction of preferential interface switching sequences, there were few reports on experimental values for Δ. Amongst them were those of those Gualtieri et al. [10] who used x-ray photoemmission core level spectroscopy to determine a Δ of 90±100 meV and those of Beerens et al. [11] who fitted their magnetotransport data to a self consistent variational calculation to predict a band overlap of between 150 and 163 meV. Both these values are consistent with those I obtained in section 6.3.1. On the theoretical front, Harrison and Tersoff [12] used a tight binding theory of heterojunction line-ups to arrive at values for Δ ranging from -90 to 300 meV without and with the inclusion of interface dipole effects respectively. This large uncertainty reflects the complexity of the calculations and also the lack of consensus regarding heterojunction valence band discontinuities at the time. A more precise value of 160 meV was predicted by Van de Walle and Martin [13] using a model solid theory where the line-up of chemical potentials between two materials is determined by the difference in their average potentials. This is very close to the values in section 6.3.1.

A growing realisation in the late 1980s that the chemical composition of the heterointerface could dramatically affect valence band offsets lead to a change in the research focus in this area. Dandrea et al. [14] for example calculated a 44 meV larger band overlap for the 'InSb-like' interface using local density functional calculations with *ab initio* nonlocal pseudopotentials. In the same year, Foulon and Priester [15] reported a 31 meV larger Δ for the 'InSb-like' interface using a self consistent tight binding treatment. Both of these theoretical treatments agree remarkably well with experimental results reported here.

Waterman et al. [16] found a 50 meV larger energy difference between the two lowest minibands E_0 and HH_0 for InAs/GaSb SLs with 'InSb-like' interfaces. The measurements were carried out on samples of nominally the same period but because of the short periodicity of the structures, their confinement energies may have been strongly dependent on bond type, possibly masking the effects of a shift in band offset. Holmes et al. [17] also find Δ to be larger for the 'InSb-like' interface but do not state

a value for the difference. Indeed, the experimentally obtained results for band overlap differences of Meyer et al. [18] provide the largest deviation from those in section 6.3.1. They find it to be 14±5 meV but do not state absolute values for Δ in either case. It is possible the smaller difference is due to alloying of one or both interfaces [19].

Hemstreet et al. [20] used *ab initio* molecular dynamics techniques to calculate a large difference for Δ between the two interfaces resulting from differences in strain. Their results are consistent with a Δ for the 'InSb-like' interface of approximately 140 meV and one for the 'GaAs-like' interface of roughly zero.

As mentioned in section 6.3.1 the recent values for Δ of Daly et al. are 155±5 meV for the 'InSb-like' interface and 125±5 meV for the 'GaAs-like' interface. These were obtained from superlattices and double heterostructures with excellent interfaces and of almost intrinsic composition, as opposed to most of the other reported experimental results whose samples were grown by MBE and had far higher n/p ratios.

The rate of decrease of band overlap with pressure have also been a region of interest over the years as $d\Delta/dP$ provides information about pressure shifts of the conduction and valence bands offsets. If for example the valence bands are fixed and the conduction bands move with respect to one another, $d\Delta/dP$ is expected to follow $dE_{g,\Gamma}^{InAs}/dP$ and vice versa for fixing of the conduction bands.

Theoretically predicted and experimentally measured values for $d\Delta/dP$ are summarised in table 6.1 and show a significant variation in reported values. The results of Claessen [21], Beerens [11] and Holmes [17] were all taken from samples grown by MBE where n is large with respect to p. As $d\Delta/dP$ was deduced in all three cases from a fit of the experimental data to a self consistent calculation, the values are only as accurate as the calculation. Since the samples were far from intrinsic, Beerens et al. [11] attributed the excess electrons to interface donor states, the pressure dependence of which are unknown, leading to a possible source of error.

Author	Year	Method	dΔ/dP
Claessen et al. [21]	1986	magneto-optical	-5.8 meV/kbar
Beerens et al. [11]	1987	magnetotransport	-6.7 meV/kbar
Van de Walle [22]	1989	model solid theory	-10.1±3 meV/kbar
Symons et al. [8]	1994	magnetotransport	-9.9±1 meV/kbar
Holmes et al. [17]	1995	magnetotransport	-7.5 meV/kbar
Daly et al. [7]	1996	magnetotransport	-9.5±0.5 meV/kbar

Table 6.1. Table of theoretical and experimental measurements for dΔ/dP.

The MOVPE grown samples tested by Symons [8] and more recently Daly [7] were much closer to being intrinsic. dΔ/dP is also much closer to the shift of $E_{g,\Gamma}^{InAs}$, implying the valence band offset remains fairly constant which has been predicted by the model solid theory of Van de Walle [22]. He calculated dΔ/dP to be -10.1±3 meV/kbar which agrees excellently with measurements on MOVPE grown samples.

In summary, there is almost unanimous agreement that the 'InSb-like' interface has a larger band overlap than the 'GaAs-like' one but less about the magnitude of this difference although the value used here of 40 meV fits in well with most reports. Additionally, dΔ/dP has the same value for both interfaces, but there is disagreement between MBE and MOVPE grown samples regarding this value. As n is much larger than p for the MBE grown samples and the MOVPE samples are nearer to being intrinsic, the difference has been attributed to the unknown pressure dependence of the interface donors which introduces errors into the MBE data fits.

6.4 Dependence of NDR on Hydrostatic Pressure

Results and analysis on the effect of pressure on reverse bias SHET I/V characteristics have so far demonstrated an interface dependent difference in 1 bar values of Δ and P_c. The purpose of this section is to investigate the forward bias resonant conduction characteristics of samples with both types of interface under applied hydrostatic

pressure

Application of hydrostatic pressure is one way of varying Δ in a controlled way whilst retaining the ability to monitor the forward bias I/V characteristics. The predicted forward bias transport mechanism at 1 bar, independent of interface, has been introduced in section 1.5.2, and will be investigated in more detail in section 6.5. Increasing hydrostatic pressure will decrease Δ which has the effect of reducing n and p and thus the energy difference between E_0 and HH_0 as described in section 6.2. These changes are expected to manifest themselves in the forward bias I/V traces in a number of ways. A direct consequence of reducing n and p is to reduce the current at a given bias and, as E_0 and HH_0 are initially closer together, V_c (the voltage at which E_0 lines up with HH_0) will occur at a lower bias, thereby decreasing the peak voltage V_p and the valley voltage V_v. For an ideal SHET therefore, I_p and V_p should decrease with increasing pressure until at P_c the 2DEG and 2DHG concentrations are zero and the NDR has disappeared at zero bias and zero current. Thus hydrostatic pressure provides a potentially very useful method for probing the origin of NDR in SHETs. The twin aims of this section can be summarised as follows :

- To determine whether the predicted model of resonant conduction is actually the method by which NDR arises in SHET structures by checking whether the resonance disappears at P_c since the band overlap has fallen to zero and there is no longer a 2DEG or 2DHG.

- To find out more about the nature of the forward bias background current.

This section is split into three sub-sections. In section 6.4.1, forward bias I/V traces for 1771 under pressure are presented and a comparison is made with the calculated results for a structure with an 'InSb-like' interface. Similar analysis is performed in section 6.4.2 for 1772, using calculations for a structure with a 'GaAs-like' interface and section 6.4.3 explores whether the variation of background current with pressure can yield an insight into its source.

6.4.1 Results for the 'InSb - like' Interface

The 1 bar band overlap, Δ, for the 'InSb-like' interface has been established as

155±5 meV [7], consistent with a value for P_c of ~ 16 kbar as discovered in section 6.3.1. According to the conduction process introduced in section 1.5.2, the resonant component of the current is expected to disappear at or very close to P_c, and so the application of pressure is an ideal way to examine the SHET vertical transport mechanism.

Forward bias I/V measurements for two mesas of 1771 taken at 77K for various pressures are shown in figures 6.8 and 6.9. 1771#3 was pressurised using the 'Cambridge cell' (section 3.3.1) which is why the maximum 77K pressure reached is only 13 kbar, close to the maximum obtainable pressure at 77K for this cell. The maximum pressure reached with 1771#4 is significantly higher as the 'Russian cell' (section 3.3.2) was used.

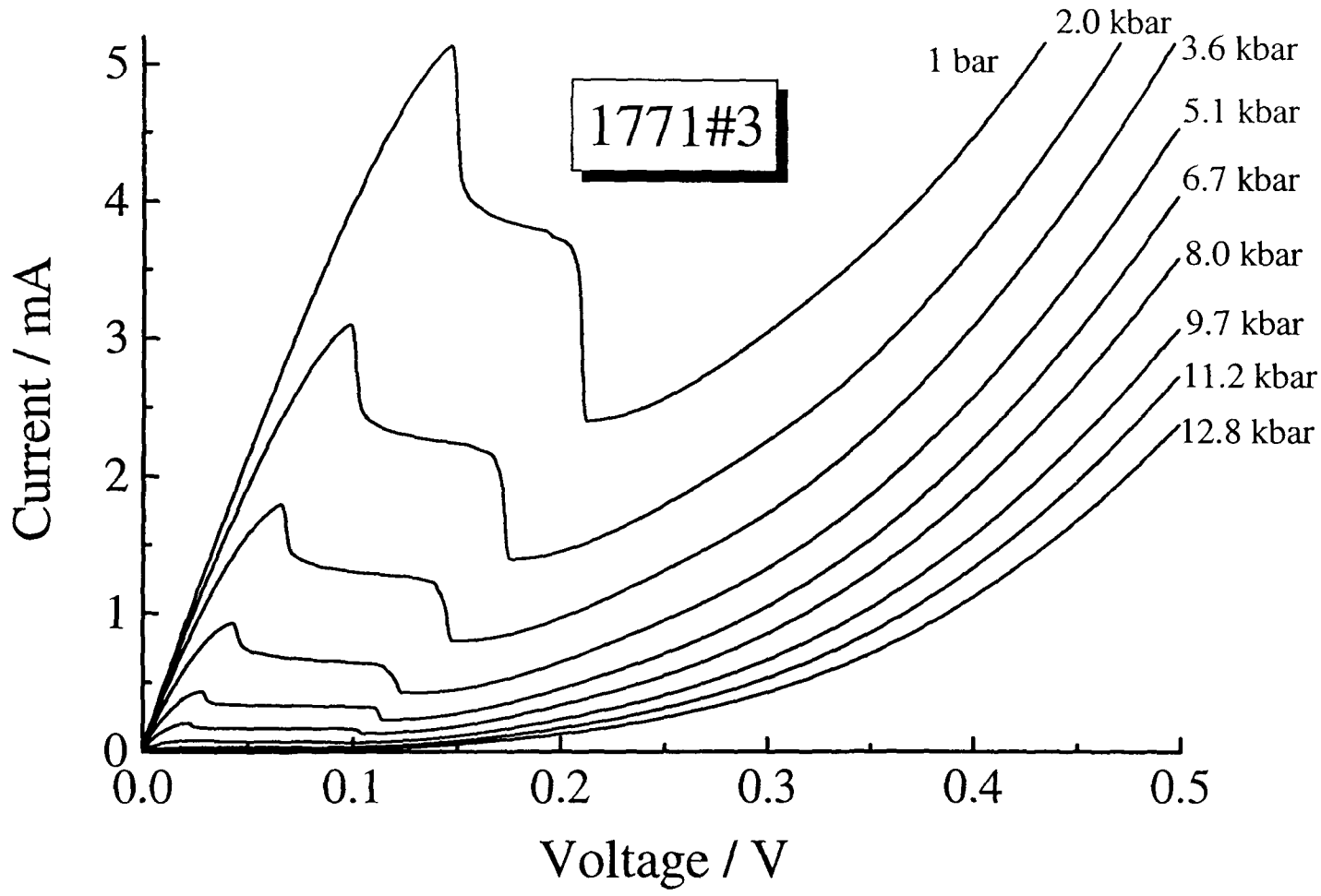


Figure 6.8. Forward bias I/V curve for 1771#3 measured at 77K for various pressures between 1 bar and 12.8 kbar.

The two mesas show identical I/V behaviour with pressure, indicative of the excellent sample quality. The peak and valley voltages do indeed fall as the pressure is increased which is consistent with E_0 moving closer to HH_0 at zero bias. The peak and valley currents also fall which, again, agrees with the model where charge recombination as the pressure is increased leaves a lower 2D charge concentration at the interface.

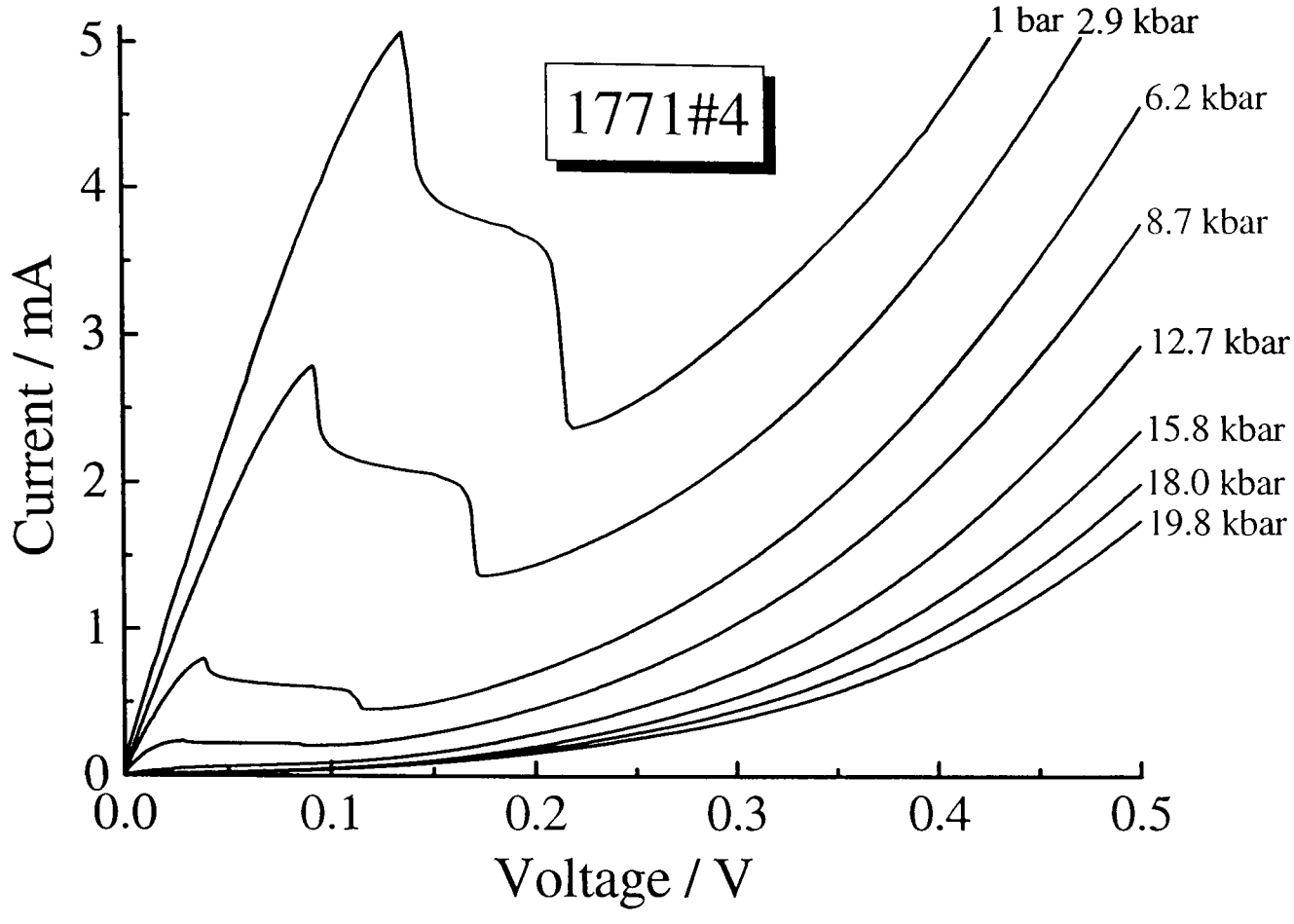


Figure 6.9. Forward bias I/V data for 1771#4 measured at 77K for pressures up to 19.8 kbar.

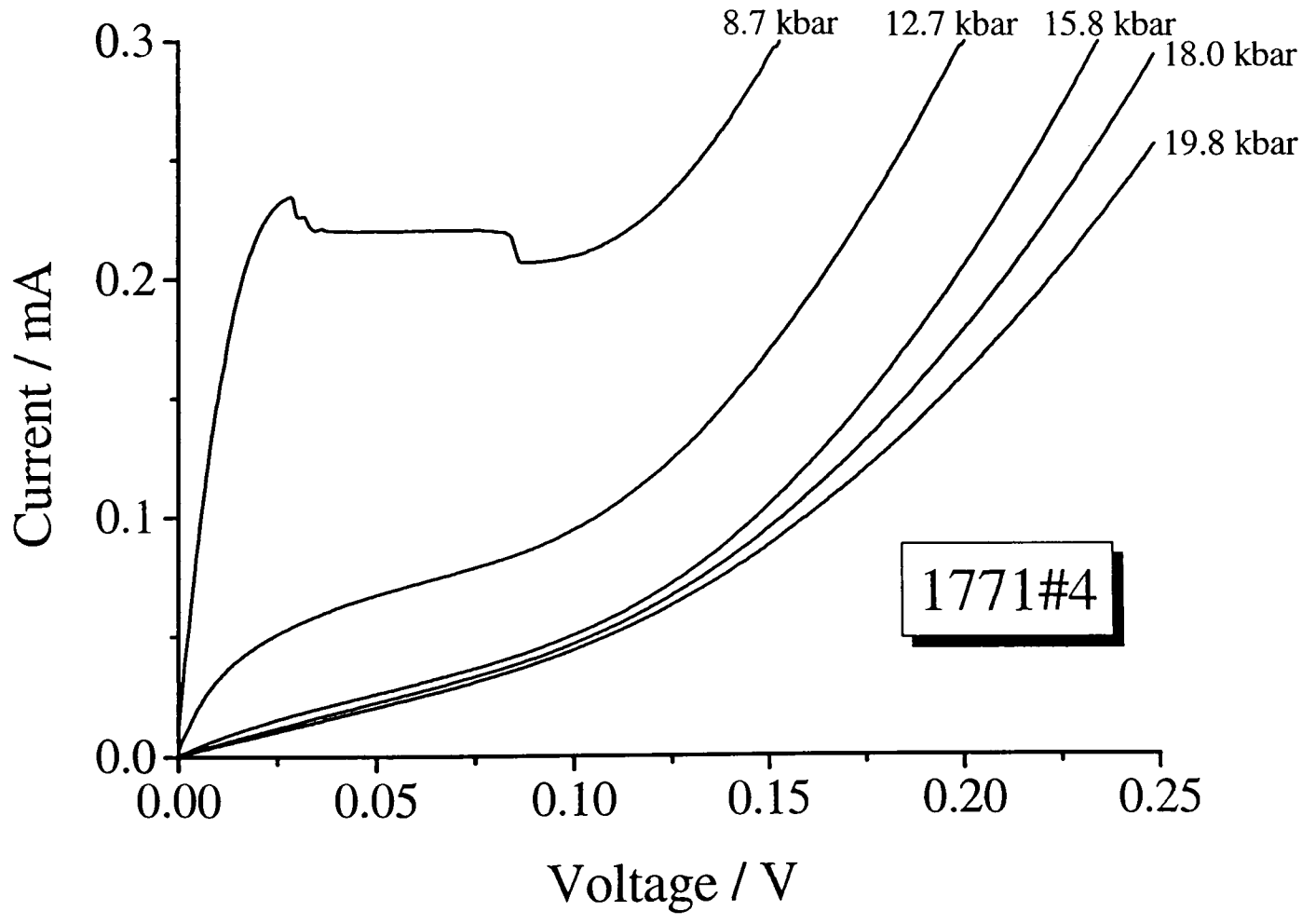


Figure 6.10. High pressure I/V plots for 1771#4 taken at 77K. The resonant feature has almost vanished by 15.8 kbar, indicating the NDR is dependent upon the existence of a positive band overlap, Δ, which falls to zero by $P_c = 16 \pm 0.5$ kbar.

In order to examine the I/V curves at high pressures, the plot for 1771#4 is exhibited in figure 6.10 with magnified axes. The NDR region can be seen at 8.7 kbar, although considerably diminished in magnitude, and a feature is visible at 12.7 kbar. This feature does not actually exhibit NDR but clearly the conductance rises and falls before the current merges with the background at roughly 0.1 V which points to the existence of a resonant conduction process drowned out by some parallel conduction path.

The low bias I/V trace at 15.8 kbar shows a *very* slight resonant conduction feature. Those at 18.0 and 19.8 kbar however are nearly coincident and show no feature. This indicates the initial current path is the same for both pressures and therefore independent of band overlap. The NDR feature vanishes at very small biases which is consistent with E_0 and HH_0 at zero bias being very close together around P_c, an exact evaluation of which is not possible. An approximate value of 16 kbar does, however, fit the data well and the results seem to show that for the 'InSb-like' interface the resonant conduction path giving rise to NDR is suppressed by 18 kbar.

The calculated position of the 2D electron and hole sub-bands with applied forward

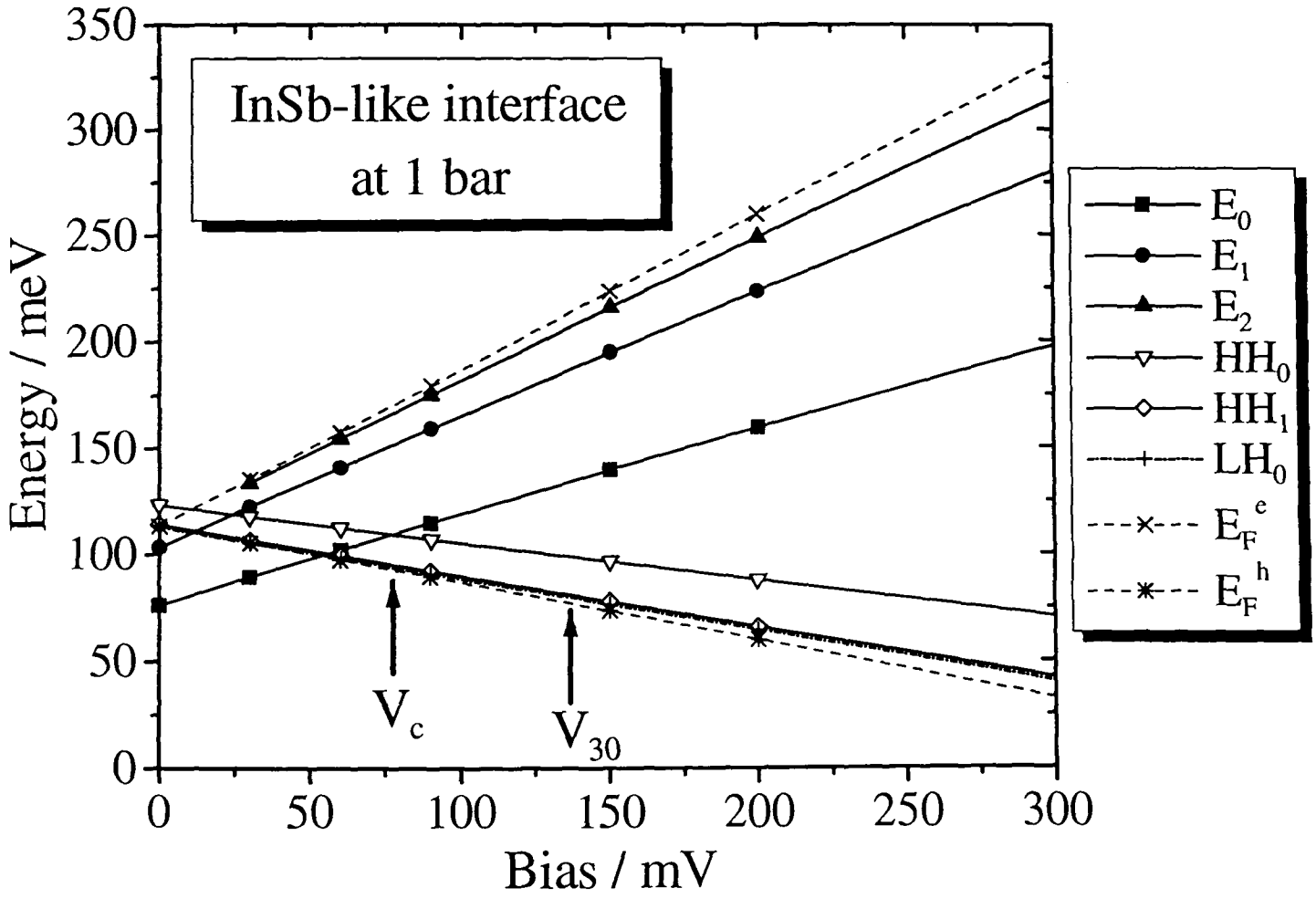


Figure 6.11. Calculated position of 2D sub-bands versus bias for a SHET with an 'InSb-like' interface at 1 bar.

bias for a SHET with an 'InSb-like' interface at 1 bar is plotted in figure 6.11. E_0 and HH_0 are seen to cross at $V_c = 77$ meV which is far lower than the observed peak voltage of 147 mV. Also indicated is V_{30} which is the bias at which E_0 is 30 meV beyond HH_0 - the approximate equivalent of one phonon energy.

Figures 6.12 and 6.13 show the calculated positions of the 2D sub-bands for the 'InSb-like' interface at 5 and 10 kbar respectively, indicating V_c moving towards 0 V with increasing pressure. It is convenient to display both calculated and experimental voltage trends with pressure on the same plot in order to best compare them. Thus, figure 6.14 shows the pressure induced variation of V_p and V_v for 1771#3 and 1771#4 together with calculated values for V_c and V_{30}. The experimental values for V_p and V_v are only plotted up to 9 kbar as the NDR ceased at approximately this pressure where the resonant and non-resonant contributions merge into each other making any distinction between the peak and valley difficult.

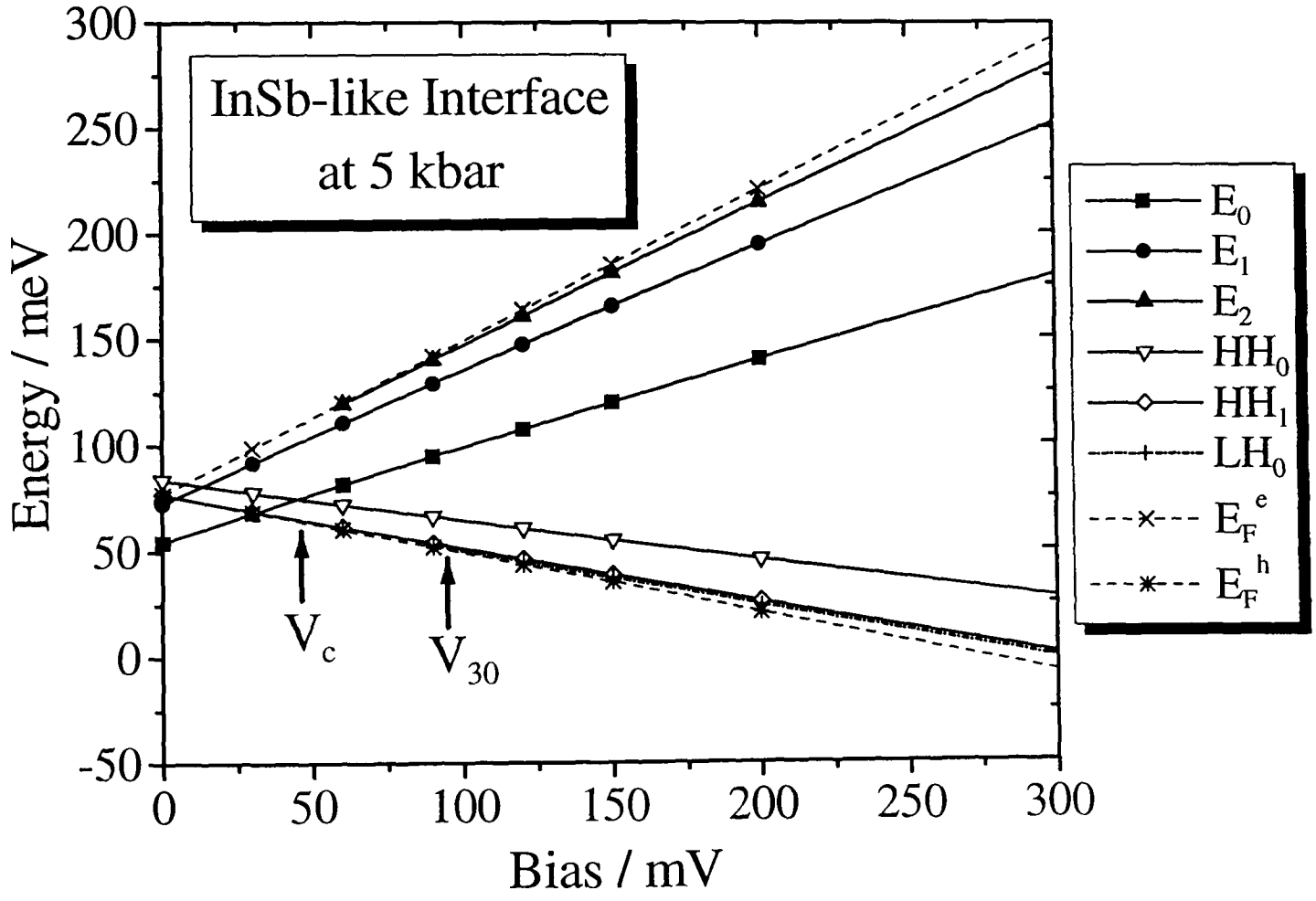


Figure 6.12. Calculated position of 2D sub-bands versus bias for a SHET with an 'InSb-like' interface at 5 kbar.

From these results it appears that neither V_p nor V_v exactly map onto the calculated values for V_c or V_{30}. One possible explanation for this is a possible resistance in series with the interface region, either from leads, contacts, or the GaSb epilayer. If this were

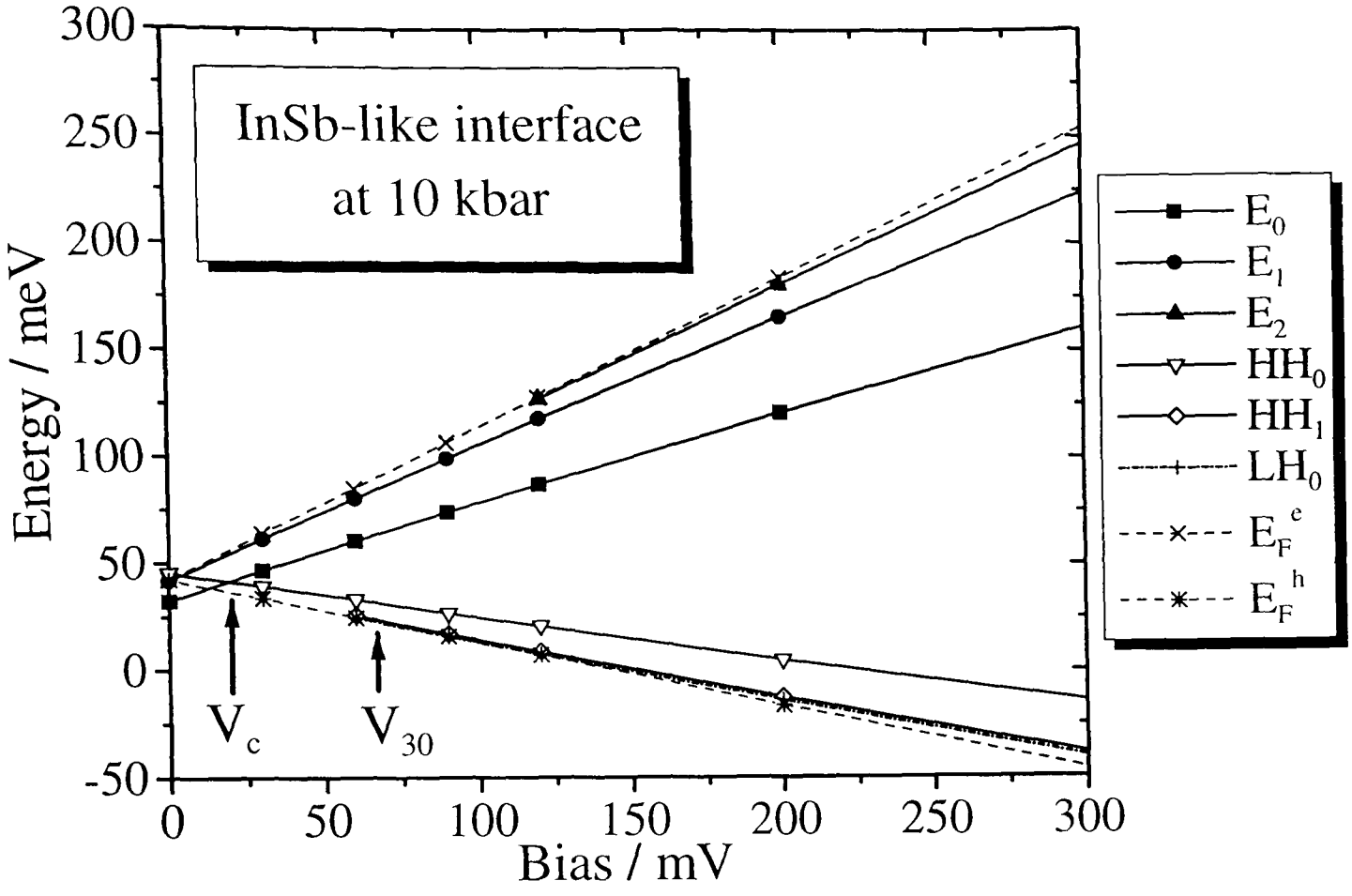


Figure 6.13. Calculated position of 2D sub-bands versus bias for a SHET with an 'InSb-like' interface at 10 kbar

the case, only a proportion of the applied voltage would be dropped across the interface itself. One way to correct for an unknown series resistance, R, in the experimental trace is to subtract the voltage dropped across this parasitic resistance (IR where I is the current) from V_p and V_v. This has been performed for R = 10 and 20 Ω, the results of which are shown as dotted lines in figure 6.14, representing V_p - I_pR and V_v - I_vR.

V_p corrected for a parasitic resistance of 20 Ω exhibits a very similar decrease with pressure to V_c. This observation is consistent with a resonant conduction mechanism where the peak voltage is the outcome of a competition between increasing n and p and less efficient electron / heavy hole coupling with increasing bias as introduced in section 1.5.2. V_{30}, where E_0 and HH_0 are approximately one phonon energy past each other, is also plotted and shows a similar trend to V_v which may indicate the valley is due to phonon emission. If this were the case, any resonant conduction feature would be expected to vanish at a very small bias when Δ is -30 meV, i.e. where any electrons and holes are roughly one phonon energy apart. This would alter the pressure at which

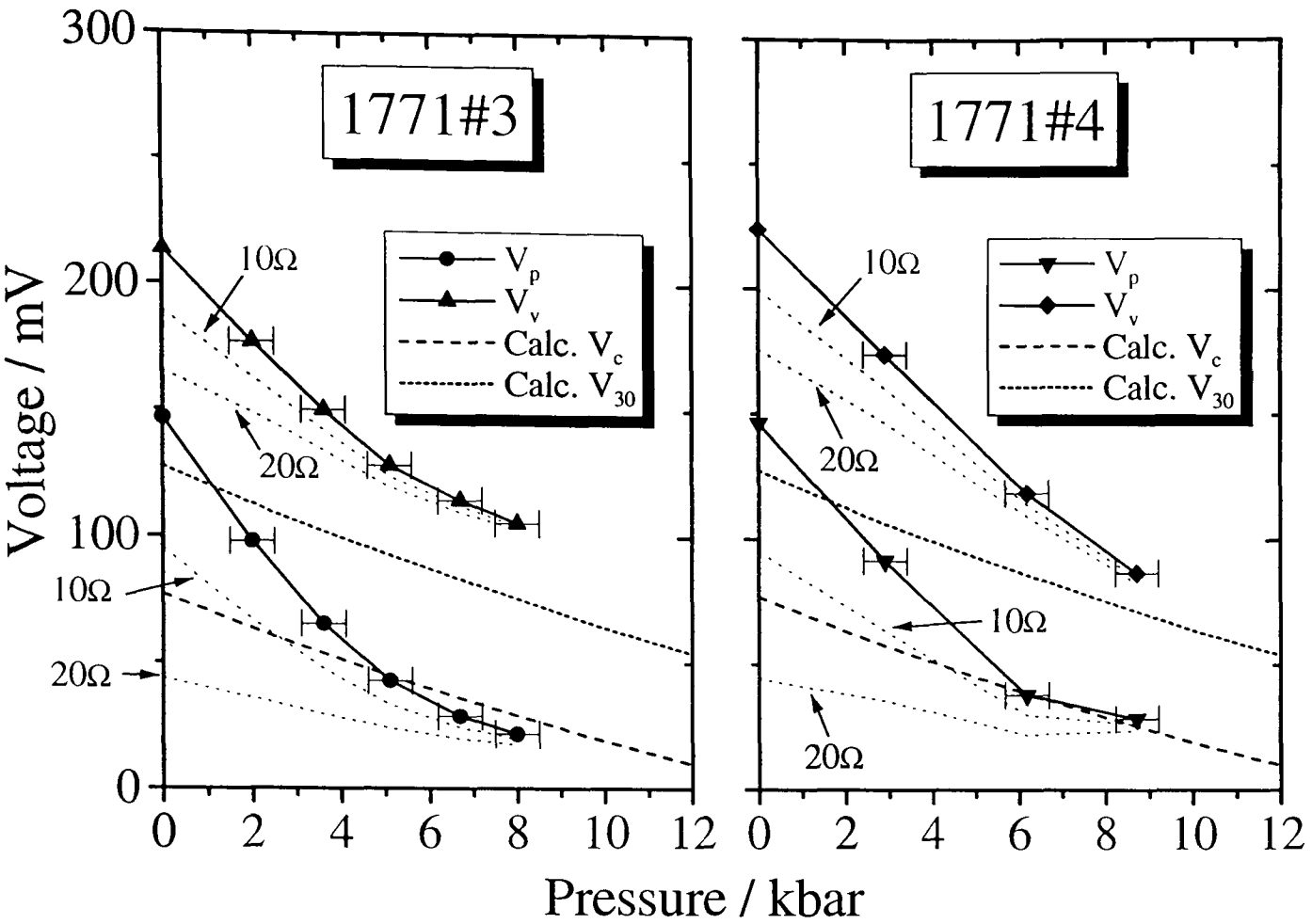


Figure 6.14. Peak and valley voltages, V_p and V_v, plotted against pressure for 1771#3 and 1771#4. The error bars indicate the ±0.5 kbar uncertainty in the manometer readings. The dashed line indicates the calculated peak voltage. The dotted lines shows how the inclusion of series resistances of 10 and 20 Ω affect the experimental data.

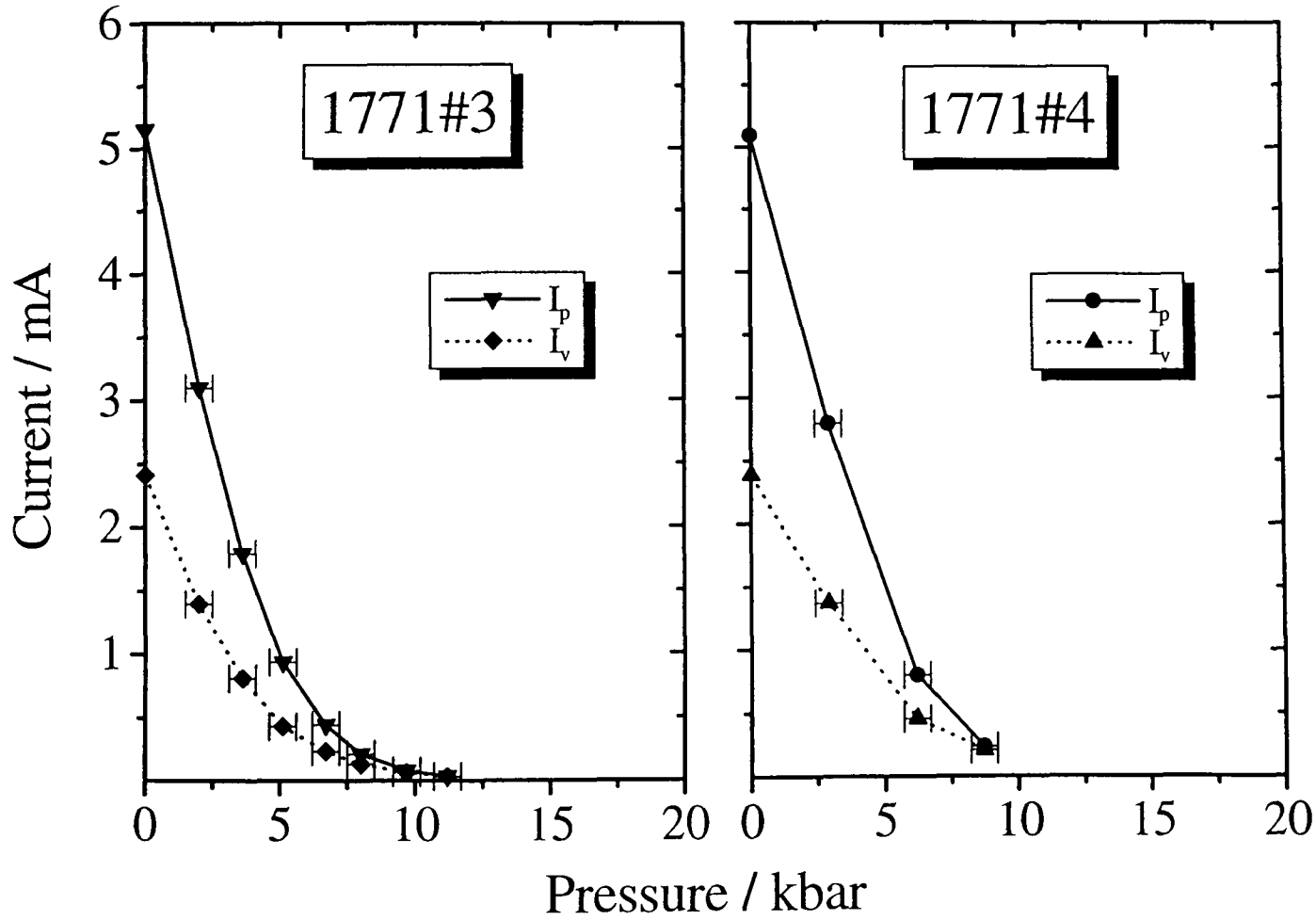


Figure 6.15. Peak and Valley currents for 1771#3 and 1771#4 versus pressure. Currents recorded above 12 kbar are small, making a clear distinction of P_c or P_d difficult.

the resonant component of the current falls to zero to $P_d \sim 16 + 3 = 19$ kbar. However, since the current is so small at these pressures, as can be seen in figure 6.15, an accurate determination of P_d for a structure with an 'InSb-like' interface is not possible.

To summarise, the pressure dependent I/V behaviour of SHETs with an 'InSb-like' interface is consistent with the vertical transport mechanism described in section 1.5.2. V_c appears to lie between V_p and V_v for all pressures if a series resistance of 20 Ω is taken into account and V_{30} follows V_v well, indicating the valley may be due to phonon emission.

6.4.2 Results for the 'GaAs - like' Interface

This section explores the pressure dependence of I/V traces in 'GaAs-like' SHETs, for which P_c has been established in section 6.3.1 as being 13 kbar. Clearly, in order for this interface to support the same conduction mechanism as the 'InSb-like' interface the resonance should disappear at a pressure no greater than 16 kbar with $V_p \rightarrow 0$ and

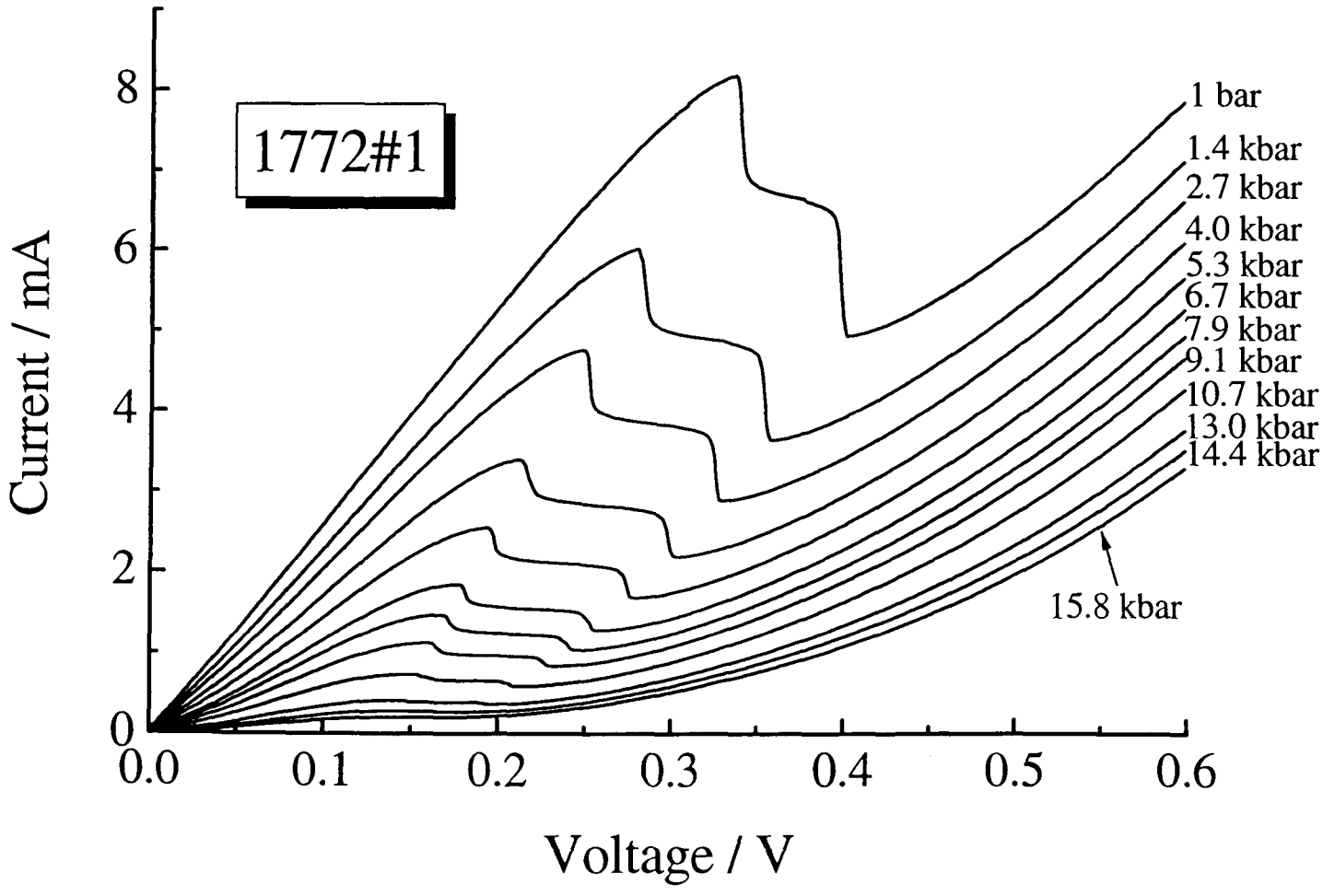


Figure 6.16. Forward bias I/V curve for 1772#1 measured at 77K for various pressures between 1 bar and 15.8 kbar.

$I_p \rightarrow 0$.

Figures 6.16 and 6.17 show I/V data for two mesas of 1772 taken at 77K and various pressures. The trend of decreasing V_p, V_v, I_p and I_v with increasing pressure appears very similar to results for the 'InSb-like' interface but the actual currents and voltages are larger.

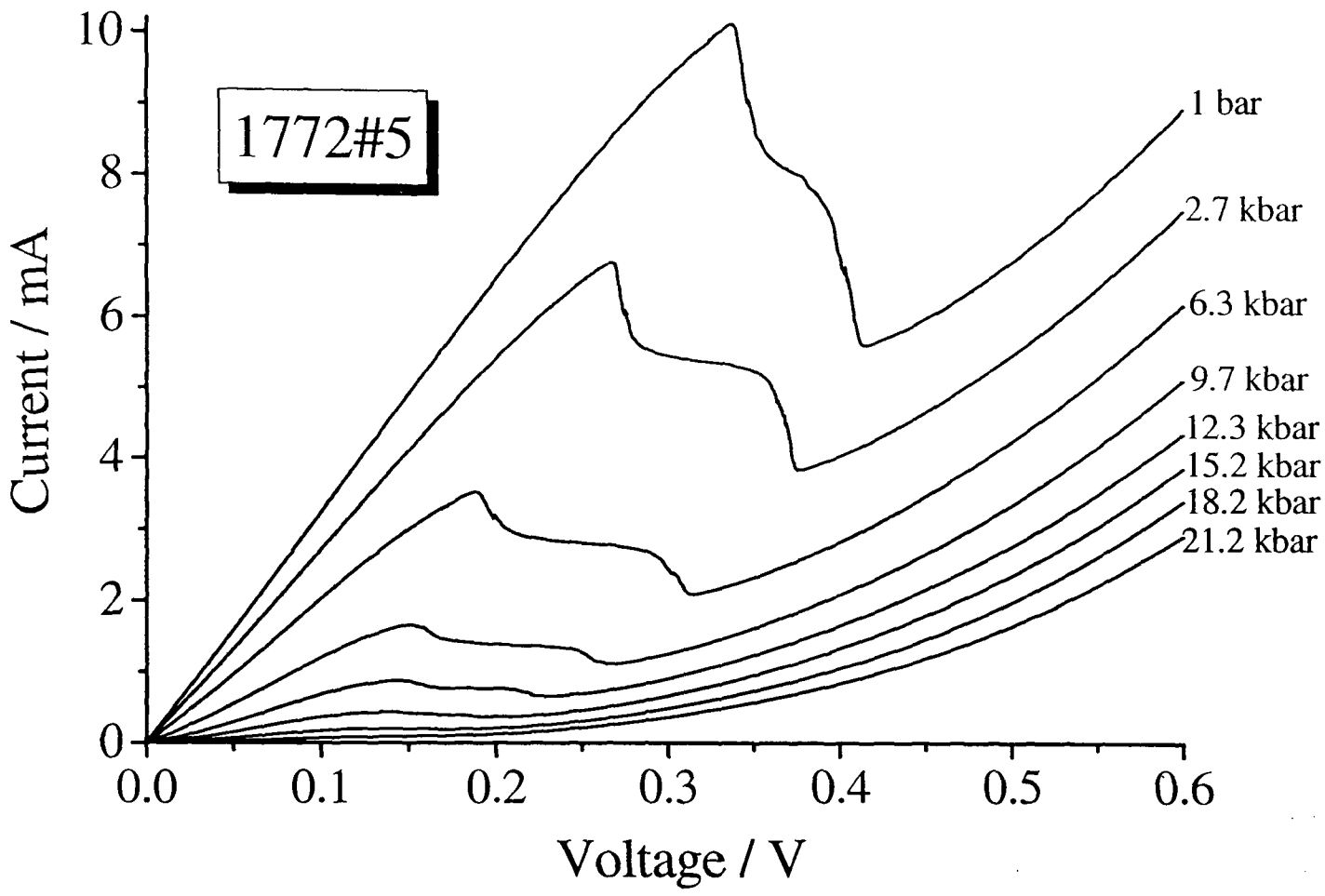


Figure 6.17. Forward bias I/V data for 1772#5 measured at 77K for pressures up to 21.2 kbar.

Peak voltages for 1772#1 and 1772#5 agree with each other to within 2%, but the peak current at 1 bar for 1772#1 is lower (at 8.199 mA) than the corresponding value for 1772#5 (at 10.194 mA). These differing peak currents can be accounted for by dissimilar active areas through inhomogenous etching. Indeed, a change in mesa radius of less than 0.5 μm could account for this discrepancy.

Figure 6.18 is a plot of high pressure I/V curves for 1772#5. Astonishingly, the forward bias I/V curve at 12.3 kbar, where $\Delta \leq 10$ meV, shows a distinct NDR which is still visible at 15.2 and 18.2 kbar - far beyond the zero band overlap situation assuming a P_c of 13 kbar. At 15.2 kbar for example, the band overlap is predicted to be approximately -20 meV and by 18.2 kbar it is close to -50 meV (all tested mesas of

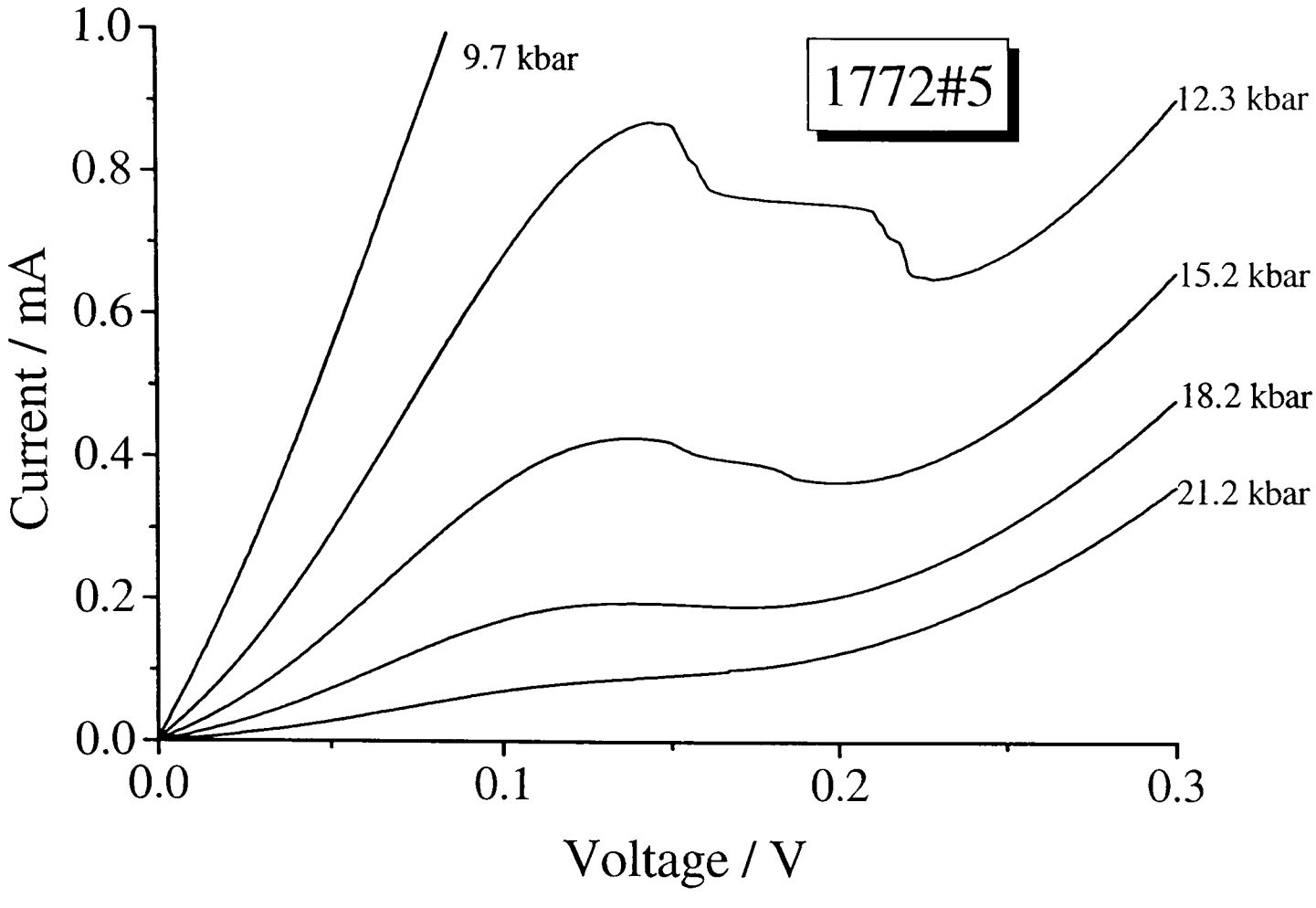


Figure 6.18. High pressure I/V plots for 1772#5 taken at 77K. The resonant feature has can still be seen at 21.2 kbar as a small hump in the I/V curve, way beyond the zero band overlap condition at $P_c = 13 \pm 0.5$ kbar.

1772 exhibited a similar response, e.g. 1772#1 at 15.8 kbar shows NDR as in figure 6.16).

The calculated variation of the 2DEG and 2DHG sub-bands with bias for a sample with a 'GaAs-like' interface is presented in figure 6.19 for the 1 bar case with a Δ of 125 meV. By 10 kbar, Δ has fallen to 30 meV and the calculated movement of electric sub-bands with bias looks as in figure 6.20. V_c in both cases occurs at a significantly lower bias than either V_p or V_v.

Figure 6.21 shows V_p, V_v and V_c plotted against pressure for the two mesas. V_p and V_v are also shown corrected for a series resistance of 10 and 20 Ω. The remarkable feature about this graph is the stark disagreement between the experimental values, in total contrast to the situation for the other interface.

Instead of decreasing to zero and vanishing as the pressure is increased as might be expected, V_p and V_v appear to saturate at 0.14 V for high pressures. Another difference between these results and those for 1771 is the currents involved at these

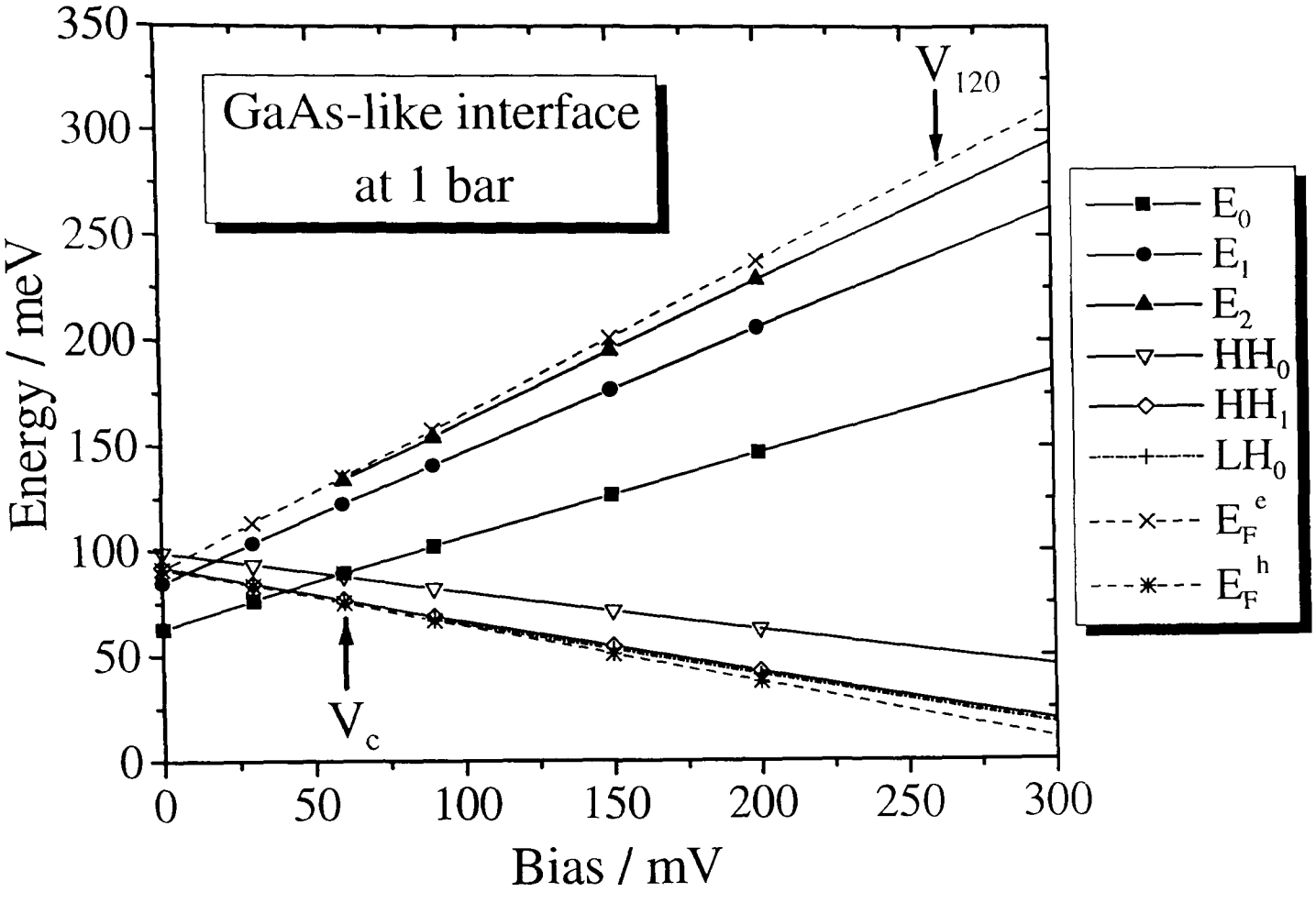


Figure 6.19. Calculated position of 2D sub-bands versus bias for a SHET with a 'GaAs-like' interface at 1 bar.

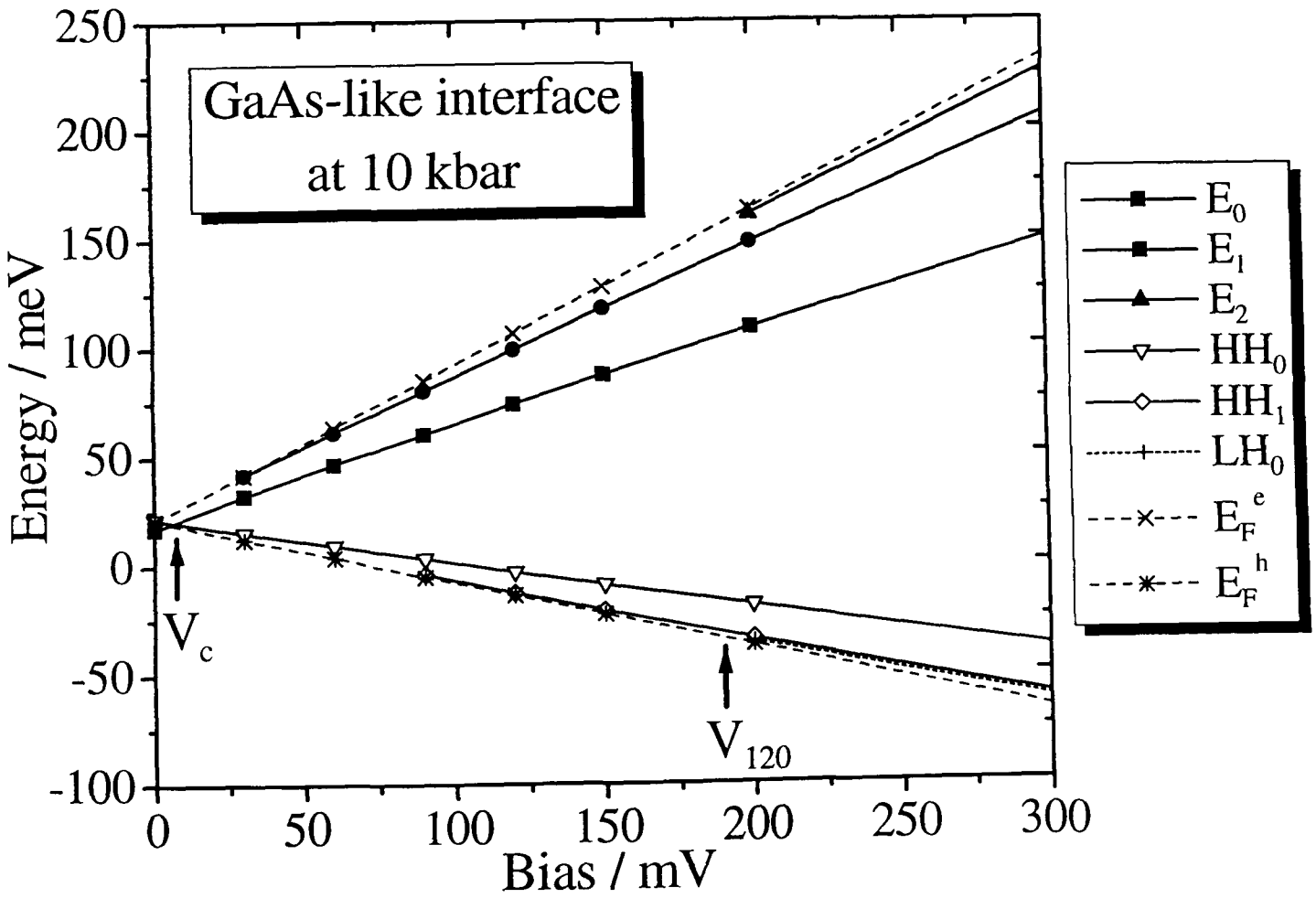


Figure 6.20. Calculated movement of 2D sub-bands with bias for a SHET with a 'GaAs-like' interface at 10 kbar.

high pressures. The peak current at 12.3 kbar for 1772#5 occurs at 0.9 mA (figure 6.18) compared to a value of less than 0.1 mA for the feature exhibited by 1771#4 at 12.7 kbar (figure 6.10) which is an order of magnitude difference.

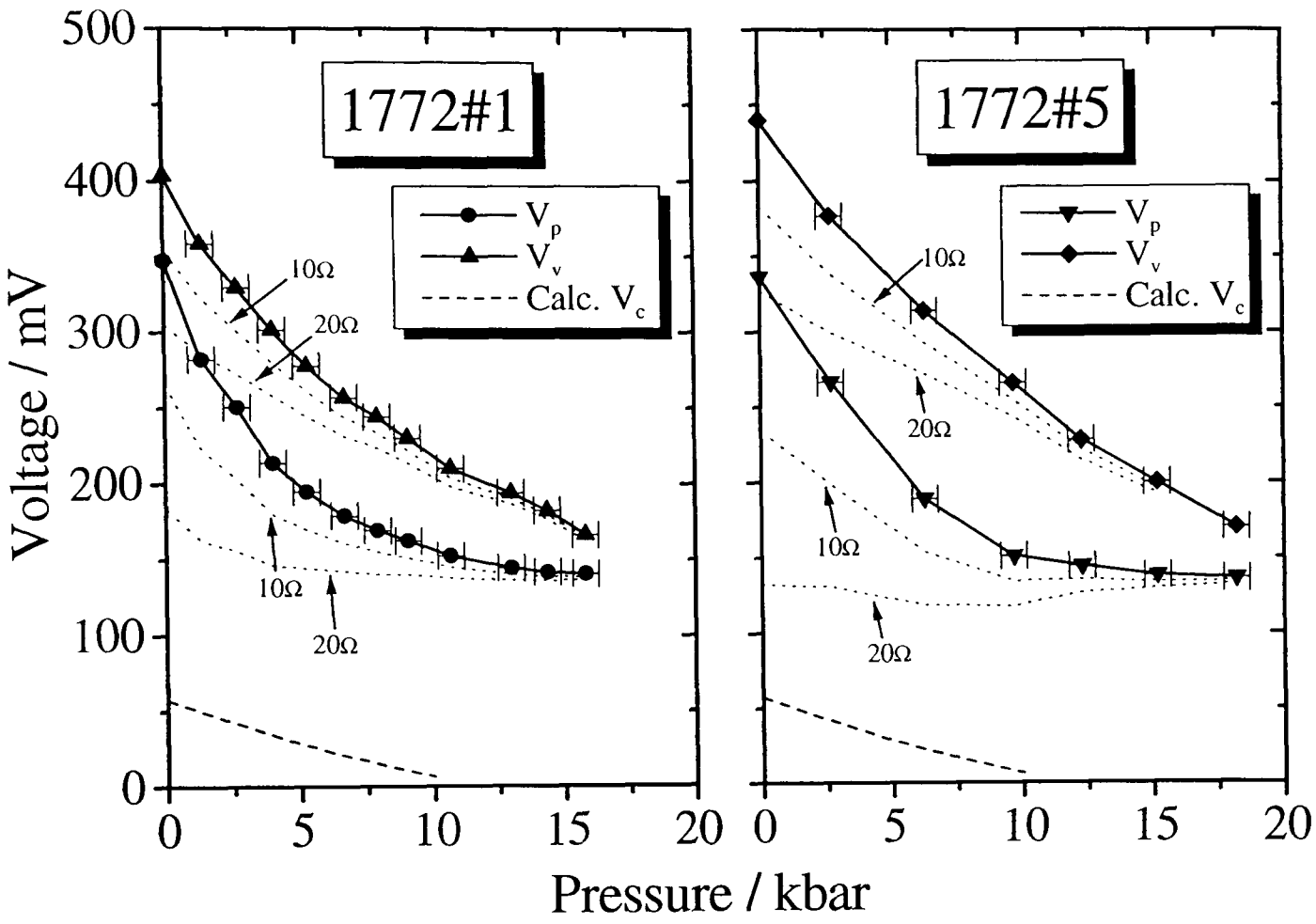


Figure 6.21. Peak and valley voltages, V_p and V_v, plotted against pressure for 1772#1 and 1772#5. The error bars indicate the ±0.5 kbar uncertainty in the manometer readings. The dashed line indicates the calculated V_c and the dotted lines shows how the inclusion of series resistances of 10 and 20 Ω affect the experimental data.

The above evidence, where :

- NDR is exhibited far beyond P_c,
- V_p and V_v appear to vanish around 0.14 V with high pressure and
- the calculated value for V_c does not fit the data,

all point to an entirely different mechanism being responsible for vertical transport in SHETs grown with a 'GaAs-like' interface than for those grown with an 'InSb-like' one. Whereas the behaviour of samples with an 'InSb-like' interface can be understood in terms of changes in the band profile as detailed in chapter 4, that of samples with a 'GaAs-like' interface cannot and an alternative explanation is needed. This is discussed further in section 6.5.2.

In summary, this is the first demonstration that simply changing the monolayer

composition of the InAs/GaSb heterointerface can drastically alter its vertical transport mechanism, and therefore its I/V trace.

6.4.3 The Background Current's Variation with Pressure

In addition to the resonant current component discussed in the previous two sections, the non resonant component also has a significant pressure dependence as figures 6.8 and 6.16 clearly demonstrate. The source of this background current is not clearly understood although the analysis in section 5.4 has shown it cannot be explained simply by thermal or tunnelling processes. The purpose of this section is therefore to document the nature of the pressure dependence of the excess current in order to further clarify its origin.

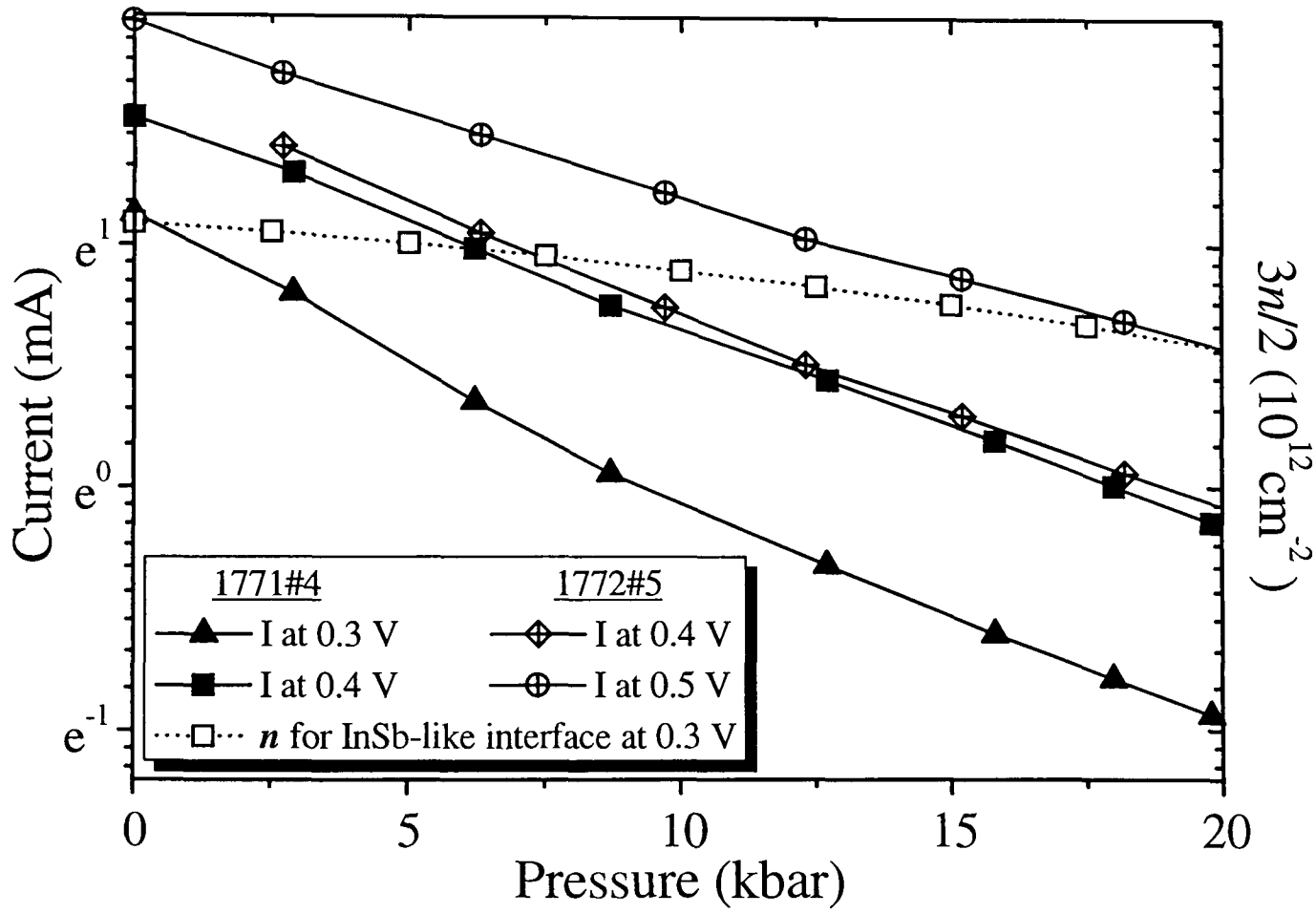


Figure 6.22. Plot of current at a fixed voltage beyond the resonance versus pressure for 1771#4 and 1772#5. Also shown is the calculated variation with pressure of the 2DEG charge density at 300 mV forward bias for a sample with an 'InSb-like' interface.

At a given bias far enough beyond the resonance, the background current for both interfaces falls approximately exponentially as the pressure is increased as shown in figure 6.22. Also plotted is the calculated variation with pressure of the 2DEG concentration n at 300 mV. Interestingly, n varies at a much slower rate than the

current, decreasing by only a small amount whilst the current decreases by one order of magnitude. The background current does not seem to scale directly with the number of electrons and holes present, so the reduction of n (and p) cannot be the dominant factor contributing to the current decrease.

One possible reason for the observed dramatic current decrease is that at a given bias, the relative energies of E_0 and HH_0 are a function of the applied hydrostatic pressure. Figure 6.23 shows this variation by plotting the calculated E_0 - HH_0 at 300 mV bias for the 'InSb-like' interface against pressure. The closest electron and hole states are almost twice the energy apart at 20 kbar compared to the 1 bar value. Whatever the dominant inelastic process is that transfers electron states into hole states giving rise to the background, it will necessarily have to be more energetic at higher pressures in order to yield the same current at the same voltage. If for example phonons are involved, it may mean a three phonon process rather than two which is less efficient. This, coupled with a slight decrease in n could be reason enough for the background current to decrease in the way that it does.

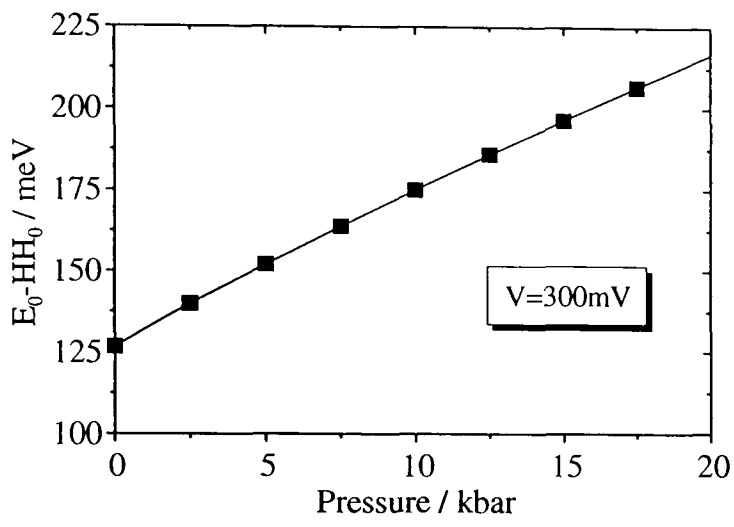


Figure 6.23. E_0 - HH_0 for the 'InSb-like' interface at 300 mV bias plotted for various pressures

If the background were due to phonon scattering, some sort of structure in the I/V trace may be expected between the two to three phonon transition for example. This is not necessarily the case though as the phonon ranges coincide. States with larger $\boldsymbol{k}_{\|}$ can start scattering using three phonons (for example) to transfer from an electron to a hole state whilst those at smaller $\boldsymbol{k}_{\|}$ still only require two, providing a smooth transition between processes.

The above explanations are qualitative, and a much more detailed study is needed in order to quantify them in any way. This section has, however, been able to demonstrate that the decrease in the non-resonant current with increasing hydrostatic pressure is entirely consistent with a rapidly increasing energy separation with

pressure between the lowest electron and highest heavy hole states.

Armed with the new information provided by the response of the forward bias resonant and non-resonant current components to pressure, the next section will attempt to elucidate upon the conduction processes for the two different interfaces.

6.5 The NDR Mechanism Revisited

Agreement between experimental I/V traces and calculations is reasonable for samples with an 'InSb-like' interface, although there are still some anomalies such as the lack of observed sub-band structure as confined electron and hole levels move past each other. 'GaAs-like' SHETs, however, have I/V curves that are not easily explained by the existing model which implies that simply changing the monolayer interface has dramatic effects on the vertical transport mechanism.

The purpose of this section is to combine all the information gained so far to clarify the SHET resonant conduction process for both interfaces. Section 6.5.1 explains the transport mechanism that gives rise to NDR in 'InSb-like' SHETs in more detail and section 6.5.2 attempts to ascertain what is actually happening to the band profile when the 'GaAs-like' SHET exhibits NDR.

6.5.1 'InSb-like' Interface

The predicted SHET resonant conduction mechanism has been introduced in section 1.5.2. The exhibited vertical transport response to pressure has provided evidence in support of this mechanism for samples with an 'InSb-like' interface. The remainder of this sub-section develops on the ideas presented in section 1.5.2 in order to provide a more complete picture of the conduction process for an 'InSb-like' SHET.

The ***k.p*** formalism [23] is often used in semiconductor physics to explore the band structure around a point of high symmetry. As such, it is particularly convenient for the system under investigation in this thesis, since it involves carrier populations in the vicinity of the Γ point. This high symmetry must also be reflected in the complete set of Γ point Bloch states, allowing them to be characterised in a very detailed

manner. Thus the Bloch states at Γ form a convenient complete set of basis states for the expansion of Bloch states close to Γ. Hence, at finite $\boldsymbol{k}$ the new Bloch states can be expressed as linear combinations of the solutions at $\boldsymbol{k} = 0$, resulting in hybrid states which have the characteristic of their constituents.

This band mixing effect occurs for example between light and heavy hole dispersions. In bulk materials, they are degenerate at $\boldsymbol{k} = 0$ and parabolic with different curvatures for small $\boldsymbol{k}$ assuming no mixing. The inclusion of coupling into the band structure calculation, however, tends to make the bands repel one another by a small amount, making them slightly non-parabolic. In a valence band quantum well, however, there may be any number of two dimensional heavy and light hole sub-bands that may all couple with each other, resulting in some dramatic effects. In the case of AlAs/GaAs/AlAs for example, coupling between the lowest light and heavy hole sub-bands actually leads to a conduction band-like dispersion for the light hole at small $\boldsymbol{k}$ as shown in figure 6.24 for a 100 Å quantum well. The dispersions for HH_0 and LH_0 are clearly very different when band mixing is included.

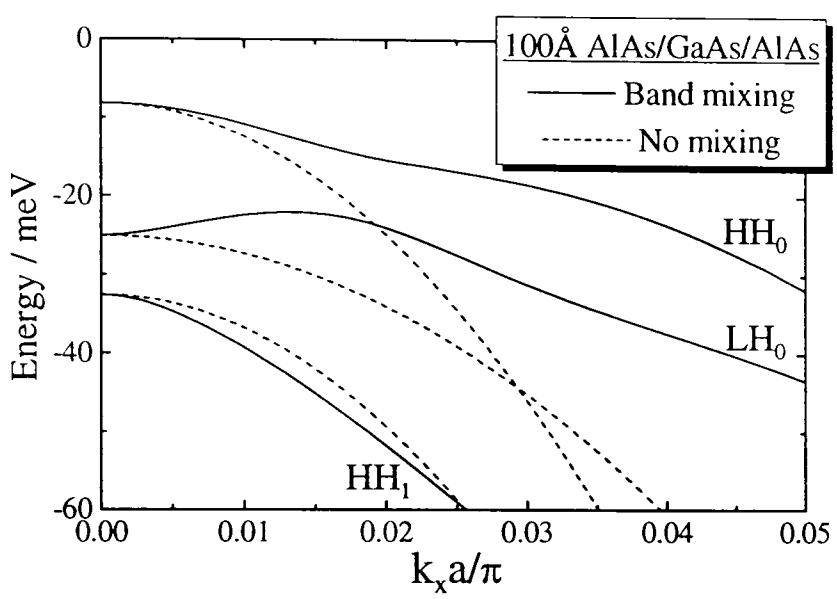


Figure 6.24. Illustration of the dramatic effects band mixing can have on the in-plane dispersions of *light* and *heavy* holes in a 100 Å AlAs/GaAs/AlAs quantum well. Courtesy of Rau [24].

The InAs/GaSb heterointerface is peculiar because electron and hole states exist in close proximity to one another so their coupling cannot be neglected. In Kane's $\boldsymbol{k.p}$ model which includes both conduction and valence band states in the Hamiltonian, the mixing between electron and *light* holes is dependent only upon k_z [25]. As this is always finite for a confined sub-band, electron and *light* hole states couple at all values of $\boldsymbol{k}_{||}$. Mixing between electron and *heavy* hole states, however, is dependent entirely upon $\boldsymbol{k}_{||}$ with a coupling that gets stronger with increasing $\boldsymbol{k}_{||}$. Since the primary mechanism for resonant conduction is thought to be electron / *heavy* hole

coupling, the remainder of this subsection focuses on mixing between these sub-bands.

Altarelli was the first to include a realistic calculation for $\boldsymbol{k}_{\|}$ into the ***k.p*** formalism to self-consistently calculate the band structure of an InAs/GaSb SL [26]. He used a three band model, the results of which did indeed show mixing of conduction-band-like and valence-band-like sub-bands for $\boldsymbol{k}_{\|}$, resulting in an anticrossing with an energy gap of ≤ 10 meV. Vaughan [27] has recently improved upon Altarelli's original work by using an 8×8 ***k.p*** formalism. The structure he modelled that is closest in character (dimensions) to a SHET is a 300 Å GaSb / 900 Å InAs SL in which the in-plane mixing effects are found to be quite strong at finite $\boldsymbol{k}_{\|}$. Additionally, *heavy* / *light* hole repulsion pushes the latter down in energy such that (at zero bias) it lies significantly below the Fermi level and is therefore unpopulated (with holes). These results also show the existence of wavefunctions that have significant probability densities on both sides of the interface, confirming electron / *heavy* hole coupling at finite $\boldsymbol{k}_{\|}$ is a possible method of electron / hole transfer.

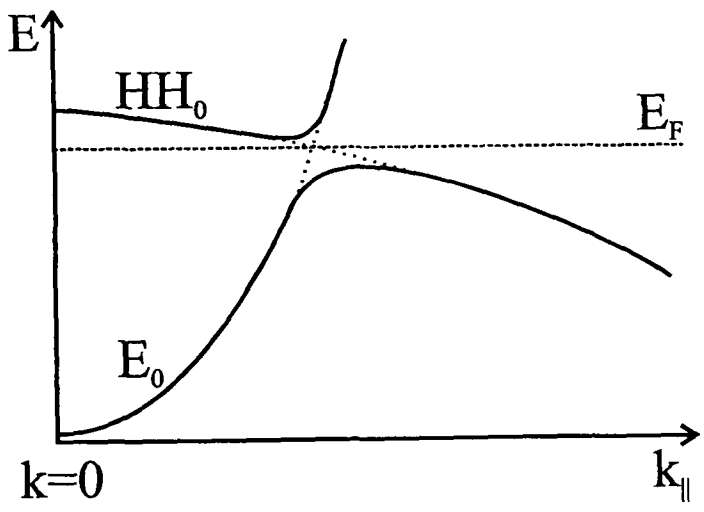


Figure 6.25. Schematic illustration showing the result of mixing between E_0 and HH_0 on the in-plane dispersions of a SHET using a simplified two sub-band model.

In order to further explain the transport mechanism, a very simplified two sub-band picture of the SHET will be used as this contains the relevant physics if not the actual complexity of the problem. The zero bias in-plane dispersions for E_0 and HH_0 are shown in figure 6.25. Here the normalised eigenvectors at $\boldsymbol{k}_{\|} = 0$, ϕ_1 and ϕ_2 form the basis for the expression of states at finite $\boldsymbol{k}_{\|}$. If the bands are allowed to couple, the result is two new eigenvectors Ψ_1 and Ψ_2, where :

$$\Psi_1 = A\phi_1 + B\phi_2$$
$$\Psi_2 = A\phi_1 - B\phi_2 \qquad \textbf{(6.1)}$$

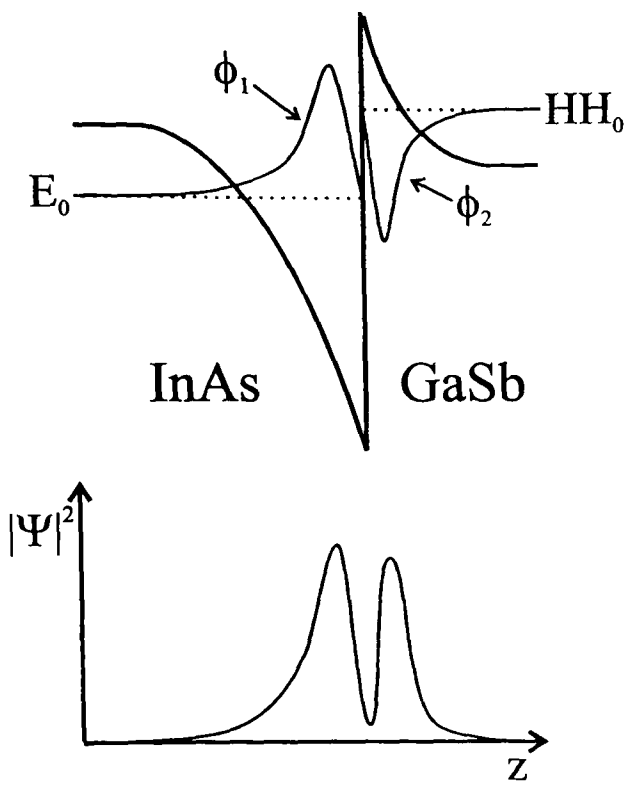


Figure 6.26. Wavefunctions ϕ_1 and ϕ_2 form the basis states for the coupled probability distribution $|\Psi|^2$, shown for a $k_{\|}$ value in the region of anticrossing.

and the coefficients *A* and *B* simply determine the contribution from each basis. In the region of anticrossing, *A* and *B* are such that the new eigenvectors have a significant spatial extension on both sides of the interface (figure 6.26). When biased it is these states that can participate in charge transport across the interface, yielding a current.

As the bias is increased the confinement energies E_0 and HH_0 increase such that without the inclusion of mixing, the two dispersions cross at a smaller $k_{\|}$. The strength of electron / *heavy* hole coupling however, decreases with decreasing $k_{\|}$, so an increasing bias tends to decrease the mixing. Another effect that increasing the bias has is to increase *n* and *p*. Thus, the elastic proportion of the current from a SHET is the net result of a competition between an increasing charge concentration and less efficient electron / *heavy* hole coupling.

To explain the data completely both elastic and inelastic contributions to the current must be considered. While elastic processes will dominate at low bias, inelastic ones will become significant as occupied electron/hole separations become comparable with phonon energies. These inelastic processes can involve phonons coupling electrons and holes directly or via intermediate impurity states. Consider the low temperature (4K) plots for samples with an 'InSb-like' interface. They have a distinctive shape which can be split into roughly 5 stages:

1) an initial region of high resistance;

2) an approximately monotonic current increase;

3) the current increases less as the voltage is increased;

4) a region of NDR;

5) the current starts increasing slowly.

In stage 1, the zero bias mismatch in the electron/hole Fermi wavevectors (see section 5.3.2.1) can account for the initial region of high resistance. This is because poor overlapping of electron/hole states at zero bias inhibits elastic processes from contributing to the current. Inelastic processes such as phonons are likewise inhibited because of the lack of occupied electron states that are a sufficiently high energy above occupied hole states.

As the bias is increased (stage 2), the Fermi wavevector mismatch is reduced until occupied electron and heavy hole states exist at the same $k_{\|}$, and a current due to the elastic processes described above can flow. This happens at the same time as an increase in the current contribution from inelastic processes such as phonons. As the energy difference between occupied electron states and occupied heavy hole states increases, so do the number of possible inelastic phonon scattering events. This increase will continue until the number of events saturates due to constraints of energy and wavevector conservation (this is only true well below V_c, but when the bias exceeds the phonon energy). This combination of elastic and inelastic current contributions is quite consistent with the initial shape of the low temperature I/V trace.

By stages 3 and 4, where the bias has been increased further, the electron/heavy hole coupling has become less efficient (as mentioned above) and so the contribution to the current from elastic processes gradually diminishes and falls to zero by V_c. The inelastic current component eventually starts to decrease in this bias region also, due to a fall in the number of scattering processes. Eventually, the bottoms of the last electron and heavy hole sub-bands are a phonon energy apart, after which this single phonon process is no longer available to contribute to the current. Two phonon events and processes in which impurities act as intermediate states, however, may already have begun by this stage and are available to contribute to the current. Stage 5 is, therefore, a consequence of increasing electron and hole concentrations with increasing bias.

The above analysis suggests that V_p occurs sometime before V_c, and that inelastic processes can contribute to the current over a bias range that extends beyond V_c. In

addition, this proposed mechanism for the I/V characteristic is able to explain why no features are seen in the characteristic or in dI/dV as the individual sub-bands move past each other (E_1 moving past HH_0 for example) since the conduction for any pair of bands smoothly increase and then decreases.

Figure 6.24 shows a significant deviation from the parabolic dispersion for HH_0 and LH_0 in the AlAs/GaAs quantum well of up to 20 meV at 4% of the Brillouin zone. Clearly, it is possible that the SHET in-plane dispersions may also exhibit dramatic departures from the parabolic case and detailed calculations including the effects of an applied bias need to be performed in order to fully analyse the I/V trace.

Note that Ting et al. [28] established that in order to calculate realistic vertical transport I/V traces for certain *interband* transport structures, it is necessary to include electron / *heavy* hole coupling. Yang and Xu [29] then demonstrated the inadequacy of the two band model (electrons and *light* holes) in the explanation of vertical transport in InAs/GaSb SHETs.

6.5.2 'GaAs-like' Interface

P_c for a SHET with a 'GaAs-like' interface has been established as 13 kbar in section 6.3.1 which is consistent with a band overlap of 125±5 meV [7]. The smaller band overlap needs less initial charge recombination in order to keep the Fermi level continuous across the interface, and should therefore have a smaller zero bias 2DEG and 2DHG concentration. As $\Delta = E_0 + E_F^e + E_F^h + HH_0$ at zero bias where E_F^e and E_F^h are the electron and hole Fermi energies respectively, the smaller band overlap implies E_0 and HH_0 are closer together than would be the case for a larger Δ. This in turn means smaller values for V_p and V_v are expected. In reality, however, V_p and V_v are much larger for this interface than the 'InSb-like' one.

Additionally, I_p and I_v are consistently much larger, the NDR is less temperature dependent (section 5.3) and the initial region of high resistance spans a greater voltage than for the 'InSb-like' interface (section 5.3.3).

By far the strangest phenomenon and the one that proves conclusively that the 'GaAs-like' interface supports a different conduction mechanism to the 'InSb-like' one is the

exhibition of a significant region of NDR far beyond P_c, when $\Delta \leq 0$.

Figure 6.27 shows the peak and valley voltages for 1772#1 corrected for series resistances of 10 and 20 Ω, together with two additional calculated biases V_{120} and V_{140}. These are the voltages at which E_0 and HH_0 are separated by 120 and 140 meV respectively. They show remarkably similar trends with pressure to the valley voltage, where the high pressure values saturate at around 140 meV.

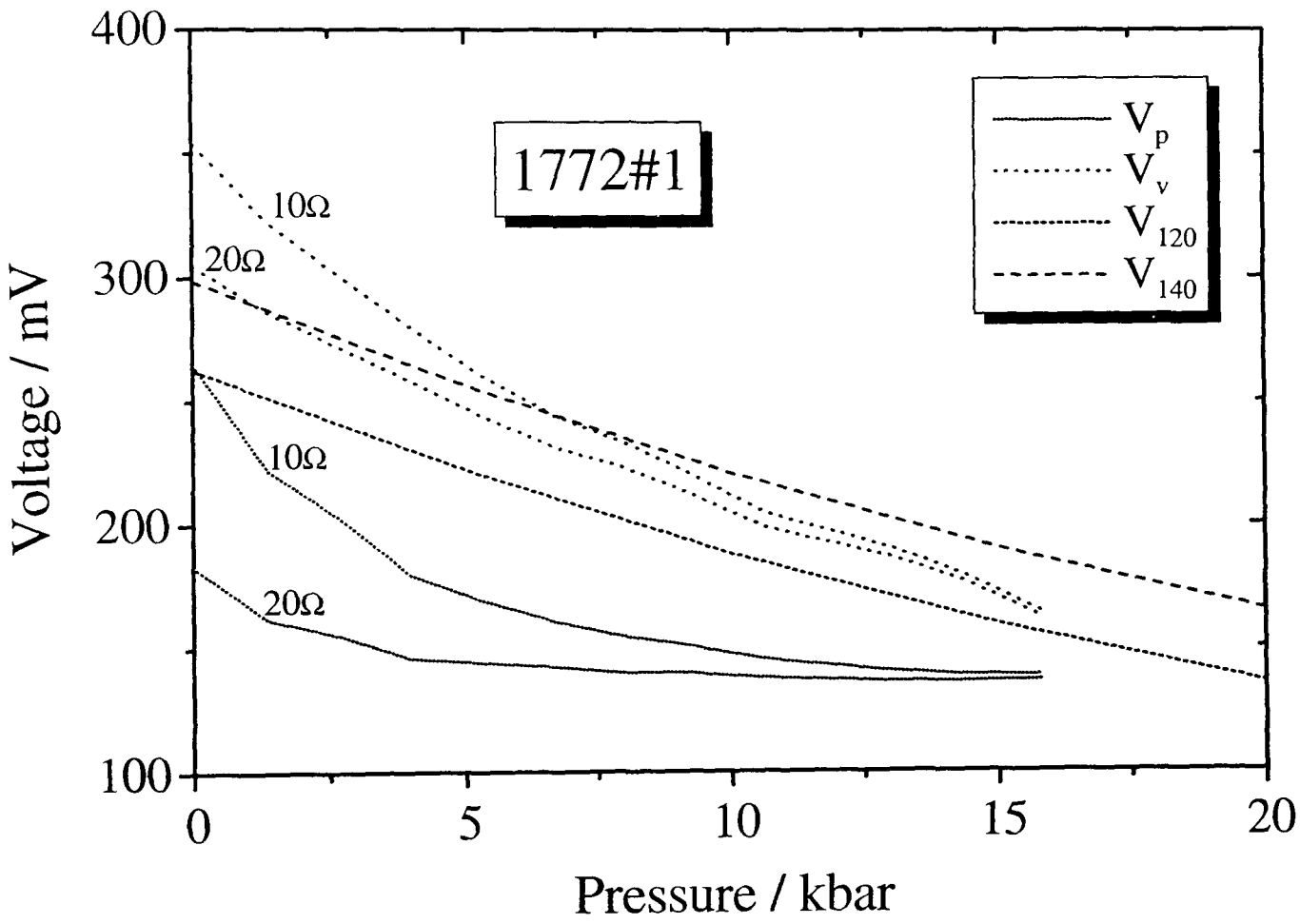


Figure 6.27. A comparison of the peak and valley voltages for 1772#1 corrected for a series resistance of 10 and 20 Ω and the calculated biases V_{120} and V_{140}. These represent the bias at which E_0 and HH_0 are separated by 120 and 140 mV respectively.

The bizarre conclusion is that SHETs with a 'GaAs-like' interface exhibit behaviour consistent with an NDR occurring when E_0 and HH_0 are greater than 100 meV apart, although an explanation of why this process should dominate over the predicted electron / *heavy* hole coupling is not an easy question to answer. This is investigated further in chapter 7 where the I/V response of the SHETs to a magnetic field should yield additional information to support or contradict this.

6.6 Summary

Reverse bias measurements indicate a P_c of 16 kbar for samples with an 'InSb-like' interface, whereas samples with a 'GaAs-like' interface have one of 13 kbar. These values are consistent with a 1 bar band overlap of 155±5 meV and 125±5 meV for each interface respectively and $d\Delta/dP$ of -9.5±5 meV/kbar, obtained by Daly et al. using parallel transport measurements on SLs from the same reactor.

In forward bias, V_p, V_v, I_p and I_v for the 'InSb-like' interface move towards zero as the pressure is increased. The resonant component of the current vanishes before approximately 18 kbar. Calculations show V_c occurs shortly after V_p when the experimental trace is corrected for a series resistance of 20Ω. V_v then corresponds to an E_0 - HH_0 of slightly more than one phonon energy. Hence, the origin of the current is consistent with a competition between increasing *n* and *p* and decreasing electron / *heavy* hole coupling.

The 'GaAs-like' interface does not behave so predictably under forward bias. Instead, a clear resonance is visible well after Δ has fallen to zero and the NDR occurs at a much higher bias than expected. The pressure dependence of the peak and valley voltages are consistent with the resonance occurring when E_0 - HH_0 is between 120 and 140 meV. Consequently, this interface must support a very different conduction mechanism to that exhibited by the 'InSb-like' one.

Additionally, the background current is not directly dependent upon *n* and *p*, but may also be a function of E_0 - HH_0.

6.7 References

[1] See for example, "Proceedings of High Pressure in Semiconductor Physics VI" Vancouver, Canada, August 7-11 (1995).

[2] The change in band structure is only completely reversible if the elastic limit of the material is not breached. See "Physical Properties of Crystals" by J F Nye. Oxford University Press, Oxford (1985).

Continued ...

References Continued ...

[3] D J Wolford T F Kuech, J A Bradley, M A Gell, D Ninno & M Jaros. Journal of Vacuum Science & Technology **B** 4, p1043 (1986).

[4] R Zallen & W Paul. Physical Review 155, p703 (1967).

[5] J F Tsay, S S Mitra & B Bendow. Physical Review **B** 10, p1476 (1974).

[6] R A Noack & W B Holzapfel. Solid State Communications 28, p177 (1978).

[7] M S Daly, D M Symons, M Lakrimi, R J Nicholas, N J Mason & P J Walker. Proceedings of International Conference on EP2DSXI, Nottingham, England, p165 (1995).

[8] D M Symons, M Lakrimi, R J Warburton, R J Nicholas, N J Mason, P J Walker, M I Eremets & G Hill. Physical Review **B** 49, p16614 (1994).

[9] G A Sai-Halasz, L L Chang, J-M Welter, C-A Chang & L Esaki. Solid State Communications 27, p935 (1978).

[10] G J Gualtieri, G P Schwartz, R G Nuzzo, R J Malik & J F Walker. Journal of Applied Physics 61, p5337 (1987).

[11] J Beerens, G Grégoris, J C Portal, E E Mendez, L L Chang L Esaki. Physical Review **B** 36, p4742 (1987).

[12] W A Harrison & J Tersoff. Journal of Vacuum Science and Technology **B** 4, p1068 (1986).

[13] C G Van de Walle & R M Martin. Journal of Vacuum Science and Technology **B** 4, p1055 (1986).

[14] R G Dandrea, C B Duke & A Zunger. Journal of Vacuum Science and Technology **B** 10, p1744 (1992).

[15] Y Foulon and C Priester. Physical Review **B** 45, p6259 (1992).

[16] J R Waterman, B V Shanabrook, R J Wagner, M J Yang, J L Davis & J P Omaggio. Semiconductor Science and Technology 8, pS106 (1993).

[17] S Holmes, W T Yuen, T Malik, J S Chung, A G Norman, R A Stradling, J J Harris, D K Maude & J C Portal. Journal of Physics and Chemistry of Solids 56, p445 (1995).

[18] J R Meyer, C A Hoffman, B V Shanabrook, B R Bennett, R J Wagner, J R Waterman & E R Youngdale. Proceedings of ICPSXXII, Vancouver, Canada, August 15-19, Volume 1, p783

Continued ...

References Continued ...

(1994).

[19] D M Symons. DPhil thesis, p95 (1994).

[20] L A Hemstreet, C Y Fong & J S Nelson. Journal of Vacuum Science and Technology **B** 11, p1693 (1993).

[21] L M Claessen, J C Maan, M Altarelli, P Wyder, L L Chang & L Esaki. Physical Review Letters 57, p2556 (1986).

[22] C G Van de Walle. Physical Review **B** 39, p1871 (1989).

[23] E O Kane. Article in Handbook on Semiconductors Volume 1. North Holland Publishing Company, Amsterdam, p193 (1982).

[24] Private Communication.

[25] The Kane Hamiltonian can be found in "Wave Mechanics Applied to Semiconductor Heterostructures" by G Bastard. Les Éditions de Physique, Paris, p43 (1992).

[26] M Altarelli. Physical Review **B** 28, p842 (1983).

[27] T A Vaughan. Private Communication.

[28] D Z-Y Ting, E T Yu & T C McGill. Applied Physics Letters 58, p292 (1991).

[29] R Q Yang & J M Xu. Journal of Applied Physics 72, p4714 (1992).

7 Magnetic Field Measurements

7.1 Introduction 137

7.1.1 Electrons in a Magnetic Field 138

7.2 Field Perpendicular to the Interface 140

7.2.1 'InSb - like' Interface 143

7.2.2 'GaAs - like' Interface 148

7.3 Field Parallel to the Interface 152

7.3.1 'InSb - like' Interface 153

7.3.2 'GaAs - like' Interface 155

7.4 Summary 156

7.5 References 157

7.1 Introduction

The behaviour of electrons when exposed to an applied magnetic field is a phenomenon that has been used for many years in industrial manufacture (microwave ovens for example). This same field induced electron effect also provides the physicist with an invaluable method for probing the electronic structure of semiconductor systems. As a consequence, experiments such as Shubnikov de Haas and cyclotron resonance have become standard methods of determining physical properties such as carrier effective masses. A further enhancement to its role in bulk materials is the effect a magnetic field can have on the optical and electrical performance of a heterostructure. This can readily be exploited to study the confined 2DEG and/or 2DHG.

The antimonide family of heterostructures has been investigated using magnetotransport and magneto-optical techniques with varying degrees of success (see section 6.3.2 for example). The few studies into their vertical transport characteristics have shown a drastic variation in the I/V trace as a field is applied. Mendez et al. [1,2] for example were able to observe individual Landau level resonances for a GaSb/AlSb/InAs/AlSb/GaSb interband resonant tunnel structure with a magnetic field applied perpendicular to the interface.

As yet there is no published paper on the magnetic field induced reaction of the SHET I/V characteristic, so this chapter constitutes the first report on vertical transport in excellent quality single interface structures under applied magnetic fields. This data is especially useful and relevant to the contents of the rest of this thesis as it is capable of providing further information about the SHET resonant conduction mechanism and any interface dependent differences.

As a direct result of the measurement of SHET I/V characteristics from structures placed in magnetic fields with their orientation both perpendicular and parallel to the interface, it has been possible to verify that the observed NDR occurs after V_c, where the last populated electron and hole sub-bands (or their lowest Landau levels) have moved past each other. Additionally, the data confirms the differing conduction

mechanisms supported by the two interfaces. The 'InSb-like' SHET reacts in a slightly more predictable manner to a magnetic field than the 'GaAs-like' one, a trend which is similar to the pressure behaviour. Detailed calculations are needed, however, in order to fully understand the I/V behaviour and so this chapter will concentrate on presenting the observed trends, some of which are very unexpected.

DC fields up to 15 T and pulsed fields up to 40 T were used to obtain the I/V plots, all of which were measured at 1 bar and 4K. Section 7.2 starts the analysis in this chapter by discussing what effect a magnetic field applied perpendicular to the sample interface might have on the zero bias energy distribution of the 2DEG and 2DHG, followed by the expected modification this change in 2DEG/2DHG energy distribution should induce in the I/V behaviour. The remainder of the section contains data from actual measurements on samples with either interface and a short discussion about the observed I/V plots.

Section 7.3 contains results from I/V runs where the magnetic field is applied parallel to the sample interface. It introduces some of the basic concepts, but mainly serves to provide additional evidence of the different responses of the two interface types to external stimuli such as magnetic field, temperature and pressure. Section 7.4 contains a short summary of the chapter's main findings.

Before the analysis, however, a short introduction to the behaviour of electrons in a magnetic field is needed, and this is provided in section 7.1.1.

7.1.1 Electrons in a Magnetic Field

Assuming an isotropic, parabolic energy band, the single particle time independent Schrödinger equation in the presence of a magnetic field can be written :

$$\frac{1}{2m^*}\left(\frac{\hbar}{i}\nabla - eA\right)^2 \Psi = E\Psi \qquad (7.1)$$

where A is the vector potential [3]. Writing this in the gauge $A=(0,Bx,0)$ so the magnetic field B is applied along z results in a Hamiltonian that does not involve y or z explicitly. After separation of variables the wavefunction can be written :

$$\Psi(x,y,z) = \exp\{i(\beta y + k_z z)\}u(x) \tag{7.2}$$

where β is a constant. This leads to motion in the x-y plane described by :

$$-\frac{\hbar^2}{2m^*}\frac{\partial^2 u(x)}{\partial x^2} + \frac{1}{2}m^*\left(\frac{eB}{m^*}x - \frac{\hbar\beta}{m^*}\right)^2 u(x) = E' u(x) \tag{7.3}$$

which has eigenvalues of the form :

$$E' = \left(q + \frac{1}{2}\right)\hbar\omega_c, \tag{7.4}$$

where $\omega_c = eB/m^*$ and q is an integer. Inspection of equation 7.2 reveals the z dependent wavefunction to be unchanged from that of the free electron, with $E_z = \hbar^2 k_z^2/2m^*$. Hence, the field quantizes the motion of the electron gas in the plane normal to B leading to Landau levels (equation 7.4), and leaves it unchanged along B's axis. The quantizing of the motion normal to B effectively changes the density of states from a continuous distribution to one of a discrete set of δ functions, each with a density of states equal to $2eB/h$ (including spin degeneracy).

Additional splitting occurs due to the spin, leading to a total electron energy of :

$$E = E_z + \left(q + \frac{1}{2}\right)\hbar\omega_c \pm \frac{1}{2}g^*\mu_B B \tag{7.5}$$

where g^* is the effective gyromagnetic ratio which is equal to 2 for the free electron, and $\mu_B = e\hbar/2m_0$ is the Bohr magneton.

The conduction band of bulk materials can usually be approximated as having a parabolic dispersion about the Γ point. For any field, therefore, equation 7.5 suggests a new conduction band dispersion results which is quantized in the plane perpendicular to B. Due to the influence of other bands, however, values for g^* can differ significantly from that of the free electron - InSb for example has a g^* equal to -51 [4].

Bulk valence band Landau Levels on the other hand have a permanently mixed character since $\boldsymbol{k}$ is always finite in a magnetic field and the coupling between light, heavy and split-off hole states can be large. Thus, in order to determine the movement

of valence band Landau levels with field it is necessary to include the relevant mixing potentials in a full or partial band structure calculation, as simple approximations no longer produce good results.

For confined quasi-two dimensional (2D) systems the effects of a magnetic field are dependent upon field orientation. If it is applied perpendicular to the interface, the 2D gas has its in-plane dispersion quantized. Any other orientation, however, introduces far more complicated combined electrical and magnetic quantization effects.

Thus in the case of the SHET, the application of a magnetic field can be expected to alter the 2DEG and 2DHG distributions. This has implications for the vertical transport characteristics, the predicted effects for which are described in the following sections and compared with experimental data. Both interface types for perpendicular (section 7.2) and parallel (section 7.3) field orientations are considered.

7.2 Field Perpendicular to the Interface

It is clear from the analysis presented in section 7.1.1 that a magnetic field applied perpendicular to a SHET interface ($B_\perp$) will result in quantization of the 2DEG into discrete Landau levels with a spacing proportional to B. For low fields where the spin splitting term is small, electron energies of the form :

$$E^i = E_z^i + \left(q + \frac{1}{2}\right)\hbar\omega_c^e \qquad \textbf{(7.6)}$$

result, where i is the sub-band index and the cyclotron frequency $\omega_c^e = eB/m_e^*$. Consider the zero bias situation. At low fields there are many closely spaced Landau levels each with a density of states $D(E) = 2eB/h$. As the field is increased the density of states of each level increases which means more charge can populate the lower levels and the highest occupied level should depopulate as it moves through the Fermi energy. The lowest Landau level (q=0) for the 2DEG (E_0^0) lies ½$\hbar\omega_c^e$ above E_0. This is split into spin-up and spin-down components, so in the case of InAs the lowest spin-split level is an energy ½$\hbar\omega_c^e - ½|g^*|\mu_B B$ above E_0 and has a density of states

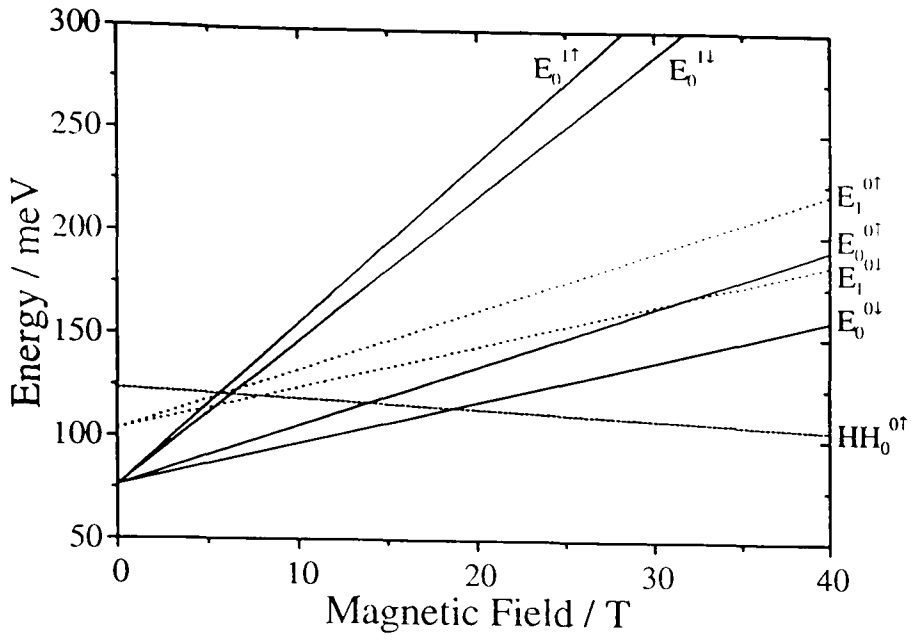


Figure 7.1. Schematic representation of the movement of Landau Levels with field for an 'InSb-like' SHET at zero bias, assuming a constant electron/hole concentration and no mixing.

equal to eB/h. This lowest spin-split Landau level will be represented by the symbol $E_0^{0\downarrow}$ since g^* is negative for electrons in the InAs conduction band, making the spin down level lowest in energy.

A similar Landau quantization of the 2DHG density of states occurs, but because of the mixing of valence band states as mentioned earlier the picture is not as simple as for the 2DEG. Vaughan [5] has calculated the movement of electron, heavy and light hole levels with a magnetic field applied perpendicular to the interface for InAs/GaSb multiple quantum well structures using an 8×8 ***k.p*** formalism. As the field is increased LH, HH_0 and HH_1 Landau levels mix making a simple analysis, as in the case of the electrons, very difficult. What is evident, however, is that the lowest spin-split Landau level for HH_0 ($HH_0^{0\uparrow}$) moves approximately linearly with field at a rate of -0.47 meV/T regardless of structure periodicity.

Hence, in the simple picture as the field is increased the number of occupied electron Landau levels decreases, together with a general decrease in the total number of occupied hole Landau levels.

Figure 7.1 shows the projected movement of the Landau levels for an 'InSb-like' SHET with field, assuming a constant electron/hole concentration and no mixing. It reveals that $E_0^{0\downarrow}$ and $HH_0^{0\uparrow}$ should cross at around 18T. In reality, however, the 2DEG and 2DHG are part of a dynamic system so n and p are constantly adjusting. In the quantum limit where only $E_0^{0\downarrow}$ and $HH_0^{0\uparrow}$ are occupied, the two spin-split levels should pin together at the Fermi energy. Any increase in field will tend to push $E_0^{0\downarrow}$ above $HH_0^{0\uparrow}$. Hence in order to preserve the continuity of the Fermi level across the interface, electrons must recombine with hole states, thus decreasing n and p.

Consequently E_0 and HH_0 become smaller, allowing $E_0^{0\downarrow}$ and $HH_0^{0\uparrow}$ to pin together once more. This continues until n and p fall to zero at the magnetic field induced semimetal to semiconductor transition B_c.

Figure 7.2 is a schematic representation of the SHET band profile at B_c, illustrating that the sum of $E_0^{0\downarrow}$ and $HH_0^{0\uparrow}$ must equal Δ at this critical field since E_0 and HH_0 are zero. Using this information, an expression of the form :

$$B_c = \frac{2\Delta m^*_{e,\parallel} e}{\hbar e - \left|g^*\right| \mu_B m^*_{e,\parallel} + 9.4\times10^{-4} m^*_{e,\parallel} e} \tag{7.7}$$

can be derived for B_c where μ_B is the Bohr magneton, g^* is the effective electron gyromagnetic ratio and Δ is in electronvolts. In the quantum limit of one occupied spin-split Landau level, $g^* \sim -15$, for InAs yielding an estimate for B_c for an 'InSb-like' SHET of 61T, and for a 'GaAs-like' one of 49T. It must be stressed that these values are merely good estimates which are used in the absence of detailed self-consistent calculations including potentially significant effects such as band non-parabolicity and heavy/light hole mixing.

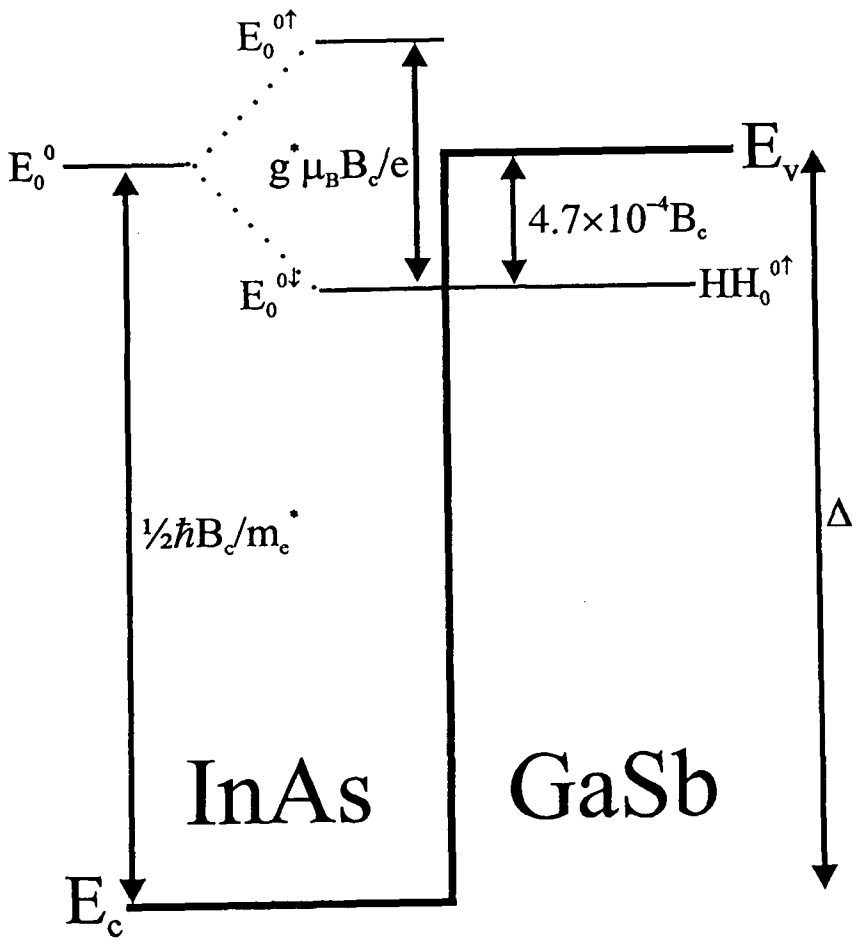


Figure 7.2. Schematic representation of the SHET band profile at the magnetic field induced semimetal to semiconductor transition B_c. All values are in electron-volts.

When a bias is applied in the presence of small $B_\perp$, n and p and therefore E_0 and HH_0 increase as is the case without $B_\perp$. Now, however, the 2DEG and 2DHG are quantized into discrete Landau levels and so one might expect many mini resonances as these levels move past each other. Additionally, at high fields where only $E_0^{0\downarrow}$ and $HH_0^{0\uparrow}$ are occupied, a decrease in peak current with increasing

magnetic field might be expected as n and p decrease. Also, as the resonant conduction mechanisms appear to be interface dependent, further differences between the I/V traces of 'InSb-like' and 'GaAs-like' SHETs may yield more information about the reason for this discrepancy.

Note that in practice the discrete δ function-like Landau level density of states is broadened due to the existence of disorder activated non-ideal localised states [6] which may have a significant effect on the I/V trace.

The following sections, 7.2.1 and 7.2.2, contain experimental results and analysis for 'InSb-like' and 'GaAs-like' SHETs respectively under $B_\perp$.

7.2.1 'InSb - like' Interface

Figure 7.3 shows how the I/V trace for an 'InSb-like' SHET evolves with $B_\perp$ up to 15T. Noticeably, there are no features before the main resonance as the Landau levels move past one another. Additionally, from 5T onwards an unexpected second region of NDR appears after the main resonance, moving up with bias as the field is increased.

The same trends are evident from the pulsed field plots as illustrated in figure 7.4 for 1771#5. In order to acquire data over the short duration of the maximum of the field pulse, a voltage sawtooth was applied across the sample. This ramped up from 0V to a pre-set maximum bias V_{max} in ¼ ms, before ramping down again. V_{max} is always timed to coincide with the field maximum B_{max}, and consequently the sample experiences a field at zero bias which is slightly less than B_{max}. This slight variation in B over the duration of the I/V trace and the small induced currents resulting from the rapid variation of B both contribute towards the observed difference in the I/V plot of figure 7.4 as the sample voltage ramps up and then down.

The lack of Landau level structure even in the second derivative is intriguing. In chapter 6, evidence was presented of the NDR occurring at biases greater than V_c. It was deduced that electron/heavy hole mixing (which is proportional to $k_\parallel$) was likely to have a significant role in the resonant conduction process. Since $B_\perp$ quantizes $k_\parallel$, the form of the resonance might be expected to change. Figure 7.4 shows that at low

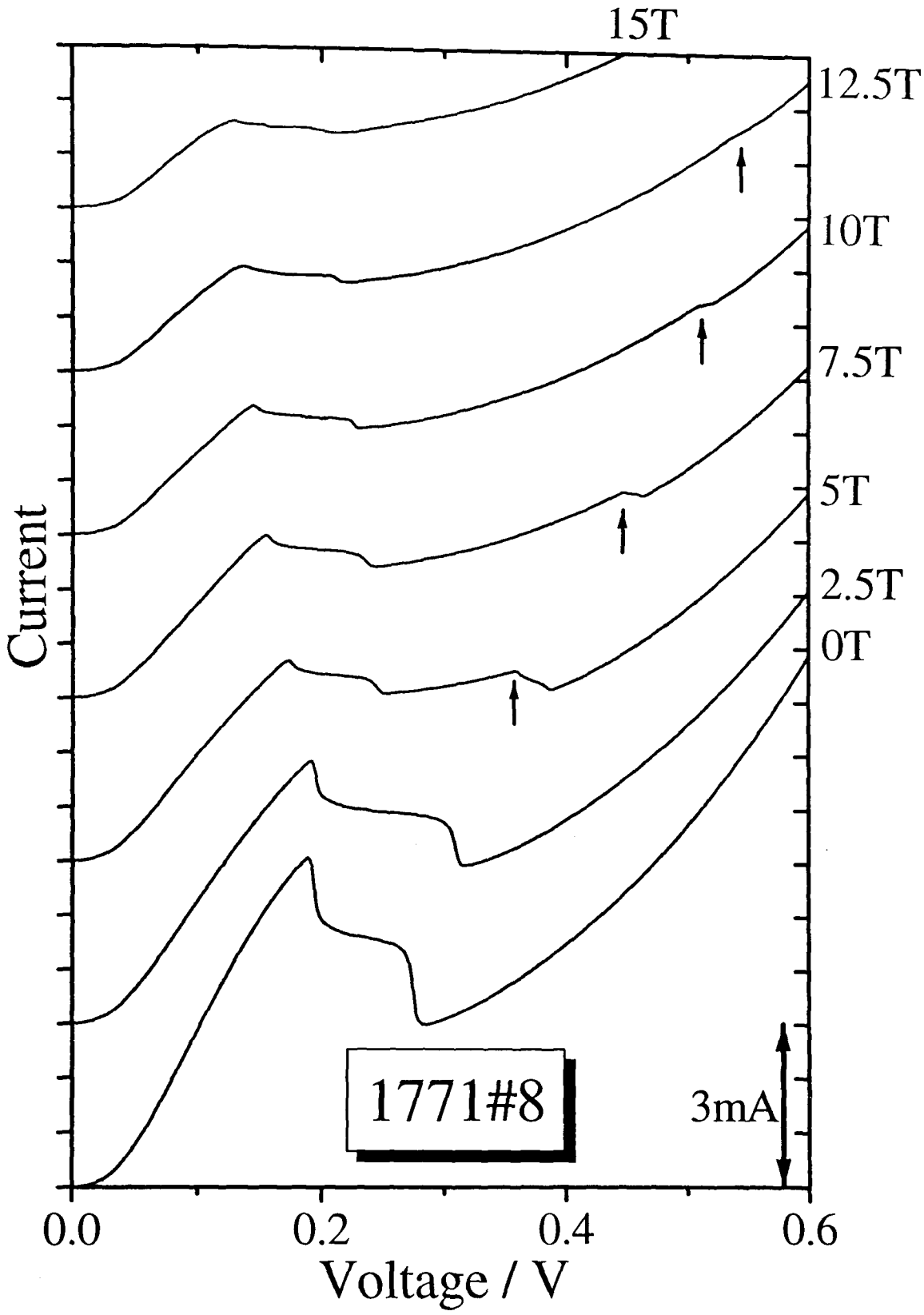


Figure 7.3. Perpendicular magnetic field-induced change in the 4K SHET I/V characteristic for 1771#8. The traces are offset for clarity and the arrows follow the evolution of the second resonance.

fields where many occupied Landau levels are closely spaced, the form of the resonance is similar to that obtained without field. This is consistent with broadening

which would produce a quasi-continuous $k_{\|}$ dispersion. At high fields, however, there are only a few occupied Landau levels. Consequently the $k_{\|}$ dispersion is very different than for the case without field, a fact that is reflected in the form of the resonance. If resonant conduction were solely a product of electron/heavy hole mixing, features before the main resonance would be seen as the Landau levels passed

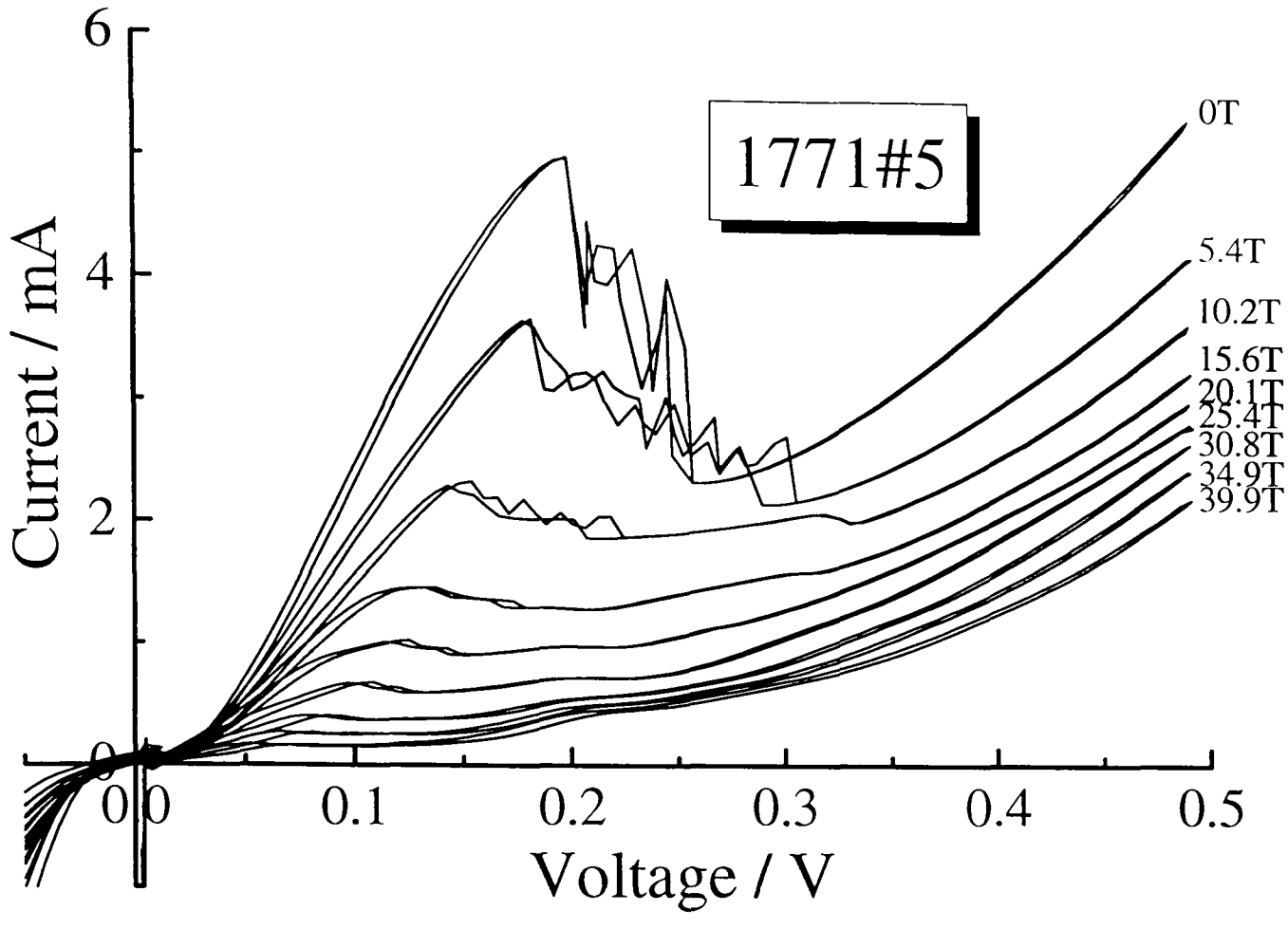


Figure 7.4. I/V traces for 1771#5 taken at pulsed magnetic fields up to 40T applied perpendicular to the SHET interface at 4K. The slight difference in the plots for measurements taken with increasing and decreasing voltage is due to an induced component in the measuring circuit.

each other. The lack of such structure can therefore be viewed as confirmation that electron/heavy hole band mixing is only partially responsible for the observed I/V trace. Additionally, above 20T there is only one occupied electron and hole level which must be pinned together at zero bias. With any voltage increase the levels move apart, inducing a semimetal/semiconductor transition. At these fields, however, the resonance occurs at a finite bias, confirming the conclusion arrived at in chapter 6; that the resonance occurs at some point after the semimetal/semiconductor transition.

Analysis of the experimental data reveals a reduction of I_p and V_p for the main resonance as $B_\perp$ is increased. Figure 7.5 plots I_p against $B_\perp$ for four different mesas of 1771. At zero field all four values of I_p differ by up to 20 %, but as soon as a field is applied the recorded I_p values seem to shift to exactly the same position, a trend that continues as far as the highest measured field. This implies that even though the shapes of the resonances at 2.5 and 0T are similar, some sort of change in the conduction process has occurred under $B_\perp$. This is a very interesting phenomenon and probably indicates that a significant extrinsic contribution to the conduction (due perhaps to interface imperfections) is suppressed at fields above ~5T.

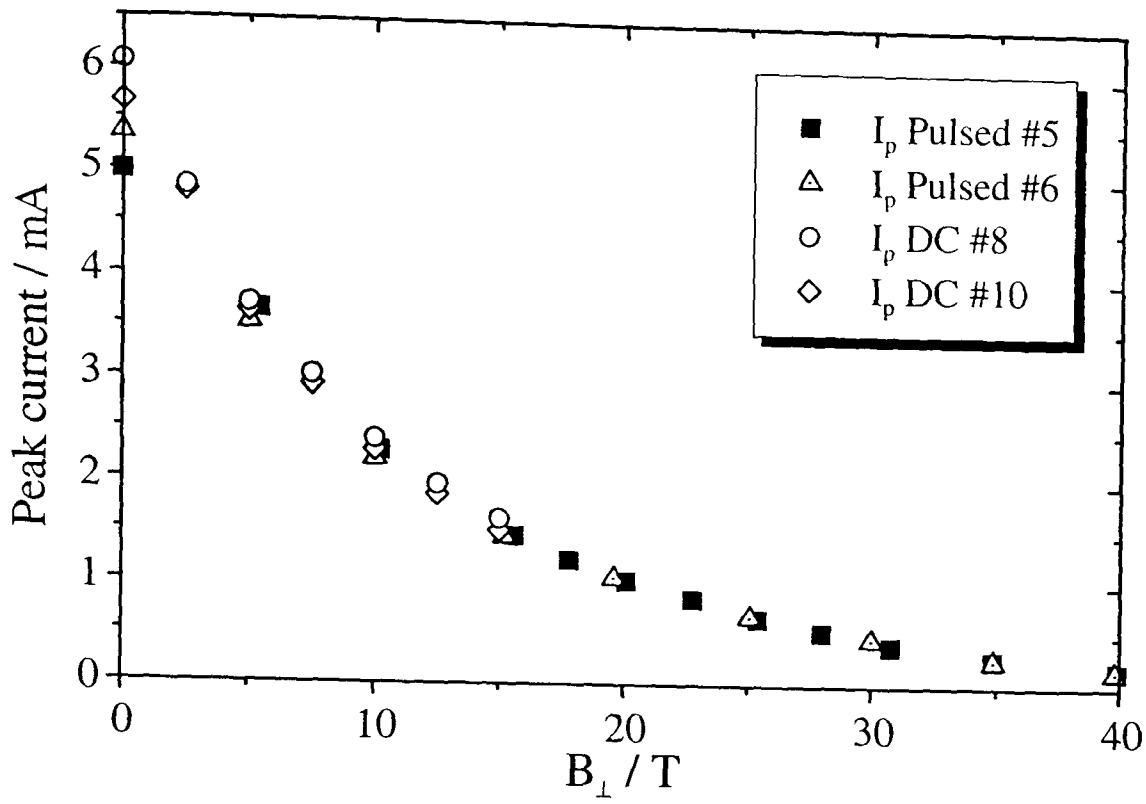


Figure 7.5. Plot of peak current of the main resonance versus magnetic field for four different mesas of 1771.

Figure 7.6 is a plot of peak voltages for the main resonance against field. The spread amongst these points is larger than for the peak currents, principally as a result of the induced e.m.f. generated by the pulsed field. The general trend of a peak voltage decreasing to zero at roughly 60T, however, is in good agreement with the simple estimate made for B_c in section 7.2 for samples with an 'InSb-like' interface.

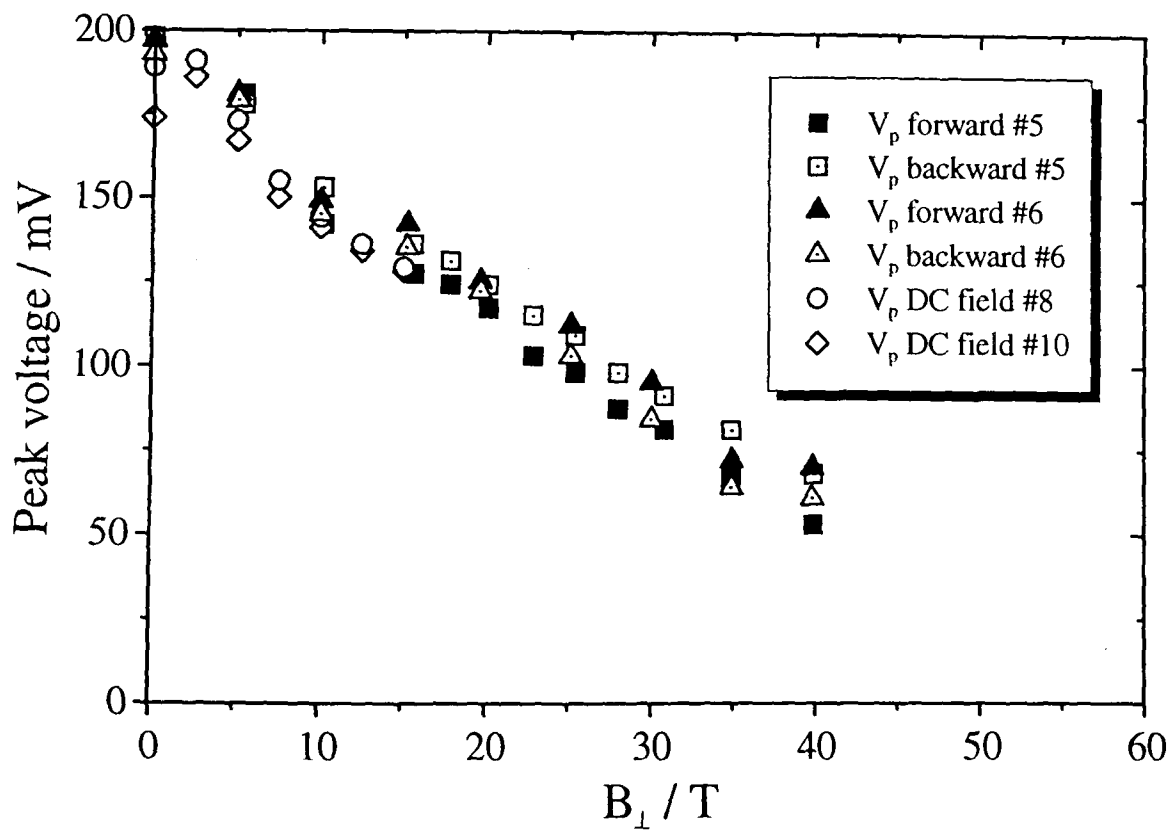


Figure 7.6. Peak voltage for the main resonance versus magnetic field for four different mesas of 1771.

Figure 7.7 shows the variation of the peak current and voltage with $B_\perp$ for the second region of NDR. Both $V_{p,2}$ and $I_{p,2}$ values appear to be very mesa dependent, entirely unlike the corresponding values for the main resonance. This is consistent with a magnetic field induced hindrance to the transfer of charge carriers through a proportion of the interface. The mesa dependent behaviour would then make sense if the affected proportion of each one were different. The NDR clearly occurs after the bands have uncrossed. A jump of the quasi Fermi energy to the next occupied Landau level may produce NDR since the values of n and p will stop increasing as the Fermi level jumps to the next level over a large change in bias. It is clear that an understanding of the origin of this second resonance requires detailed calculations in order to establish the energies and occupations of the Landau levels as a function of field and bias.

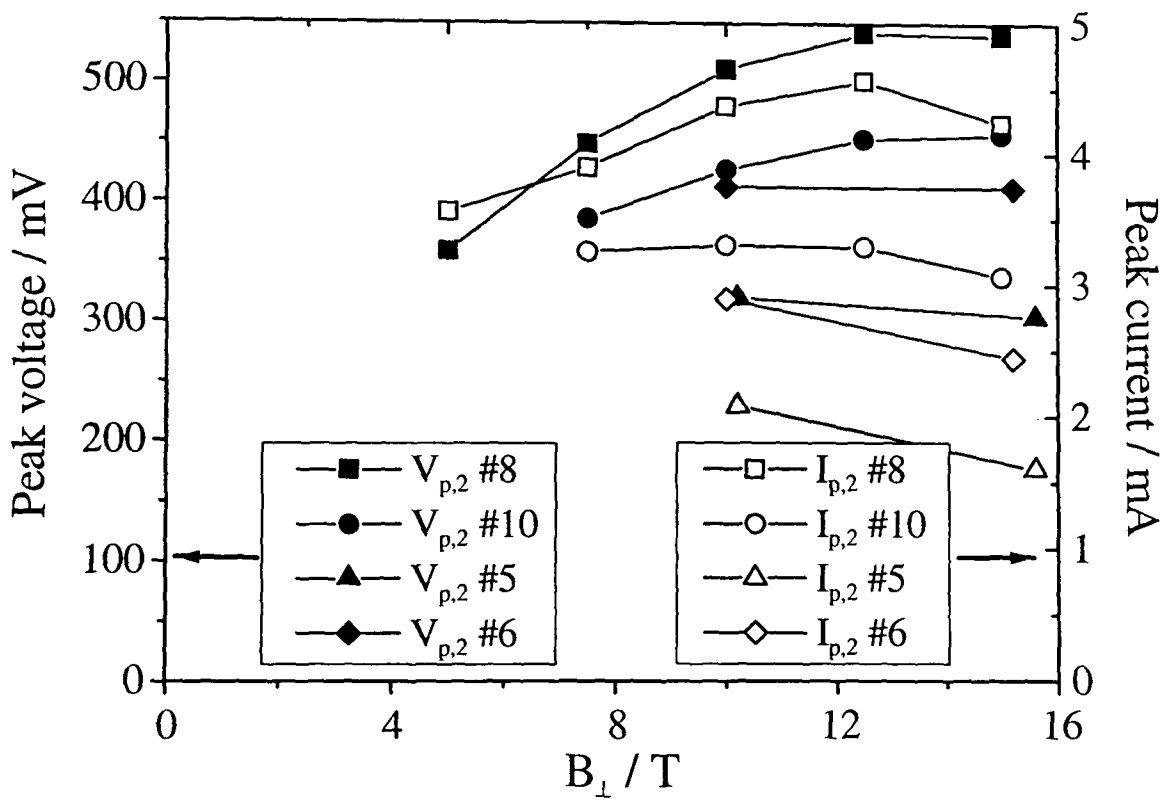


Figure 7.7. Peak currents and voltages for the second low field resonance taken from four different mesas. This shows the random nature of this second resonance when compared with the first one.

Above 20T additional I/V structure appears. A plot of the movement of the voltages at which these features appear against $B_\perp$ is displayed in figure 7.8. A Fang-Howard type calculation in the quantum limit of one occupied electron and hole spin split Landau level has been used to estimate the bias at which n is sufficiently large to wholly populate one spin-split Landau level. Around the bias at which this n is reached, the electron quasi Fermi energy should jump from $E_0^{0\downarrow}$ to $E_0^{0\uparrow}$. Subsequent resonances,

therefore, may be due to these discontinuities. Figure 7.8, however, shows that the calculated trend is quite different from that of the experimental results. Again, we conclude that detailed calculations are needed in order to fully appreciate the behaviour of the SHET under $B_{\perp}$.

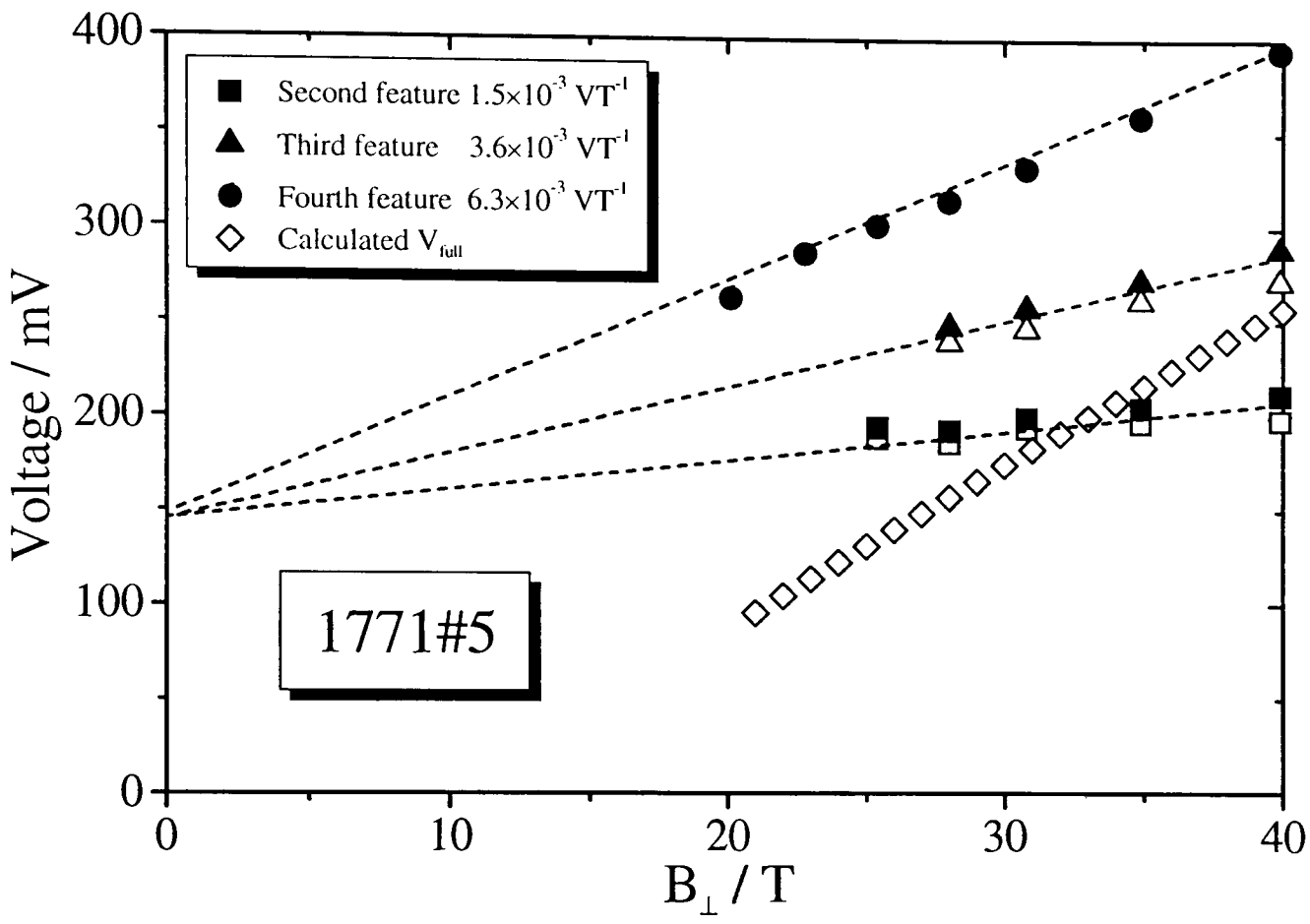


Figure 7.8. Plot of the bias at which the additional high field resonances occur against field for 1771#5. Also shown is V_{full}, which is the voltage, calculated using a Fang-Howard type variational method, at which n is equal to the density of states for one spin-split Landau level.

7.2.2 'GaAs - like' Interface

Figure 7.9 shows the I/V response of 1772 to $B_{\perp}$, illustrating the large difference between the field dependence of vertical transport for the two interface types. The peak currents and voltages decrease as the field is increased, but at a much slower rate than for 1771. Again, there is no evidence for the existence of Landau levels before the main resonance.

Figure 7.10 shows I/V curves for 1772 taken in pulsed fields up to 40T. These results exhibit similar trends to the pressure behaviour, where it is much harder to suppress the resonance in the 'GaAs-like' SHET. It clearly disappears at a much higher field for this interface, whereas the smaller band overlap would imply that it should vanish

sooner.

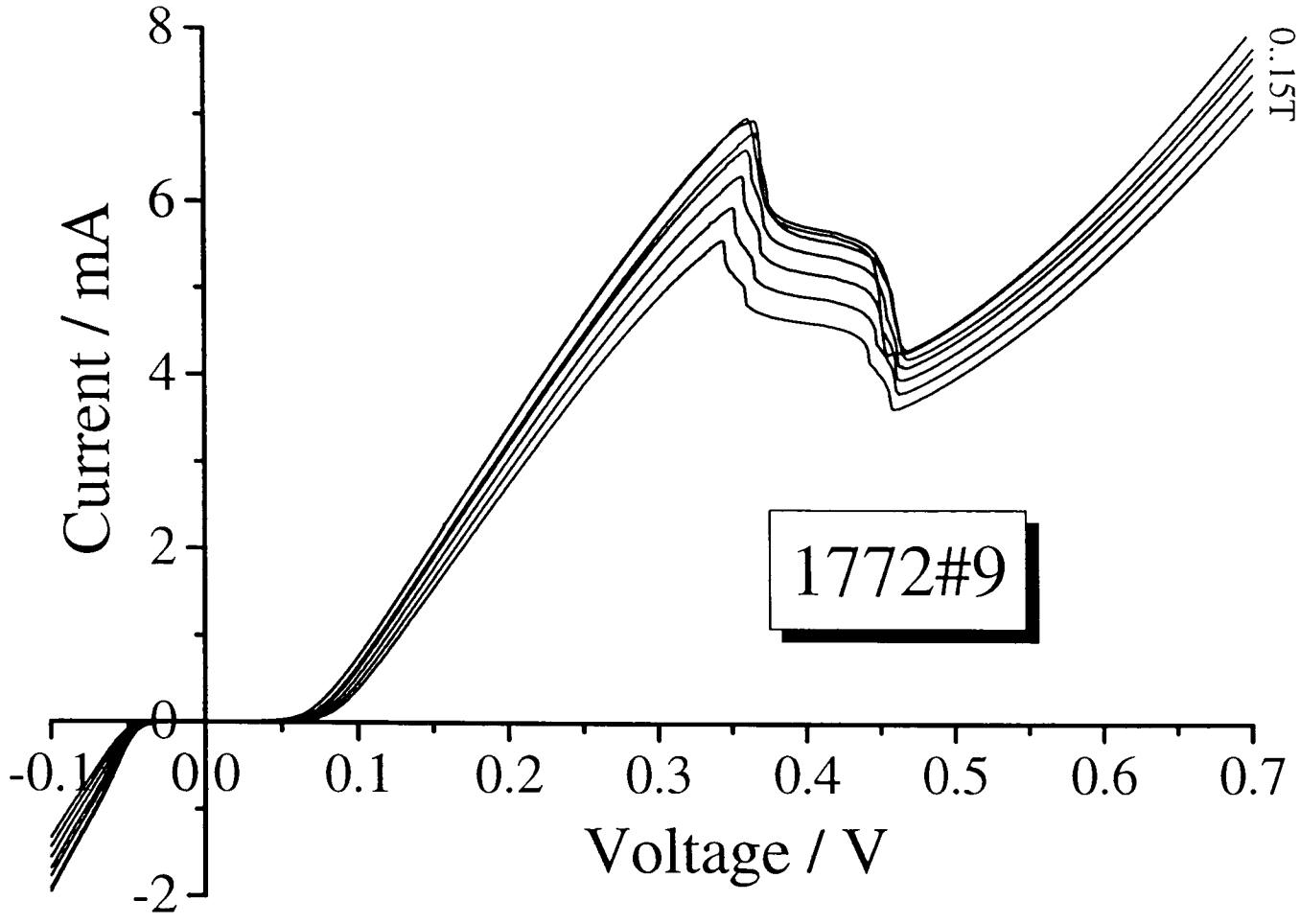


Figure 7.9. Perpendicular magnetic field-induced change in the 4K SHET I/V characteristic for 1772#9.

The low bias I/V plots for 1772#6 in figure 7.10 show a decreasing resistance as the field is increased, a feature that is absent in 1772#9 (figure 7.9). This resistance decrease could be due to sample heating, as the H4 package in which the sample sits is made from a significant amount of metal. Experiments in the near future using the same mesa in both DC and pulsed fields should resolve whether this effect is a property of the mesa or the H4 package.

Figure 7.11 shows the peak currents for 1772#4, 1772#6 and 1772#9 plotted against $B_\perp$. 1772#9 was tested in the DC magnet, whereas results for the other two mesas were obtained using the pulsed field facility. 1772#4 and 1772#6 seem to indicate that $I_p \rightarrow 0$ at around 50T, but this may be misleading as, if higher field data were available, it would probably show an exponential trend for I_p vs. $B_\perp$ (as in figure 7.5). Figure 7.12 is a plot of V_p against $B_\perp$ for the same three mesas which, for 1772#4 and 1772#6, implies that $V_p \rightarrow 0$ at over 100T. In chapter 6, a comparison of I/V traces taken at high pressure and band profile calculations lead to the conclusion that the resonance for the

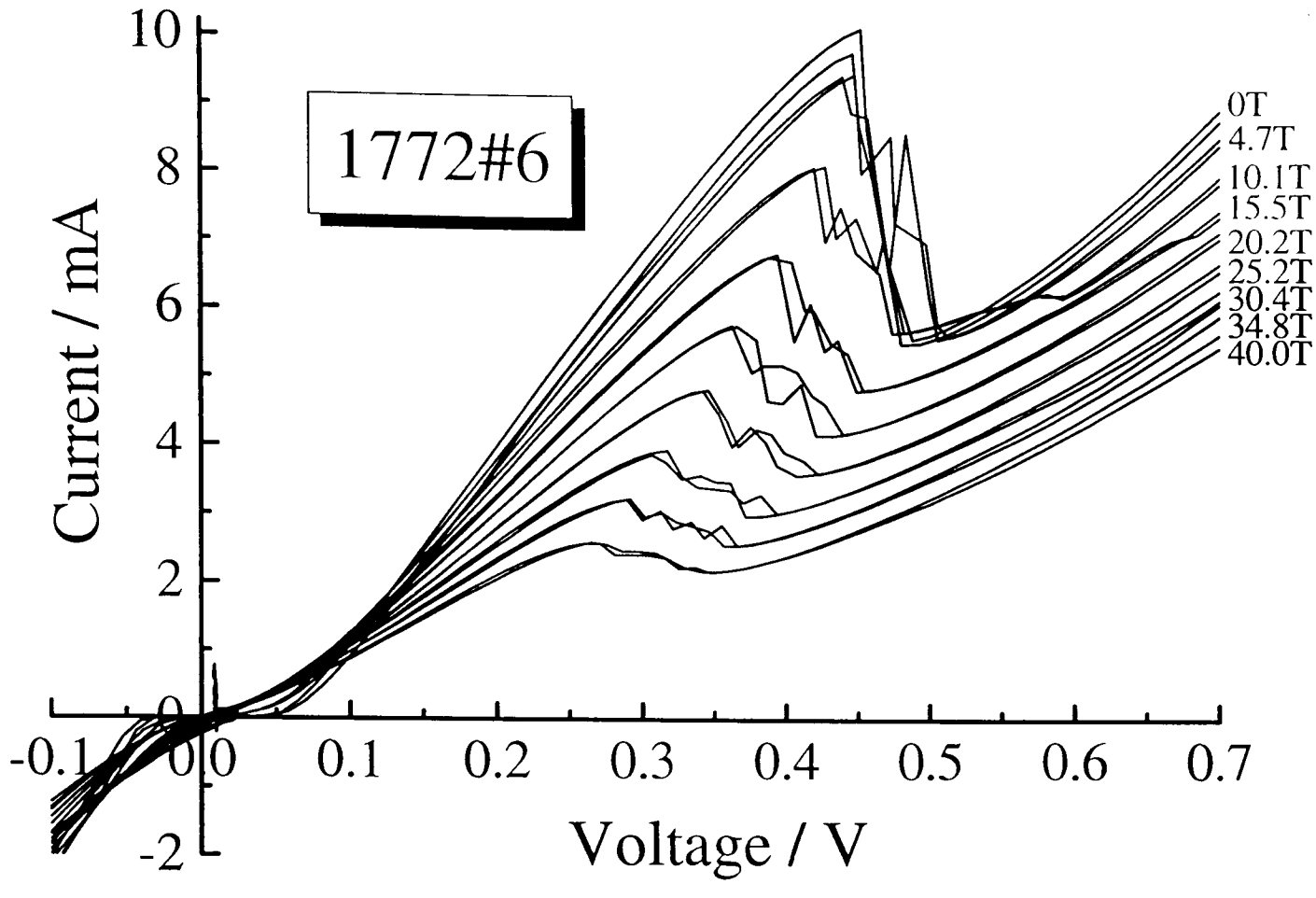


Figure 7.10. I/V traces for 1772#6 taken at pulsed magnetic fields up to 40T applied perpendicular to the SHET interface at 4K.

'GaAs-like' SHET occurs when E_0 and HH_0 are separated by roughly 140 meV. 1772#4 and 1772#6 in figure 7.12 seem to indicate that $V_p \rightarrow 140$ mV at approximately 65T, although the spread of data points makes the error on this figure large. Higher field data is needed in order to clarify these matters.

Figures 7.11 and 7.12 both show the resonance in 1772#9 exhibiting different behaviour to 1772#4 or 1772#6. Furthermore, figures 7.9 and 7.10 reveal that there are no signs of a second resonance in 1772#9. The above evidence suggests that 1772#9 is a sample that may have an alternative interface nature, for example it may have been processed from the wafer edge or the substrate may have had a poor surface morphology in that region. Experiments are soon to be carried out using the same mesa in both pulsed and DC fields to enable a comparison of changes in zero bias resistances and the bias at which the second resonance occurs (if at all).

Note that Takamasu et al. have produced papers [7,8] on the effect of pulsed $B_\perp$ up to 40T on MOVPE grown InAs/GaSb/InAs DHET structures. Although this is a different heterostructure, where the GaSb layer width determines the hole confinement energies, it is useful to note that they did not observe any additional I/V structure

before the main resonance and concluded that the observed peak currents were the sum of transmission coefficients of many resonances rather than individual separate ones.

In summary, therefore, this relatively unexplored area requires complex calculations and theoretical analysis before it is understood fully. Section 7.2 has, however, demonstrated that the I/V traces of 'InSb-like' and 'GaAs-like' SHETs exhibit different dependences on $B_\perp$, with the 'GaAs-like' SHET having an I/V trace that is far more difficult to suppress than its 'InSb-like' counterpart. The latter has a region of NDR that appears to disappear at about the magnetic field induced semimetal/semiconductor transition B_c at zero bias. The former, though, exhibits a strong NDR at 40T, whereas its smaller band overlap value suggests it should have disappeared by 50T. Additionally, the data provides strong evidence that the current resonance occurs after the voltage induced semimetal/semiconductor transition. In the quantum limit of one occupied electron and hole spin-split Landau level for example, the two levels pin together at zero bias and any voltage increase should immediately induce the semimetal/semiconductor transition. However, the experimental I/V traces show clear regions of NDR at a finite bias after the quantum limit has been reached.

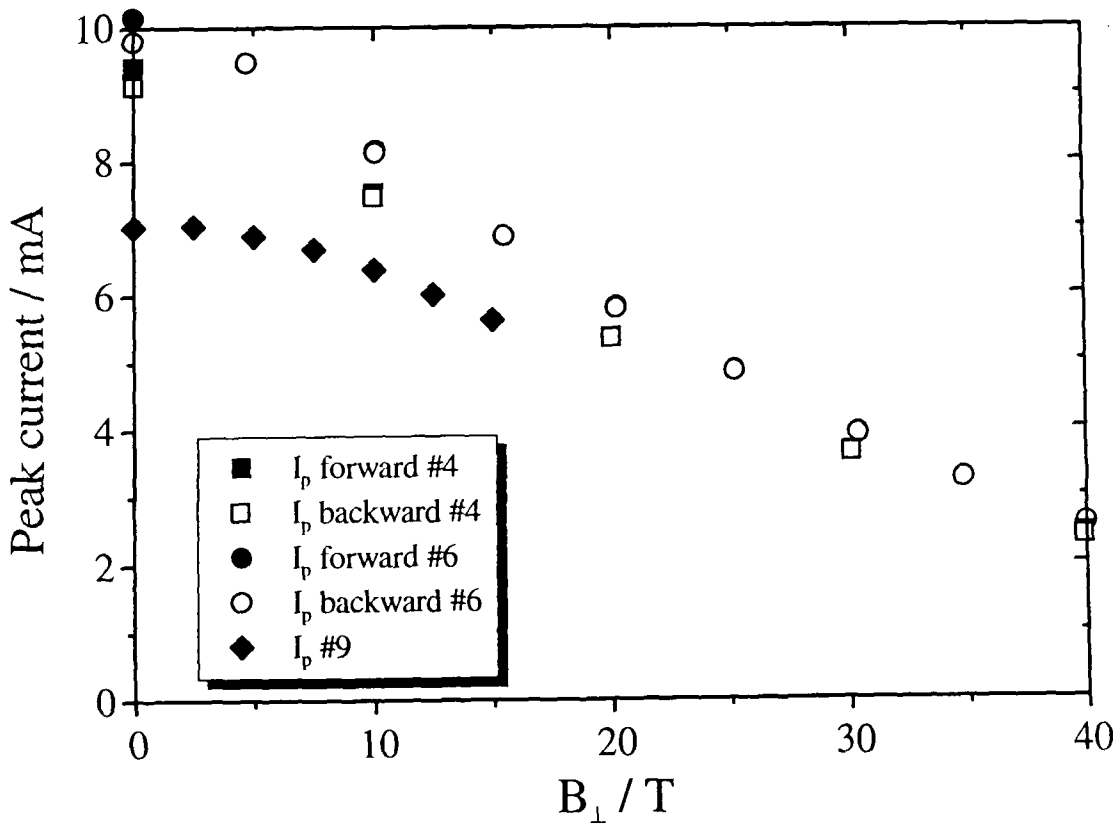


Figure 7.11. Plot of peak current of the main resonance versus magnetic field for three different mesas of 1772.

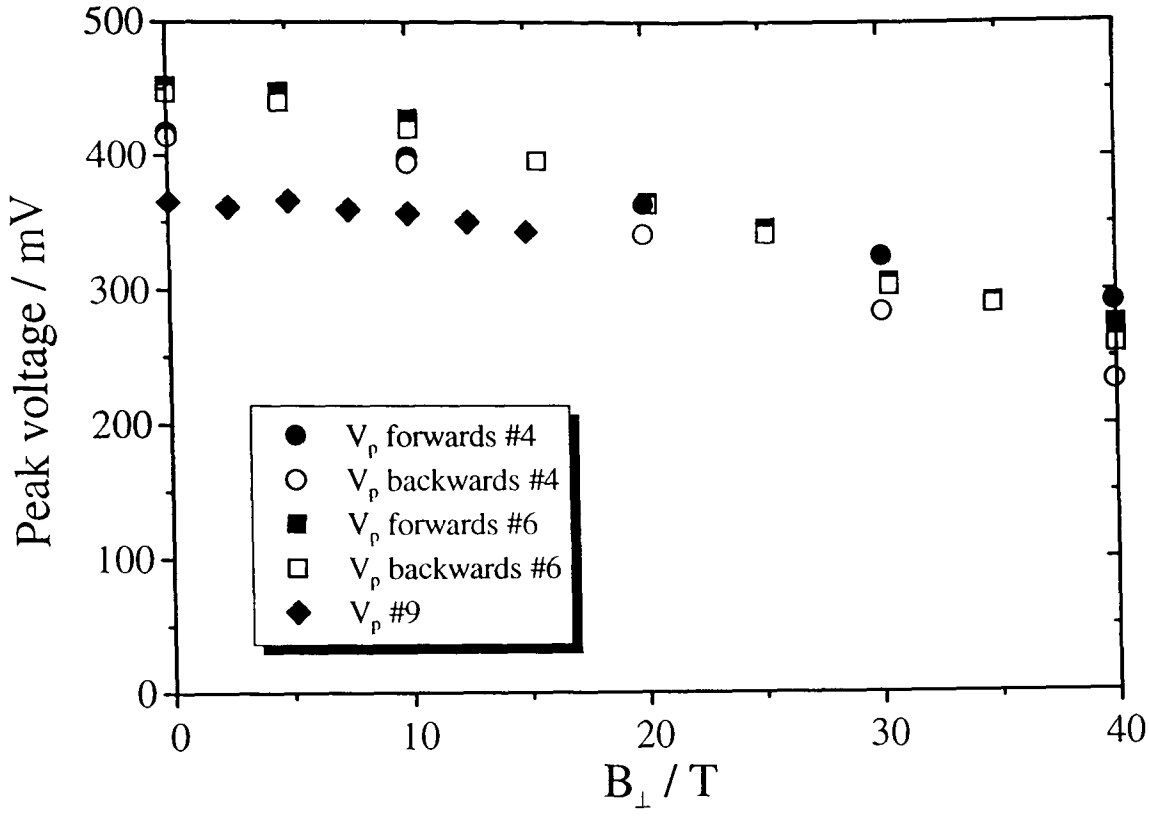


Figure 7.12. Peak voltage for the main resonance versus magnetic field for three different mesas of 1772.

7.3 Field Parallel to the Interface

An electron or hole in a heterostructure under the influence of an external electric field applied perpendicular to the interface acquires no additional in-plane momentum as it propagates through the structure unless it is scattered. When a magnetic field is applied parallel to the heterostructure interface, however, the carrier gains an in-plane wavevector perpendicular to the field. For localised quasibound states this magnetic field can be treated as a perturbation, yielding an expression for the gained in-plane wavevector of:

$$\Delta k_{\parallel} = \frac{eB}{\hbar} \Delta s \,, \tag{7.8}$$

where Δs is the average separation between the quasibound states. This means that, with Δs = 200Å, the in-plane dispersions are completely misaligned by around 10 T, where $\Delta k_{\parallel} \sim 0.016$ Bohr^{-1} (see figures 5.23 and 5.24).

This phenomenon has been used by Hayden et al. [9] to probe the dispersion curves of the confined holes in the valence band of a GaAs/AlGaAs/GaAs/AlGaAs/GaAs double barrier structure. They studied the shift in voltage position of the resonant

peaks with $B_{\|}$, since the criterion for resonant tunnelling is that $\Delta k_{\|}$ has to match that of the quasibound quantum well hole level. This allowed them to reveal experimentally the light/heavy hole admixing.

In the case of the InAs/GaSb SHET, however, the analysis is not so easy because of the non-trivial coupling of the various subbands and their subsequent mixing, and the seemingly explicit dependence of the resonant conduction mechanism on $k_{\|}$. An in-depth calculation taking into account the complicated combined effects of the magnetic and electric fields on the confined charge carriers would be needed in order to predict the effects on the SHET vertical transport I/V trace.

The following two sections contain data from samples whose I/V traces were measured whilst under the influence of $B_{\|}$. Section 7.3.1 considers 'InSb-like' SHETs in DC and pulsed fields, and 7.3.2 considers 'GaAs-like' samples.

7.3.1 'InSb - like' Interface

Figure 7.13 shows the I/V trace for 1771#8 under $B_{\|}$ up to 15T. V_p is seen to increase

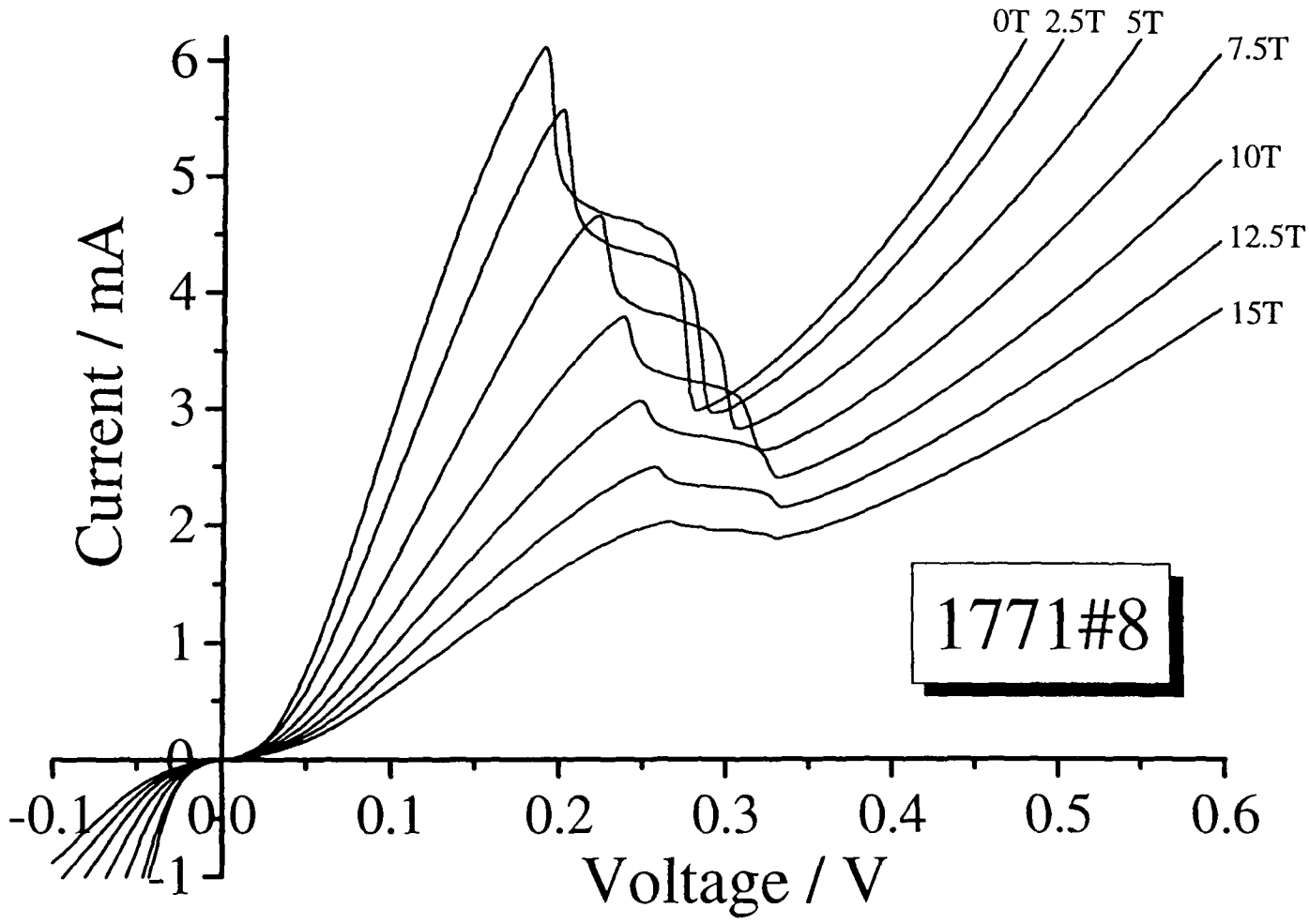


Figure 7.13. Response of the SHET I/V trace for 1771#8 to a DC magnetic field applied parallel to the interface at 4K.

as a function of field, and no additional features emerge. This is in contrast to the behaviour of the same mesa under $B_\perp$ (figure 7.3) which provides clear proof that the second resonance exhibited there is a genuine feature induced by the application of $B_\perp$.

Figure 7.14 contains plots of 1771#5 under the influence of pulsed $B_\parallel$ up to 40T. This confirms the trends of figure 7.13 where V_p moves to a higher voltage as $B_\parallel$ increases to 15T. After this point, however, V_p starts to decrease and by 40T the resonance is small but observable. Figure 7.15 illustrates this trend by plotting V_p against $B_\parallel$ for both 1771#8 and 1771#5.

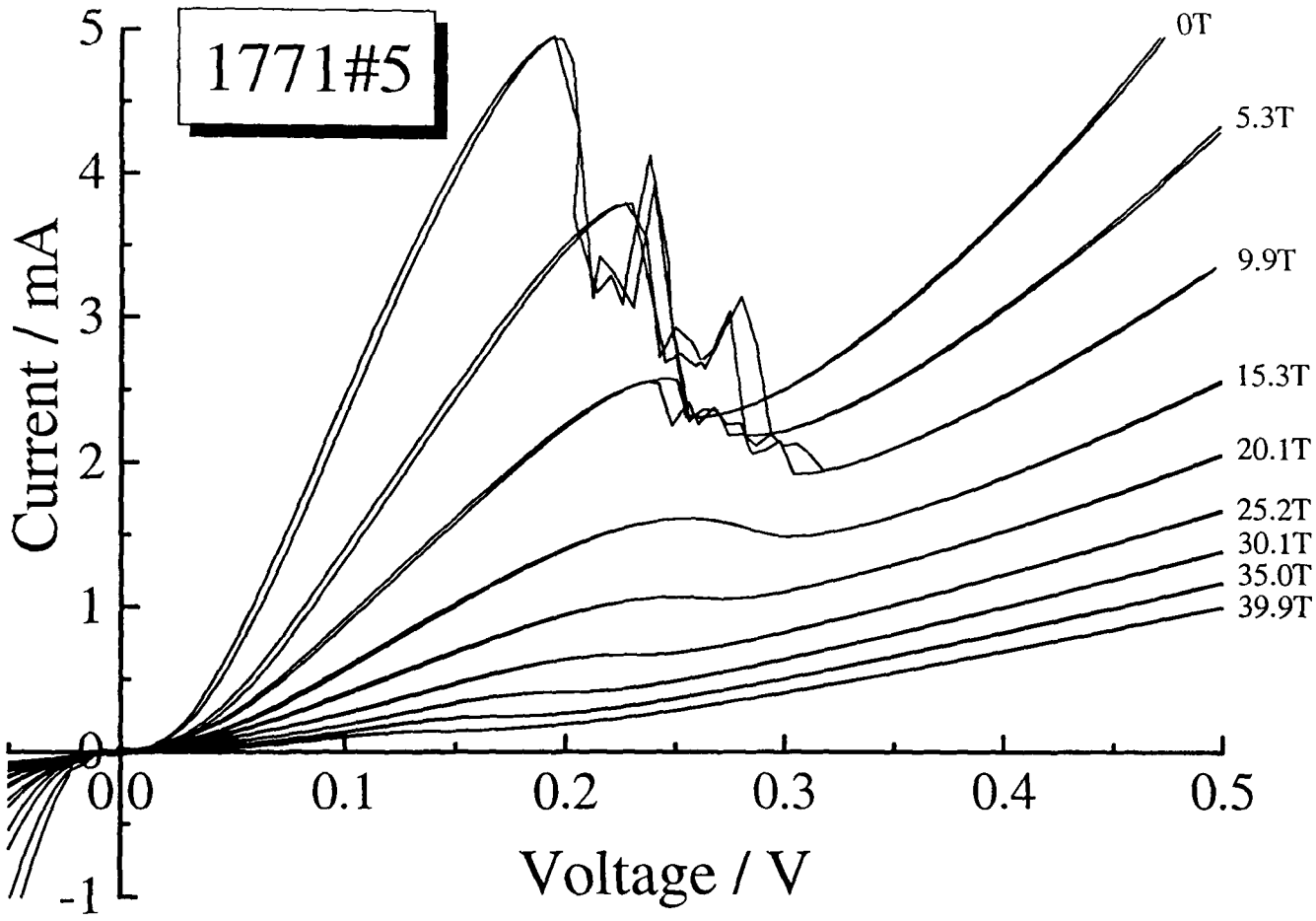


Figure 7.14. I/V traces for 1771#5 taken at pulsed magnetic fields up to 40T applied parallel to the SHET interface at 4K.

The results of figure 7.14 are qualitatively similar to those observed by Takamasu et al. [10] from an InAs/GaSb/InAs DHET structure under pulsed $B_\parallel$ up to 40T. They too saw a voltage increase followed by a decrease as the field increased. They tried to model this behaviour using a two band model of a SHET, assuming the second interface (essentially another SHET in reverse bias) was transparent. Results from these calculations, however, were disappointing with the theoretical trends bearing little resemblance to the experimental traces. This is not an entirely surprising result,

supporting the contention that a detailed theoretical model is needed in order to explain the observed experimental plots.

Figure 7.16 shows the peak currents decreasing with increasing $B_{\|}$.

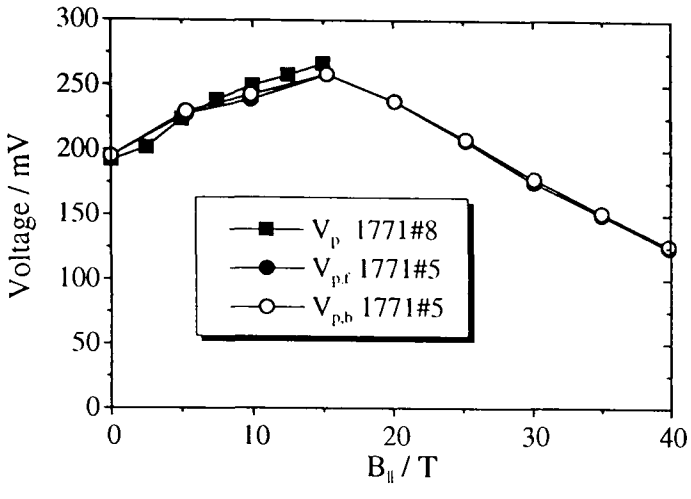


Figure 7.15. Plot of V_p against $B_{\|}$ for 'InSb-like' SHETs.

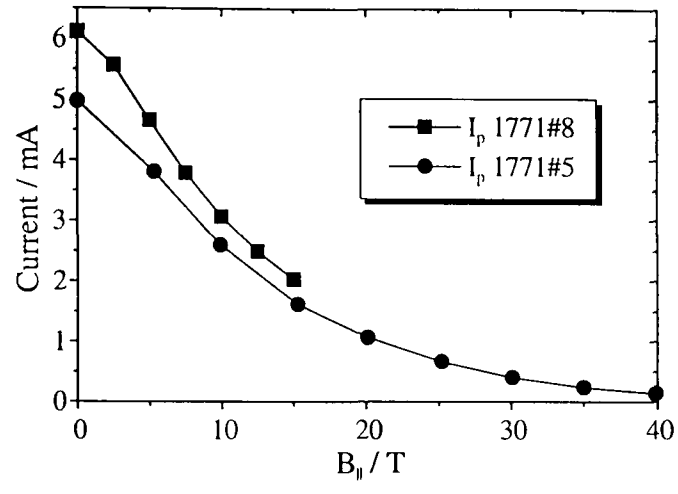


Figure 7.16. Peak currents versus $B_{\|}$ for 'InSb-like' SHETs.

7.3.2 'GaAs - like' Interface

Figure 7.17 shows the I/V plots for 1772#9 under $B_{\|}$ up to 15T. Again, the trends

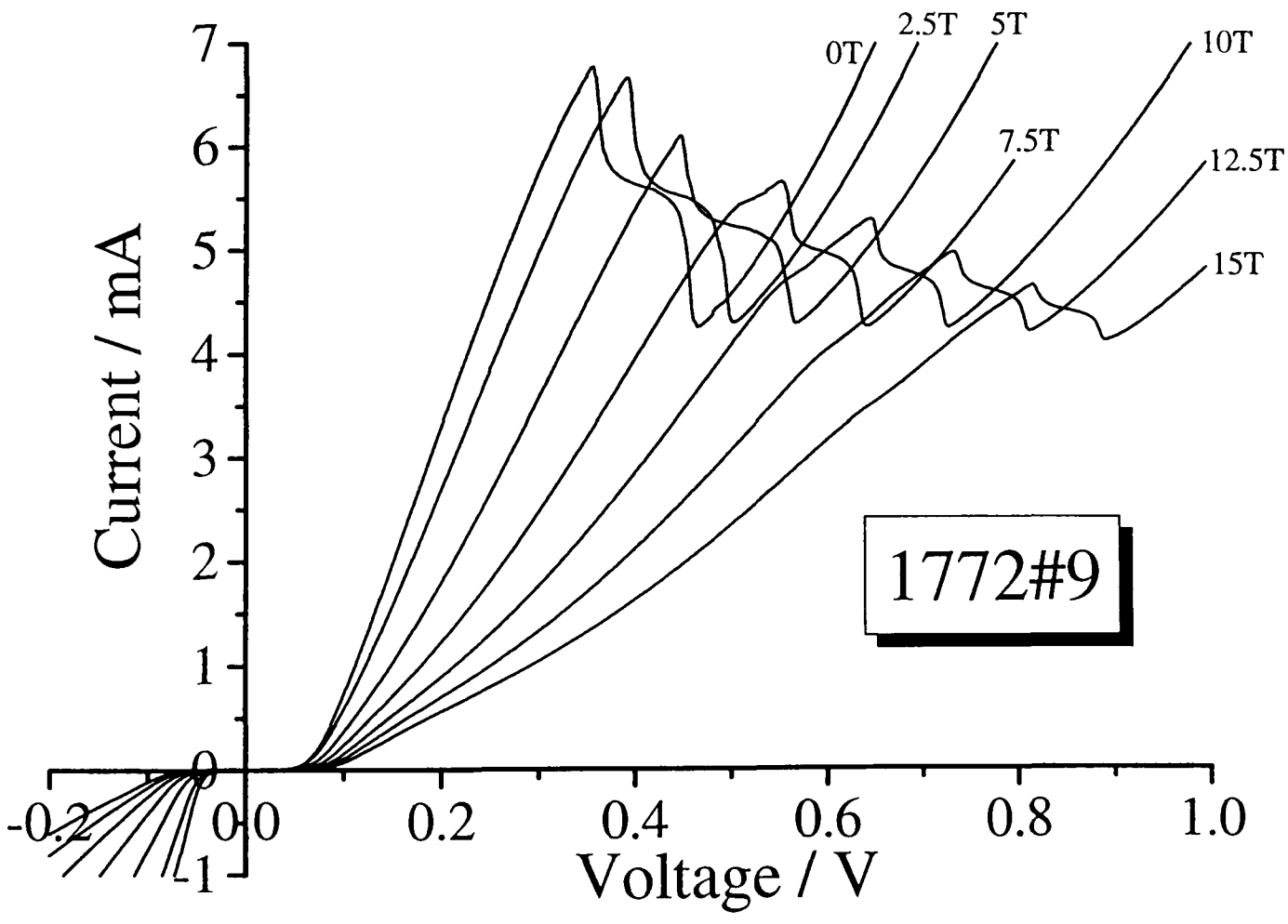


Figure 7.17. Response of the SHET I/V trace for 1772#9 to a DC magnetic field applied parallel to the interface at 4K.

exhibited by this 'GaAs-like' SHET are different to its 'InSb-like' counterpart. V_p increases with increasing $B_{\|}$ as in figure 7.13, but at a faster rate, whereas the valley current remains virtually constant. Additionally, a second feature can be seen emerging below the main resonance at 7.5T. This continues getting weaker until at 15T it becomes a small kink in the I/V plot. Figure 7.18 which contains pulsed field data up to 40T for 1772#6 shows the resonant voltage increasing with $B_{\|}$ even at 34.8T and it also shows a small feature before the main resonance at 9.9T.

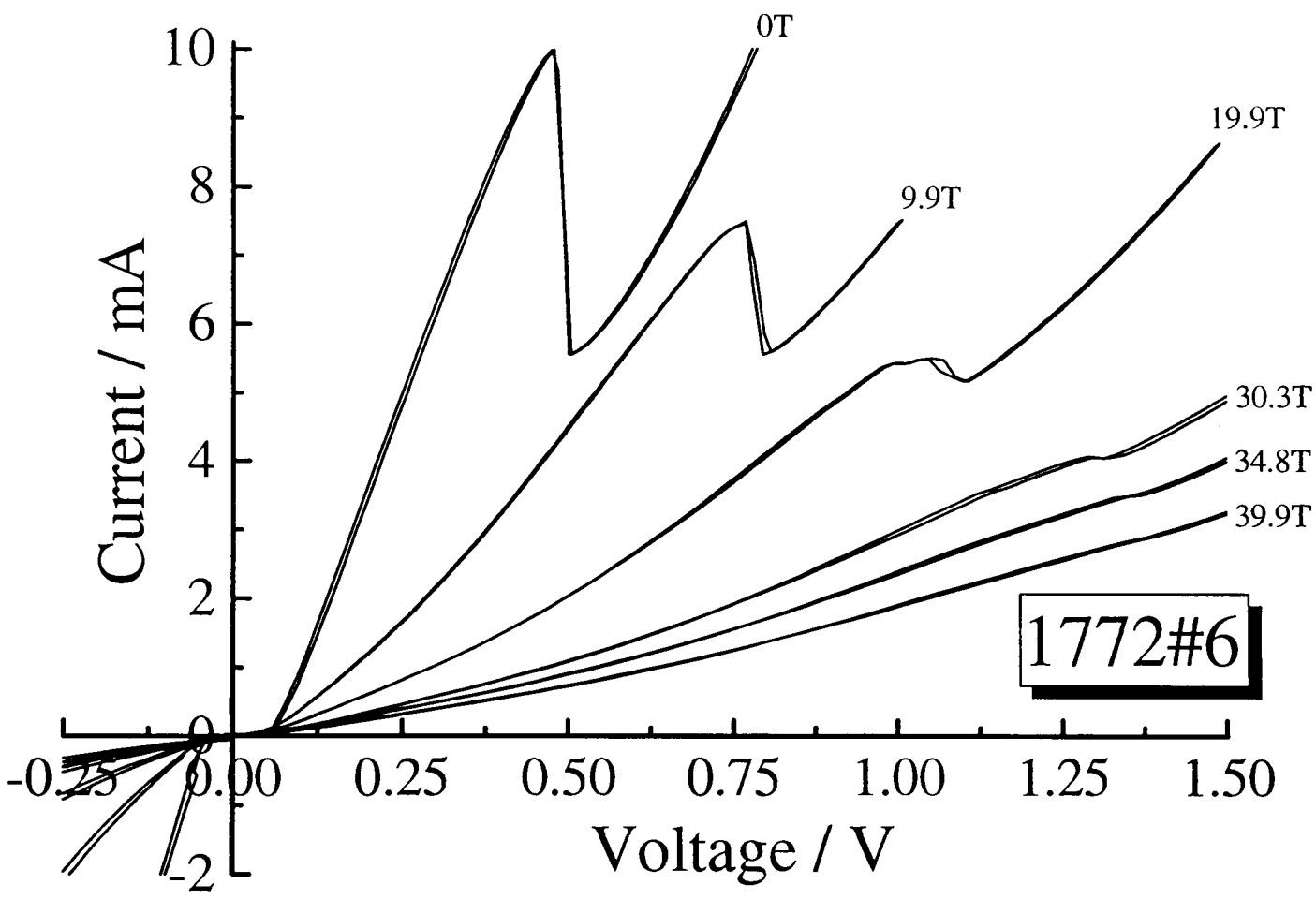


Figure 7.18. I/V traces for 1772#6 taken at pulsed magnetic fields up to 40T applied parallel to the SHET interface at 4K.

This data illustrates that the general trend is for an initial increase in V_p with increasing $B_{\|}$ for both interface types. However, this starts to decrease after 15T for 'InSb-like' SHETs and does not for 'GaAs-like' SHETs. Note that it is quite possible for the 'GaAs-like' resonance to shift towards a lower voltage after 39.9T, and experiments are planned using higher fields.

7.4 Summary

Both $B_{\perp}$ and $B_{\|}$ measurements have provided additional confirmation that the vertical

transport I/V characteristic of the two interface types respond in a very different manner to external stimuli and therefore must be the result of some fundamental difference.

For $B_{\perp}$, the 'GaAs-like' SHET has an I/V trace that is far more difficult to suppress than its 'InSb-like' counterpart. The latter has a region of NDR that disappears at about the magnetic field induced semimetal/semiconductor transition B_c at zero bias. The former, however, exhibits a strong NDR at 40T, whereas its smaller band overlap value suggests it should have disappeared by 50T. Additionally, the data provides strong evidence that the current resonance occurs after the voltage induced semimetal/semiconductor transition. In the quantum limit of one occupied electron and hole spin-split Landau level for example, the two levels pin together at zero bias and any voltage increase should immediately induce the semimetal/semiconductor transition. The experimental I/V traces, however, show clear regions of NDR at a finite bias after the quantum limit has been reached. Complex calculations are needed in order to understand these results in more detail.

For $B_{\parallel}$, V_p increases as the field is increased in both 'InSb-like' and 'GaAs-like' SHETs. The difference, however, is that at 15T, V_p starts to decrease in the 'InSb-like' samples, whereas in samples with a 'GaAs-like' interface, V_p continues to increase until 40T which was the maximum attainable field. Another significant difference between the two interface types is the emergence of a second feature before the main one between 7.5 and 15T for the 'GaAs-like' SHET. The valley current also decreases at a much slower rate for the 'GaAs-like' interface than the 'InSb-like' one. Detailed analysis of these trends, however, awaits results from more sophisticated calculations than are available at present.

7.5 References

[1] E E Mendez, H Ohno, L Esaki & W I Wang. Physical Review **B** 43, p5196 (1991).

[2] E E Mendez, J Nocera & W I Wang. Physical Review **B** 45, p3910 (1992).

Continued ...

References Continued ...

[3] J Singh. Physics of Semiconductors and their Heterostructures International Edition, McGraw-Hill, Singapore, p676 (1993).

[4] Landölt & Bornstein. Semiconductors, Physics of Group IV Elements and III-V Compounds, Springer-Verlag, Berlin, p312 (1982).

[5] T Vaughan. Private Communication.

[6] M J Kelly. Low Dimensional Semiconductors - Materials, Physics, Technology and Devices, p88 (1995).

[7] T Takamasu, N Miura, K Taira, K Funato & H Kawai. Surface Science 263, p217 (1992).

[8] T Takamasu, N Miura, K Taira, K Funato & H Kawai. Physica B 184, p259 (1993).

[9] R K Hayden, D K Maude, L Eaves, E C Valadares, M Henini, F W Sheard, O H Hughes, J C Portal & L Cury. Physical Review Letters 66, p1749 (1991).

[10] T Takamasu, N Miura, K Taira, K Funato & H Kawai. Physica B 201, p380 (1994).

8 Concluding Remarks

8.1 Summary

This study has shown that clear NDR features can be seen in single heterojunction n-InAs/p-GaSb diodes. By investigating the NDR in samples with interfaces grown by three different MOVPE switching sequences, it is found that that sequence A (as defined in section 2.2) produces SHET structures with a vertical transport I/V characteristic that is both the strongest and the most uniform across the wafer. This confirms the Raman evidence taken from multiple interface structures grown in the same reactor, that the use of sequence A results in near ideal monolayer interfaces.

This thesis has also demonstrated that the SHET vertical transport I/V characteristics are different depending upon whether the interface is 'InSb-like' or 'GaAs-like'. An investigation into the temperature dependence of the I/V traces further highlights this discrepancy. The 'GaSb-like' SHET has a weak temperature dependence with a PVR of approximately 1.8 at 77K, whereas the 'InSb-like' SHET has an NDR that is virtually invisible at room temperature, and yet has risen above 2 by 77K. This has possible repercussions for any future components. If operation at room temperature is desired for example, then components grown with a 'GaAs-like' interface are the obvious choice.

Reverse bias transport measurements as a function of hydrostatic pressure have successfully provided a means of probing the band overlap Δ. Their use has lead to the discovery that 'InSb-like' single interface structures have a larger Δ than those grown with a 'GaAs-like' interface. These experiments also produce data that is consistent with results obtained by Daly et al. using parallel transport measurements on multiple interface structures grown in the same MOVPE reactor [1]. These are that Δ decreases at around -9.5±5 meV/kbar for both interfaces, P_c is roughly 16 kbar and 13 kbar for an 'InSb-like' and 'GaAs-like' SHET respectively and that Δ^{InSb} is 155±5 meV and Δ^{GaAs} is 125±5 meV.

Forward bias I/V measurements under pressure reveal more differences in the vertical transport behaviour of the two interface types. The NDR feature is found to disappear with Vp→0 and Ip→0 as Δ→0 (i.e. as the pressure is increased) for samples with an 'InSb-like' interface, and the resonant component of the current is seen to vanish before 18 kbar. Self consistent calculations have been performed, modelling an 'InSb-like' interface using a value for Δ of 160 meV. When compared with experimental observations, results from these calculations indicate that (with the experimental traces corrected for a series resistance of 20Ω) the voltage at which E_0 and HH_0 cross each other V_c occurs shortly after V_p (the voltage at which the NDR peak occurs). The valley voltage V_v then corresponds to an energy difference between E_0 and HH_0 of slightly more than one phonon energy. This is consistent with the current resonance consisting of elastic processes (due to electron/hole mixing) that reduce zo zero around V_c and inelastic processes (due to phonons and impurities) that are able to carry on past V_c.

The 'GaAs-like' interface does not behave so predictably with pressure under forward bias. Not only does a noticeable feature exist at 21 kbar where the band overlap is calculated to be in the region of -100 meV, but the NDR also occurs at a much higher bias than expected. The pressure and perpendicular magnetic field dependence of the peak and valley voltages are consistent with the resonance occurring when E_0 - HH_0 is between 120 and 140 meV. Consequently this interface must support a very different conduction mechanism to that exhibited by the 'InSb-like' one.

A mechanism attributed solely to single or multiple phonon events would either imply a single phonon with an energy of 140 meV (which is the calculated value for E_0-HH_0 at resonance for a 'GaAs-like' SHET) or an extremely efficient 'cascade of phonons' process, where each electron (for example) travels through multiple intermediate states, emitting a phonon at each stage.

The first explanation is not plausible because of the phonon energy required and the second is unlikely to produce the high current densities observed in 'GaAs-like' SHETs if the intermediate states are virtual states.

A mechanism that may provide single stage energy losses in the 140 meV range that

does not involve phonons is one comprising electrons excited by Auger processes. In this case an electron in the E_0 sub-band can lose energy by exciting another electron in E_0 into a higher unoccupied sub-band or into the conduction band continuum. Analysis of these processes is complex and beyond the scope of this thesis, but it is difficult to explain why the Auger mechanism occurs specifically when E_0-HH_0 is 140 meV (i.e. why it does not occur at 60 or 200 meV) although it is consistent with the high charge densities exhibited by the 'GaAs-like' SHET, a necessary requirement for Auger effects.

An alternative explanation for multiple stage energy losses and perhaps the most plausible one is that of interface impurity scattering. A high concentration of interface states for SHETs with a 'GaAs-like' interface may provide the necessary real intermediate states for charge carriers travelling through the interface. An 'imperfect' interface containing many dislocations or impurities introduced at growth time could, for example, provide the necessary concentration. Electrons are then able to scatter into these states at voltages significantly greater than V_c. The high density of states this process requires only exist in a region localised to the interface and so the electron has to lose energy (via phonon emmission for example) in order for a current path to exist.

The background current is found to be relatively insensitive to temperature changes for both interface types, ruling out a thermally activated process. Tunnelling as a one step mechanism is also discounted since this would be blocked by the bulk band gaps. Phonon assisted processes such as charge transport through interface states (mediated by phonon emission) or tunnelling into band gap impurity states in the vicinity of the interface (with intermediate phonon emission) seem to be the most likely candidates, although a thorough investigation is needed in order to further clarify the origin of the background current. Analysis of the pressure dependence has shown that this non-resonant current component is not simply proportional to n or p. In fact, the decrease in the background current with hydrostatic pressure is entirely consistent with a rapidly increasing energy separation with pressure between the lowest electron and highest heavy hole states.

$B_\perp$ measurements have provided additional confirmation that the vertical transport I/V characteristic of the two interface types respond in a very different manner to external

stimuli (e.g. pressure, temperature, magnetic fields). The 'GaAs-like' SHET has an I/V trace that is far more difficult to suppress than its 'InSb-like' counterpart. The latter has a region of NDR that disappears at about the magnetic field induced semimetal/semiconductor transition B_c at zero bias. The former, however, exhibits a strong NDR at 40T, whereas its smaller band overlap value suggests it should have disappeared by 50T. Additionally, the data provides strong evidence that the current resonance occurs after the voltage induced semimetal/semiconductor transition. In the quantum limit of one occupied electron and hole spin-split Landau level for example, the two levels pin together at zero bias and any voltage increase should immediately induce the semimetal/semiconductor transition. The experimental I/V traces, however, show clear regions of NDR at a finite bias after the quantum limit has been reached. Complex calculations are needed in order to understand these results in more detail.

I/V traces from 'InSb-like' and 'GaAs-like' SHETs under $B_{\|}$ also show strong interface dependent differences. The bias at which the main resonance occurs in samples with a 'GaAs-like' interface, for example, increases significantly with increasing $B_{\|}$, and another feature develops before the main resonance. V_p for the 'InSb-like' SHET, however, increases initially and then starts to decrease as the field is raised. Detailed analysis of these trends await results from more sophisticated calculations than are available at present.

Although this thesis has provided a significant contribution to the understanding of vertical transport in a SHET, there is still much to learn. There are key experimental and theoretical areas that require investigation to further improve the comprehension of this area of physics. These are summarised below, together with proposals for future research in MOVPE grown InAs/GaSb vertical transport structures.

8.2 Future Development

Apart from the ***k.p*** type calculations that are needed in order to better understand the phenomena reported in this thesis, there are experimental areas that are closely linked with this research. The first of these is to combine pressure, field and temperature in order to reduce B_c. By pressurising samples in the 'Russian cell' and placing them in

the DC magnet, I/V traces at 4K can be taken. With a sufficiently high pressure (around 10 kbar) it is possible to reduce Δ by nearly 100 meV. Under these conditions, n and p are far smaller initially and the $B_{\perp}$ needed to induce the semimetal/ semiconductor transition is far smaller. This would allow detailed probing of the high field traces in both bias directions, analysis that is currently difficult due to the induced e.m.f. and variable B in the pulsed field I/V traces. Additionally, pulsed fields of 50-60T should soon be attainable and the new pressure cell designed to fit into the pulsed field facility should be operational in the near future.

The next MOVPE growth run for vertical transport structures will include SHETs grown on GaAs substrates. This will facilitate a comparison between nominally identical structures grown on different substrates. Samples with GaAs substrates will, of course, be top contacted, i.e. a contact will be made to the GaSb from the mesa side of the wafer. In this way it may be possible to eliminate inconsistencies in the I/V trace caused by variation in the GaSb substrates. Also, if this investigation proves successful, [111] oriented GaAs substrates can be used which would alter the band profile by introducing a piezoelectric field across the structure. Variation of other growth-time parameters such as the doping level or the InAs cap layer thickness can also be used to tune device performance.

There are many varieties of InAs/GaSb DHET structures whose vertical transport behaviour can be investigated. At present only GaSb/InAs/GaSb single quantum wells can be grown because of the non epi-ready nature of InAs substrates and difficulties with the growth of InAs buffer layers. Even with this constraint, however, samples with a single interface type (i.e. both 'InSb-like' or both 'GaAs-like') can be used to compare vertical transport through interfaces that are grown with InAs on GaSb and those grown with GaSb on InAs. The effect of mixed interface structures (i.e. 'InSb-like' and 'GaAs-like' in the same sample) on the I/V trace can also be studied, and the ability to vary the quantum well width provides an additional experimental variable.

Apart from the SHET and DHET, there exists the possibility of incorporating $In_{1-x}Ga_xSb$ into the structures in order to alter the electrostatics. The $In_{1-x}Ga_xSb$ is capable of acting as a well or barrier for the electrons depending upon the value of x. Also, analysis of the effects of strain on the I/V trace is possible because of the lattice

mismatch.

The rich variety of research that remains in this material system before it can become commercially viable will provide much scope for experimental and theoretical work in the near future.

---

[1] M S Daly, D M Symons, M Lakrimi, R J Nicholas, N J Mason & P J Walker. Proceedings of International Conference on EP2DSXI, Nottingham, England, p165 (1995).

Appendix A

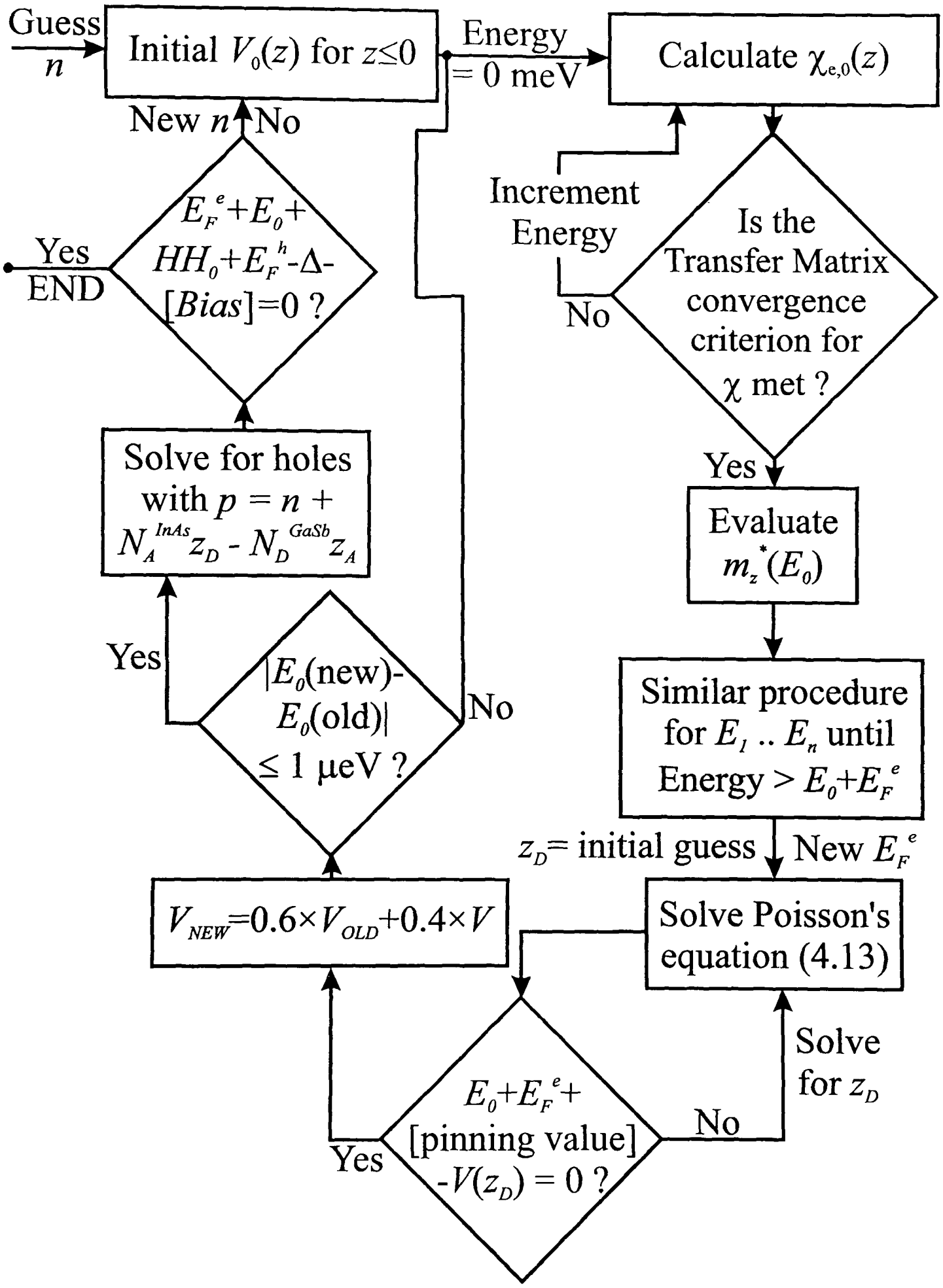


Figure A.1. Flow diagram of the band edge profile calculations described in chapter 4.

Appendix B

Parameter	InAs	GaSb
Band edge electron effective mass m_e^*	$0.023m_0$	-
In-plane heavy hole mass $m_{||}^*$	-	$0.1m_0$
Heavy hole mass perpendicular to the interface m_z^{hh*}	-	$0.3m_0$
Light hole mass perpendicular to the interface m_z^{lh*}	-	$0.05m_0$
Non parabolicity parameter K_2	-0.86	-
Relative permittivity ε_r	15.15	15.69
Concentration of compensated minority donors N_D^{GaSb}	-	10^{15} cm^{-3}
Concentration of compensated minority acceptors N_A^{InAs}	10^{15} cm^{-3}	-
Band gap at 0K E_g	418 meV	811 meV
Rate of Γ point band gap increase with pressure	10 meV/kbar	14 meV/kbar

Table B.1. Table of variables used in calculations in this thesis